Author:
Lawrence Bright, Eleanor S

Title:
Understanding UN Nuclear Fuel

A Study of the Fundamental Physical Behaviour and Degradation of Uranium Nitrides

Understanding UN Nuclear Fuel:
A Study of the Fundamental Physical Behaviour and Degradation of Uranium Nitrides

---

By Eleanor Lawrence Bright

School of Physics

A dissertation submitted to the University of Bristol in accordance with the requirements of the degree of Doctor of Philosophy in the Faculty of Science.

August 2019

Word count: 51 233

Abstract

Improvements in safety and economic performance are sought for the future of the commercial nuclear power industry and can partly be provided by an improved fuel. Uranium mononitride, UN, offers higher thermal conductivity and uranium density compared to the widely used UO_2, however, understanding of the fundamental and applied behaviour of UN must be improved if it is to be used as a nuclear fuel. Thin films provide highly versatile, idealised samples that are well suited for investigations into such properties. Epitaxial UN and U_2N_3 thin films have been grown for the first time using reactive DC magnetron sputter deposition, enabling new measurements of the intrinsic properties of these materials. Characterising these samples, x-ray photoelectron spectroscopy and anisotropic resonant scattering performed at the M_4 edge for first time show the mixed bonding present in U_2N_3, highlighting the differences between UN and U_2N_3. Resonant scattering measurements also provide insight into the antiferromagnetic ordering of both UN and U_2N_3. Thin films also provide ideal samples for surface investigations, facilitating a highly controlled approach to researching the degradation of UN. A study of UN oxidation shows that a passivating oxide layer forms and a U_2N_3 interlayer is present even during room temperature oxidation. The effect of radiation on corrosion is also considered, with investigations comparing the the effect of exposure to H_2O_2, mimicking radiolytic products, on UN, U_2N_3, and UO_2. The relative corrosion resistance of UN shows that this is an area of research that needs further consideration. Finally, the implications of these results for the fundamental understanding of UN and its application as a nuclear fuel are considered.

Acknowledgements

I would like to thank everyone who has helped and guided me through my PhD. I am grateful to the Engineering and Physical Sciences Research Council and the National Nuclear Laboratory for providing funding for this project.

Many thanks to Ross Springell for providing excellent supervision and making my PhD a thoroughly enjoyable experience. To Gerry Lander, thank you for your kind guidance and invaluable depth of knowledge. Thanks to Dave Goddard for your insight and understanding of the context of our work. The Interface Analysis Centre has been an entertaining and welcoming research group to be a part of, and I would like to thank all its members, but especially the thin film team: Sophie, Ed, Joe, Dan, Jacek, Lottie, and Angus.

I would like to express my gratitude to Mattia Cattelan and Neil Fox for providing easy access and training at the nanoESCA lab. Thanks to Dan Porter and Steve Collins for facilitating a rewarding experiment at Diamond I16 beamline. To Angus Siberry, Keivan Samani, and Kasia Clarke, thanks for your assistance with the corrosion investigations. Many thanks to James Darnbrough for your proactivity and work on the oxidation study, especially the TEM. To Sophie Rennie, thank you for your enthusiastic help with everything, but most of all with phone calls.

On a more personal note, I am so thankful to Kate, Lottie, and Sophie for keeping me human throughout my PhD with great friendship, chat, and food. Thank you to Anya for taking me on adventures. I am very grateful to my mother for your unwaivering support, especially when writing my thesis, and to my father for always taking an interest in my work. Finally, thank you to all my family for the constant encouragement.

Author's declaration

I declare that the work in this dissertation was carried out in accordance with the requirements of the University's *Regulations and Code of Practice for Research Degree Programmes* and that it has not been submitted for any other academic award. Except where indicated by specific reference in the text, the work is the candidate's own work. Work done in collaboration with, or with the assistance of, others, is indicated as such. Any views expressed in the dissertation are those of the author.

SIGNED: ..... DATE: .....

Contents

List of Figures

List of Tables

Chapter 1

Introduction

Nuclear power provides a ready and reliable solution for the challenge of meeting increasing global energy demands while decreasing carbon dioxide emissions. Consequently, over the past 8 years the global power output from nuclear reactors has been growing, currently making up 10.5 % of the worlds supply, as shown in Figure 1.1 [1]. This growth has come with a drive for increased efficiency to improve the economic viability of nuclear power and improved safety in reaction to the issues highlighted by the Fukushima Daiichi accident in 2011. With this comes the potential need for a new, advanced technology fuel (ATF) with greater safety margins and economic performance.

The excellent thermal properties of uranium mononitride, UN, make it a standout amongst the ATF candidates, however, UN remains a relatively understudied material. Consequently, the main aim of this thesis is to improve fundamental understanding of the properties of UN relevant to a nuclear fuel. As it is always important to understand the context of research, we begin with an introduction to the nuclear power industry and advanced technology fuels.

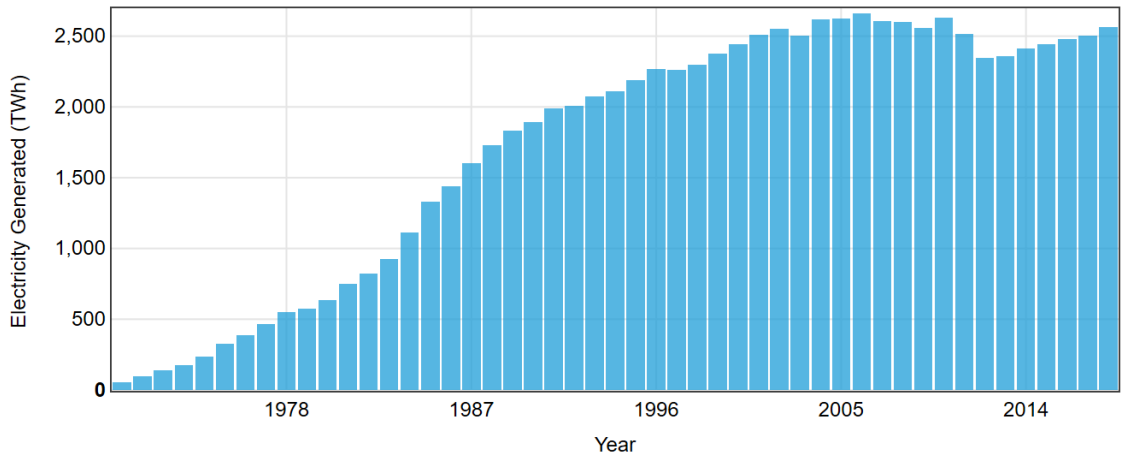

Figure 1.1: *Net global nuclear electricity production, from [1].*

1.1 The Nuclear Power Industry

1.1.1 A Brief History

The birth of nuclear technologies arguably occurred when Otto Hahn found that the bombardment of uranium with neutron produced barium, and Lise Meitner correctly interpreted this as the splitting of the uranium nucleus, coining the term 'nuclear fission' [21]. The realisation that a chain reaction of nuclear fission could be created and weaponised occurred just as World War II was starting and prompted rapid interest and funding in nuclear technologies [22]. Subsequently, the first successful chain reaction was achieved in 1942 by Enrico Fermi, who used graphite blocks to moderate the neutrons (decrease their kinetic energy) released by fission of the uranium fuel. This increased the probability that they would be captured by ^{235}U, causing a further fission event, releasing more neutrons, and therefore creating a chain reaction [23].

After the devastating consequences of nuclear weapons were displayed, the peaceful applications of nuclear technologies became a greater focus. The ability to harness the vast amounts of thermal energy released by nuclear fission and transform it into electricity was first shown by EBR-1 in Idaho, USA [24]. Later, Calder Hall was built in the UK, the first reactor to generate electricity on an industrial scale, showing the viability of commercial nuclear power generation, though the reactor was also intended to produce plutonium for weapons [25].

As the focus of nuclear technologies continued to shift further away from weapons and towards power production, the designs of nuclear reactors also changed to better suit this purpose. Commercial reactors moved away from metallic fuels in favour of UO_2, marking the start of generation II of nuclear reactor designs. Likewise, graphite moderation and gas cooling became less prevalent (though is still widely used in the UK's ageing fleet today), with water preferred as both a coolant and moderator. These choices of moderator material, coolant fluid, and fuel form are the characteristics used to categorise different reactor designs.

1.1.2 Reactor Designs

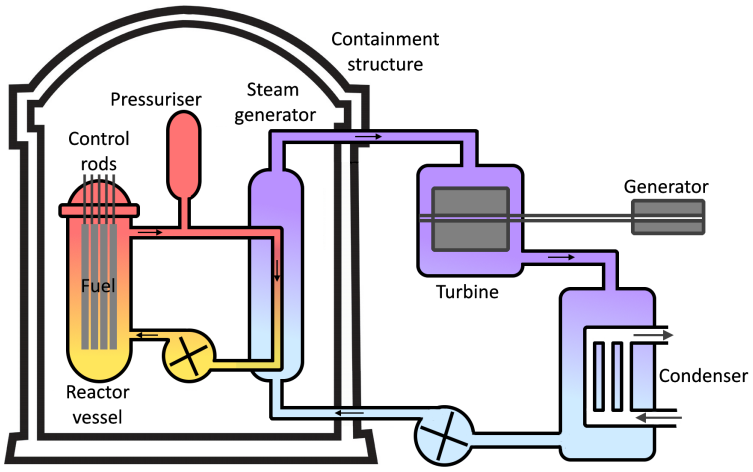

Figure 1.2: *Diagram of a pressurised water reactor, showing primary (orange) and secondary (blue) loops.*

Currently, the majority of commercial nuclear reactors are light water reactors (LWRs), using light water moderation and cooling. These reactors are responsible for over 89 % of the global nuclear electricity capcity [1]. Furthermore, 48 of the 54 commercial reactors currently under construction are LWRs [1].

LWRs commonly use UO_2 fuel pellets, enriched up to 5 % in ^{235}U, clad in a zirconium alloy. This cladding acts as both a fission product containment system and a corrosion barrier from the water coolant and moderator. Using water for both moderation and cooling means that as the reactivity and therefore thermal output of a reactor increases, the temperature of the water also increases, causing the density to decrease. As the water density decreases, the moderation of neutrons also decreases, causing a decrease in the reactivity and creating a negative feedback loop that provides

stability and safety to the reactor.

LWRs can be sub-divided into two categories depending on whether the water coolant is designed to boil or stay liquid as it removes thermal energy from the fuel. Pressurised water reactors (PWRs) maintain pressures of around 155 bar, keeping the water liquid as it is heated from 275 °C to 315 °C as it flows through the reactor core [26]. Boiling water reactors (BWRs) allow boiling of the water coolant under a pressure of 75 bar [26]. As BWRs produce steam, this can be used to directly drive turbines and generate electricity, whereas PWRs require a steam generator with a secondary cooling loop at lower pressures to produce steam for driving turbines, as shown in Figure 1.2. BWRs and PWRs also have other differences in design, such as control rods (neutron absorbers used to control the reactivity) that are loaded from the top in a PWR and from the bottom in a BWR to avoid corrosion that could occur in the steam environment at the top of the reactor vessel.

At present, the majority of the reactors that are under construction or recently completed use what are known as generation III designs, having improved economics and passive safety features making then safe for a number of days without operator action or electrical power [1]. Though these improvements are a step in the right direction, further improvements in reactor economics are required to compete with the cost efficiencies of other power sources.

The Carnot efficiency of a heat engine such as a nuclear reactor is limited by its output temperature, which in the case of a PWR is the triple point of water [27]. Consequently, alternative coolants that can operate at higher temperatures will be used in the next generation of nuclear reactor design, increasing the Carnot efficiency. With these higher temperatures comes a need for a fuel that has robust thermal properties. Though UO_2 has a very high melting point of 2874 °C, its low thermal conductivity means that the centre of UO_2 fuel pellets can reach very high temperatures (above 1800 °C in a LWR [28]), making them unsuitable for use in a high temperature reactor [29]. Consequently, a nuclear fuel with improved thermal conductivity is sought for generation IV nuclear reactors.

1.1.3 Nuclear Accidents and Response

Despite the many benefits of commercial nuclear power generation, one of its most significant drawbacks is safety concerns and public perception of this safety. Nuclear accidents have had a detrimental effect on this perception, however, they have prompted those involved in nuclear power to improve the safety of different aspects of the industry.

Though the Chernobyl disaster in 1986 was the most severe, the reactor design (graphite moderated and water cooled) and scenario were very different to most reactors today, and it is therefore not an accident of particular interest in this work.

An accident occurred at a PWR at Three Mile Island Nuclear Generating Station, USA in 1979 [30]. A steam release valve in the pressuriser was opened to accommodate the rise in temperature created by a malfunction in the secondary loop, but then did not close when it was ordered and believed to be closed. This allowed a loss of coolant in the primary loop of the reactor that was not recognised by the operators, eventually exposing the fuel elements. With this loss of cooling, the core temperature increased, causing the zirconium cladding to react with the steam, releasing hydrogen gas. The reactor core suffered a partial meltdown, releasing fission products into the coolant. This accident occurred due to the compounding factors of mechanical failure, design flaws, user interface issues, and human factors [30]. In response to this, aspects such as reactor core monitoring systems, control room layout, and operator training were significantly improved [31].

More recently, an accident occurred at the Fukushima Daiichi Nuclear Power Plant due to the catastrophic Tohoku earthquake in 2011. After the tsunami caused by the earthquake breached the defenses of the power plant and flooded back-up generators, cooling of the BWRs was lost. In 3 reactors, the subsequent temperature rise due to decay heat led to fuel meltdown and the oxidation of the zirconium cladding, releasing hydrogen gas [32]. This gas leaked, leading to an explosion that released radioactive material into the environment [33, 34]. In response to fears raised by this accident, global nuclear energy production decreased significantly, as shown in Figure 1.1.

Both of the accidents described above were complex in their causes and how they transpired, however, they both highlighted issues with zirconium cladding and the ability to remove thermal energy from the reactor core. When considering changes and advancements in the nuclear industry, whether for the current generation of reactors or the next, it is imperative to improve safety margins in all possible areas. Consequently, improvements to nuclear fuel and cladding in not only economic, but also safety, performance are being pursued.

1.2 Advanced Technology Fuels

Though research and development on the currently used UO_2 fuel and zirconium alloy cladding continues, alternatives, referred to as advanced technology fuels (ATFs) or sometimes accident tolerant fuels, are also being sought [35, 36]. Ideally, these ATFs should improve on the safety issues caused by the high temperature oxidation of zirconium cladding and the residual heat stored in the fuel during an accident scenario. Additionally, the performance of ATFs during normal operation should be improved compared to UO_2 and zirconium cladding, overcoming the issues of pellet-clad interaction, and the low thermal conductivity of UO_2 which decreases with burn-up, limiting the lifetime of the fuel. Furthermore, ATFs should offer economic benefits if they are to be widely adopted by commercial industry.

1.2.1 Claddings

Corrosion resistant materials are sought for potential ATF claddings to improve on the oxidation and hydrogen generation behaviour of zirconium. However, these materials should also have properties that make them suitable for normal operation, such as a low neutron absorption, robust thermo-mechanical properties, and ability to retain fission products [36]. A number of possible options have been identified and are currently being investigated, with a good summary provided by Youinou *et al.* [37].

Metallic alloys such as iron chromium aluminum (FeCrAl) are of interest due to their good corrosion resistance and mechanical properties, though their relatively large neutron cross-section would have to be offset with either higher enrichment or a higher U density fuel [38, 39]. Molybdenum alloys with improved ductility, corrosion, and oxidation performance are also being considered. Mo has a high melting point of 2600 °C and good mechanical properties, however, as its corrosion resistance is less favourable, coating options are being considered [40]. Corrosion resistant coatings are also being considered for the currently used zirconium alloy cladding [41]. Silicon carbide composites offer many positive attributes such as excellent irradiation, high-temperature corrosion, and neutronic performance, but fabricating thin-walled tubes with hermetically sealed ends is challenging with these materials [38, 42].

1.2.2 Fuels

An improvement in fuel thermal conductivity has benefits for the normal operation, economics, and safety of a nuclear power station. Centreline temperatures during normal operation will be lower, reducing the rate of fission gas release [37]. This will allow extended burn-up of fuels and the ability to operate at higher temperatures, improving reactor economics. Safety margins are increased by a larger difference between centreline temperature and melting point, and with faster cooling and less stored heat in an accident scenario [43]. An increased U density is another desired property for potential ATFs, giving the economic benefit of either higher burn-up or lower enrichment, or offsetting the neutron cost of some of the potential ATF claddings.

Table 1.1: *Physical properties of potential ATFs compared to UO_2. Data from [3, 4, 18–20].*

	Thermal conductivity at 300 °C (W/m·K)	Melting temperature (°C)	U density (g/cm^3)
UO_2	5	2874	9.6
U-10%Mo	22	1122	16.9
U_3Si_2	14	1665	11.3
UN	17	2830	13.5

Some of the physical properties of potential ATFs and UO_2 are shown in Table 1.1. U-10% Mo alloys show very high thermal conductivity and fissile density compared to UO_2, however, the melting point is considerably lower. U_3Si_2 has improved U density and thermal conductivity compared to UO_2 and has a higher melting point than U-10% Mo, though it is still well below that of UO_2. UN has thermal conductivity and U density higher than U_3Si_2 and UO_2, and its melting point is very close to that of UO_2. Based on these properties, UN may appear to be an ideal ATF, but there are drawbacks in the neutron absorption cross-section of ^{14}N and its reactivity in air and steam. A more in-depth description of these properties of UN in comparison to UO_2 is provided in the following chapter.

Chapter 2

UN as a Nuclear Fuel

An overview of the fundamental properties of the uranium nitrides is presented in this chapter, followed by a comparison of the properties of UN and UO_2 relevant to nuclear fuel performance. Subsequently, an outline of the areas of research presented in this thesis is given.

When considering the potential for UN to be used as an advanced technology fuel, it is essential to compare its properties to those of the most widely used fuel, UO_2. Not only does UN need to provide improved safety characteristics compared to UO_2, as the nuclear power industry is a commercial industry, UN should also provide improved economic performance if it is to be widely adopted. This chapter aims to provide an overview and comparison of the properties of UN pertinent to the safety and economic performance of a nuclear fuel, based on current literature. This will also allow the areas where improved understanding is needed to be highlighted, showing some of the problems that this thesis aims to investigate.

First, it is important to have an understanding of the fundamental properties of UN as these form the basis of the more functional properties of UN as a nuclear fuel. As it is unlikely that UN will exist solely as a single phase material

throughout the fuel cycle, it is necessary to consider all phases that may form. Consequently, this chapter begins with an introduction into the uranium-nitrogen system and some of the fundamental properties of UN and U_2N_3, before going on to compare UN and UO_2 properties.

2.1 The Uranium-Nitrogen System

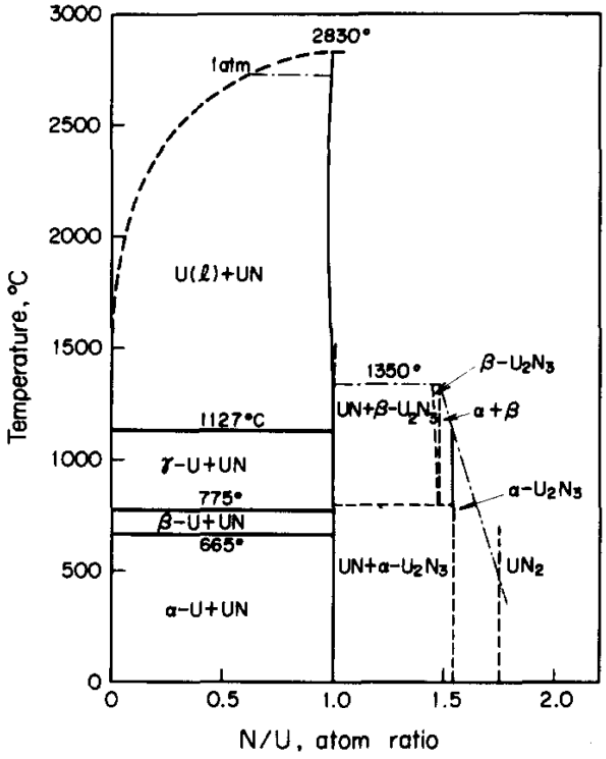

Figure 2.1: *Phase diagram of the uranium-nitrogen system, from [2].*

Uranium is the heaviest of the naturally occurring elements with Z = 92, and is a member of the actinide series of elements, the series corresponding to the filling of $5f$ orbitals. The complicated and extensive nature of these $5f$ electrons gives uranium a range of interesting and unusual properties. Uranium is able to bond with nitrogen, Z = 7, in a range of different structures and stoichiometries, creating the uranium-nitrogen system. These are displayed in the phase diagram of the uranium-nitrogen system, shown in Figure 2.1.

Of the various compounds present in this phase diagram, the focus of this work is on UN, the potential nuclear fuel,

and α-U_2N_3, as it may form during the oxidation of UN [44]. The hexagonal high temperature U_2N_3 phase, β-U_2N_3, forms only above 800 °C, and is not of interest here. Consequently, α-U_2N_3 will hereafter be referred to simply as U_2N_3.

2.1.1 UN

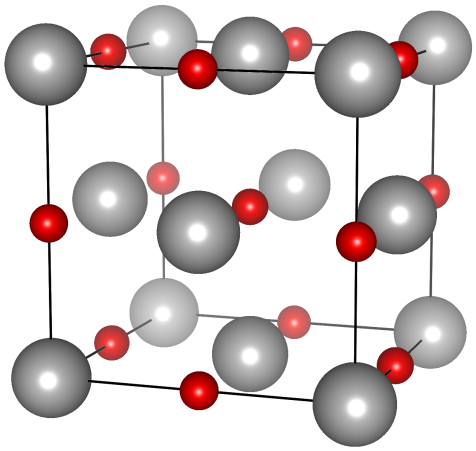

Figure 2.2: *Diagram of the crystal structure of UN, with U shown in grey and N shown in red.*

Uranium mononitride, UN, crystallises in the face-centered cubic (f.c.c.) NaCl structure, space group $Fm\bar{3}m$, with a lattice parameter of 4.890 Å [45]. This structure is depicted in Figure 2.2, where is can be seen that each N atom is surrounded by 6 equidistant U atoms in orthogonal directions. Having a light N atom encaged in heavy U atoms causes the unusual feature of equally spaced, high-energy vibrational modes in the phonon spectrum as the N atoms act as independent isotropic quantum harmonic oscillators, contributing to thermal conductivity [46].

Unlike U_2N_3, pure UN is not stable in a wide range of stoichiometries, instead only existing as the slightly hypostoichiometric $UN_{0.995}$ at temperatures below 1100 °C [47]. Consequently, uranium nitrides with stoichiometries between around 1 and 1.45 are formed of $UN_{0.995}$ and $UN_{1.45}$. Above 1100 °C, investigations found a narrow stoichiometry range, expanding to higher N with increasing temperature, with a upper limit of $UN_{0.999}$ [2, 47]. DFT calculations give some insight into this, with Kuksin *et al.* showing that it is possible that antisite U (a U atom replacing and N atom on the N site) accommodates this deviation from stoichiometry [48]. Furthermore, N vacancies are expected

to have hardly any effect on the UN lattice constant [49].

The electronic structure of UN is a topic of much interest as its unusual $5f$ electron behaviour has led to some contradicting descriptions in the literature of being either fully itinerant or partially localised. Electron spectroscopy investigations and high pressure magnetism experiments on UN give evidence of the itinerant nature of the $5f$ electrons [50–54]. However, investigations into electrical and thermal transport properties as well as neutron diffraction show some evidence of localisation, suggesting that a dual-nature interpretation of the character of the $5f$ electrons may be more appropriate [55–58]. Consequently, there are also a range of different results reported for the number of $5f$ electrons in UN, with calculated and experimental values ranging from 1.8 to 2.7 [50, 56, 59, 60].

UN is known to order antiferromagnetically, with T_N = 53 K, but there are disagreements in the literature as to whether the magnetic structure is type 1-1**k** or type 1-3**k** [55]. Attempts to determine the magnetic structure by searching for the tetragonal distortion that would be present in a type 1-1**k** structure have led to contradicting results [14, 61, 62].

2.1.2 U_2N_3

When considering UN as a nuclear fuel, U_2N_3 is of interest due to its formation during high temperature oxidation, where it forms a layer between UN and the oxidation product, UO_2 [44, 63]. This occurs as the N in UN is released during oxidation and then diffuses away from the UN / UO_2 interface, where it either reacts with N, forming N_2, or reacts with the UN, forming U_2N_3. Consequently, if a UN fuel pellet is oxidised, it may be expected that U_2N_3 will form and therefore be present in the fuel pellet, having some influence on fuel behaviour. To understand and predict the behaviour of a UN fuel pellet it is therefore important to be able to understand and predict the behaviour of U_2N_3.

U_2N_3 exists in the body-centered cubic Mn_2O_3 structure, space group $Ia\bar{3}$, with a lattice parameter of 10.678 Å [45]. This structure is displayed in Figure 2.3, and is most easily described as a distortion of the f.c.c. UN_2 structure with every 4^{th} N atom removed. Unlike UN, this slight distortion of the U f.c.c. lattice causes there to be two unique U sites in the U_2N_3 structure. This is displayed in Figure 2.3, with the two U sites, U_1 and U_2, displayed in blue and grey, respectively. U_1 is defined as the high symmetry site, with 8 U atoms, while the U_2 site has 24 U atoms.

U_2N_3 is known to form with a wide range of stoichiometries, from N/U = 1.45 to 1.75, as the empty N site, in comparison to UN_2, becomes partially filled. It is well documented that the lattice parameter decreases linearly with

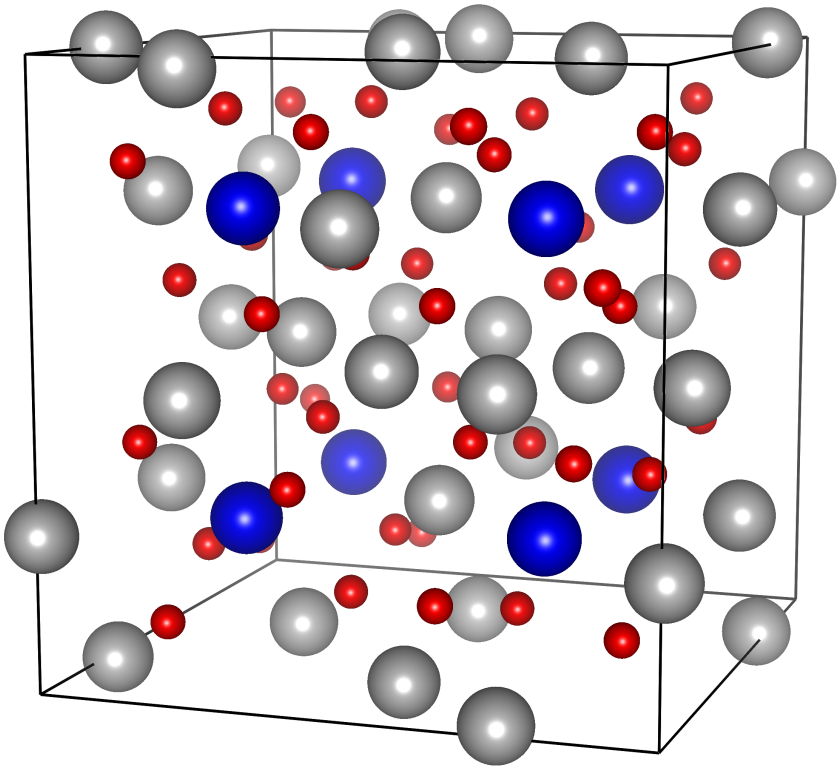

Figure 2.3: *Diagram of the U_2N_3 structure, with U_1 sites shown in blue, U_2 sites shown in grey, and N shown in red.*

stoichiometry, reaching a value of 10.63 Å at a stoichiometry of 1.75, as shown in Figure 2.4. Beyond this stoichiometry, the f.c.c. UN_{2-x} phase is formed [45]. This phase also exists with a wide range of stoichiometries, however, there is disagreement in the literature about whether or not stoichiometric UN_2 is stable [2, 64].

Considering the 3- valency of N, it may be expected that in U_2N_3 the 8 U_1 sites would have a valency of 6+ and 24 U_2 sites a valency of 4+, balancing the 3+ charge of N. As with UN, this has been shown to not be the case. Bonding in U_2N_3 shows similarities to that seen in UN, with electron spectroscopy studies showing that bonding is not ionic, instead showing mixed metallic-covalent character [65, 66]. However, a shift of core levels to higher binding energy and a decrease in the density of states at the Fermi edge as the majority of $5f$ states also shift to higher binding energy is seen in U_2N_3 in comparison to UN [6]. This shows an increase in $5f$ localisation, showing U_2N_3 to be somewhat intermetallic.

Considering the effect of stoichiometry on the electronic structure of U_2N_3, the only investigation that looks

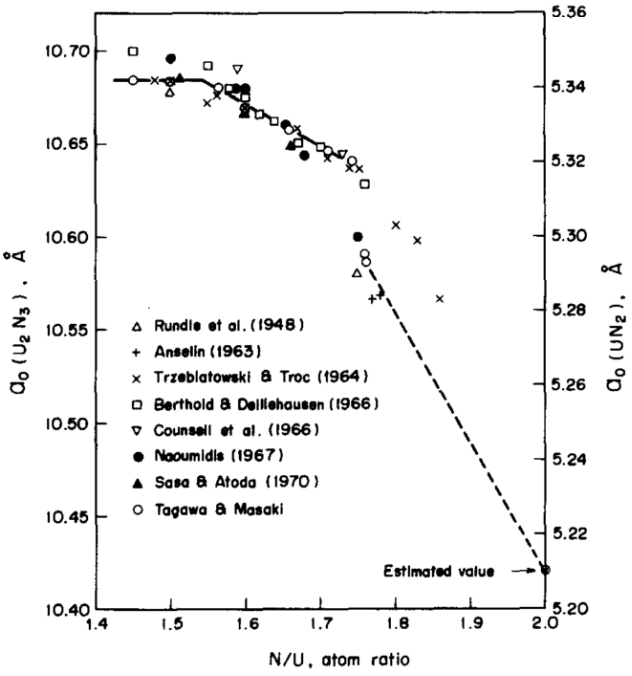

Figure 2.4: *Literature values of lattice parameters in the U_2N_3-UN_2 system, with U_2N_{3+x} lattice parameter on the left axis and UN_{2-x} lattice parameter on the right axis, from [2].*

into these effects, or any effects of stoichiometry on physical properties of U_2N_3 other than crystal structure, is the investigation into the magnetic susceptibility of the uranium nitrides, performed by Troć [16]. This investigation showed U_2N_3 to order antiferromagnetically, having a T_N of 94 K at a stoichiometry of 1.55, with T_N decreasing with increasing stoichiometry. Unfortunately, attempts to determine the magnetic structure of U_2N_3 using neutron diffraction were unsuccessful, and the magnetic structure remains unknown.

Black *et al.* tentatively attributed this magnetic behaviour to the reduction in metallic character with increasing stoichiometry as the U charge increases, rather than the negligible change in U-U spacing [6]. Following this trend, calculations by Erarestov *et al.* predicted UN_2 to be semiconducting in nature, though this has not yet been shown experimentally [67].

2.2 A Comparison of UN and UO_2

Knowledge of properties of the uranium nitrides described above is essential for fundamental understanding, but the material properties relevant to a nuclear fuel must also be considered.

2.2.1 Thermal Properties

In a PWR fuel assembly, each pellet will be releasing thermal energy at an average rate of 220 W. While this remarkably high output is part of what makes nuclear power a very useful energy source, it restricts the fissile materials that could be used as a nuclear fuel to those with robust thermal properties.

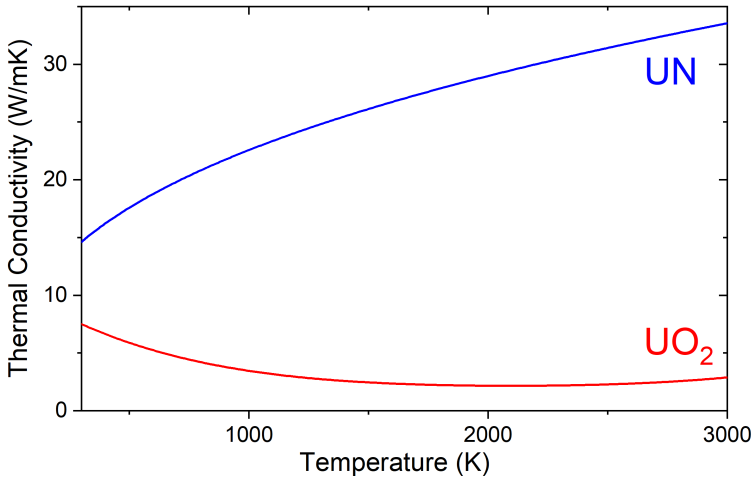

Figure 2.5: *Thermal conductivity of UO_2 and UN, from [3, 4].*

With a melting point of 2830 °C, UN is one of the few uranium compounds that is stable up to temperatures comparable with the high value of UO_2 at 2874 °C [2, 29]. The thermal expansion of UN is uniform and isotropic from room temperature to melting point, as it has a cubic structure and does not undergo any phase changes [68]. This is very similar to UO_2 and ideal for a nuclear fuel, as anisotropic thermal expansion and phase changes can lead to anisotropic strain and consequent deformation of a fuel pellet [69].

One of the most attractive properties of UN when considering it as a nuclear fuel is its high thermal conductivity. The thermal conductivity of UN is double that of UO_2 at room temperature and increases further as temperature

increases, as illustrated in Figure 2.5. This is the opposite to the trend seen in UO_2, where thermal conductivity decreases with temperature until 2000 K, after which a slight increase is seen. Calculations investigating the phonon and electron contributions to thermal conductivity of UN have shown this trend to be due to the electron contribution, which increases with increasing temperature [4]. This is converse to the phonon contribution, which decreases with increasing temperature as increased disorder in the crystal decreases phonon lifetimes. As UN is metallic and UO_2 is a semi-conductor, there is a finite density of states at the Fermi edge in UN that is not present in UO_2 meaning that the density of electrons that can contribute to the thermal conductivity is greater in UN than in UO_2, explaining their differences in conductivity as a function of temperature.

2.2.2 Neutronics

When evaluating the neutronics of UN as a nuclear fuel, there are some simple considerations that can be made. Firstly, the density of U atoms in UN is 13.5 g/cm^3, much greater than the UO_2 value of 9.6 g/cm^3. This can pose an economic advantage as a higher fissile density can increase the power released from the fuel during burning, or a lower level of ^{235}U enrichment can be used in UN than UO_2 while still achieving the same fissile density. Alternatively, the higher fissile density of UN could be used to offset the neutron cost of advanced cladding materials such as stainless steel, which has a larger neutron absorption cross-section than the widely used zirconium alloy cladding.

Secondly, the neutron cross-section of N should be considered. ^{14}N is known to have a strong neutron absorption cross-section due to the n, p reaction, which leads to the formation of ^{14}C. The effect this large cross-section will have on fuel performance is a topic of some disagreement in the literature, possibly due to the different forms of the UN fuel that are used in simulations [5, 37]. A further concern with this strong absorption cross-section of ^{14}N is the production of ^{14}C, which poses a danger to the environment as C can easily be taken up by biological matter.

A solution to this issue is enriching 99.6 % naturally occuring ^{14}N with the less abundant ^{15}N. As shown in Figure 2.6, the neutron cross-section of ^{15}N is significantly lower than ^{14}N, and similar to that of ^{16}O, which is present in UO_2 fuel [5]. Consequently, a UN fuel enriched in ^{15}N could potentially have some neutronic advantages, however, enrichment to over 99.9 % would be reqired to keep ^{14}C production levels to that of UO_2 [37].

More rigorous investigations into the neutronics of UN as a nuclear fuel have been performed using computational

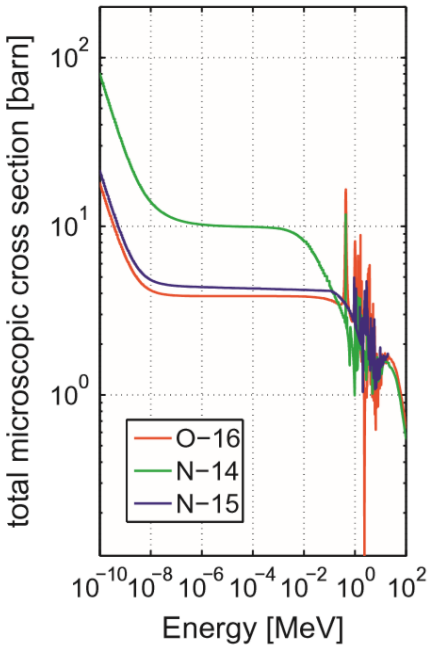

Figure 2.6: *Total neutron cross-sections of* ^{14}N, ^{15}N, *and* ^{16}O, *from [5].*

simulations. BWR simulations by Zakova *et al.* found that UN fuels decrease the efficiency of burnable poisons and control rods relative to UO_2. With the consequently necessary increase in burnable poisons needed, the UN fuel has a 1.4 year longer in-core lifetime, equivalent to a 1 % increase in the enrichment of UO_2 [5].

Simulations for a PWR performed by Brown *et al.* found similar results of longer fuel lifetimes and decreased reactivity worth of burnable poisons and control rod materials when compared to UO_2. Overall, it was found that reactivity coefficients for UN and UN-composite fuels were within the design limits of the simulated PWR [70]. Youinou *et al.* found that UN produced lower operating temperatures compared to UO_2, due to the higher thermal conductivity [37].

2.2.3 Corrosion Resistance

Corrosion resistance is an essential property of a nuclear fuel as it keeps it in the desired phase, maintaining the important material properties of that phase, such as thermal conductivity and melting point. It is also essential to prevent degradation of the fuel structure in order to maintain the desired microstructure, which plays an important role in

accommodating fission products and swelling due to fission [71]. Additionally, as the fuel matrix is responsible for the retention of over 90 % of fission products in UO_2, maintaining structural integrity of a fuel pellet is also critically important for saftey during use and in spent fuel storage [72]. Corrosion of a nuclear fuel is most likely to occur on exposure to water or steam, whether in an accident scenario where a pellet is exposed to the water coolant, in a spend fuel storage pond, or during long-term disposal in a deep geological repository where groundwater ingress may occur.

Corrosion of UO_2 occurs as it is oxidised from the U(IV) state to the U(VI) state. This U(VI) state is several orders of magnitude more soluble in water, forming the UO_2^{2+} ion, allowing oxidative dissolution to occur [73]. As this process corrodes the fuel material, the fission products contained within its matrix as well as the UO_2^{2+} ions will be released into the fuel environment.

However, this oxidation of UO_2 does not occur easily, requiring the highly corrosive products of water radiolysis or low pH solutions to take place at low temperatures [74–77]. Consequently, UO_2 is considered highly corrosion resistance, with fuel degradation only expected to occur in accident scenarios or long-term disposal [72].

In comparison, UN was found to react readily with water, showing high reaction rates at temperatures as low as 90 °C at both pH 6 and pH 10, while UO_2 was shown to be stable under the same conditions [78]. Though pellet fabrication methods (decreasing grain size and porosity) have shown to improve the corrosion resistance of UN to close to that of UO_2, corrosion and degradation of fuel pellets is still seen in steam environments above 200 °C [79–83]. These varied results are also seen by the oxidation of UN by O_2, with reports of complete oxidation of UN powders in low pressure O_2 at room temperature, contradicting the stability of UN powder to over 200 °C seen in other work [44, 84–86].

The relative corrosion resistance of UN compared to similar compounds, such as PuN, ThN and UC, is attributed to the formation of a surface oxide layer, though this surface layer and the role it plays in protecting the UN bulk is not well understood [81, 84]. It is known that a U_2N_3 interlayer forms between this surface oxide and the UN bulk at high temperatures, however, it is not known whether this is also present at room temperatures, and whether it has an affect on oxidation rate [44, 63, 85, 86].

2.2.4 Irradiation Performance

Irradiation performance of a nuclear fuel is of great importance as it can significantly alter many of the physical properties of the fuel material. The fission and irradiation of fuel during its lifetime can cause degradation of the microstructure and amorphisation of the crystal structure. Properties such as thermal conductivity, fission product retention, and corrosion resistance are highly dependent on these structures, and can therefore be notably affected by irradiation performance.

The irradiation performance of UO_2 nuclear fuel is a well studied topic, with many experimental and computational studies investigating its effects [87–91]. The good irradiation resistance of the UO_2 structure has been attributed to the f.c.c. U lattice, which holds its structure to high burn-up levels [92, 93].

Unlike UO_2, very little research has been performed on the irradiation performance of UN as a nuclear fuel. In the few studies that have been performed, fuel swelling has been the main focus, with Albrecht *et al.* and Ross *et al.* finding that the irradiation swelling rate of UN fuel pellets is greater at higher temperatures and dependent on microstructure [94, 95]. Work investigating the irradiation of Zr-clad UN fuel pellets by Matthews *et al.* found that swelling was greater than anticipated, however, fission-gas release was as expected and the fuel pellet did not crack or restructure, concluding that the UN fuel operated as designed, demonstrating the technical feasibility of the UN fuel pellet [96]. This work suggested that formation of free U was a significant cause of irradiation swelling and that the use of stoichiometric or hyperstoichiometric UN would improve swelling and compatibility.

As UN and UO_2 both share the same f.c.c. U lattice, differing in size by 0.5 Å, it may be expected that UN will share the same resistance to irradiation as seen in UO_2. This is likely to be true when considering the effects of irradiation on properties such as crystallinity, microstrucure, and fission product retention, however, as UN is known to be more reactive than UO_2, results of the effect of irradiation on dissolution may differ.

2.3 Thesis Outline

Though the content above is by no means a complete summary of the available literature on the uranium nitrides, it provides an introduction to the current understanding of the wide range of properties relevant to a nuclear fuel. A more complete review of the relevant literature is provided in each experimental chapter. This summary has shown some of

the advantages and disadvantages of using UN as a nuclear fuel compared to UO_2. While an increased uranium density and improved thermal conductivity give promise of better fuel performance, they must be weighed against the safety concerns of the higher reactivity of UN and the neutronic and economic cost of the large neutron cross-section of ^{14}N. Furthermore, some of the areas in which greater knowledge and understanding of the uranium nitrides is needed have been highlighted and these form the main focus of this thesis.

The primary aim of this thesis is to improve understanding of the uranium nitrides using an experimental approach, gaining knowledge that is relevant to the application of UN as a nuclear fuel. Though realistic investigations can be very useful, such complex scenarios can be challenging to replicate and make it difficult to determine effects of individual parameters. Instead, the intention here is to reduce this complexity, allowing single variable studies to be performed. Additionally, this approach facilitates comparison of experimental results to theoretical and computational studies, for which it is challenging to replicate the complexity of realistic scenarios.

This will be achieved by developing novel thin films of uranium nitrides to serve as ideal samples. The many advantages of using such thin film samples, in particular for nuclear fuel research, are discussed in Chapter 3. Furthermore, the methods by which these samples will be produced are described. As it is essential to fully characterise samples before performing investigations on them, measurements of the chemical and structural properties of samples are presented in Chapter 4. Analysis of these measurements should additionally provide further insight into the intrinsic properties of these materials.

These novel samples provide the ability to investigate some of the fundamental properties of the uranium nitrides, such as the debated magnetic structure of UN and unknown magnetic structure of U_2N_3. Such properties are investigated using resonant scattering, as described in Chapter 5. Additionally, resonant scattering will be used to further understanding of the relatively unknown electronic structure and bonding in U_2N_3.

Moving on to some of the chemical properties of UN, the multi-technique approach used to investigate UN oxidation is presented in Chapter 6. These highly controlled investigations are analysed in an attempt to answer questions on the formation, composition, and evolution of the oxidised surface of UN. In Chapter 7, the effects of radiation on the dissolution of UN are investigated for the first time, with H_2O_2 used to mimic the products of water radiolysis. The corrosion rates of UN, U_2N_3, and UO_2 thin films are determined using x-ray reflectivity, providing insight into the

differing ways in which corrosion progresses.

Finally, a summary of the findings presented here, along with the implications and further questions raised by these results are given in Chapter 8.

Chapter 3

Sample Synthesis

In this chapter, the advantages of and reasons for using thin films for nuclear fuels research are discussed. The technique used to deposit the samples used in this thesis, DC magnetron sputtering, is described and the methodology used for sample synthesis is reported. Finally, the growth conditions for all samples used are listed.

3.1 Thin Film Approach to Research

Thin films are layers of materials ranging from nanometers to micrometers in thickness and created by controlled deposition on to a bulk substrate, the production, investigation, and application of which is a vast topic [97]. A wide range of thin film deposition techniques has been developed to suit the needs of applications such as electronic components, protective surface coatings, and optical coatings [97]. However, the focus of this chapter is on the fabrication and use of thin films for scientific investigation. These materials provide advantages over traditional bulk samples in many areas of research, and are particularly useful when investigating the surface reactions of nuclear materials [76, 98–101].

3.1.1 Surface Reactions

The oxidation and corrosion of nuclear materials is of great importance as the material structure provides protection against radiation, either acting as a barrier such as with fuel cladding, or as a retention matrix such as with nuclear fuels, where it has been shown to be responsible for retention of 95% of radionuclides [72]. Consequently, oxidation and corrosion reactions are highly pertinent to nuclear safety. When considering UN as a potential nuclear fuel, one of the main concerns is the oxidation and corrosion resistance of the material. This topic is therefore an area of significant research, and one of the main topics of this thesis.

Oxidation and corrosion reactions occur at the surfaces of materials so when investigating these reactions it is possible to use thin film samples, with the film acting as a model of the surface of a bulk sample. By using a thin film sample, the volume of material being investigated is greatly reduced and becomes comparable to the volume of oxidation or corrosion products. Consequently, analytical techniques used to investigate these products and any loss of starting material will be more sensitive to small changes. Thin film samples also facilitate the use of techniques such as x-ray reflectivity, which can be difficult to perform on bulk samples due to surface roughness, and provide useful information on sample thickness and morphology, which are important properties when investigating corrosion.

Additionally, when using thin films it is possible to adjust many properties of the sample by varying deposition conditions, creating highly controlled samples. These samples can then be used to reduce the complexity of the problem being investigated and perform precise single-parameter studies [100]. Studies such as these are of crucial importance when attempting to improve fundamental understanding of a material, reaction, or property.

3.1.2 Nuclear Fuels Research

To date, UN and especially U_2N_3 are relatively understudied compared to the widely used nuclear fuel, UO_2. Consequently, if UN is to be used as a nuclear fuel, it is important to improve fundamental understanding of UN and U_2N_3 to be better able to predict how UN will behave as a nuclear fuel. This is especially important as much of the nuclear industry relies on computational predictions of fuel behaviour in reactor and in long-term storage in safety cases, which are necessary to investigate scenarios that are often too intricate or dangerous to investigate experimentally [102, 103].

Performing precise, single-parameter studies provides experimental results which can be compared to these theoretical and computational models that have much lower complexity than realistic experiments. This allows models to be tested at a more fundamental level than complex realistic scenarios, helping to bridge the gap between theory and experiment.

When performing experiments on materials such as nuclear fuels, the risks of radiation must be considered. A simple but effective way of reducing these risks it to reduce sample volume, and therefore activity, which can easily be achieved by using using thin films in place of bulk samples. For example, a 600 Å UN film on a $10 \times 10 \times 0.5$ mm Al_2O_3 substrate has an activity of 0.12 Bq, lower than background levels, whereas a UN sample of the same volume would have an activity of 10 kBq. These low activity levels make thin films safer to work with and also transport, which is particularly useful for investigating samples at large research facilities, such as synchrotron sources.

3.1.3 Phase Stabilisation

A further aspect in which the use of thin film samples instead of bulk samples can be advantageous is in producing and isolating phases. By using epitaxial deposition (described in Section 3.2.3), it is possible to lock-in unusual phases that may not be accessible in bulk [104, 105]. Epitaxy also provides a way to produce single crystal samples which can be challenging to produce in bulk due to the nature of the material. For example, U_2N_3 is known to thermally decompose, limiting the effectiveness of annealing to promote grain growth in order to extract a single crystal grain [106].

When using samples, such as UN, which will oxidise in air, it is often advantageous to be able to protect them from this reaction. Thin films can easily be protected from air by depositing a protective capping layer, creating a sample that is encapsulated while still being easy to handle, transport, and perform measurements on.

3.2 Thin Films Deposition Techniques

With the wide ranging applications of thin films, many different deposition techniques have been developed to suit their different needs. These techniques can broadly be divided into two categories: chemical vapour deposition and physical vapour deposition. Chemical vapour deposition uses a fluid precursor that undergoes a chemical reaction causing the

deposition of a solid phase on a substrate, whereas physical vapour deposition involves the condensing of a vapour phase onto a substrate [97]. In this work, the physical vapour deposition technique of magnetron sputtering has been used and is described below.

3.2.1 DC Magnetron Sputtering

DC magnetron sputtering is a method of thin film deposition in which ionised gaseous atoms, commonly Ar, are accelerated towards a negatively biased target material [97]. The bombardment of ions onto the target will then cause sputtering of target atoms and a portion of these sputtered atoms will condense on a substrate placed opposite the target, forming a thin film. This process is illustrated in Figure 3.1. By altering the composition of the gaseous environment, the target material, the bias of the target, and the substrate material and temperature, the properties of the deposited thin film can be altered.

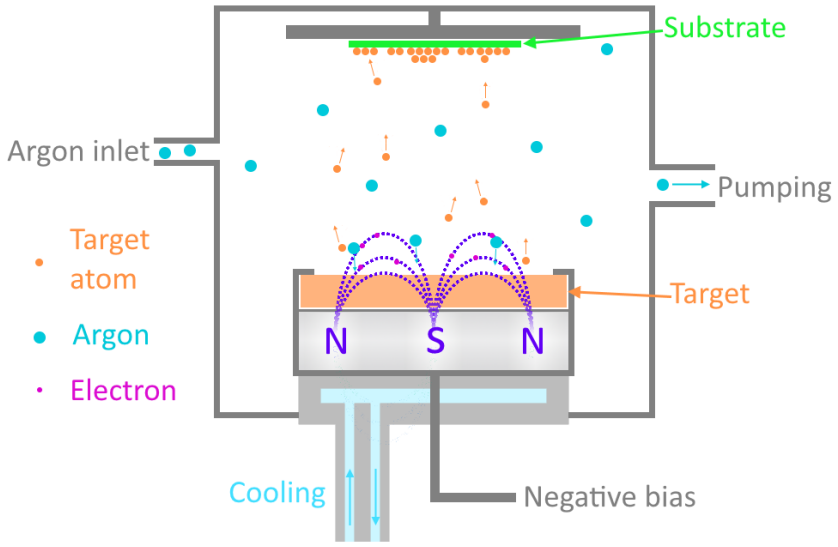

Figure 3.1: *Diagram illustrating DC magnetron sputtering in an Ar atmosphere.*

The defining characteristic of magnetron sputtering is the use of an annular magnet below the target material, as displayed in Figure 3.1. The magnetic field created by this will entrap some of the electrons freed by the ionisation of Ar atoms, creating a plasma. The collisions of these entrapped electrons with Ar atoms will increase the ionisation rate near the target. As each ionisation again frees electrons, a feedback loop is created, sustaining the mechanism. This

allows the sputtering rate to be significantly increased without the detrimental effects of increasing Ar pressure, making it possible to continuously pump during deposition, i.e. maintain an open system.

The pressure and composition of sputtering gas used is significant as it can react with the target material, sputtered atoms, and deposited film, influencing the composition of the deposited film. To enable good control of the composition of the sputtering gas, an ultra-high vacuum (UHV) system is used to minimise contamination from atmospheric gases, most significantly O_2. To eliminate reactions with the sputtering gas, noble gases are required. As noble gas prices are extremely limiting, most sputtering is performed with Ar.

Pressure of the Ar sputtering gas used will have a significant effect on the deposition rate, the rate as which target atoms condense on the substrate. As Ar pressure and therefore density increases, there will be more Ar atoms available to be ionised and accelerated towards the target, increasing the sputtering rate. However, increased Ar density will increase the chance of collision between Ar and sputtered target atoms, increasing the dispersion of target atoms and reducing the deposition rate. Consequently, the interplay between these two factors will create a peak in deposition rate as a function of Ar pressure [107]. This optimum pressure will be dependent on properties of the sputter system and so will vary between different systems.

The sputtering rate will also depend on the power through the target. This is defined by the magnitude of the potential difference on the target, and the current caused by it. If an insulating target is used, as this potential difference ionises and accelerates the Ar atoms, a positive charge will build up at the target as no current will flow. This build-up of charge will soon counteract the applied bias, stopping the sputtering process from being sustained. It is therefore important to use a conductive sputtering target when performing DC magnetron sputtering. Thermal conductivity of the target is also important, as the heat created by Ar bombardment can be significant. If this heat is not removed, it can cause demagnetisation of the magnets or even melting of the target. Subsequently, it is standard to water cool the target and magnet.

Deposition rate and substrate heating can have significant effects on the morphology and crystallinity of the deposited film [107–109]. As target atoms condense on a substrate, there will be some diffusion of atoms and the formation of chemical bonds, which requires energy. A high deposition rate will decrease the time over which these processes can occur. In order to influence the amount of energy available to the condensed atoms, the substrate material can be heated

or cooled. The additional energy provided by heating will aid in the diffusion and crystallisation of the thin film material, often improving crystallinity [109, 110]. This is particularly useful when producing single crystal or epitaxial samples.

3.2.2 Reactive Sputtering

Reactive sputtering allows many different compounds to be made from a single target by adding a partial pressure of a reactive gas when sputtering. This is often preferential to using targets of the desired compounds in several ways. Firstly, the compounds may not be thermally or electrically conductive, making them unable to sustain an Ar plasma in a DC sputtering system [97]. Secondly, it is best to use an elemental target material as sputtering rates of different elements in a compound may be different, causing the deposited film to have a different stoichiometry or phase [111, 112]. Thirdly, it can be possible to produce films of different phases and stoichiometries without the need to change targets [6, 113, 114].

Stoichiometry control is achieved by altering the partial pressure of the reactive gas. As the target atoms are sputtered, they may react with the reactive gas, creating compound molecules which will then condense on the substrate. Increasing the reactive gas pressure will increase the probability of this reaction, and the probability of further reactions to create higher stoichiometry molecules. Consequently, the stoichiometry of the deposited film will be increased, making it possible to control the phase deposited.

3.2.3 Epitaxial Growth

Another way to control the properties of deposited films is by using epitaxy. Epitaxy is the growth of a single crystal thin film on a single crystal substrate, caused by the substrate surface structure acting as a template for the crystallisation of the deposited film. The deposited film will only grow epitaxially if it is energetically favourable, limiting the epitaxial relationships that will work. For ideal epitaxy, the two structures grow in perfect registry, but in reality there will be some imperfections. These imperfections can be caused by anomalies in the substrate surface or deposited material, however, interfacial strains will also play a large role in the creation of epitaxial imperfections.

Interfacial strain, ϵ, in an epitaxial film is charactrised as the difference between the in-plane lattice parameters of

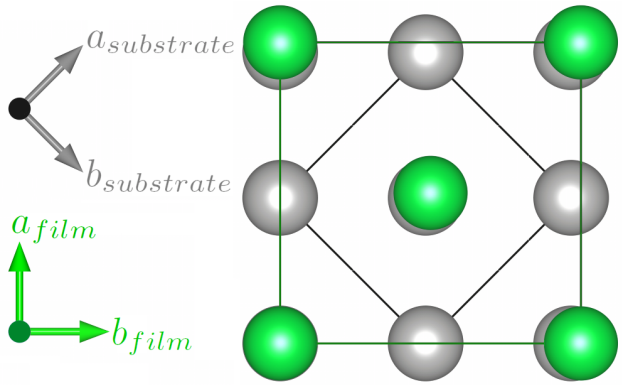

Figure 3.2: *Diagram showing epitaxial film (green) on substrate (grey) with a 45 ° rotation and 1:$\sqrt{2}$ relation. Solid lines show the unit cells of each structure.*

the film and substrate, a and b, divided by their average, as shown below.

$$\epsilon_a = \frac{a_{film} - x_a \cdot a_{substrate}}{(a_{film} + x_a \cdot a_{substrate})/2}, \; \epsilon_b = \frac{b_{film} - x_b \cdot b_{substrate}}{(b_{film} + x_b \cdot b_{substrate})/2} \tag{3.1}$$

If the film and substrate planes have equal rotational symmetry which is greater than 2, then $\epsilon_a = \epsilon_b$ and strain is equal and uniform across film. In these equations, factors x_a and x_b are included to account for the epitaxial relationship between the film and substrate. For example, for the simplest relationship of a direct epitaxial match, x_a = x_b = 1, and for a cubic match with a 45 ° rotation, x_a = x_b = $\sqrt{2}$, as shown in Figure 3.2.

This interfacial strain can have a significant effect on the crystalline quality of the epitaxial film, as the strain distorts the structure of the deposited film and imperfections form in an attempt to reduce this strain. If epitaxial films are sufficiently thick, at some distance from the substrate / film interface, the film structure will relax from the interfacially strained structure to the bulk structure. More defects may appear to accommodate the change in lattice parameter as this relaxation occurs.

3.3 Experimental Procedures

This section details the methodology employed to produce the thin film samples studied in this work, which were produced using the bespoke sputter deposition system located at the University of Bristol. This sputter system houses four DC magnetron sputter guns in its main chamber, all directed towards a sample holder, with a loading chamber

located on the side, as shown in Figure 3.3. Each sputter gun has a shutter to improve precision in deposition times and protect targets from deposition from other guns. The bias on each sputter gun is controlled to hold a constant power, voltage, or current.

To minimise contamination, UHV conditions are maintained in both the main chamber and loading chamber. This is achieved by using only knife edge and copper gasket seals or gold wire seals in the main chamber. Both chambers are evacuated with turbomelecular pumps, which are backed by scroll pumps, which are oil-free to reduce possible carbon contamination. Consequently, pressures of 10^{-8} and 10^{-10} mbar are maintained in the loading and main chambers, respectively.

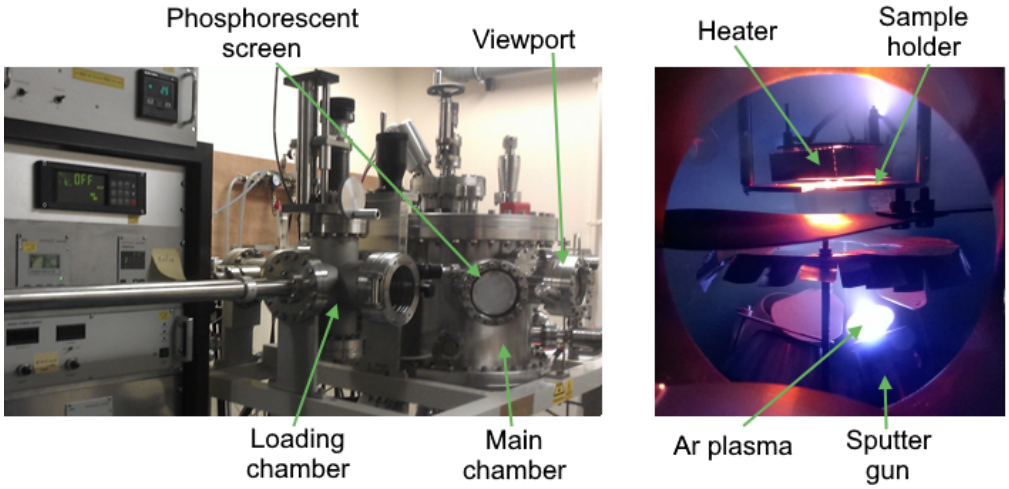

Figure 3.3: *Picture of sputter deposition used to produce samples (left), and view through viewport during high temperature deposition (right).*

To further minimise contamination of the main sputtering chamber, substrates mounted onto sample plates are entered into the loading chamber before being transfered into the main chamber under UHV. This is possible as the two chambers have their own pumping systems and are separated by a UHV gate. When loading samples plates, this gate valve is kept closed and the turbomolecular and rotary pumps are switched off and allowed to spin down. N_2 venting gas is then leaked into the loading chamber to reduce exposure to air. As maintenance of low pressure is less important in the loading chamber, for speed of access the loading chamber has an rubber o-ring sealed fast entry port for loading samples.

Substrates are mounted onto molybdenum sample plates and mechanically held in place with clips. These plates are then loaded into the chamber and the evacuation of the chamber is resumed. Once the loading chamber has been sufficiently evacuated, the UHV gate can be opened and sample plates transfered through to the main chamber substrate holder. When sample loading and unloading is not being performed, the UHV gate is kept closed.

To heat the sample plate, a heater is mounted behind the sample holder in the main chamber. This heater uses a Nb wire resistive heating element, built in-house and powered by a variable resistor. The substrate temperature was measured using a pyrometer as a function of heater current to calibrate the heater. To withstand the heating cycles that they undergo, the sample plates, sample holder, and heater casing are made with molybdenum, a refractory metal.

When attempting to deposit single crystal thin films, it is useful to be able to investigate the crystallinity of the substrate and any deposited films and a reflection high energy electron diffraction (RHEED) system has been installed on the main chamber for this purpose. This system consists of an electron source at grazing incidence to the sample surface and directly opposite a phosphorescent screen. As the electron beam reflects off the sample surface, in the case of a single crystal sample, interference effects will lead to the appearance of bright spots on the phosphorescent screen. In order to investigate the symmetry of the RHEED pattern, the sample holder can be rotated. If the sample is not single crystal, no spots will appear on the phosphorescent screen, though streaks and rings may appear depending on the crystallinity of the film.

Gas pressure in the sputter system is measured by ion gauges in both chambers, and in the main chamber gas pressure is controlled by leak valves connected to compressed gas bottles. Sputter deposition is performed with the sputter system open, i.e. active pumping is maintained, so that sputtering can be performed for long durations and without any decrease in reactive gas partial pressure. As the reactive gas partial pressure is often lower and more important than the sputtering gas pressure, when performing reactive sputter deposition, the reactive gas is leaked into the chamber first and allowed to stabilise at the desired pressure. The sputtering gas, Ar, is then leaked in and again allowed to stabilise before sputtering is commenced.

3.3.1 Deposition Preparation

Prior to deposition, several steps were taken to optimise the sputter system and reduce contamination, thereby improving the quality of the samples produced.

High purity targets were acquired from Goodfellow Cambridge Ltd., in the case of Nb and Au, and from AWE plc., in the case of U. As Nb and Au do not readily oxidise in air, they were installed in sputter guns as purchased. This is not the case for U metal, so to reduce contamination from the oxidised surface layer, the target was polished to remove all visible trace of oxidation before being installed in a sputter gun. Once the targets had been installed in the sputter system and the system had been baked-out, all targets were then cleaned by sputtering for varying times to remove any oxidised layers from their surface.

To reduce the possibility of O_2 contamination from a shared gas line when reactive sputter depositing nitride films, a separate N_2 line and leak valve was installed on the sputter system. This line was fed with N5.5 (research grade) N_2 compressed gas. Prior to each deposition session, this line was purged a minimum of three times to remove any O_2 and H_2O that may have leaked in.

All substrates used in this work were purchased from MTI Corporation, and were supplied highly polished and cleaned such that no substrate preparations were necessary.

3.3.2 N_2 Pressure

Previous work has been performed by Black *et al.* investigating the effect of N_2 pressure when performing reactive DC magnetron sputtering from a uranium target [6]. This investigation focused on the deposition of polycrystalline films and the change in deposited film stoichiometry as a function of N_2 pressure, as shown in Figure 3.4. These results showed that N_2 pressure could be used to successfully alter the electronic structure and composition of the deposited film, however, no investigation was made into the crystalline phase of the material.

The study described above served as an important starting point when synthesising samples for the present work, however a different sputter system was used and therefore the sputtering conditions required to produce films of a desired stoichiometry will be different. Subsequently, an investigation into the effect of N_2 pressure was performed in

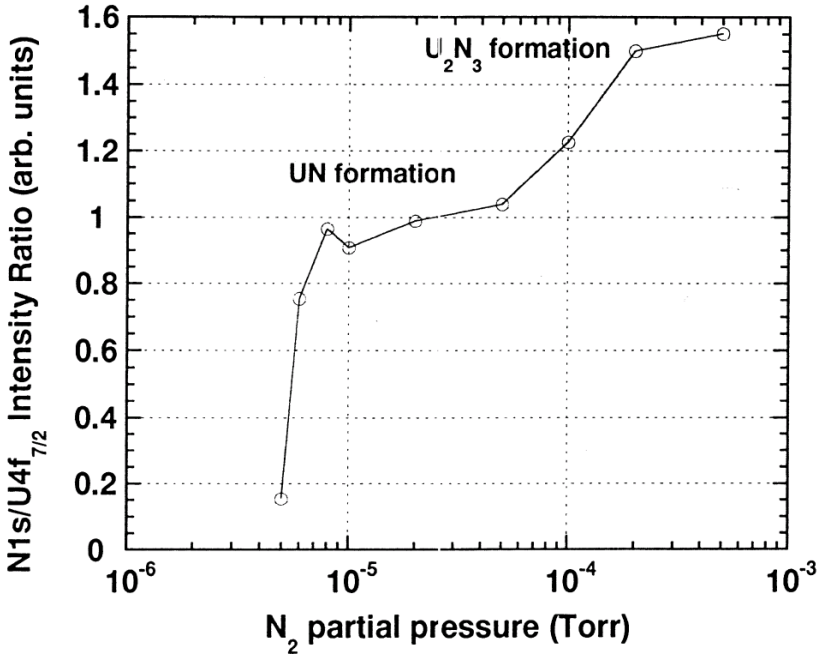

Figure 3.4: *Ratio of the intensities of N-1s and U-4$f_{7/2}$ lines, showing the development of the UN composition as the function of the partial pressure of N_2, from [6].*

order to calibrate the sputter system at the University of Bristol. This additionally provided an opportunity to investigate how structural properties, measured with x-ray diffraction, change with N_2 pressure.

To perform this study, samples were deposited on Corning glass substrate using a range of N_2 pressures, from $1\times10^{-}5$ to $2.5\times10^{-}3$ mbar, above which sputtering could not be sustained. This was carried out at room temperature, with the specific pressures used listed in Table 3.1.

3.3.3 Substrate Selection

When depositing thin films, the substrate used can have a significant influence on the phase, morphology and microstructure of the film. The crystal structure of the substrate used may cause epitaxial growth, which can be favourable for the growth of single crystal films, however, this is not ideal when polycrystalline films are desired. Additionally, a strong epitaxial relationship may cause the deposition of an undesired phase. The chemical properties of the substrate can also cause the deposition of an undesired phase as the substrate reacts with the deposited material. Many of the studies

reported here are performed using x-ray reflectivity to investigate morphological changes of the thin film samples, which is a technique that requires films to have very low roughness in order to obtain meaningful data. Consequently, it is of great importance that any substrates used are highly polished.

3.3.3.1 Polycrystalline Thin Films

For the deposition of polycrystalline UN and U_2N_3 samples, amorphous Corning Eagle XG glass substrates were used. Corning glass is chemically unreactive, making the substrates suitable for experiments in corrosive environments, such as the H_2O_2 corrosion study described in Section 7.3, and stable at temperatures up to 660 °C, allowing for high temperature growth and oxidation experiments.

3.3.3.2 Epitaxial Thin Films

As described above, substrate selection is of great importance when attempting to deposit epitaxial films. No epitaxial UN or U_2N_3 thin films have previously been successfully deposited, so substrate selection has been an area of significant research in the synthesis of these films.

To facilitate the process of substrate selection, a programme was written to find possible epitaxial matches suitable for a user-input structure and desired $(h\,k\,l)$ film orientation, within user-defined upper and lower bounds on the interfacial strain in the in-plane directions. This programme works by taking the user-input $(h\,k\,l)$ plane and attempting to match it to a library of crystal structures of materials that are available to buy as substrates, as well as transition metals structures. The programme considers a range of possible epitaxial relationships for each structure, based on literature evidence, and accepts them as solutions if the calculated interfacial strain is within the user-defined limits. The advantage provided by this programme was to speed up the process of considering many different options for epitaxial matches to UN and U_2N_3, including possible buffer layers such as transition metals.

Even with the help of this epitaxial matching programme, finding successful matches for UN and U_2N_3 was still a process of trial and error. After several attempts to deposit epitaxial UN films on yttria stabilised zirconia and MgO resulting in epitaxial UO_2 films, it was discovered that oxygen in the film was oxidising the deposited UN. However, a

successful match was found with the use of R-plane Al_2O_3 substrate with a $(0\,0\,1)$ Nb buffer layer, a match which is well documented in the literature [115]. With a lattice parameter of 3.300 Å, the Nb $(0\,0\,1)$ buffer layer was matched to the UN $(0\,0\,1)$ plane with a 1:$\sqrt{2}$ relation with 45 ° rotation, resulting in a theoretical interfacial strain of 4.7% [116, 117]. The Nb layer acts as both a chemical and physical buffer, preventing any oxidation of the deposited UN material by the Al_2O_3 substrate, while also improving the epitaxial relationship between the UN film and Al_2O_3 substrate. All epitaxial $(0\,0\,1)$ UN films grown for the present work used the R-plane Al_2O_3 substrate and $(0\,0\,1)$ Nb buffer described above, with the Nb layer deposited at 800 °C, and UN deposited at 500 - 750 °C.

When depositing U_2N_3 thin films, $(0\,0\,1)$ CaF_2 substrates were found to produce a successful epitaxial match. CaF_2 has a cubic structure, with a lattice parameter of 5.463 Å, providing a 2:1 match to U_2N_3 with theoretical interfacial strain of 2.3 % [118]. These epitaxial U_2N_3 samples were deposited at temperatures of 700 - 750 °C.

3.3.4 UO_2 Thin Films

As the most widely used nuclear fuel, UO_2 is the benchmark to which other potential nuclear fuels should be compared. Consequently, when investigating corrosion properties of UN and U_2N_3, polycrystalline UO_2 samples were also investigated as a comparison. These thin film samples were grown in using the same methods as UN and U_2N_3 polycrystalline samples, but with 2×10^{-5} mbar O_2 used as the reactive gas [100].

3.3.5 Capping

When investigating materials, such as UN and U_2N_3, which are known to oxidise on exposure to air, it is important to be able to protect them from oxidation. This will decrease the probability that any experimental results are influenced by the presence of oxidation products of the material. When using thin film samples, this can easily be achieved by depositing a protective 'capping' layer over the film. This will be most effective when using a capping material that passivates in air, theoretically protecting the film below from oxidation indefinitely.

All samples produced for the work presented in this thesis, excluding investigations into surface reactions, were capped with 50 - 100 Å of either Nb or Au. These elements were used as they both passivate in air, providing good

oxidation protection, with the choice between them dependent on the target materials available in the sputter system at the time of deposition [110]. These capping layers were deposited at room temperature to avoid epitaxial growth, and the thickness of the layer was selected such that it would facilitate the analysis of XRR data while still providing sufficient oxidation protection.

3.4 Thin Film Samples

The growth condition of all samples used for studies presented in this thesis are listed in Table 3.1. The N_2 pressures used were selected based on calibration samples produced for each growth session. Deposition temperatures of epitaxial films were selected as a compromise between high temperature and low base pressure.

Table 3.1: *Samples grown for studies presented in this thesis, with growth details and chapter in which they are used.*

Sample Number	Substrate	Buffer	Film	Cap	Film Deposition Temperature (°C)	N_2 Pressure (mbar)	Chapter
1384	Corning glass		UN_x	Nb	20	1×10^{-5}	4
1388	Corning glass		UN_x	Nb	20	2.5×10^{-5}	4
1383	Corning glass		UN_x	Nb	20	5×10^{-5}	4
1385	Corning glass		UN_x	Nb	20	7.5×10^{-5}	4
1392	Corning glass		UN_x	Nb	20	1×10^{-4}	4
1399	Corning glass		UN_x	Nb	20	3.2×10^{-4}	4
1393	Corning glass		UN_x	Nb	20	7×10^{-4}	4
1395	Corning glass		UN_x	Nb	20	1×10^{-3}	4
1396	Corning glass		UN_x	Nb	20	2.5×10^{-3}	4
1408	Corning glass		UN_x	Nb	500	2.5×10^{-5}	4
1246	$(0\,0\,1)$ Al_2O_3	$(0\,0\,1)$ Nb	$(0\,0\,1)$ UN	Nb	700	1.5×10^{-5}	4
1077	$(0\,0\,1)$ CaF_2		$(0\,0\,1)$ U_2N_3	Nb	700	7×10^{-4}	4
1028	$(0\,0\,1)$ Al_2O_3	$(0\,0\,1)$ Nb	$(0\,0\,1)$ UN	Nb	500	2.1×10^{-5}	4
1189	$(0\,0\,1)$ CaF_2		$(0\,0\,1)$ U_2N_3	Au	700	7×10^{-4}	4
1431	$(0\,0\,1)$ CaF_2		$(0\,0\,1)$ U_2N_3	Nb	750	7×10^{-4}	4, 5
1180	$(0\,0\,1)$ Al_2O_3	$(0\,0\,1)$ Nb	$(0\,0\,1)$ UN	Nb	650	2×10^{-5}	5
1430	$(0\,0\,1)$ Al_2O_3	$(0\,0\,1)$ Nb	$(0\,0\,1)$ UN		650	5×10^{-5}	6
1062	$(0\,0\,1)$ Al_2O_3	$(0\,0\,1)$ Nb	$(0\,0\,1)$ UN		500	2×10^{-5}	6
1029	$(0\,0\,1)$ Al_2O_3	$(0\,0\,1)$ Nb	$(0\,0\,1)$ UN	Nb	500	2.1×10^{-5}	6
1056 & 1057	Corning glass		UN		20	1.5×10^{-5}	7
1058 & 1059	Corning glass		U_2N_3		20	7×10^{-4}	7
1050 & 1051	Corning glass		UO_2		20	2.5×10^{-5} O_2	7

Chapter 4

Sample Characterisation

This chapter provides an introduction to x-rays and their interaction with matter, with a focus on the use of x-ray photoelectron spectroscopy for chemical characterisation and the methods used for structural characterisation of samples throughout this thesis: x-ray diffraction and x-ray reflectivity. X-ray photoelectron spectroscopy has been used to obtain high resolution spectra of UN and U_2N_3 thin films, with the results giving insight into the stoichiometry and bonding in these materials. Structural analysis of polycrystalline and epitaxial uranium nitride thin films are presented, showing that single phase and single crystal samples have successfully been produced. Some of the results presented in this chapter have been published in Thin Solid Films [119].

4.1 X-rays

Since their discovery in 1895, x-rays have become an important tool across all scientific disciplines [120]. With the defining property of a wavelength between 0.1 Å and 100 Å, which is the scale of inter-atomic distances, x-rays are a form of electromagnetic radiation that is ideally suited to structural investigations of materials, as covered in Section 4.3.

In addition, they have energies of 100 eV to 100 keV, similar to that of electron binding energies, making x-ray-electron interactions a vital method for chemical bonding analysis, as detailed in Section 4.2. Furthermore, as electrons are responsible for the magnetic properties of materials, x-ray scattering can also be used to investigate the magnetic properties of material, which is a topic described in Chapter 5.

When characterising thin films, x-rays provide certain advantages compared to other probes. The attenuation length of x-rays in uranium nitride is on the order of 0.1 μm at commonly used energies, which, combined with the relatively broad x-ray beam, means that results will be a good representation of sample averages. This would not be the case with a probe such as electrons, which have a much lower attenuation length. Certain neutron techniques would produce the opposite problem, with high signal to noise and film to substrate ratios. Consequently, x-ray techniques form the basis of the majority of the work undertaken in this thesis.

4.1.1 X-ray Interaction with Matter

Before delving into the applications of x-ray-matter interactions, let us first consider the different ways in which the interaction can proceed, as shown in Figure 4.1. These interactions can be categorised into scattering (top row), and absorption (bottom row) processes.

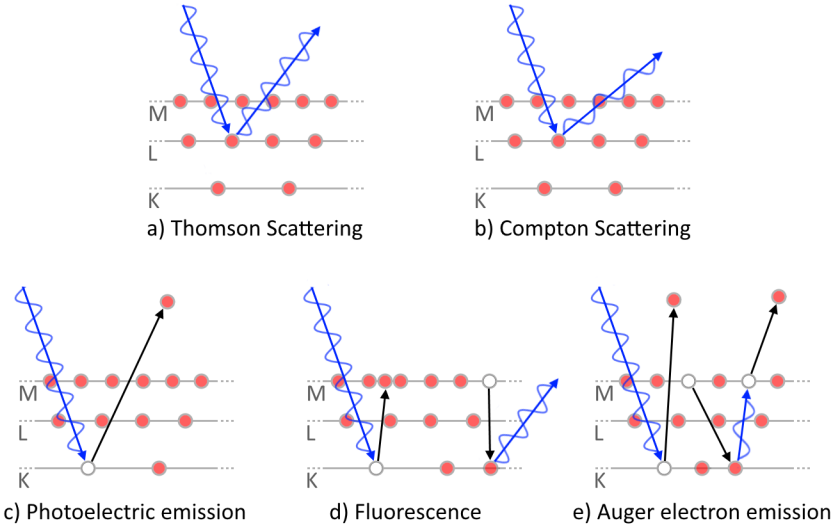

Figure 4.1: *Diagram showing possible methods of x-ray-electron interaction.*

As an x-ray photon is incident on an atom, it may interact with an electron causing it to be scattered with the same energy, known as Thomson scattering, as shown in Figure 4.1 a). If the scattered x-ray is changed in energy, it is known as Compton scattering, shown in b).

As an x-ray photon is incident on an electron it may be absorbed, exciting the electron. If the electron is excited with energy greater than its binding energy, it may be cause it to escape the atom in a process called photoelectric emission, as shown in Figure 4.1 c). Alternatively, the electron may instead be excited to a higher energy level, e.g. from the K edge to the M edge, as shown in Figure 4.1 d). This will create a core hole, which may then be filled by the transition of an electron at a higher energy level, causing a photon with energy equal to the difference in energy levels to be emitted, known as fluorescence. Subsequently, this photon may excite an electron, causing it to be emitted from the atom, termed Auger electron emission, show in 4.1 e).

These processes are described for interactions with an individual atom but in reality these atoms will be part of an ensemble and the radiation resulting from these processes will be influenced by the ensemble in which the atom lies. This can be due to the effect of the ensemble on the electronic properties of the atom, due to the interaction of the resultant radiation with the ensemble, or due to the interaction of the resultant radiation with radiation from the ensemble.

Therefore, analysing the intensity, spacial dependence, energy dependence, or other properties of this radiation gives unique insight into the material. Consequently, these different interaction processes have been developed into widely used characterisation techniques. Each of these different forms of interaction provides a method with which to investigate different properties of the incident material. This work focuses on x-ray scattering processes, covered both in this chapter and in Chapter 5, and photoelectric emission, covered in this chapter.

4.1.2 X-ray Sources

To be able to use x-rays as an investigative tool, it is essential to be able to produce them in the form required for each method of investigation. As electromagnetic radiation is produced by the acceleration of charged particles, and the electron has a high charge to mass ratio, all common sources use the acceleration of electrons to produce x-rays. The method by which this is performed will define properties such as the wavelength, flux, and coherence of the x-rays,

which are important factors in many experimental techniques.

4.1.2.1 Tube Sources

The x-ray tube source dates back to the discovery of x-rays by Roentgen, and the basic design is still widely used in laboratories today [120]. Early versions of the tube source used the ionisation of air inside a partially evacuated chamber to produce an acceleration of charge, however, modern designs heat a tungsten filament cathode to produce electrons by the thermionic effect [121]. The electrons generated will then accelerate towards a metal anode, most commonly made of copper or molybdenum. The collision of the electrons with the anode causes rapid deceleration, where kinetic energy is dissipated as x-rays and heat. These x-rays can arise either due to a series of inelastic interactions, creating Bremsstrahlung radiation, or due to x-ray fluorescence.

Bremsstrahlung radiation creates x-rays with a broad, continuous range of energies, as shown in Figure 4.2. As it is undesirable to have a x-rays with a wide energy range for most characterisation techniques, this Bremsstrahlung radiation is normally filtered out.

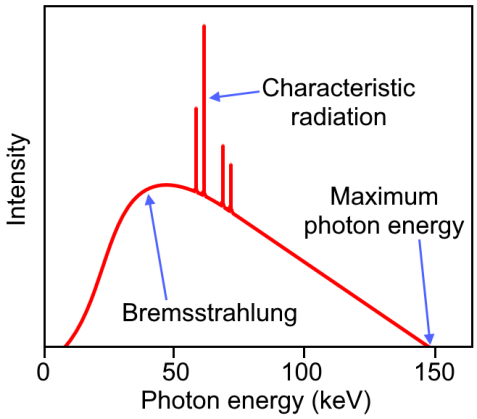

Figure 4.2: *Spectrum of x-ray energies generated from electrons incident on a metal anode.*

Conversely, the x-rays produced by fluorescence have discrete wavelengths as they arise from the transitions of electrons between the energy levels of the anode metal. This process involves the incident electrons exciting an electron in the core levels of the anode to higher orbitals. As the core hole created is filled by an electron in a higher orbital, an x-ray with energy equal to the energy difference between the two levels is produced. Figure 4.1 depicts this process for

x-ray fluorescence, which is the same except for the initial electron excitation being caused by an incident x-ray rather than an electron.

The x-rays produced by this method are known as characteristic x-rays as their energy is unique to each element and transition, and it is common to describe them by these details. For example, the x-ray produced by transition from the L to K orbitals in copper is known as Cu K_α radiation, whereas that produced by the transition from M to K is known as Cu K_β.

As x-ray tubes produce x-rays of a range of energies propagating in any direction, it is often necessary to monochromate and spatially confine the beam in order to use it for measurements. This is achieved by using Bragg reflections (covered in Section 4.3.1) of a single crystal at a fixed angle such that only x-rays of a specific energy are reflected or using filters that will absorb radiation at the energies that are not wanted. This monochromated beam is then collimated and controlled with slits such that the x-ray beam is only incident on desired areas and resolution is optimised.

In practice, x-ray tube sources provide a simple way to produce monochromated x-rays, which is essential for many techniques, and is the main reason for their wide use. There are, however, downsides to x-ray tubes, such the as the lack of ability to alter the x-ray energy produced and the relatively low flux achievable. The latter problem is due to the heating of the anode, which increases with increasing anode current. Water cooling of the anode, and the use of a rotating anode source so that only a small area is struck by electrons at any one time, helps to reduce heating, but the achievable flux is still much lower than that of synchrotron sources.

4.1.2.2 Synchrotron Sources

Many of the limitations of tube sources are overcome in the production of x-rays by synchrotron sources. Unlike a tube source, it is possible to alter the energy and coherence of the radiation produced by a synchrotron source, allowing a much broader range of investigations to be performed. Additionally, the achievable brilliance of a synchrotron source is 10 orders of magnitude higher than that of a tube source [122].

Synchrotrons produce x-rays by accelerating bunches of charged particles, normally electrons, around a storage ring at relativistic speeds. Along this storage ring, the electrons pass through insertion devices which consist of a lattice of magnets. These magnets produce an alternating electric field which causes the electrons to oscillate, as shown in

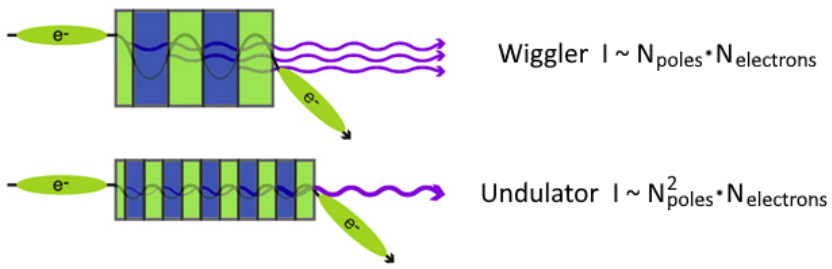

Figure 4.3: *Radiation produced from wiggler (above) and undulator (below) insertion devices. From [7].*

Figure 4.3. In the case of a wiggler insertion device, the electric field will cause the electrons to move in a sinusoidal path, producing radiation with an intensity that is the sum of the intensities caused by each oscillation. If an undulator insertion device is used, the oscillation amplitude will be much smaller and in phase with the photons produced, creating coherent radiation. This radiation will be much more intense, being proportional to the sum of the square of the radiated amplitudes [122].

Due to the wide range of photon energies and the broad beam produced by these devices, the beam is then monochromated and focused. Similar to a tube-source, this is normally achieved by using the Bragg reflections of high quality single crystals, often Ge or Si. It is common to use two monochromating crystals in this configuration in order to maintain the direction of the monochromated beam at different energies and additionally reduce the energy bandwidth. The desired photon energy can then be selected by the scattering angle at the crystal. Alternatively, the temperature of the single crystal monochromater can be used to control the lattice spacing of the crystal, therefore altering the energy of the photon that will be reflected at a fixed angle. Finally, x-ray mirrors and Fresnel lenses can be used to focus the beam and slits used to control the beam size before it is delivered to the sample to be measured.

4.2 Chemical Characterisation

Chemical characterisation using x-ray photoelectron spectroscopy has been performed on the thin films studied in this thesis in order to quantify the elemental composition of the films and therefore determine the stoichiometry of the samples. This characterisation also provides information on the electronic structure and chemical bonding in the films, giving insight into the chemistry of the film material and how this compares with bulk literature data.

4.2.1 X-ray Photoelectron Spectroscopy

4.2.1.1 Theory

X-ray photoelectron spectroscopy (XPS) is a technique that analyses the energy of electrons emitted from a material by the photoelectric effect. As the escape depth of a photoelectron is on the order of nanometers, XPS is a surface sensitive technique.

The photoelectric effect is a processes in which energy is imparted to an electron by an incident photon, in this case an x-ray photon. If the energy is greater than the binding energy of the electron, $E_{binding}$, it will be emitted from the atom with some kinetic energy, $E_{kinetic}$. By analysing the energy of this electron, $E_{binding}$, can be determined using the equation below, Koopmans' theorem, where $h\nu$ is the energy of the incident photon, and ϕ is the work function of the electron spectroscopy analyser [123].

$$E_{binding} = h\nu - E_{kinetic} - \phi \tag{4.1}$$

Thus, by fixing the value of $h\nu$ and ϕ by using a monochromatic x-ray source, it is possible to investigate the binding energies of electronic states in a material. As each element has a unique electronic configuration, with energies affected by their local environment and bonding, this technique can be used to identify elements and their chemical bonding state within a material.

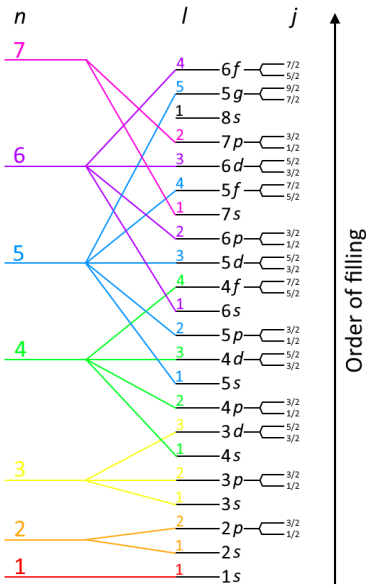

Figure 4.4: *Diagram of electron configuration in order of filling, showing principal quantum number, n, orbital angular momentum quantum number, l, and total angular momentum quantum number, j.*

Electronic Configuration

Each electron in an element's unique configuration can be described by a set of quantum numbers, which has been depicted in Figure 4.4. The principal quantum number, n, defines electron shells of different energies which correspond to different absorption edges. The orbital angular momentum quantum number, l, determines the electron sub-shell, labeled with s, p, d, f for l = 0, 1, 2, 3, respectively. As each orbital can hold 2 electrons, one with spin, s, 1/2 and one with spin -1/2. Each electron shell can hold $2n^2$ electrons and each sub-shell $2(2l+1)$ electrons. Each sub-shell is then split into different energy levels by spin-orbit splitting, described by j, the total angular momentum quantum number. This number is defined by $j = |l + s|$, meaning there will be two values of j for $l \geq 1$, and only one for $l = 0$. The degeneracy of these spin-orbit split states is defined by $2j + 1$.

For example, electrons in the $4f$ orbital have $n = 4$ and $l = 3$, and are spin-orbit split into $j = 7/2$ and $j = 5/2$ levels which will have relative degeneracy of 4 and 3, respectively. Consequently, when measuring the spectra of a material with fully occupied $4f$ states, such as uranium, it can be seen that the relative occupancy and therefore intensity of the $4f_{7/2}$ and $4f_{5/2}$ states is 4:3.

Chemical Bonding

As an atom forms a chemical bond, the energy of electrons in bonding states will be altered, and the energies of other core states may also be altered as a consequence, causing a 'chemical shift' in core electron energies. This arises as the energies of electronic states are determined by electrostatic interaction the with nucleus. This interaction is influenced by shielding from other electrons, even valence electrons, which causes a reduction in the binding energies of states. Since chemical bonding changes the number and/or energies of electrons of an atom, the contributions to these shielding effects will be changed. Therefore, oxidation, a loss of electrons, reduces the amount of shielding, causing an increase in the binding energy of electronic states. Similarly, reduction will cause a decrease in the binding energy of electronic states. Consequently, the observed binding energy can be used to determine the oxidation state of an element [124].

The effects above are termed initial state effects and are dependent on the intrinsic properties of the material. However, as photoemission creates core holes, the electron states of an atom will be affected by this hole, causing effects known as final state effects. The electron relaxation caused by this core hole will cause a lowering of observed binding energies, with core hole screening and polarisation of surrounding ions also contributing to this effect. As outer shell electrons will contribute more to relaxation effects and valence electrons can move more freely in a metal, comparing spectra of the same element with metallic and non-metallic bonding, the spectra from the metal can be expected to have lower binding energy [124, 125].

Further Effects

In addition to initial and final state effects, there are further effects that will influence measured photoelectron spectra. Each measured state will have some intrinsic width in energy, due to temperature effects and lifetime effects. This will be convoluted with width effects due to the energy resolution of the photon source and detector.

As photoelectrons are emitted from an atom, they may interact inelastically with other electrons. Inelastic interaction with valence electrons is most likely, and will cause the photoelectron to lose energy to the valence electron, which then move to higher energy states. In the case of an insulating material, this valence band will be away from the Fermi edge and therefore the elastically scattered photoelectrons will appear as a separate peak in the photoelectron spectra, known

as a shake-up satellite [121]. For a metallic material, the valence band will be on the Fermi edge, causing the satellite to appear as an asymmetric tail on the scattered state [125].

As well as inelastic scattering of photoelectrons with valence states, other interactions will also occur. Electron-electron interactions will cause photoelectron energy losses resulting in tails in intensity on the high energy side of the peak in the photoelectron spectra. This background tail will also have some contribution from electron-phonon interactions. As the probability of these interactions will increase with the depth of material the photoelectron travels through before reaching the detector, this background contribution is depth sensitive.

Auger electrons, described in Section 4.1.1, can be produced by the hole created by photoemission, and will create peaks in the photoelectron spectra. These Auger electrons can be distinguished from photoelectrons as the measured kinetic energy of Auger electrons is not dependent on the energy of the incident photon.

The intensity of peaks from a single element in photoelectron spectra will be different for each state, with the relative ratios equal to the ratios of the energy dependent cross-sections for each state. These cross-sections are well documented in literature [126]. If they are taken into account, the intensities of peaks from different elements can be used to determine the stoichiometry of the material being analysed.

4.2.1.2 Measurement

All XPS measurements presented in this thesis were taken at the Bristol NanoESCA facility which uses an Al x-ray tube source. For high energy resolution, lab based x-ray sources typically use Al or Mg radiation, due to the low width in energy of their characteristic radiation.

A ScientaOmicron XPS Argus analyser was used to measure the kinetic energy of photoelectrons. This is a concentric hemispherical analyser that utilises a electrostatic field to spatially separate electrons of different kinetic energies, as depicted in Figure 4.5. Before electrons enter the analyser, they first pass through an aperture and are retarded and focused. Within the analyser, potentials V_1 and V_2 are applied to two concentric hemispherical electrodes with inner radius R_1 and outer radius R_2 This creates an electrostatic field between the two hemispheres with a $1/R^2$ dependence. Consequently, the electrons that travel through this potential will be linearly separated by kinetic energy before they reach the detector on the opposite side of the hemisphere.

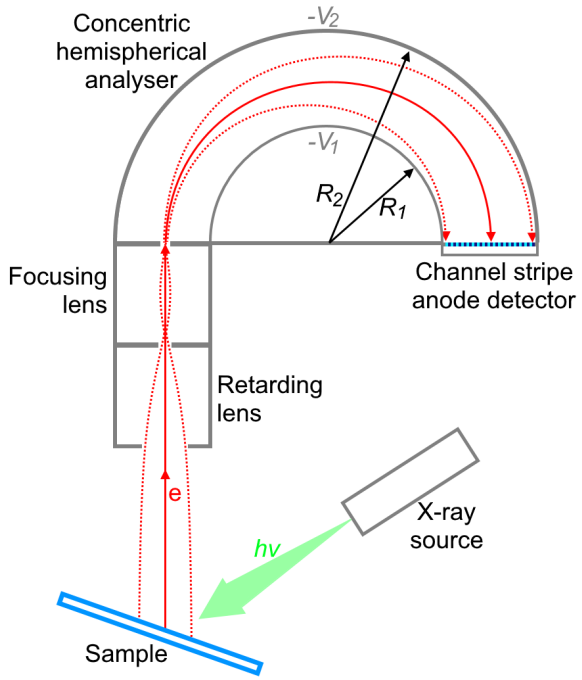

Figure 4.5: *Diagram of a concentric hemispherical analyser, as used in XPS measurements. Electrons with energy E_0 will reach the centre of the detector, following the red solid line, while those with energy in the range $E_0 \pm dE$ will reach the detector within the red dotted lines.*

$$E_0 = e\Delta V R_0^2 \frac{R_1 R_2}{R_2^2 - R_1^2} \tag{4.2}$$

For a given electrostatic field in the hemisphere, only electrons with a certain kinetic energy, E_0 will reach the centre of the detector at R_0. This energy is called the pass energy, and can be altered by changing the field strength, as shown in Equation 4.2. Electrons with a range of energies $E_0 \pm dE$ will also reach the detector at a distance $R_0 \pm dR$. Since $dE/dR \propto E_0/R_0$, i.e. the spread of energies that reach the detector decreases with pass energy, lowering the pass energy will improve the energy resolution of the detector [127]. However, electron transmission will decrease with pass energy, decreasing counts at the detector. It is common practice to take scans with a fixed pass energy, as the energy resolution will then be independent of energy. To scan in kinetic energy, the retardation voltage is altered.

It is necessary to take XPS measurements under UHV as electron transmission, and therefore counts at the detector, will decrease with increasing pressure. Measurements taken at the Bristol nanoESCA facility were performed at

pressures below 10^{-9}, achieved using UHV equipment. These low pressures also reduce the level of contamination, which is particularly important when investigating air sensitive materials such as the uranium nitrides.

In order to further reduce possible contamination of uranium nitride thin films, measurements were taken from capped samples to avoid sample oxidation in air when transferring the samples to the XPS UHV chamber. This cap was then removed by Ar sputtering, as described in Section 3.2.1, but with the Ar^+ ions bombarding the sample surface. This causes the surface layer to be sputtered away, removing the cap and exposing the underlying film.

For each sample measured, survey scans were taken with a pass energy of 50 eV, before scans of the N-1s, U-4f, O-1s, C-1s, and valence band states were taken with a pass energy of 6 eV.

4.2.1.3 Analysis

XPS analysis was performed using CasaXPS software [128]. Before peak fitting was performed, all XPS data was calibrated using the Fermi edge. Calibration of XPS data is necessary as ϕ, the work function of the electron spectroscopy analyser, as shown in equation 4.1, is not constant. This is often performed using peaks that are present in most spectra, such as the C-1s peak, however, calibration using the Fermi edge gives better accuracy in energy values, though this is only possible with metallic materials.

Fitting of XPS spectra was performed using a Shirley background. This background is calculated such that the intensity at a given energy, E_x is proportional to the total area minus background for $E < E_x$. Peaks were fitted with a Gaussian Lorentzian product, GL(x), with mixing value %GL, where %GL = 0 for pure Gaussian and 100 for pure Lorentzian. For metallic peaks centred on x_c, an asymmetrical tail modifying factor $T(x)$ is included, which spreads the GL peak for $x \leq x_c$, as defined below

$$Y(x) = GL(x) + (1 - GL(x)) \cdot T(x) \qquad T(x, t, w, x_c) = \begin{cases} e^{t(x-x_c)/w} & \text{for } x \geq x_c \\ 0 & \text{for } x < x_c \end{cases} \tag{4.3}$$

In this equation, t is a value from 0 to 1 that defines the level of peak asymmetry, with $t = 1$ giving no asymmetry [128].

To perform data fitting, initial guesses of peak position, shape, intensity, and width are made. These values are then optimised using the in-built CasaXPS fitting function to reduce the residual standard deviation between the fit and data.

This function is capable of fitting width, intensity, and position, but not line shape. It is necessary to put constraints on the values to be fitted, however, these were kept very broad, with the width limited at 2.5 eV.

To investigate the stoichiometry of samples, quantitative area analysis was performed by normalising peak areas by their orbital cross-sections, as defined by Yeh *et al.*, and by the total fitted area of the U-4$f_{7/2}$ peak [126].

4.2.1.4 XPS Results

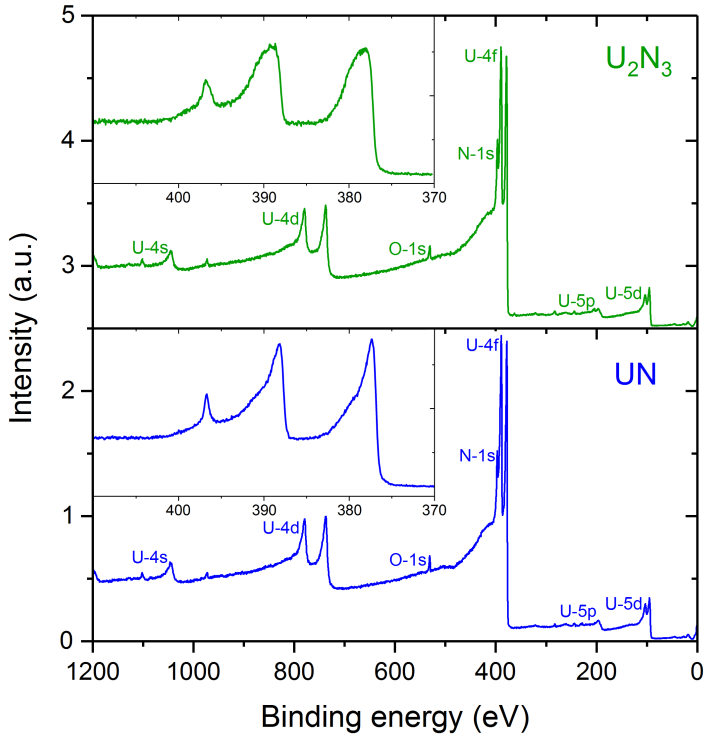

Figure 4.6: *XPS survey scans of the* $(0\,0\,1)$ U_2N_3 *and UN samples, with U-4*f *and N-1*s *states inset.*

XPS survey scans of UN (SN1246) and U_2N_3 (SN1077) samples after their Nb cap had been removed by Ar sputtering are shown in Figure 4.6. In these spectra, only peaks from U, N, and O are visible, showing that the only contamination present on the samples is from O. No peaks from the Nb and Au caps and Nb buffer and CaF_2 substrate are visible, showing that the spectra were collected only from the films.

Inset in Figure 4.6 is a close-up of the U-4f and N-1s states. A clear asymmetry can be seen in the U-4f peaks,

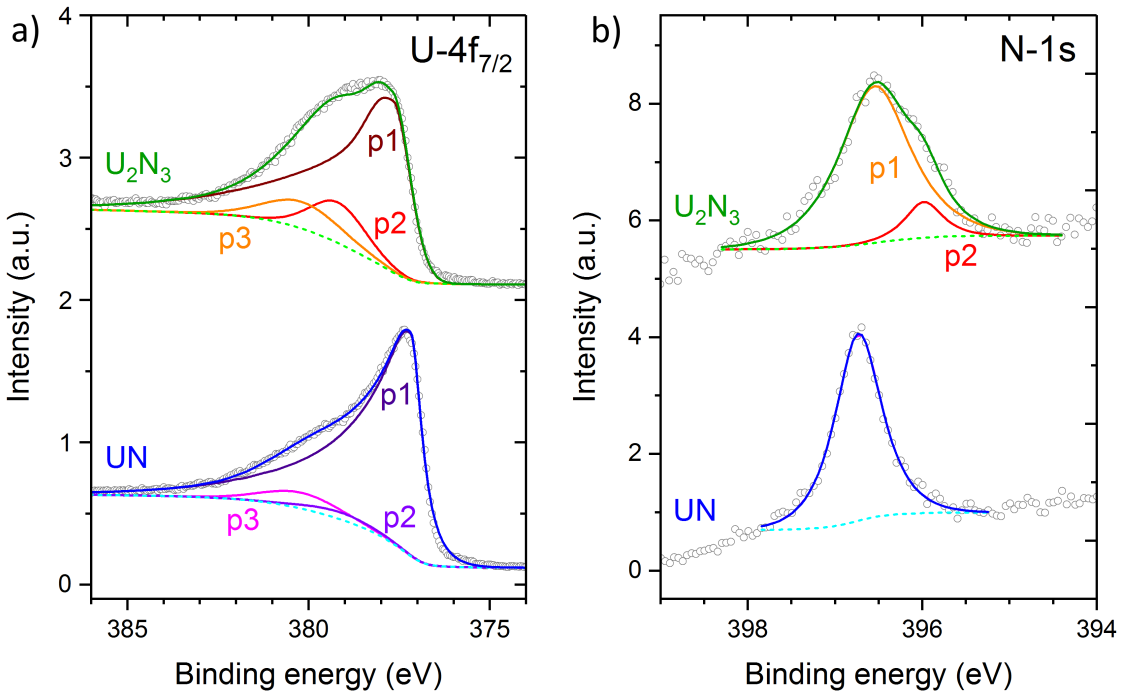

Figure 4.7: *Fitted a) U-4$f_{7/2}$ and b) N-1s spectra of the* (0 0 1) *U_2N_3 and UN samples, with total fit shown in green and blue, respectively, and background shown by a dashed line.*

which is more pronounced for UN than for U_2N_3. The width of the U-4f peaks also differs between the two materials, with peaks from UN being narrower. This is also true of the N-1s state, and the intensity of the N-1s state in U_2N_3 is higher than in UN, which is to be expected of the higher stoichiometry material.

The differences in the U-4$f_{7/2}$ states of UN and U_2N_3 can more clearly be seen in Figure 4.7 a), which shows their fitted U-4$f_{7/2}$ spectra. In this plot, the different peaks that were used to fit the grey data points are labeled, with the background shown as a dashed line and total fit shown in green and blue for U_2N_3 and UN, respectively.

As can be seen in Figure 4.7 a), the U-4$f_{7/2}$ states were fitted with three peaks, with the lowest binding energy peaks, p1, containing the asymmetry factor $T(x)$, described above. There is a pronounced difference in the level of asymmetry between UN and U_2N_3, with p1 in UN being sharper and more asymmetric. This peak is also at a lower binding energy in UN than in U_2N_3.

In UN and U_2N_3, the p2 and p3 peaks appear at the same binding energy but have different intensities. For UN, p2

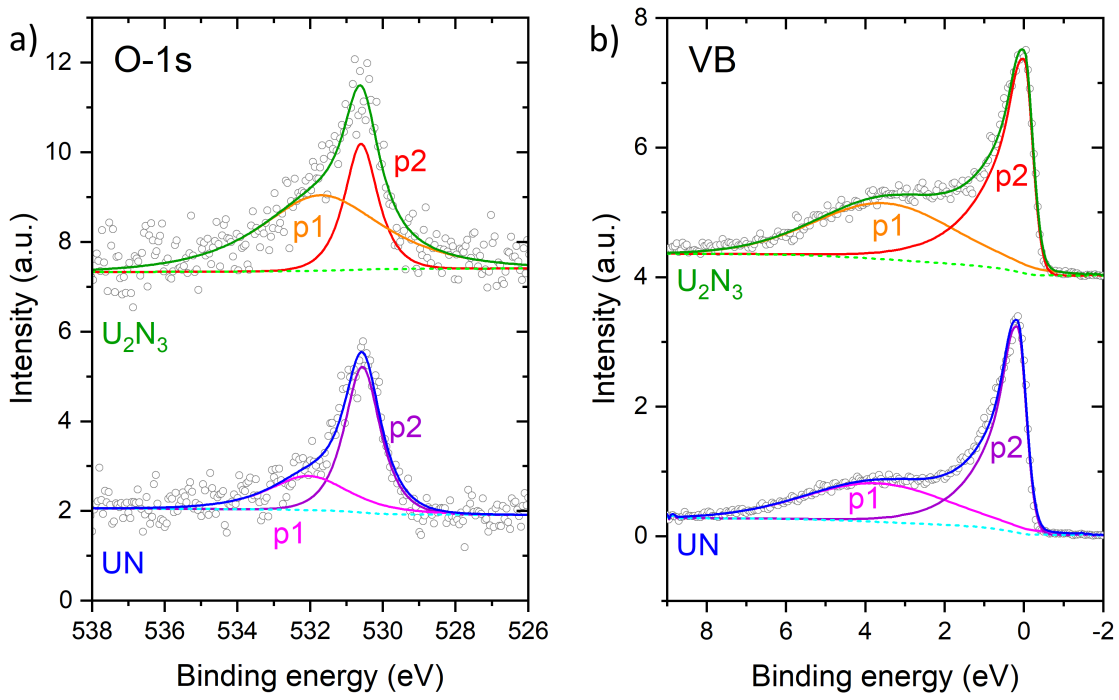

Figure 4.8: *Fitted a) O-1s and b) valence band spectra of the* $(0\,0\,1)$ U_2N_3 *and UN samples, with total fit shown in green and blue, respectively, and background shown by a dashed line.*

has very low, almost negligible, intensity contrasting with the relatively high intensity seen in U_2N_3. Intensities of the p3 peaks are more similar between the two material, but still higher in U_2N_3.

The fitted N-1s state spectra of UN and U_2N_3 samples are displayed in Figure 4.7 b), with the background shown with a dashed line and total fit shown in green and blue for U_2N_3 and UN, respectively. Comparing the two spectra, the N-1s state in U_2N_3 appears to be broader and more asymmetric than in UN. Consequently, these spectra were fitted with two peaks in the case of U_2N_3 and one peak in the case of UN. The position of the main peak, p1, in U_2N_3 is at slightly lower binding energy than in UN, and is also broader.

O-1s spectra from UN and U_2N_3 samples are shown in Figure 4.8 a), where it can be seen that both spectra were fitted with two symmetric peaks. The higher energy of these two peaks was found to be broader and to have higher intensity in U_2N_3 compared to UN, though, due to the low intensity of these peaks, the uncertainty in these fits is high.

The valence band spectra collected for UN and U_2N_3 samples are displayed in Figure 4.8 b). Both spectra show the U-5f state on the Fermi edge, p2, evidence of the metallic nature of UN and U_2N_3. Additionally, a broad peak, labeled

p1, is present in both spectra. This peak is attributed to the N-2p state and the relative intensity of this peak is greater in U_2N_3 than in UN.

Spectra of the C-1s peaks were also collected for the UN and U_2N_3 samples, however, as no peaks were detected, the results have not been shown here.

Table 4.1: *X-ray photoemission line fit values for UN and U_2N_3 films.*

Sample	Peak		Position (eV)	FWHM (eV)	%GL	t	Area
U_2N_3	U-4$f_{7/2}$	p1	377.7	1.1	15	0.50	0.769
	U-4$f_{7/2}$	p2	379.2	1.8	30	0	0.121
	U-4$f_{7/2}$	p3	380.3	2.5	30	0	0.110
	N-1s	p1	396.6	0.9	80	0	0.071
	N-1s	p2	396.0	0.6	80	0	0.009
	O-1s	p1	531.7	3.9	80	0	0.015
	O-1s	p2	530.6	1.1	80	0	0.048
	VB	p1	3.8	4.0	30	0	0.022
	VB	p2	0.0	0.5	30	0.5	0.033
UN	U-4$f_{7/2}$	p1	377.2	0.7	90	0.38	0.904
	U-4$f_{7/2}$	p2	379.2	2.3	30	0	0.027
	U-4$f_{7/2}$	p3	380.2	2.5	30	0	0.069
	N-1s	p1	396.7	0.6	80	0	0.056
	O-1s	p1	532.0	2.6	80	0	0.015
	O-1s	p2	530.6	1.2	80	0	0.029
	VB	p1	3.8	4.0	30	0	0.019
	VB	p2	0.0	0.5	30	0.5	0.031

The above discussion has provided a qualitative description of the XPS results from UN and U_2N_3 samples, while a

quantitative description is provided by the fitted peak positions, areas, widths, and line-shapes of each state in Table 4.1.

From the areas shown in Table 4.1, which have been normalised to the total area of the U-4$f_{7/2}$ peaks and the photoionisation cross-sections provided by Yeh *et al.*, it has been calculated that the N:U ratio for UN and U_2N_3 samples is 1.02±0.02 and 1.52±0.04, respectively [126]. The area of p3 in the U-4$f_{7/2}$ state was not included in these calculations as the position of the peak at 380.2 eV corresponds to U(IV), suggesting that this may be due to oxide contamination in the films [60].

The position of p2 in the U-4$f_{7/2}$ state in both UN and U_2N_3 samples was found to be the same, however, p1 was 0.5 eV lower in UN. Additionally, there were differences in the p1 line shape between the two materials, with p1 in UN showing higher asymmetry with $t = 0.38$, whereas a value of $t = 0.5$ was used to fit p1 in U_2N_3. This peak was also found to be 0.4 eV narrower in UN.

Similarly, UN was shown to have a 0.3 eV narrower N-1s peak than the p1 peak, the higher intensity peak, in the N-1s state of U_2N_3. These peaks also showed a small energy gap of 0.1 eV. The most notable difference in the two N-1s spectra is the presence of a second peak at lower binding energy for U_2N_3.

Comparing the fit values from the valence band spectra of UN and U_2N_3 samples, all values are the same except for the relative areas of p1 and p2, with UN having a p2 peak with greater relative area.

4.2.2 Discussion of Chemical Charcterisation Results

Quantitative XPS area analysis has shown UN and U_2N_3 thin film samples to have N:U ratios of 1.02±0.02 and 1.52±0.04, respectively, showing them to be stoichiometric within errors. While this is an important result, these XPS results can be further analysed and compared to literature, providing insight into the bonding and electronic properties of not only these thin film samples, but of all UN and U_2N_3 material.

4.2.2.1 U_2N_3

Comparing the results from the XPS of the U-4f state in the U_2N_3 sample to literature, it can be seen that the sample yielded results similar to those of Wang $et\ al.$, Long $et\ al.$, and Black $et\ al.$ [6, 65, 129]. The position of the highest

intensity peak, p1, at 377.7 eV is 0.5 eV higher than the similar peak in in the spectra of UN at 377.2 eV. This peak was fitted as asymmetric, which along with the energy position show it to be consistent with the results and analysis provided by Wang $et\ al.$. This asymmetry, due to electron-hole excitations near E_F, and the relatively low binding energy show the somewhat metallic nature of U in U_2N_3. However, the peak is not as asymmetric or as low in binding energy as that seen in UN and U metal, showing the partial localisation of the $5f$ states, as described by Black $et\ al.$. This peak is also 0.3 eV broader in U_2N_3 than in UN. As all experimental parameters were the same for both measurements, this broadening must be due to chemical effects, and suggests that bonding is more mixed in U_2N_3 than in UN.

Another difference between the U-$4f$ spectra of UN and U_2N_3 is intensity of p2, which is almost negligible in UN. This peak appears at a binding energy of 379.2 eV, between the metallic and U(IV) peaks. Due to the strong similarities in the measured valence band spectra of UN and U_2N_3, it is unlikely that this peak is due to shake-up effects. Considering the possible origin of this peak, it could be attributed to U(III), which would be expected for a peak at lower binding energy than U(IV) at 380.2 eV. This U(III) state has been found at positions between 378.1 and 379.8 eV by Thibaut *et al.* in uranium halide and oxyhalide systems [130]. In the uranium oxynitrides, a similar state has been found at 378.7 eV by Eckle *et al.* and 379.7 eV by Luo *et al.*, with this range likely to be due to the wide range of possible UN_xO_y stoichiometries [66, 113]. Though not explicitly stated in the literature, it is possible that these peaks in uranium oxynitrides show the presence of U(III). The position of this peak in the present U_2N_3 sample, p2, is within both of these ranges, showing that it is likely that it caused by the presence of U(III) in the U_2N_3.

To determine whether this U(III) state can also be attributed to the presence of uranium oxynitrides, it is necessary to consider the O-$1s$ spectra. These spectra have been fitted with two peaks in both UN and U_2N_3, with p2 at 530.6 eV, corresponding to the binding energy seen in UO_2 [131]. However, Luo *et al.* found the O-$1s$ peak in uranium oxynitrides at the same position, so it cannot be determined if p2 peak seen in the present spectra is due to the presence of uranium oxynitrides or UO_2 contamination [66].

Instead, let us compare the O-$1s$ results of U_2N_3, with a strong U(III) peak, to UN, with an extremely weak, almost negligible, U(III) peak. Calculating the area ratios of U(III):O-$1s$ p1, U(III):O-$1s$ p2, and U(III):O-$1s$ (p1 + p2), we consistently find that the values are higher for UN than U_2N_3, showing a proportionally larger quantity of O in the UN system. Additionally, the U(IV) peak has a larger area in U_2N_3 than in UN, meaning more of the O in the system can be

attributed to UO_2. This is contrary to the results that would be expected if the U(III) state measured in U_2N_3 were due to the presence of oxynitride. Consequently, it is possible that the presence of this U(III) state is not a result of uranium oxynitride contamination, and is instead an intrinsic property of U_2N_3.

Wang *et al.* attribute this peak to UN_2. Though not fitted, their results seem to show that this peak has much higher intensity than observed in U_2N_3 here. As stoichiometry increases from U_2N_3 to UN_2, trends in magnetic ordering (see Figure 5.16 and [16]) suggest an increase in localisation of the $5f$ electrons as bonding becomes increasingly covalent. Consequently, it would be expected that the intensity of the U(III) peak compared to the metallic peak increases with stoichiometry. Though a comparison with the result of Wang *et al.* is indicative of this, a study of the effect of stoichiometry on observed spectra is necessary to test this hypothesis.

The results from the N-1s spectra of UN are as expected, considering the literature, but this is not true for U_2N_3. Though Long *et al.* and Wang *et al.* both state that their data does not show any difference in the N-1s state between UN and U_2N_3, the data presented here shows a broadening and a 0.1 eV shift in binding energy of p1 and the presence of a shoulder at lower binding energy, which was fitted with a separate peak, p2. This broadening, as seen in p1 in the U-4f state, could be further evidence of mixed bonding states in U_2N_3.

Considering the origin of the N-1s p2 peak, Luo *et al.* found a shift in the N-1s peak to a position of 396.0 eV during the oxidation of $UN_{1.66}$, matching the position of the p2 peak [132]. We can also compare the present results to N-1s spectra in different mononitride systems, such as TiN. In a study of TiN oxidation, a similar shift in energy and appearance of a shoulder at lower binding energy was seen as the O_2 dose was increased [133]. This shows that the N-1s state in U_2N_3 could be due to oxynitride contamination.

4.2.2.2 UN

The sharp asymmetric peak of the U-4$f_{7/2}$ state taken from the UN sample is positioned at 377.2 eV, the same position as in U metal [131]. This is evidence of the itinerant nature of the $5f$ electrons in UN, as has been described by Fujimori *et al.* and Reihl *et al.* [52–54]. This result is comparable to the spectra presented by Norton *et al.*, Long *et al.*, Black *et al.*, and Wang *et al.*, though there are slight differences in the spectra on the high energy side of the peak, likely due to differing levels of contamination in each sample [6, 60, 65, 129]. The only fitted spectra available in the literature

is that of Samsel-Czekała $et\ al.$, taken from a single crystal UN sample [57]. Compared to this work, the results of Samsel-Czekała show a much greater relative contribution from the peaks at 379.2 eV (p2 here) and 380.2 eV (p3 here). This is probably due to the purity of the sample, or due to the oxidation product present on the surface when the spectra were collected.

Though the present results show some differences between the N-1s spectra of UN and U_2N_3, which is unexpected, the results for UN are consistent with literature, with all previously referenced studies reporting similar N-1s peak positions and widths. This shows that the chemistry of the UN thin film samples is analogous to bulk UN. Furthermore, the results presented here have relatively low oxide contamination, are of high resolution, and have been well characterised, making them exemplary spectra.

4.2.3 Conclusion

The x-ray photoelectron spectroscopy measurements conducted at the Bristol nanoESCA Laboratory on $(0\,0\,1)$ UN and U_2N_3 films synthesised by reactive DC magnetron sputtering have been reported in this section. Quantitative analysis of the results has shown that both UN and U_2N_3 samples are stoichiometric, within errors. The presence of U(IV) and O-1s states in the spectra collected from both samples showed that oxide contamination was present.

The asymmetric peaks seen in the U-4f spectra of UN are indicative of the itinerant nature of the 5f electrons in UN, as has been reported in the literature. This asymmetry was also observed in the U-4f spectra of U_2N_3, but to a lesser extent, with the peak at higher binding energy than in UN, indicating that a more localised description of the 5f electrons is appropriate for U_2N_3. A higher binding energy component was also identified in the U-4f spectra of U_2N_3, which has been attributed to U(III). Though this is likely to be an intrinsic property of U_2N_3, from the present data it is not certain if this peak is not caused by the presence of oxynitride contamination.

The high resolution data, high purity samples, and analysis of spectra presented here has allowed new insight into the chemistry of U_2N_3. Contrary to literature reports, the present results have shown differences in the N-1s spectra of UN and U_2N_3, with the latter showing a broader main component at lower binding energy and a second component at even lower binding energy. With broadening also recognised in the U-4f spectra, is likely there is mixed bonding in U_2N_3.

4.3 Structural Characterisation

4.3.1 X-ray Diffraction

The technique of x-ray diffraction, XRD, is one of the leading methods of crystallographic structural analysis in the sciences, providing insight into crystal structure, as well as strain, orientation, and crystallite size of a material, among other properties. In order to extract meaningful information out of the results of this and any other technique, it is important to have a good understanding of the theory behind it. This section provides an overview of the classical theory of XRD, starting with the simple interaction of x-rays with an electron and building up to scattering from bulk crystalline material. Much of the theory presented here has been obtained from *Elements of modern X-ray physics* by J. Als-Nielsen and D. McMorrow and *Diffraction Physics* by J. M. Cowley [122, 134].

4.3.1.1 Theory

Scattering from an Electron

To begin, let us consider a plane, linearly polarised x-ray beam with amplitude E_0, frequency ω, and phase ϕ. The electric field, $E_{incident}$, from this beam at a time t, will then be given by

$$E_{incident} = E_0 \, e^{i(\omega t - \phi)}. \tag{4.4}$$

If this wave is incident on an electron, it will experience coulombic force equal to the product of the electron charge, q_e, and electric field, $E_{incident}$. The subsequent acceleration of the electron will then be

$$a = \frac{q_e}{m_e} \, E_0 \, e^{i(\omega t - \phi)}, \tag{4.5}$$

where a is acceleration, and m_e is mass of an electron. This accelerating charge will then create a field, $E(\mathbf{r})$, at a position $\mathbf{r}$, that will be equal to

$$E(\mathbf{r}) = \frac{q_e \, \mathbf{a} \, sin\alpha}{c^2 \, \mathbf{r}} = -E_0 \, \frac{q_e^2}{m_e \, c^2} \, \frac{1}{\mathbf{r}} \, sin\alpha \, e^{i(\omega t - \phi)}, \tag{4.6}$$

where α is the angle between the direction of electron acceleration, $\mathbf{a}$, and the position vector, $\mathbf{r}$, as shown in Figure 4.9.

From the negative sign on the right hand side of this equation, it can be seen that the resultant scattered radiation is 180 ° out of phase with $E_{incident}$.

The constant, r_0, in the ratio of scattered to incident amplitude, is known as the classical electron radius and is termed the Thomson scattering length after J.J. Thomson, who discovered the electron.

$$\frac{E(\mathbf{r})}{E_0} = -\frac{q_e^2}{m_e\, c^2}\frac{1}{\mathbf{r}} = -\frac{r_0}{\mathbf{r}} \tag{4.7}$$

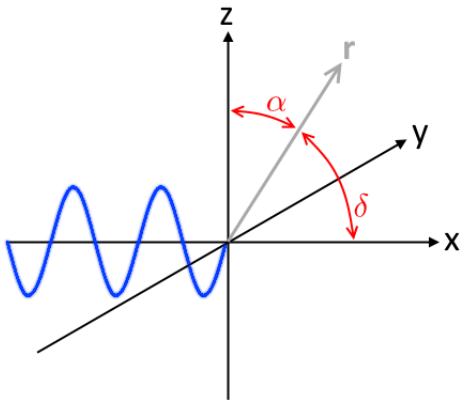

Figure 4.9: *Diagram showing coordinate system for polarisation factor discussion.*

Let us consider the effect of polarisation on the intensity, I, of the scattered radiation. This is visualised in Figure 4.9, with the polarisation in the x-z plane. If **r** lies in the x-y plane, perpendicular to the polaristaion, α = π/2 and sin α = 1, and therefore

$$|E| = E_0\, \frac{q_e^2}{m_e\, c^2}\, \frac{1}{\mathbf{r}}. \tag{4.8}$$

This is known as σ polarisation. However, if **r** does not lie in the x-y plane, the field at **r** will be proportional to $sin\alpha$. If δ is 90 - α, the magnitude of the field in this case is

$$|E| = E_0\, \frac{q_e^2}{m_e\, c^2}\, \frac{1}{\mathbf{r}}\, cos\delta. \tag{4.9}$$

In the case that **r** lies in the x-z plane, the plane of polarisation, this is known as π polarisation.

For unpolarised x-rays incident on the electron, the scattered intensity will be a sum of these terms, such that

$$I = I_0\, \left(\frac{q_e^2}{m_e\, c^2}\, \frac{1}{\mathbf{r}}\right)^2 \frac{1\, +\, cos^2\, \delta}{2}. \tag{4.10}$$

The final term in this equation is known as the polarisation factor.

Scattering from an Atom

Scattering from an atom can be considered as scattering from a time-averaged electron density function, a superposition of the scattering from all n electrons in the atom. If the n^{th} electron is described as having an electron density function $\rho_n(\mathbf{r})$, then the total electron density of the atom will be

$$\rho(\mathbf{r}) = \sum_n \rho_n(\mathbf{r}). \tag{4.11}$$

The finite volume dV at each point **r** in this density distribution will cause incident radiation with wavenumber **k** to be scattered as **k'** with a phase change of $\Delta\phi(\mathbf{r})$ such that

$$\Delta\phi(\mathbf{r}) = (\mathbf{k'} - \mathbf{k}) \cdot \mathbf{r} = \mathbf{Q} \cdot \mathbf{r} \tag{4.12}$$

As elastic scattering is being considered, |**k**| = |**k'**| = $2\pi/\lambda$, and their difference, **k**-**k'**, is the wavevector transfer, **Q**. It can then be shown that

$$|\mathbf{Q}| = 2\,|\mathbf{k}|\,sin\theta = \frac{2\pi}{\lambda} sin\theta \tag{4.13}$$

The total atomic scattering form factor, $f^0(\mathbf{Q})$, can now be obtained by integrating over **r**, with phase factor $\Delta\phi(\mathbf{r})$, giving

$$f^0(\mathbf{Q}) = \int \rho(\mathbf{r}) e^{i\mathbf{Q}\cdot\mathbf{r}} d\mathbf{r} \tag{4.14}$$

Note that this is essentially a Fourier transform of $\rho(\mathbf{r})$, the charge distribution.

The intensity, $I_{elastic}(\mathbf{Q})$, of the radiation elastically scattered from the n^{th} electron will be proportional to $|f_n(\mathbf{Q})|^2$. Using Equation 4.13, it can then be seen that as **Q** approaches 0, $I_{elastic}(\mathbf{Q})$ will be proportional to the total number of electrons, i.e. Z.

The above statements hold true if the energy of the incident radiation is much greater than that of the electron binding energy. However, if the energy of the incident radiation is less than that of the electron binding energy, the electron response is reduced and therefore scattering is reduced, creating what is known as an absorption edge. This

reduced response is taken into account in the atomic form factor by the inclusion of a real part, f', and an imaginary part, f'', such that

$$f = f^0 + f' + if'' \tag{4.15}$$

These additional terms, f' and f'', are obtained from the Fourier transforms of highly localised scattering distributions. Therefore, scattering at absorption edges, known as resonant scattering, can give information about the local electronic structure. This is a topic coved further in Chapter 5.

Scattering from an Array of Atoms

Moving from scattering from a single atom to multiple atoms, the electron density can be defined as the sum of over i atoms at a position r_i, giving

$$\rho^{array}(\mathbf{r}) = \sum_i \rho_i(\mathbf{r}) \cdot \delta(\mathbf{r} - \mathbf{r}_i) \tag{4.16}$$

In the case of a crystalline material, which is made of a periodic lattice, we can describe the lattice with basis vectors $\mathbf{a}_1$, $\mathbf{a}_2$, and $\mathbf{a}_3$, and integers n_1, n_2, and n_3, such that

$$\mathbf{R}_n = n_1\mathbf{a}_1 + n_2\mathbf{a}_2 + n_3\mathbf{a}_3 \tag{4.17}$$

The total electron density function for a crystalline material with i atoms in its unit cell and lattice vectors $\mathbf{R}_n$ can then be described as

$$\rho^{crystal}(\mathbf{r}) = \sum_i \rho_i(\mathbf{r})\delta(\mathbf{r} - \mathbf{r}_i) \sum_n \delta(\mathbf{r} - \mathbf{R}_n) \tag{4.18}$$

As shown previously, the scattering factor for the crystal will then be the Fourier transform:

$$F^{crystal}(\mathbf{Q}) = \underbrace{\sum_i f_i e^{i\mathbf{Q}\cdot\mathbf{r}_i}}_{unit\ cell\ s.f.} \underbrace{\sum_n e^{i\mathbf{Q}\cdot\mathbf{R}_n}}_{phase\ factor}. \tag{4.19}$$

Examining this equation, let us first consider the phase factor. For random values of $\mathbf{Q}\cdot\mathbf{R}_n$, this term will sum to 0. However, if $\mathbf{Q}\cdot\mathbf{R}_n = 2\pi \times integer$, this phase factor will be non-zero. A solution to this equation can be found by defining a set of vectors, $\mathbf{G} = h\mathbf{b}_1 + k\mathbf{b}_2 + l\mathbf{b}_3$, such that $\mathbf{G}\cdot\mathbf{R}_n = 2\pi \times integer$. The vectors $\mathbf{b}_1$, $\mathbf{b}_2$, and $\mathbf{b}_3$ are defined as

$$\mathbf{b}_1 = 2\pi\frac{\mathbf{a}_2 \times \mathbf{a}_3}{\mathbf{a}_1 \cdot (\mathbf{a}_2 \times \mathbf{a}_3)}, \quad \mathbf{b}_2 = 2\pi\frac{\mathbf{a}_3 \times \mathbf{a}_1}{\mathbf{a}_2 \cdot (\mathbf{a}_3 \times \mathbf{a}_1)}, \quad \mathbf{b}_3 = 2\pi\frac{\mathbf{a}_1 \times \mathbf{a}_2}{\mathbf{a}_3 \cdot (\mathbf{a}_1 \times \mathbf{a}_2)}, \tag{4.20}$$

such that $\mathbf{a}_i \cdot \mathbf{b}_j = \delta_{ij}$.

The vector **G** is known as the reciprocal lattice vector, with basis vectors $\mathbf{b}_1$, $\mathbf{b}_2$, and $\mathbf{b}_3$. The values h, k, and l describe the plane that is perpendicular to the vector $\mathbf{G}_{hkl}$. This reciprocal lattice vector provides a solution to the equation $\mathbf{Q}\cdot\mathbf{R}_n = 2\pi \times integer$ when **Q** = **G**, giving rise to non-zero values of $F^{crystal}(\mathbf{Q})$. This is known as the Laue condition.

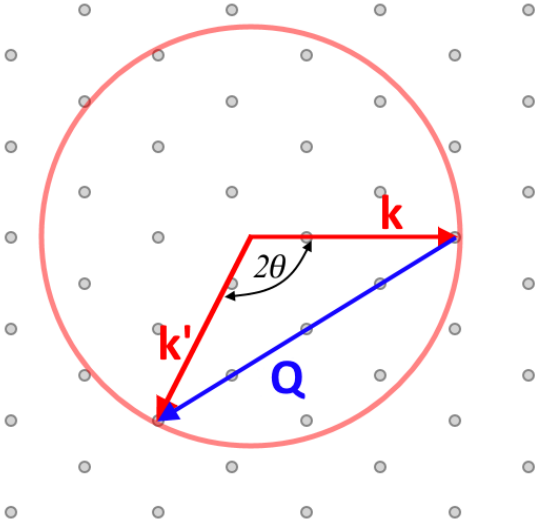

Figure 4.10: *Ewald sphere construction showing Laue condition.*

A Ewald sphere construction can be used to visualise the Laue condition, and is depicted in Figure 4.10. In this diagram, the incident wavevector, **k**, is placed on a reciprocal lattice point as the radius of a circle. Any point at which this circle intercepts a reciprocal point, a vector, **k'**, can be drawn from the centre of the circle to this point. By definition, **Q** = **k** - **k'**, and it can be seen from the Ewald sphere that **Q** connects two reciprocal lattice points. This therefore shows that **Q** = **G**, and the Laue condition is satisfied, giving rise to peaks in x-ray intensity. This intensity will be proportional to the square of the $|\rho(\mathbf{r})|$, so only $|\rho(\mathbf{r})|$ can be determined, not $\rho(\mathbf{r})$. This is a limitation of XRD, and is called the phase problem of XRD.

Taking the equation **k'** = **G** + **k** and squaring both sides, we arrive at the result:

$$|\mathbf{G}| \,/\, 2 = -sin\theta \,|\mathbf{k}| \,. \tag{4.21}$$

The negative sign in this equation is insignificant since if **G** is a reciprocal lattice vector, -**G** is also one. This result shows the projection of **k** onto **G** is $|\mathbf{G}| \,/\, 2$, showing that constructive scattering that occurs when **G = Q** results from scattering from planes that are perpendicular to **G**. As previously discussed, these planes can be described by the h, k, and l values of **G**, the Miller indicies. These planes will have a spacing of $|\mathbf{G}| \,/2$ in reciprocal space, equating to $2\pi/(|\mathbf{G}| \,/2)$ in real space. Calling this real space distance d_{hkl}, and using Equation 4.13, it can be shown that

$$m\lambda = 2d_{hkl}sin\theta. \tag{4.22}$$

As this condition will also be true for 2**G**, 3**G**, etc., a factor, m, which represents any integer number is included. We have now arrived at the Bragg result. In the case that the crystal from which the x-rays are scattered is orthorhombic, the value for d_{hkl} can be related to the crystal lattice with the equation

$$\frac{1}{d_{hkl}} = \frac{h^2}{a_1} + \frac{k^2}{a_2} + \frac{l^2}{a_3} \tag{4.23}$$

The previous discussion on the phase factor of Equation 4.19 shows at which values of **Q** peaks in x-ray intensity will appear, but does not hold any information about the relative intensities of each peak. To obtain this, we must evaluate the unit cell structure factor:

$$F_{hkl} = \sum_i f_i e^{i\mathbf{G}_{hkl}\cdot\mathbf{r}_i} \tag{4.24}$$

Consider, for example, a body-centred cubic structure with atoms at $(0\,,\,0\,,\,0)$ and $(1\,/\,2\,,\,1\,/\,2\,,\,1\,/\,2)$. The structure factor will then be

$$F_{hkl} = fe^0 + fe^{2\pi i(\frac{h}{2}+\frac{k}{2}+\frac{l}{2})} \tag{4.25}$$

Therefore if h+k+l is odd, F_{hkl} = 0, and if h+k+l is even, F_{hkl} = $2f$.

4.3.1.2 Measurement

Throughout this work, XRD has been used as the main method of characterising phase, crystalinity, strain, and microstructure of uranium nitride thin films. The methods used to collect XRD data and the information that can be obtained using these methods are described below.

The majority of the XRD data in this work was collected using a laboratory diffractometer, with the exceptions to this being the work presented in Chapter 5, which was conducted using synchrotron radiation. Details of this set-up are provided in Section 5.1.5.

Instrumentation

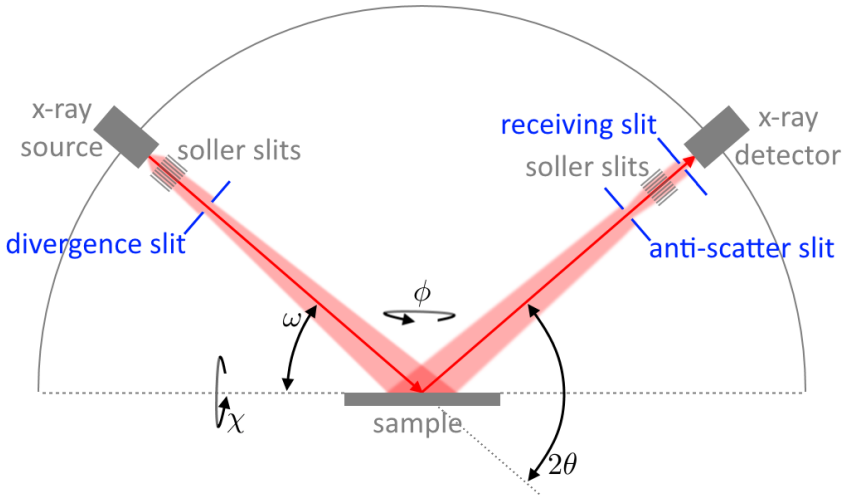

Figure 4.11: *Diagram showing configuration of Philips X'pert diffractometer in the scattering plane.*

Measurements were taken using a Philips X'pert diffractometer, with a rotating Cu anode tube source and Xe gas filled proportional detector, located at the University of Bristol. This diffractometer uses Bragg-Brentano geometry, as depicted in Figure 4.11. In this configuration, the source and detector rotate around the sample stage, with angles ω between the stage and x-ray source and 2θ between the directions of the source and detector. Additionally, the sample stage can be rotated in the plane of the sample stage by an angle ϕ and in the plane perpendicular to both the sample stage and scattering plane by an angle χ. In order to align the sample surface to the centre of the ω-θ circle, the height of the sample stage is adjustable.

The Cu radiation produced by the x-ray source is monochromated using single crystal Ge to produce a Cu Kα beam, with a nickel foil to reduce any Cu Kβ background radiation, resulting in an x-ray beam of wavelength 1.54060 Å for Cu Kα_1 and 1.54443 Å for Cu Kα_2.

The x-ray beam is then further refined by passing through soller slits, formed of a stack of parallel plates, which collimates the beam, and a divergence slit which controls the vertical height of the beam at the sample. On the detector side, diffracted radiation passes through anti-scatter slits to reduce background radiation, soller slits, and a receiving slit before reaching the x-ray detector. All these slits are important in increasing the resolution of the detector, however, as they will also reduce the count rate of the detector and therefore increase errors, a balance between counts and resolution for each sample is sought.

Q scans

The most useful of all XRD diffraction measurements that can be taken is a scan in the magnitude of **Q**, often referred to as a high angle or 2θ scan. In the four circle Bragg-Brentano geometry, this is achieved by scanning in 2θ and ω simultaneously, with the source and detector moving around the sample at a constant rate. As the sample is stationary, this ensures that the direction of **Q** does not change.

In the case that **Q** is perpendicular to the sample surface, $\theta = \omega$, and the scan is known as a specular scan. To investigate non-specular **Q** directions, an ω offset, $\Delta\omega$, is applied to ω and an offset of $-\Delta\omega$ is applied to θ.

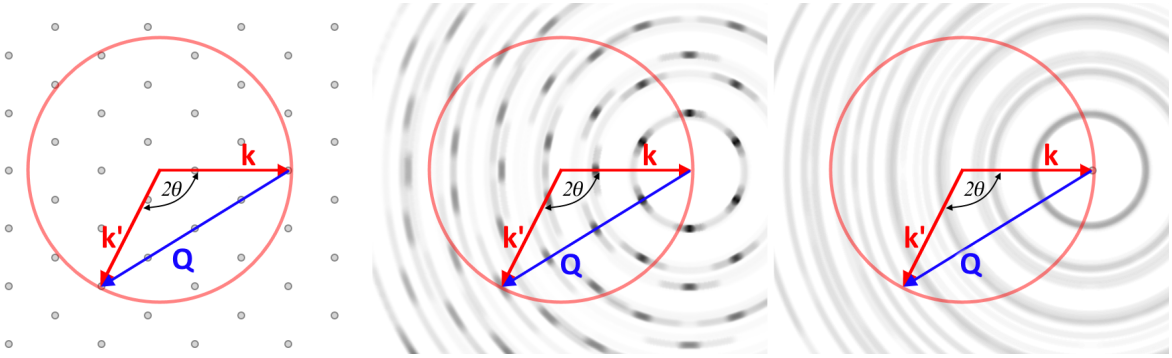

Figure 4.12: *Ewald sphere constructions for a) an ideal crystal, b) a textured polycrystal, and c) an ideal polycrystal.*

As the magnitude of **Q** is changed but the direction fixed, only reflections from planes perpendicular to **Q** will be detected. In the case of XRD of a single crystal, only a single set of reflections, $\{h\,k\,l\}$, will contribute to the detected scattering. If scattering is from a perfect polycrystal, composed of crystallites with a uniform orientation distribution, for any possible reflection, $(h\,k\,l)$, there will be crystallites oriented such that the $(h\,k\,l)$ plane is perpendicular to **Q**. This is

illustrated in Figure 4.12 c), where it can be seen that in comparison to a), the reciprocal lattice has been rotationally spread around **k**. Keeping the origin of **Q** at the same point, it can be seen that no matter the direction of **k** and **Q**, the **Q** vector will always intercept a reciprocal lattice circle at the same magnitude. In this idealised case, the intensity of each peak will be proportional to the corresponding structure factor.

The perfect polycrystal and single crystal described above are two ideal systems but the reality is often somewhere between the two, as shown in Figure 4.12 b). This image shows the Ewald construction for a material where orientation distribution of crystallites is not uniform, which is known as a textured material.

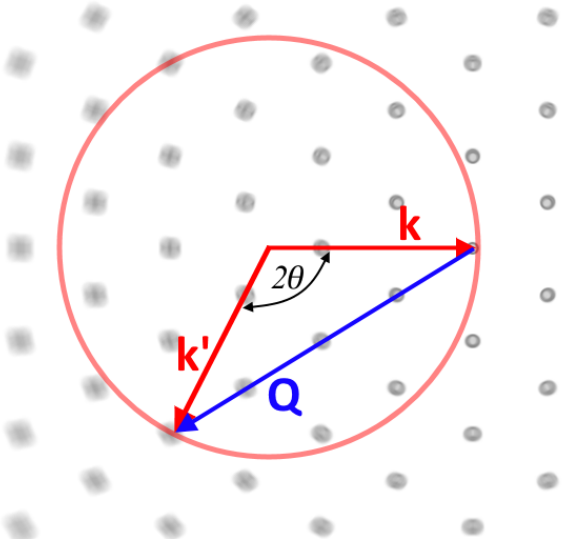

Figure 4.13: *Ewald sphere constructions illustrating peak broadening.*

So far, only diffraction peak position has been discussed, however, peak width is also an important feature to be considered. The width of a diffraction peak is determined by a number of factors relating to both the instrument and the sample. The finite size of the x-ray source and detector and beam divergence will mean that scattering from a finite range of **Q** values will be measured. Additionally, the wavelength range of the x-ray beam, such as a beam containing both Cu Kα_1 and Cu Kα_2 radiation, will cause peak broadening. Together, the broadening due to these instrument properties is called the instrument resolution. Considering the footprint of a finite beam on the sample, it can shown that the area is inversely proportion to $sin\theta$, and therefore instrument resolution will increase with θ.

Sample contributions to diffraction peak broadening can be caused by crystallite size, phase inhomogeneity, and

strain. Strain on crystallites causes lattice distortions and therefore changes in lattice spacing. As the amount of distortion will depend on the amount of strain, if the strain is inhomogeneous, lattice spacing will also be inhomogeneous. Each different lattice spacing will contribute to intensity at a different magnitude of **Q**, causing a broadening of the diffraction peak in **Q**. This has been depicted in Figure 4.13, where the reciprocal lattice shows averaging over a range of d spacing, centred on **k**. It can then be seen that the result of this broadening is to increase the area in reciprocal space over which **Q** intercepts a reciprocal lattice point.

To consider the effect of crystallite sizes on diffraction peaks, let us consider Equation 4.18. Here, the range of **r** is approximated to be infinite, and so the Fourier transform of Equation 4.18 to obtain Equation 4.19 uses an infinite integral over **r**. This is a reasonable approximation for large crystallites as the structure factor approaches a delta function. The resultant diffraction peak is limited by other factors such as the ones described above, before the limit of this approximation is reached.

This approximation fails as crystallite size decreases and the range of **r** over which scattering occurs becomes significant. Consequently, the structure factor will then become a Fourier series with a finite number of components. This will produce a poorer approximation of a delta function, with the width increasing as the number of terms decreases, and fringes caused by interference effects. As the number of terms relates to range of **r**, i.e. range of periodic lattice, which is the crystallite size, the width of the diffraction peak will be related to crystallite size. Since crystallites will not be all the same size, these fringes will be blurred out by averaging over different values of **r** and the resultant effect will be a broadening of the diffraction peak.

In the special case of a film which has uniform thickness and highly smooth interfaces, which is often the case of high quality epitaxial thin films, these fringes are visible in a **Q** scan. These fringes are called Laue fringes and can be used to determine film thickness.

Transverse Scans

In addition to scans of the magnitude of **Q**, scans of the direction of **Q** can provide valuable information on the crystallinity and texture of a sample. Though the relative intensities in **Q** scans give some indication of texture and crystallinity, more information can be obtained about the planes giving rise to reflections by scanning the direction of **Q**.

This can be achieved by scanning either ω or χ with fixed 2θ, however, due to poor horizontal resolution on the x-ray detector, only ω scans are used in this work.

The presence and width of a peak in an ω scan is an indication of the relative alignment of the crystal planes contributing to the reflection. A narrow width width shows good alignment of planes, indicative of a high quality single crystal or highly textured polycrystal. This is illustrated in Figure 4.14, where broadening in an ω scan is shown by a small rotational spreading of the reciprocal lattice. This shows the effect of a slight misalignment in the planes perpendicular to **Q**. It can then be easily seen that the magnitude of this misalignment will create a proportional broadness in intensity when rotating **Q**.

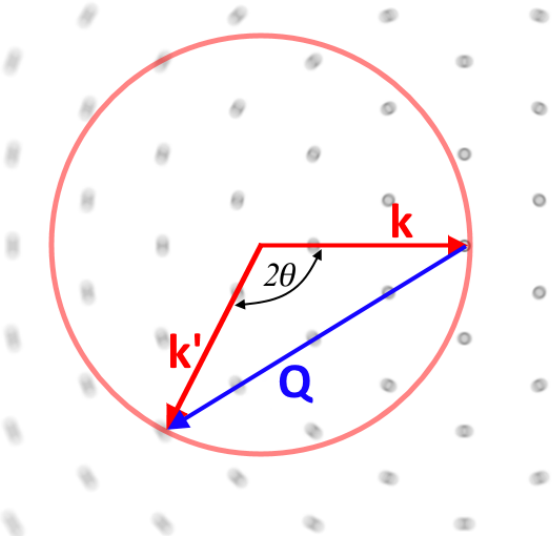

Figure 4.14: *Ewald sphere construction showing broadening in a transverse scan.*

An ω scan can show the alignment of planes perpendicular to any one **Q** direction, but it does not give any information of the relative orientation of these planes. Obtaining this information is essential to determining whether a sample is single crystal, meaning the crystallites all have the same orientation, or is instead just highly textured.

If **Q** and ω scans shows anisotropy in reciprocal space in one direction, e.g. z, as described above, it is necessary to investigate the symmetry in the two perpendicular directions, x and y in order to determine whether the sample is single crystal or textured. This can most easily be achieved by selecting a value of **Q** that has some component in either or both the x or y directions and rotating **Q** about the z direction. Using the Bragg-Brentano geometry, if z is in the

specular direction, this will be achieved by scanning ϕ with ω and 2θ aligned to an off-specular reflection.

In the case of a single crystal, comparing the symmetry of a ϕ scan to the symmetry of the lattice structure, it can be determined whether there are one or more domains present in the sample. When there is more than one phase present, such as with a thin film and substrate, a ϕ scan can also be used to show relative alignment of the phases. This is particularly useful for determining the epitaxial match between a film and a substrate.

4.3.1.3 Analysis

To obtain structural information from XRD measurements, analysis was performed by fitting functions to the data. The functions used were Gaussian, Lorentzian, or PseudoVoight, as described below. From these fits, the Amplitude, A, centre, c, and width, w, could be obtained.

Lorentzian

$$f_{Lorentz}(x, c, w, A) = \frac{A}{\pi} \frac{w}{(x-c)^2 + w^2}, \quad FWHM_{Lorentz} = 2w \tag{4.26}$$

Gaussian

$$f_{Gauss}(x, c, w, A) = Ae^{-\frac{(x-c)^2}{2w^2}}, \quad FWHM_{Gauss} = 2\sqrt{2ln2}w \tag{4.27}$$

PseudoVoight This is a linear combination of a Gaussian and a Lorentzian with η defining the weighting between the two functions.

$$f_{PV} = \eta f_{Gauss} + (1-\eta) f_{Lorentz} \tag{4.28}$$

The fitting of these functions to the data was performed using either MATLAB or GenX software. When using MATLAB, the Mfit program was used to perform data fitting. In this program, user defined functions with initial guesses are optimised to fit the data using a least squares fitting routine following the Marquardt-Levenberg method.

For data for which the Mfit program did not provide a sufficiently good fit or more control over the fitting routine was desired, GenX software was used. GenX software utilises a differential evolution algorithm with a user defined fitting range, allowing local minima to be avoided [135] . Additionally, it allows weighting in the fit analysis, making it ideal for fitting data which spans multiple orders of magnitude.

The GenX program allows python scripts of models to be implemented for fitting, which were used when fitting XRD data. Models consisted of Gaussian or PseudoVoight peaks, which, where appropriate, were coupled. For example, when fitting XRD data with a Cu Kα_1 and Cu Kα_2 doublet, the positions and intensities were constrained with the ratios $\lambda_{\alpha1}$:$\lambda_{\alpha2}$ and 2:1, respectively.

Analysis of crystallite size was performed using the Scherrer equation, obtained by mathematical analysis of the peak broadening described previously [136]. This equation is shown below, where D is crystallite size, w is FWHM, and K is the shape factor.

$$D = \frac{K\lambda}{w\,cos\theta} \tag{4.29}$$

Most of these values can easily be obtained by analysis of XRD results, however, the shape factor is more difficult to determine. This shape factor is a dimensionless quantity, and is included to account for the effect of the shape of the crystallites on peak broadening. Due to the difficulty in determining this value, it is common to use the value for spherical crystallites, K = 0.9. As this equation does not take into account other possible sources of broadening, it provides only a lower limit on the crystallite size. Additionally, this equation is only appropriate for crystallite sizes below 0.1 μm.

4.3.1.4 XRD Results

The results of structural characterisation by x-ray diffraction of polycrystalline and epitaxial uranium nitride thin film samples are presented below. All samples investigated were capped with either Nb or Au to prevent oxidation of the film.

Polycrystalline Thin Films

Effect of N_2 Pressure

The results of specular x-ray diffraction of uranium nitride thin film samples deposited using reactive sputtering with a range of N_2 partial pressures are shown in Figure 4.15. The results in this figure have been normalised to the background and offset for clarity, however, as film thickness is not consistent between all samples, the intensities of different scans

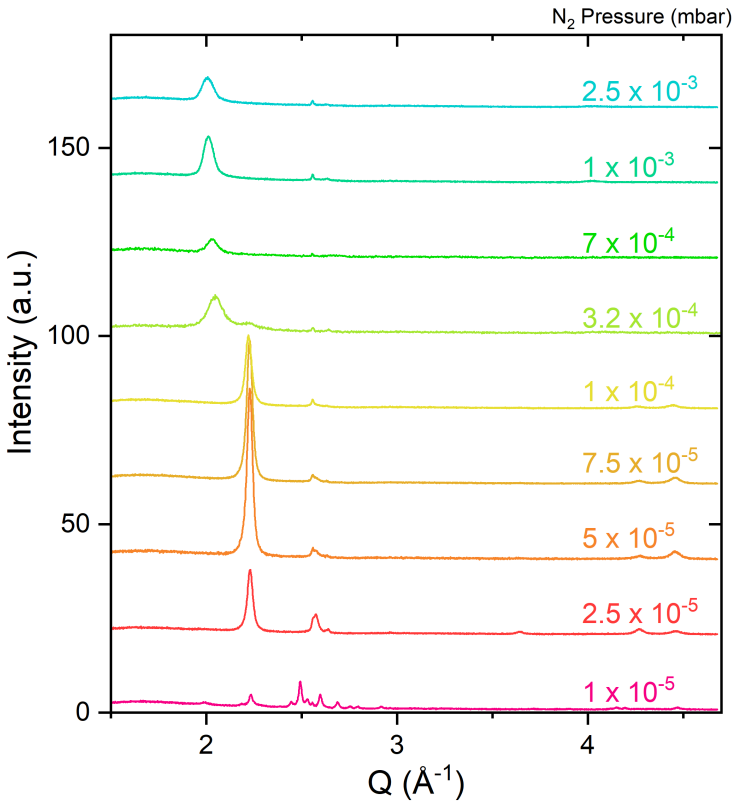

Figure 4.15: *XRD results of capped uranium nitride thin films deposited on glass using a range of different N_2 pressures, as labeled on the right in mbar.*

cannot be fairly compared. In each of these scans, a low intensity peak at 2.56 Å^{-1} is visible from the $(0\,1\,1)$ reflection of Nb, the material used to cap the samples.

Below 7×10^{-4} mbar N_2 pressure, peaks at 2.2 Å^{-1} can be seen in all scans, corresponding to the $(1\,1\,1)$ reflection of UN. In addition, the broad peaks of higher order UN reflections are present at around 4.3 and 4.45 Å^{-1}. The UN $(0\,0\,2)$ reflection at 2.6 Å^{-1} decreases in intensity relative to the $(1\,1\,1)$ reflection as N_2 deposition pressure increases, showing changes in the textures of the samples.

At 1×10^{-5} mbar N_2 pressure, the $(1\,1\,1)$ UN peak is lower in intensity and a trio of peaks can be seen around 2.5 Å^{-1}. These peaks correspond to the highest intensity reflections of α-U metal, showing that not all of the U deposited at this N_2 pressure is nitrided.

At N_2 pressures above 3.2×10^{-4} mbar, the highest intensity peak is at 2.0 Å^{-1}, corresponding to the $(2\,2\,2)$

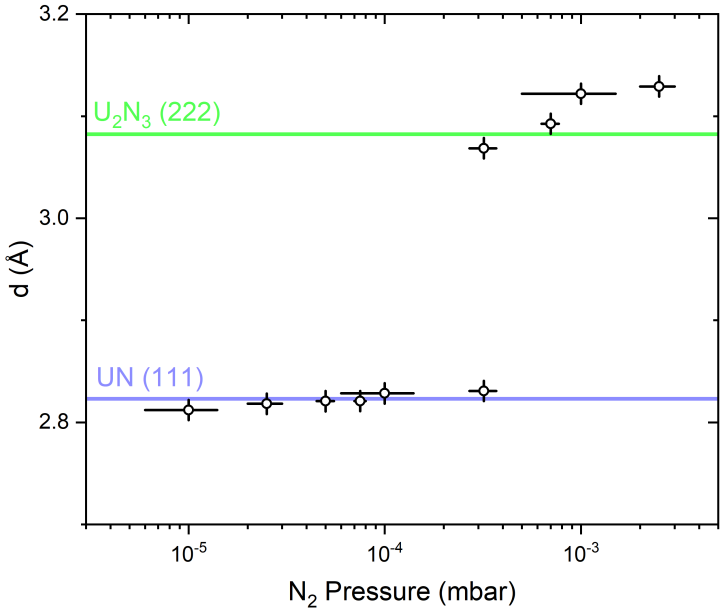

Figure 4.16: *Graph showing d spacing of uranium nitride Bragg reflections in XRD results of samples deposited using different N_2 sputtering pressures. The literature values of the UN* $(1\,1\,1)$ *and* U_2N_3 $(2\,2\,2)$ *reflections are shown in blue and green, respectively.*

reflection of higher nitrides. No other peaks are present in these scans, showing strong texturing in these films.

Results from the sample deposited at 3.2×10^{-4} mbar N_2 pressure show peaks at both 2.0 and 2.2 $Å^{-1}$, indicating that both UN and U_2N_3 are present in the sample.

The spacing between the close-packed planes of U atoms, derived from the position of the $(1\,1\,1)$ UN and $(2\,2\,2)$ U_2N_3 peaks discussed above, have been plotted against N_2 pressure in Figure 4.16. The literature values for these reflections are shown by the blue and green lines, respectively, for reference. This figure shows that between 1×10^{-5} and 3.4×10^{-4} mbar N_2 pressure, the deposited UN has a lattice parameter equal to the literature value, within errors. These values show a trend of lattice parameter increasing with increasing N_2 deposition pressure. This trend is also seen to a larger extent in the samples deposited at higher N_2 pressures, however, only the value for 7×10^{-4} mbar matches the literature value for stoichiometric U_2N_3.

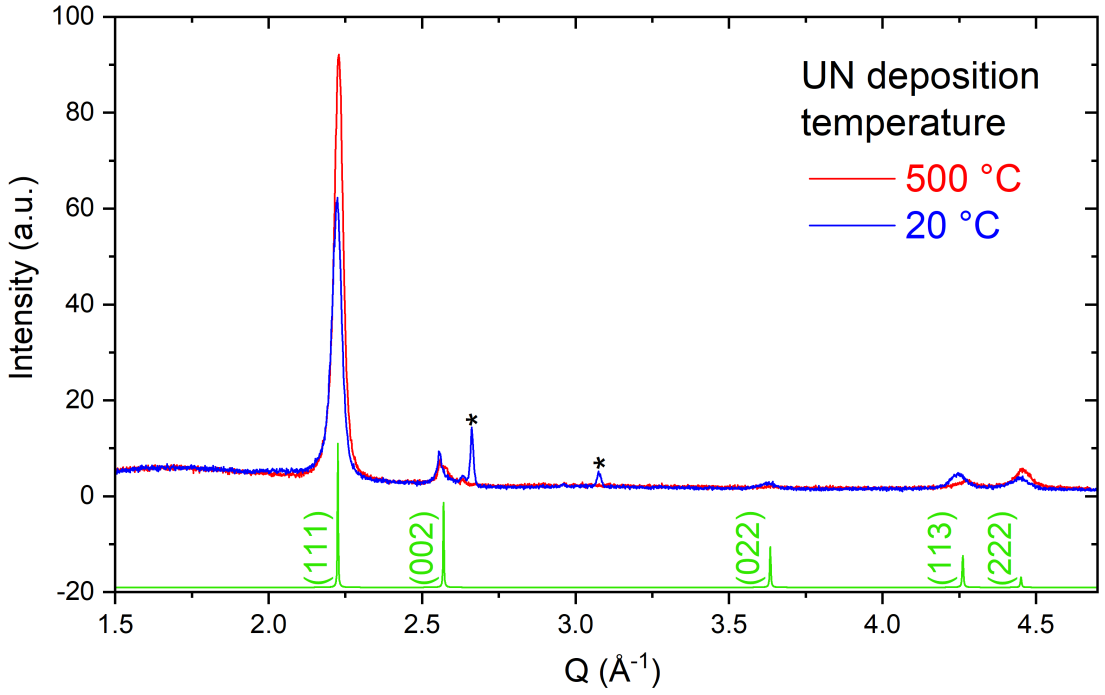

Figure 4.17: *XRD results of UN films deposited on glass at 500 °C (red) and 20 °C (blue). The calculated data for ideal polycrystalline UN is shown in green, with reflections labeled, and was produced using Vesta software [8].*

Effect of Temperature

The specular XRD scans of UN samples deposited at 2.5×10^{-4} mbar N_2 pressure and at 20 (room temperature) and 500 °C are shown in Figure 4.17 in blue and red, respectively. The calculated data for ideal polycrystalline UN is shown in green, with reflections labeled, and was produced using Vesta software [8]. Peaks present due to the Al sample stage are marked with an asterisk. This figure shows that all UN reflections are present in both samples, however, the intensities and positions of these reflections are different. The positions of the peaks for the sample deposited at 500 °C are at higher values of Q than the sample deposited at 20 °C, giving lattice parameter values of 4.88±0.01 Å and 4.89±0.01 Å, respectively.

Comparing the texture of these samples, it is clear that both have a stronger than expected $(1\,1\,1)$ and $(2\,2\,2)$ reflection, displaying the preferred orientation in this direction. The relative intensities of the other reflections are higher in the sample deposited at 20 °C than in that deposited at 500 °, showing that UN deposition produces a more

polycrystalline film at lower temperatures.

Crystallite Size

Table 4.2: *Table showing crystallite size analysis results of capped UN, and U_2N_3 thin films.*

Sample	2θ position (°)	FWHM (°)	Crystallite size (nm)
UN	31.43 ±0.01	0.93 ±0.1	9 ± 1
U_2N_3	28.84 ±0.01	0.96 ±0.1	9 ± 1

Analysis of the crystallite size of polycrystalline UN and U_2N_3 films was conducted using the Scherrer equation, shown in Equation 4.29. As the intensity of the Bragg peaks from the small scattering volume of a thin film is low and therefore the errors on the values obtained from fitting these peaks is high, in order to reduce errors, only the the highest intensity Bragg reflections were used to calculate crystallite size.

Results from this analysis of UN and U_2N_3 samples grown at room temperature with N_2 pressures of 2.5×10^{-5} and 7×10^{-4} mbar, respectively, are shown in Table 4.2. These results give a minimum crystallite size of both UN and U_2N_3 films deposited at room temperature of 9 ± 1 nm, showing that both samples are nanocrystalline.

Epitaxial UN Thin Film

Throughout this work, several epitaxial UN thin films, deposited on Al_2O_3 $(1\,\overline{1}\,0\,2)$ with an Nb buffer, have been produced, as detailed in Table 3.1. Each sample that was produced underwent structural characterisation to verify that it was single crystal UN with a single domain and minimal contamination. The results presented in this section are from the XRD characterisation of SN1028, as this sample was subjected to the most extensive characterisation, however, all other epitaxial UN samples showed very similar results.

Figure 4.18 shows the fitted results from a Q scan of SN1028, with data shown as grey circles and fit shown as a blue line. This measurement was taken aligned on the UN $(0\,0\,2)$ reflection, as there was found to be a misalignment between the specular direction (the surface normal) and the UN $[0\,0\,2]$ direction, showing a miscut between the UN

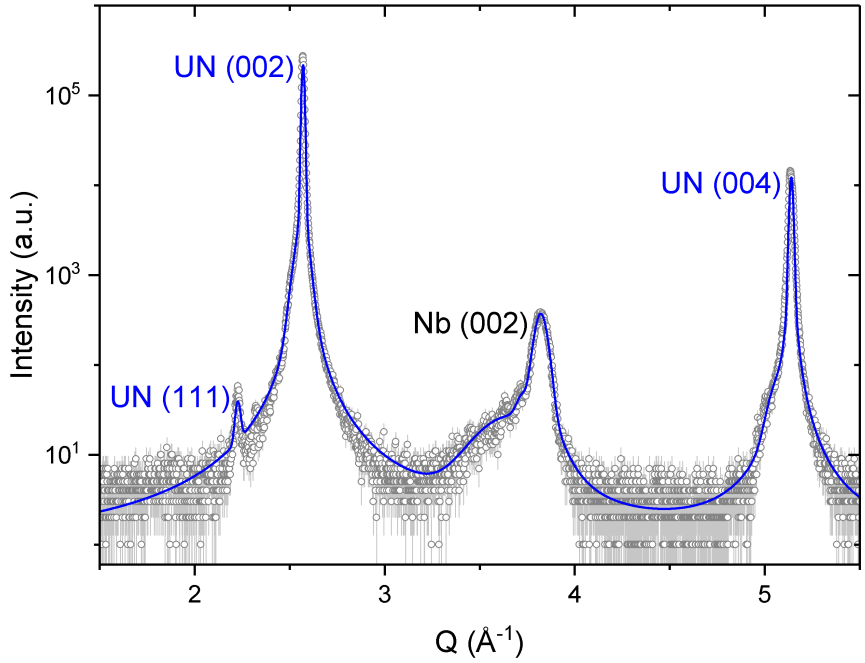

Figure 4.18: *XRD pattern of epitaxial UN film aligned on the UN* $(0\,0\,2)$ *reflection. Open circles show data points and solid lines show fits.*

$(0\,0\,2)$ plane and Al_2O_3 substrate surface. Consequently, no substrate peak is present in this figure.

This XRD pattern shows sharp, high intensity UN $(0\,0\,2)$ and $(0\,0\,4)$ reflections, with a very low intensity $(1\,1\,1)$ reflection, showing the alignment of the $\{0\,0\,1\}$ planes in the UN layer of SN1028. The $(0\,0\,2)$ and $(0\,0\,4)$ peaks both show asymmetry due to a second component to the peak appearing at lower Q values, however, as this plot is on a log scale, the relative contribution of this second component is very small.

The $(0\,0\,2)$ Nb reflection is also visible in the figure, showing that, like the UN layer, the Nb buffer is miscut with respect to the Al_2O_3 substrate. Some small, rough fringes are visible on the low Q side of this Nb peak which are likely to be Laue fringes.

The ω scans of the Al_2O_3 $(0\,1\,2)$, Nb $(0\,0\,4)$, and UN $(0\,0\,2)$ reflections, centered on their peak, are plotted in Figure 4.19. The data is represented by open circles and has been fitted with a two-component peak, comprised of Gaussian and Lorentzian^2 components, shown by the solid lines. The Al_2O_3 substrate peak is very narrow in ω, with a FWHM of $0.04\pm0.01\,^\circ$, which is likely to be limited by instrument resolution. The Nb buffer and UN film are much broader in ω,

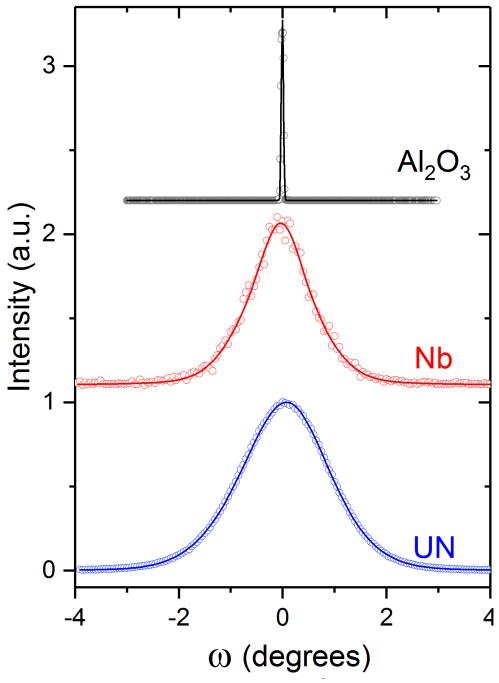

Figure 4.19: *ω scans of the UN $(0\,0\,2)$, Nb $(0\,0\,4)$, and Al_2O_3 $(0\,1\,2)$ reflections, centered on their peaks. Open circles show data points and solid lines show fits.*

with FWHM values of 1.22±0.01 ° and 1.73±0.01 °, respectively. The large FWHM values of these layers compared to the substrate shows poor registry between the UN film and Nb buffer and the Al_2O_3 substrate.

The ϕ scans of the Al_2O_3 $(0\,2\,10)$, Nb $(0\,1\,3)$ and equivalent, and UN $(0\,2\,4)$ and equivalent reflections are shown in Figure 4.20, fitted with Gaussian peaks. Due to the miscut between the Nb and UN $(0\,0\,1)$ planes and the substrate, data for each Nb and UN reflection was taken separately and stitched as each reflection required a different ω offset value. The clear ϕ dependence of both the Nb and UN reflections show that both layers are comprised of crystallites oriented in the same direction and therefore are single crystal. In addition, there is a 90 ° separation between all UN reflection and all Nb reflections. As both materials have cubic symmetry, this shows that there is only one domain present in the film.

Figure 4.20 gives insight into the epitaxial relationship between the substrate, buffer and film in SN1028. The 45 ° spacing between the Nb and UN $(0\,k\,l)$ reflections shows a $\sqrt{2}$ relationship between the two layers, as expected. The alignment of the Al_2O_3 $(0\,2\,10)$ and UN $(0\,2\,4)$ reflections show that the Al_2O_3 a-axis and UN a-axis are aligned as the projection of the Al_2O_3 $[0\,2\,10]$ direction onto the $[0\,1\,2]$ surface is perpendicular to the Al_2O_3 a-axis.

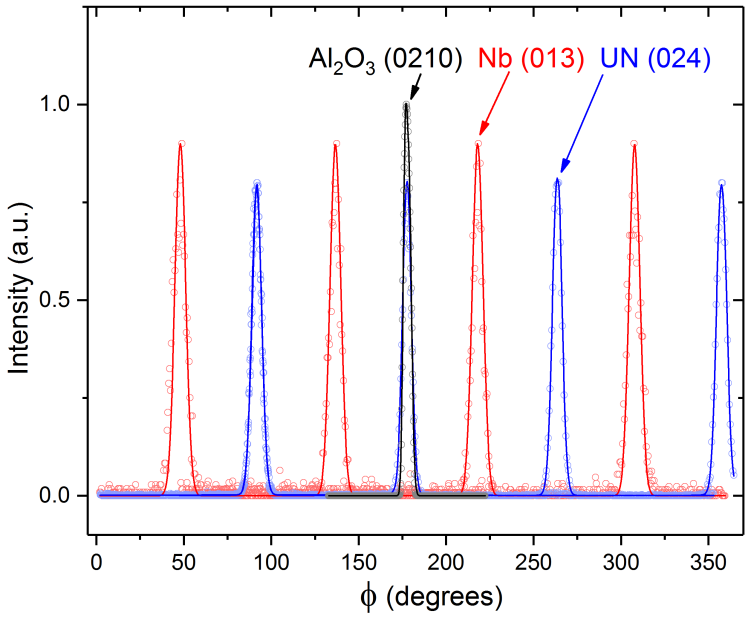

Figure 4.20: *ϕ scans of the UN $(0\,2\,4)$, Nb $(0\,1\,3)$, and Al_2O_3 reflections. Open circles show data points and solid lines show fits.*

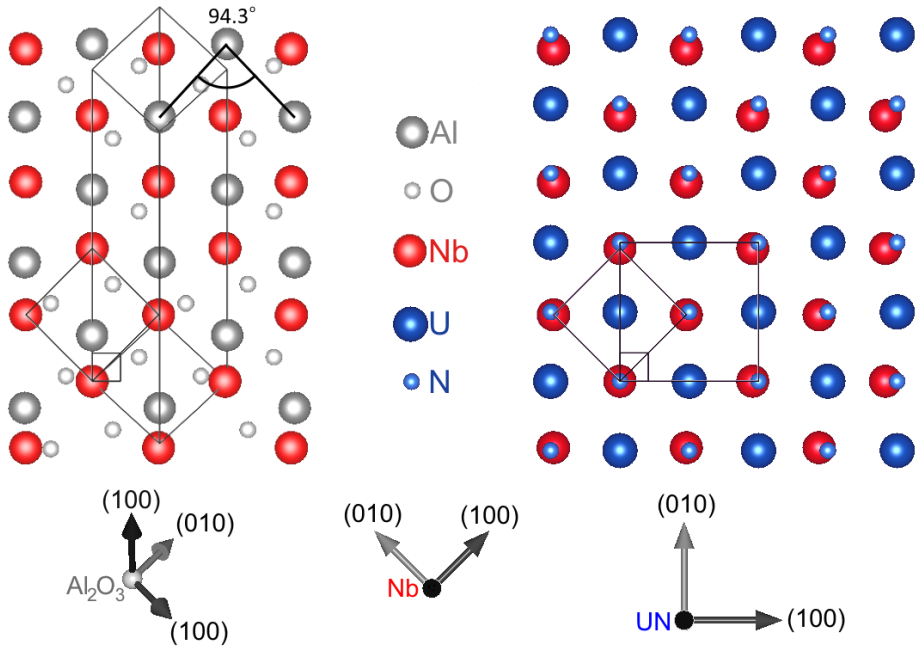

Figure 4.21: *Diagram showing the epitaxial relationship between the Al_2O_3 substrate (grey), Nb buffer (red), and UN film (blue), with unit cells shown in black.*

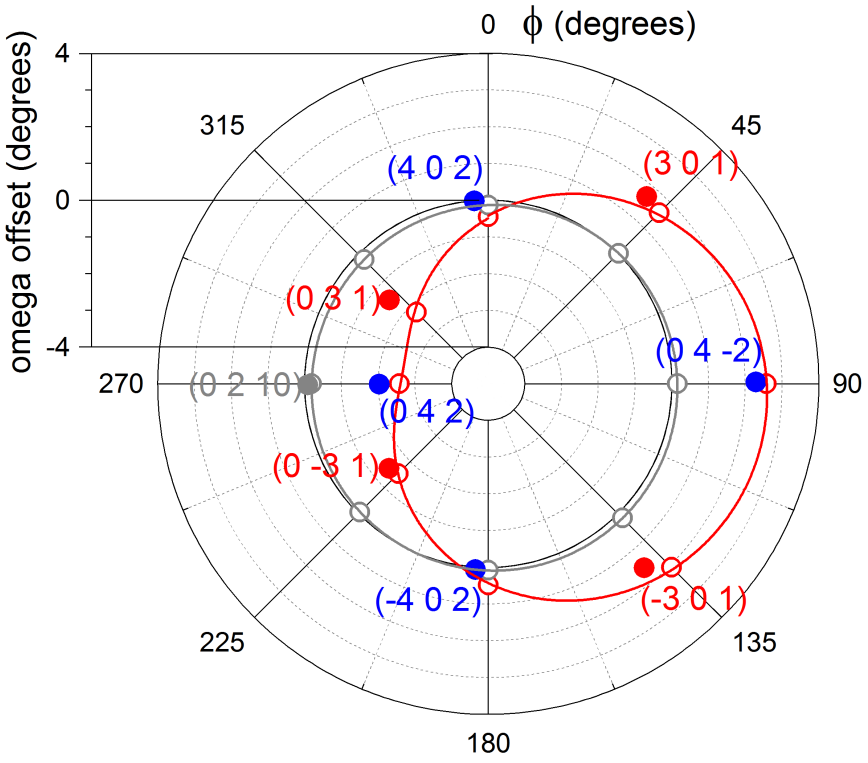

Figure 4.22: *Plot of $\Delta\omega$ against ϕ for the UN, Nb, and Al_2O_3 reflections in blue, red, and grey, respectively. Open circles show specular reflections, closed circles show off-specular reflections, and solid lines show sine fits.*

To aid with the difficultly in understanding Miller indices in hexagonal geometry, Figure 4.21 shows an illustration of the epitaxial relationship based on the results of Figure 4.20. In this figure, the $\sqrt{2}$ relationship between the Nb buffer $(0\,0\,1)$ plane and UN film $(0\,0\,1)$ plane can be seen on the right, along with the close lattice match between these two layers. On the left, the almost square Al_2O_3 $(0\,1\,2)$ plane is shown. The overlaid Nb $(0\,0\,1)$ plane is shown to have a good match in the horizontal direction, parallel to the UN a-axis, but a poorer match in the vertical direction, parallel to the UN b-axis.

To further examine the miscut between the UN and Nb $(0\,0\,1)$ planes and substrate surface, the ω offset of both the specular and off-specular reflections of Al_2O_3 (grey), Nb (red), and UN (blue) are plotted against ϕ in Figure 4.22. The specular reflections are shown as open circles and the off-specular reflections are shown as closed circles and labeled. Additionally, the data has been fitted with a sine function, shown by the solid lines.

This figure clearly shows that the $\Delta\omega$ of UN and Nb reflections have the same ϕ dependence, showing that the

miscut with respect to the substrate in both structures is in the same direction. The sine fit to these data points has an amplitude of 2.6±0.1 °, which shows the magnitude of the miscut, and has a maximum at ϕ = 90 °, showing the miscut to be along the UN b-axis. A small miscut between the Al_2O_3 $(0\,1\,2)$ plane and surface of 0.2 ° is also shown in this figure. Reconsidering Figure 4.21, it has now been shown that the miscut in the UN an Nb lies in the vertical direction in this diagram, which is the direction in which the Al_2O_3 to Nb match is poorest.

The lattice parameters of the $(0\,0\,1)$ UN film were determined using fitted peak positions of the $(0\,0\,2)$ and $(0\,0\,4)$ specular reflections, and all four equivalent off-specular reflections of $(0\,2\,4)$ and $(1\,1\,3)$. Assuming the film to be tetragonal, values of 4.885±0.008 Å for a and 4.895±0.001 Å for c were obtained, giving a unit-cell volume of 116.8±0.5 Å^3.

Epitaxial U_2N_3 Thin Film

Below, the results from XRD characterisation of a 30 nm thick U_2N_3 $(0\,0\,1)$ film, SN1189, are presented, with some results from SN1431, a 200 nm thick film, provided for comparison.

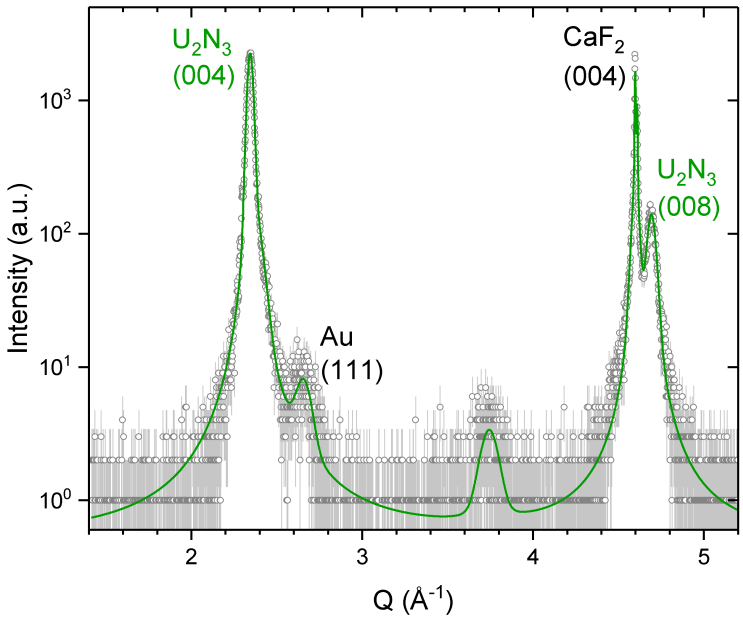

Figure 4.23: *XRD pattern of epitaxial* $(0\,0\,1)$ *U_2N_3 film, with open circles showing data points and solid lines showing fits.*

The result from high angle XRD of the epitaxial U_2N_3 film SN1189 are shown in Figure 4.23. The strong peaks of

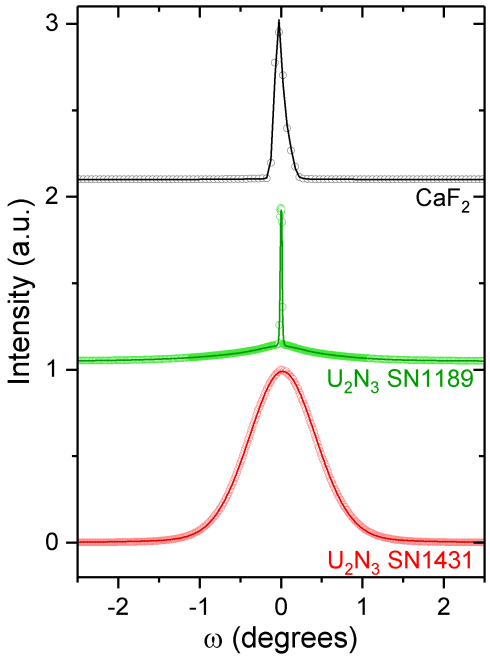

Figure 4.24: *ω scans of the CaF_2 $(0\,0\,4)$ reflection (grey) and U_2N_3 $(0\,0\,4)$ reflection from SN1189 (green) and SN1431 (red), centred on their peaks. Open circles show data points and solid lines show fits.*

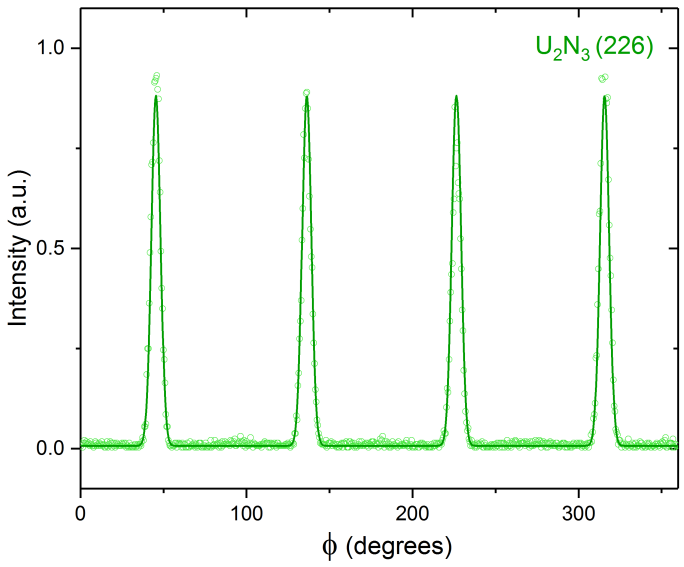

Figure 4.25: *ϕ scan of the U_2N_3 $(2\,2\,6)$ reflection. Open circles show data points and solid lines show fits.*

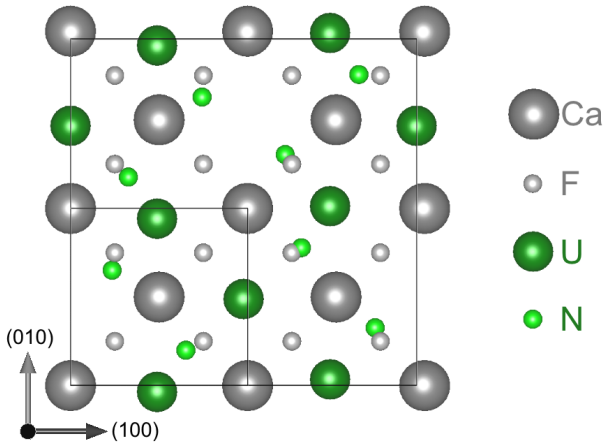

Figure 4.26: *Diagram showing the epitaxial relationship between the CaF_2 substrate (grey) and U_2N_3 film (green), with unit cells shown in black.*

the $(0\,0\,4)$ and $(0\,0\,8)$ U_2N_3 reflections can be seen, along with the absence of any other U_2N_3 reflections, showing the alignment of the $\{0\,0\,1\}$ U_2N_3 planes in the specular direction. The close positioning of the $(0\,0\,4)$ CaF_2 and $(0\,0\,8)$ U_2N_3 reflections shows the close lattice match between the two structures. Additionally, the $(1\,1\,1)$ reflection from the Au cap and an unidentified peak at 3.75 $Å^{-1}$ are visible.

The ω scans of the $(0\,0\,4)$ reflections of CaF_2 and U_2N_3 from SN1189 and U_2N_3 from SN1431 are displayed in Figure 4.24. There is a clear contrast between the U_2N_3 peak from the SN1189, 30 nm thick film, and SN1431, the 200 nm thick film, with FWHM of 0.03±0.01 and 0.98±0.01 °, respectively, showing much stronger crystal alignment in the thinner film. There is also a difference in shape between the peaks from the two samples, with the thinner film, SN1189, clearly showing a low intensity broad component and a sharp, narrow component. It should be noted that the width of this narrow component is lower than that of the CaF_2 substrate peak.

A ϕ scan of the $(2\,2\,6)$ U_2N_3 peak is shown in Figure 4.25. The clear separation of the peaks in this figure shows that the deposited film is single crystal, with the 4-fold symmetry showing that there is only one domain of the cubic U_2N_3 structure. Though not displayed in the figure, off-specular reflections from the CaF_2 substrate showed the $(1\,0\,0)$ and $(0\,1\,0)$ direction to be aligned to that of the U_2N_3 film. These results show that the epitaxial relationship between film and substrate is a simple cube on cube match with a 1:2 lattice parameter ratio, as shown in Figure 4.26.

Lattice parameters of the a 30 nm thick U_2N_3 $(0\,0\,1)$ film, SN1189, were determined using the specular $(0\,0\,4)$

and $(0\,0\,8)$ reflections and four off-specular $(2\,2\,6)$ reflections. This resulted in values of 10.7±0.1 Å for a and b and 10.72±0.01 Å for c, giving a a unit-cell volume of 1230±20 Å^3. The large error on a and b is a result of the low intensity of the accessible off-specular reflections and the low contribution of a and b relative to c in the $(2\,2\,6)$ reflections.

The lattice parameters of the 200 nm thick $(0\,0\,1)$ U_2N_3 film, SN1431, were also calculated. The larger scattering volume of this film increased the intensity of reflections, allowing more to be found. Consequently, the sets of $(4\,4\,8)$, $(0\,4\,8)$, and $(2\,2\,1\,0)$ reflections, as well as those previously listed, were used to calculate the lattice parameters, obtaining values of 10.61±0.03 Å for a and 10.802±0.005 Å for c. This give a unit-cell volume of 1216±7 Å^3.

4.3.2 X-ray Reflectivity

X-ray reflectivity (XRR) is a technique that uses the low angle reflection and refraction of x-rays at interfaces to investigate the morphology and structure of surfaces and thin films. In particular, XRR provides an accurate, non-destructive method for determining the thickness and roughness of thin films and consequently it is used frequently throughout this work. As with XRD, this technique will be introduced with a brief explanation of the theory here, and a more rigorous explanation is provided by Als-Nielsen and McMorrow [122].

4.3.2.1 Theory

As x-rays pass through an interface, the change in the refractive index, n, causes the x-ray wavevector, **k**, to change to $n\mathbf{k}$ in a process known as refraction. This refractive index is dependent on photon energy as resonances with electronic transitions causes dispersion, increasing the value of n. As x-rays have energies greater than most electronic transitions, values of n in the x-ray region tend to be lower than the value for a vacuum, $n = 1$. Consequently, at very low angles of incidence, total external reflection occurs, with the upper limit on this range of angles known as the critical angle, θ_c.

Above θ_c, the x-rays will both reflect and refract at the interface. Within the medium, x-rays will be scattered and absorbed, causing attenuation of the intensity of the x-ray beam proportional to $e^{-\mu z}$, where μ is the absorption coefficient and z is the distance traveled in the medium. As the intensity is the square of the amplitude, amplitude will decrease with $e^{-\mu z/2}$.

If the incident x-rays are described by $e^{i\mathbf{k}z}$, the refracted x-rays can be described by $e^{in\mathbf{k}z}$ within the medium, with

$$e^{in\mathbf{k}z} = e^{i(1-\delta)\mathbf{k}z}e^{-\beta\mathbf{k}z}. \tag{4.30}$$

The refractive index can then be described as

$$n = 1 - \delta + i\beta, \quad with \quad \delta = \frac{2\pi\,\rho_a\,f^0\,r_0}{k^2} \quad and \quad \beta = \frac{\mu}{2k}, \tag{4.31}$$

where ρ and f^0 are the atomic density and atomic scattering length, respectively, and can be described as the electron density, ρ_e. Taking the product of the electron density and Thomson scattering length, $\rho_e r_0$, we obtain the scattering length density. This equation shows that the absorption coefficient relates to the imaginary part of the refractive index.

Reflectivity from an Ideal Surface

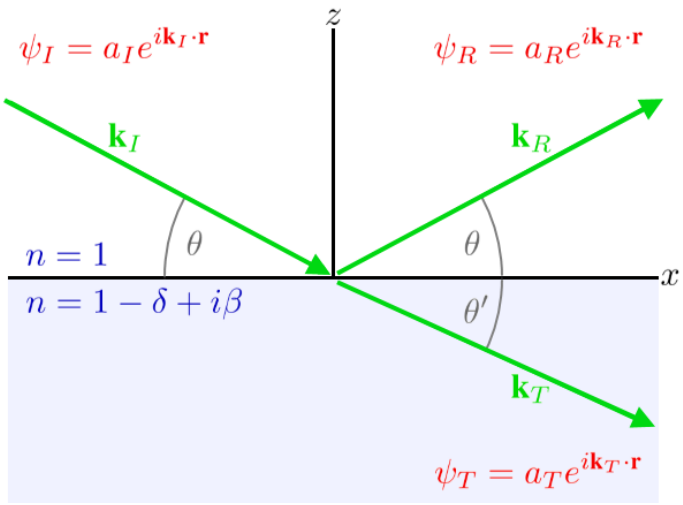

Figure 4.27: *Diagram of the reflection and transmission of x-rays at an ideal surface.*

Let us now consider the incident, reflected, and transmitted wavevectors, k_I, k_R, and k_T, respectively, of an x-ray beam incident on an ideal surface. This is depicted in Figure 4.27, where a wave, ψ_I, with amplitude a_I is incident on the surface of a material with refractive index n at an angle to the surface of θ. Using small angle approximations and the boundary conditions that the incident wave and its derivative are continuous at the interface, it is found that

$$a_I + a_R = a_T \quad and \quad a_I\mathbf{k}_I + a_R\mathbf{k}_R = a_T\mathbf{k}_T \tag{4.32}$$

Decomposing the wavevector **k** into components parallel and perpendicular to the surface, it is found that, respectively,

$$a_I k\, cos\theta + a_R k\, cos\theta = a_T nk\, cos\theta' \quad and \quad (a_I - a_R)k\, sin\theta = a_T nk\, sin\theta' \tag{4.33}$$

The value k is the magnitude of the wavevector in the medium, i.e. $k = |\mathbf{k}_I| = |\mathbf{k}_R|$ in the vacuum and $nk = |\mathbf{k}_T|$ in the material.

Using Equations 4.32 and 4.33, Snell's law can be derived:

$$cos\theta = n\, cos\theta' \tag{4.34}$$

Taking the small angle cosine expansion of Snell's law, it can be approximated that $\theta^2 \cong \theta'^2 - 2\delta + 2i\beta$. Since $\theta' = 0$ at the critical angle, θ_c, it is found that $\theta_c \approx \sqrt{2\delta}$, and therefore

$$\theta^2 \cong \theta'^2 - \theta_c^2 + 2i\beta \tag{4.35}$$

Decomposing θ' into real and imaginary parts gives $\theta' \equiv \Re(\theta') + i\Im(\theta')$, which when substituted into ψ_T gives

$$a_T e^{ik\theta' z} = a_T e^{ik\Re(\theta')z} e^{-k\Im(\theta')z} \tag{4.36}$$

Comparing this to Equation 4.30, intensity of the transmitted wave will therefore decrease with characteristic length $\Lambda = \mu^{-1}$, equivalent to

$$\Lambda = \frac{1}{2k\Im(\theta')} \tag{4.37}$$

Using Equations 4.32 and 4.33, it is found that

$$\frac{a_I - a_R}{a_I + a_R} = n\frac{sin\theta'}{sin\theta} \cong \frac{\theta'}{\theta} \tag{4.38}$$

from which the Fresnel equations for the reflectivity amplitude, r, and transmittivity amplitude, t, can be derived, giving

$$r \equiv \frac{a_R}{a_I} = \frac{\theta - \theta'}{\theta + \theta'} \quad and \quad t \equiv \frac{a_T}{a_I} = \frac{2\theta}{\theta + \theta'} \tag{4.39}$$

It should be noted that the reflected and transmitted intensities are $R = r^2$ and $T = t^2$, respectively.

The momentum transfer wavevector, **Q**, is defined as

$$Q = 2k\, sin\theta \cong 2k\theta \quad with \quad Q_c = 2k\, sin\theta_c \cong 2k\theta_c \cong 2k\sqrt{2\delta} \tag{4.40}$$

with the dimensionless quantities

$$q \equiv \frac{Q}{Q_c} \cong \frac{2k}{Q_c}\theta \quad and \quad q' \equiv \frac{Q'}{Q_c} \cong \frac{2k}{Q_c}\theta' \tag{4.41}$$

These can then be substituted into the Fresnel equations to give

$$r = \frac{q - q'}{q + q'} \quad and \quad t = \frac{2q}{q + q'} \tag{4.42}$$

The same substitution can be performed on Equations 4.35 and 4.37 to give

$$q^2 = q'^2 + 1 - 2ib_\mu \quad with \quad b_\mu = \beta \left(\frac{2k}{Q_c}\right)^2 = \frac{2k}{Q_c^2}\mu \tag{4.43}$$

and

$$\Lambda(q) = \frac{1}{Q_c \Im(q')} \tag{4.44}$$

Equations 4.42, 4.43 and 4.44 can now be used to calculate the reflectivity and transmittivity amplitudes. The values can easily be calculated for some limiting cases, assuming $b_\mu \ll 1$, as shown below.

q $\gg 1$:

At this limit, Equation 4.43 gives $\Re(q') \approx q$ and $\Im(q') \approx b_\mu/q$, with Equation 4.42 being approximate to

$$r(q) = \frac{q^2 - q'^2}{(q^2 + q'^2)} \approx \frac{1}{(2q)^2} \quad and \quad t(q) \approx 1 \tag{4.45}$$

This shows that the reflected and incident wave are in phase and almost complete transmission of the wave occurs. As reflected intensity, R, is the square of the amplitude, r, we find that the reflected intensity follows the trend $R(q) = ((2q)^{-2})^2 = (2q)^{-4}$.

q $\ll 1$:

With $\Im(q') \approx 1$, $r(q) \approx -1$, and $t(q) \approx 0$, the reflected wave is out of phase with the incident wave and almost complete reflection occurs. The transmitted wave is very weak and has a penetration depth $\Lambda = 1/Q_c$. This is termed an evanescent wave.

$\mathbf{q} = 1$:

In this case, $q' = \sqrt{b_\mu}(1+i)$ and $\Lambda = 1/\sqrt{b_\mu}Q_c$. Since $b_\mu \ll 1$, the reflected amplitude is approximately 1, with the incident and reflected waves in phase and the penetration depth is greater than the evanescent wave.

Reflectivity from an Ideal Film

Having evaluated the reflection and transmission at an interface, we can move on to consider the effects of a finite layer of material 1 with refractive index n and thickness d on an infinite substrate of material 2 in a vacuum (denoted with 0). In this system, a portion of the incident x-rays will be reflected at the surface with amplitude r_{01}, while some will be transmitted with t_{01}. At the interface between the film and substrate, some x-rays will be transmitted, t_{12}, and some reflected, r_{12}. These reflected x-rays can then either be transmitted at the surface, t_{10}, or reflected, r_{10}. This process can then repeat infinitely.

To calculate the total reflectivity, these factors are summed, taking into account the phase factor $p^2 = e^{iQd}$, giving

$$\begin{aligned} r &= r_{01} + t_{01}t_{10}r_{12}p^2 + t_{01}t_{10}r_{10}r_{12}^2p^4 + t_{01}t_{10}r_{10}^2r_{12}^3p^6 + ... \\ &= r_{01} + t_{01}t_{10}r_{12}p^2\sum_{N=0}^{\infty}(r_{10}r_{12}p^2)^N \end{aligned} \tag{4.46}$$

This geometric series can be evaluated to give

$$r = r_{01} + \frac{t_{01}t_{10}r_{12}p^2}{1 - r_{10}r_{12}p^2} \tag{4.47}$$

Taking Equation 4.42 with $q = Q_0$ and $q' = Q_1$, it is then clear that $r_{01} = -r_{10}$, and as

$$r_{01}^2 + t_{01}t_{10} = \frac{(Q_0 - Q_1)^2}{(Q_0 + Q_1)^2} + \frac{2Q_0\,2Q_1}{(Q_0 + Q_1)^2} = \frac{(Q_0 + Q_1)^2}{(Q_0 + Q_1)^2} = 1, \tag{4.48}$$

it is shown that $t_{01}t_{10} = 1 - r_{01}^2$. Equation 4.47 can then be simplified to

$$r = \frac{r_{01} + r_{12}p^2}{1 + r_{01}r_{12}p^2} \tag{4.49}$$

Plotting the square of this equation, the reflected intensity R, as a function of Q, we obtain the reflectivity curve seen in Figure 4.28 a). The periodic oscillations in the reflected intensity seen in this plot are a result of interference between reflection from the film surface and film / substrate interface, with the peaks and troughs corresponding to in

phase and out of phase scattering, respectively. The oscillations are known as Kiessig fringes, and have a spacing of $\Delta Q = 2\pi/d$, with d being the thickness of the film in Å.

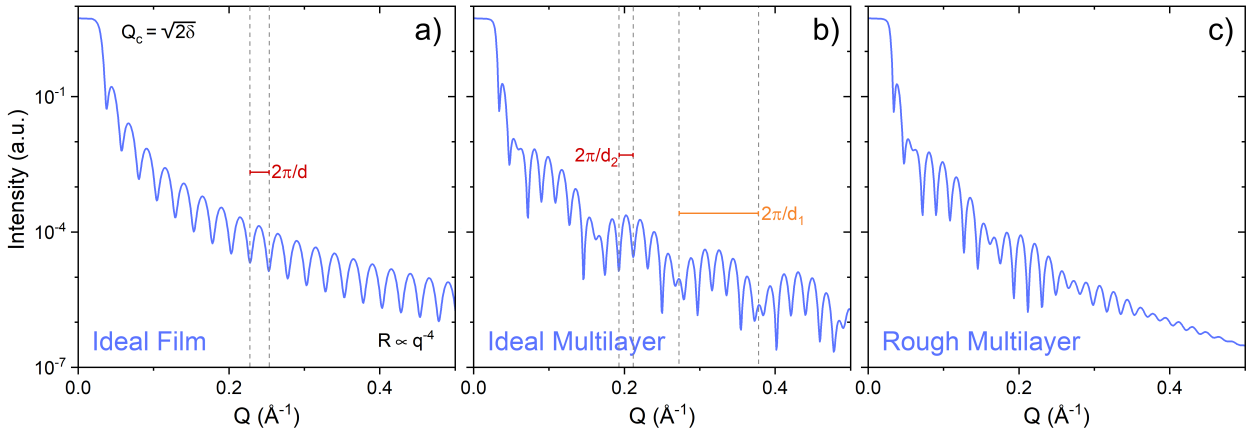

Figure 4.28: *Example reflectivity curve for a) and ideal film on infinite substrate, b) an ideal multilayer film, and c) a rough multilayer film.*

Reflectivity from Multiple Layers

The reflected intensity from an ideal single layer film has been shown, but calculating this for a film of multiple layers is more challenging and approximations must be made. In the region where $Q \gg Q_c$, known as the kinematical regime, approximations that refraction effects are negligible and multiple scattering is weak enough to be negligible can be made, simplifying this calculation. With Q close to Q_c, refraction and multiple reflection effects are significant and must be considered.

To deal with this intricate problem, Parratt developed a recursive method that considers a film composed of N layers, with the first layer at the surface and N^{th} layer at the infinitely thick substrate [137]. Each j^{th} layer will have a refractive index $n_j = 1 - \delta_j + i\beta_j$ and thickness d_j. This refractive index will determine the wavevector in each j^{th} layer, giving $k_j = n_j k$. The component of this wavevector along the surface (the x direction) is conserved in each layer such that $k_{x,j} = k_x$ for all values of j. This is not true of the component k normal to the surface (the z direction), with this value found by

$$k_{z,j}^2 = (n_j k)^2 - k_x^2 = (1 - \delta_j + i\beta_j)^2 k^2 - k_x^2 \approx k_z^2 - 2\delta_j k^2 + 2i\beta_j k^2 \tag{4.50}$$

Recalling that $Q_j = 2k_j\, sin\theta_j = 2k_{z,j}$, the wavector transfer in the j^{th} layer can be found to be

$$Q_j = \sqrt{Q^2 - 8\delta_j k^2 + 8i\beta_j k^2} \tag{4.51}$$

Taking Equation 4.42, the Fresnel equation for the interface between the j^{th} and $j+1^{th}$ layer, neglecting multiple reflections (denoted '), is

$$r'_{j,j+1} = \frac{Q_j - Q_{j+1}}{Q_j + Q_{j+1}} \tag{4.52}$$

Using this result, and the reflectivity for an single layer shown in Equation 4.49, the reflectivity of the interface between the $j-1^{th}$ and j^{th} layer is

$$r_{j-1,j} = \frac{r'_{j-1,1} - r_{j,j+1}p_j^2}{1 + r'_{j,j-1}r_{j,j+1}p_j^2}, \tag{4.53}$$

where $p_j^2 = e^{id_jQ_j}$ is the phase factor in the j^{th} layer.

This equation can be recursively applied from $j = N-1$ to $j = 1$ to account for the reflectivity from each interface in the multilayer film, therefore allowing the reflectivity intensity, R, to be calculated.

An example of the reflectivity curve from a layer of thickness d_1 on a thicker layer of thickness d_2 is shown in Figure 4.28 b). In this plot, the interference effects resulting from the thick layer can be seen by the narrow Keissig fringes, while the effects of the thin layer can be seen by the broader fringes.

Reflectivity from Non-Ideal Films

The previous discussions have considered only ideally sharp and smooth interfaces, but to apply these results to real films, non-ideal interfaces must be considered. These interfaces can deviate from the ideal in two main ways: being graded, i.e. being non-ideal in z, and being rough, i.e. being non-ideal in x.

Let us first consider the effects of a graded interface on the ideal reflectivity, r_{ideal}. The effect of this graded interface can be described by the sum of reflectivity contributions from finite layers of varying electron density. Describing this electron density profile as $f(z)$, we can account for the induced phase changes of each layer of this graded interface by integrating the density gradient over z, giving

$$r(Q) = r_{ideal}(Q) \int_{-\infty}^{\infty} \frac{df(z)}{dz} e^{iQz} dz \tag{4.54}$$

This description allows any function to be used to describe the gradient of $f(z)$, and it is common to use a Gaussian. As Equation 4.54 uses the Fourier transform of this function and the Fourier transform of a Gaussian is another Gaussian, the reflectivity intensity can be described as

$$R(Q) = R_{ideal}(Q)e^{-Q^2\sigma^2}, \tag{4.55}$$

where σ represents the thickness of the graded region.

Considering the effect of rough interfaces, changes in layer thickness as a function of x can be averaged to give a thickness distribution in z [138–140]. This uncorrelated roughness can then be described for the interface between layer j and $j+1$ as a change in the refractive index

$$n_{j,j+1}(z) = n_j + (n_{j+1} - n_j)g(z,\sigma) \;\; with \quad g(z) = \frac{1}{\sigma_j}\int_{-\infty}^{\infty} e^{-z/2\sigma_j}dz \tag{4.56}$$

As with $f(z)$, the function $g(z)$ can be any function that describes the thickness distribution, and in this case a commonly used Gaussian distribution function has been used, with σ_j representing the root mean square (RMS) roughness. As before, the reflectivity intensity is then found to be

$$R(Q) = R_{ideal}(Q)e^{-Q^2\sigma_j^2} \tag{4.57}$$

Comparing Equations 4.55 and 4.57, it can be clearly seen that the effects of graded interfaces and rough interfaces on the reflectivity intensity are very similar and consequently difficult to distinguish. This is in part due to the averaging effects of using grazing incidence x-rays to investigate rough surfaces as the volumes measured are far greater than the volumes over which thickness is constant.

To illustrate the effects of surface roughness, Figure 4.28 b) and c) display modeled reflectivity curves for a multilayer film with ideal interfaces and rough interfaces, respectively. At low Q, the effects of this roughness are not discernible, however, as Q increases, the amplitude and resolution of the Keissig fringes in the reflectivity of the rough film decreases.

4.3.2.2 Measurement and Analysis

X-ray reflectivity measurements are taken using the same experimental set-up as specular x-ray diffraction. As described in Section 4.3.1.2, all XRR measurements were taken using a Philips X'pert diffractometer. As XRR is performed at

very low angles of incidence, it is highly sensitive to sample alignment. Consequently, before measurements were taken, the sample surface was aligned in ω and χ such that the surface normal was in the specular direction.

XRR analysis was performed using GenX software. As described previously, this software utilises a differential evolution algorithm for fitting the model parameters to the data [135]. GenX contains an in-built model for fitting specular x-ray reflectivity data which uses the Parratt recursion method described earlier [137]. The interface roughness in this model is assumed to have a Gaussian distribution, as described by Nevot and Croce [138]. Additionally, this model takes into account sample and instrument factors such as diffractometer resolution and beam footprint effects, as described by Gibaud [141].

A GenX reflectivity model is built by constructing a sample consisting of a substrate of infinite thickness with a scattering length density, SLD_{sub}, calculated from the element specific density of the material, and a RMS roughness, σ_{sub}, in Å. The SLD is calculated in the units of the real part of the total electron scattering length ($\rho_e r_0$) per Å^3, written $\text{r}_e/\text{Å}$. Subsequent n layers of the sample are then described with SLD_n, σ_n, and thickness d_n. All these parameters are then used to construct a scattering length density profile as a function of distance from the substrate surface. This profile is then used to calculate the modeled reflectivity intensity.

To optimise the calculated model, user-selected instrument and sample parameters are altered over a user-defined range using a differential evolution algorithm to minimise the difference between the calculated model and the data. This method provides a robust method of optimisation that allows local minima to be avoided. The difference between the model and the data is calculated using a figure of merit (FOM) function, which evaluates their differences over all Q values. As reflectivity intensities span many orders of magnitude, it is essential to give appropriate weighting to each value, often achieved using logarithmic scaling. All XRR data modeled in this work has used the 'LogR1' FOM formula shown below, where i is all Q values, D is normalised reflectivity data, and M is modeled reflectivity.

$$FOM = \frac{\sum_i |\log_{10} D_i - \log_{10} M_i|}{\sum_i \log_{10} D_i} \tag{4.58}$$

The chosen FOM function also plays an important role in determining the errors on values obtained from XRR fitting. The error on each fitted parameter is found by calculating the FOM as a function of the parameter value and then finding the range of this parameter value over which the increase in FOM is below 5 %. This method of calculating

errors therefore indicates how much altering a value in the model worsens the fit of the model.

4.3.2.3 XRR Results

Epitaxial UN Thin Film

XRR was used to investigate the effect of the miscut between the $(0\,1\,2)$ plane of the Al_2O_3 substrate and $(0\,0\,1)$ plane of the UN film. This was performed by taking measurements with the scattering plane parallel and perpendicular to the plane of the miscut (the plane in which both the $[0\,1\,2]$ Al_2O_3 and $[0\,0\,1]$ directions lie), with the results shown in Figure 4.29 a) in blue and red, respectively. In this plot, the broad Keissig fringes of the Nb buffer can be seen extending to high Q values, while the narrow fringes of the UN film are seen only at low Q values. These narrow fringes show a significant difference in the XRR taken parallel to the miscut and the XRR taken perpendicular to the miscut, with the fringes in the perpendicular data having greater amplitude and extending further out in Q. This is indicative of differing roughnesses of the UN layer in these two directions.

Figure 4.29 b) shows the fitted XRR taken perpendicular to the miscut, with data shown in circles and modeled XRR shown with a solid red line. There is close alignment of the modeled XRR with the data, showing that the fitted thickness and roughness values accurately describe the film, with UN layer roughness, σ_{UN}, of 15.0±0.8 Å, Nb layer roughness, σ_{Nb}, of 3.4±0.3 Å, and Al_2O_3 substrate roughness, σ_{sub}, of 1.6±0.1 Å.

Figure 4.29 c) shows the XRR data and models for XRR taken parallel to the plane of the sample miscut. Both fits shown have σ_{Nb} = 3.0±0.3 Å and σ_{sub} = 2.0±0.2 Å The lower curve shows a model with σ_{UN} = 15.0 Å, the value determined from the fitting of the perpendicular data. The amplitude of the modeled narrow fringes, shown by the dark blue solid line, is clearly greater than in the data, showing that the UN layer roughness value used is not correct, however, the overall intensity of the model fits well with the data. The upper curve of Figure 4.29 c) shows the same data taken parallel to the miscut but modeled with σ_{UN} = 16.5 Å, shown by the light blue solid line. Here the amplitude of the modeled fringes are much closer to those seen in the data, however, the overall modeled intensity at low Q is lower than that of the data.

The demonstrated difficulty in modeling the narrow fringes of the UN film in the data taken parallel to the miscut

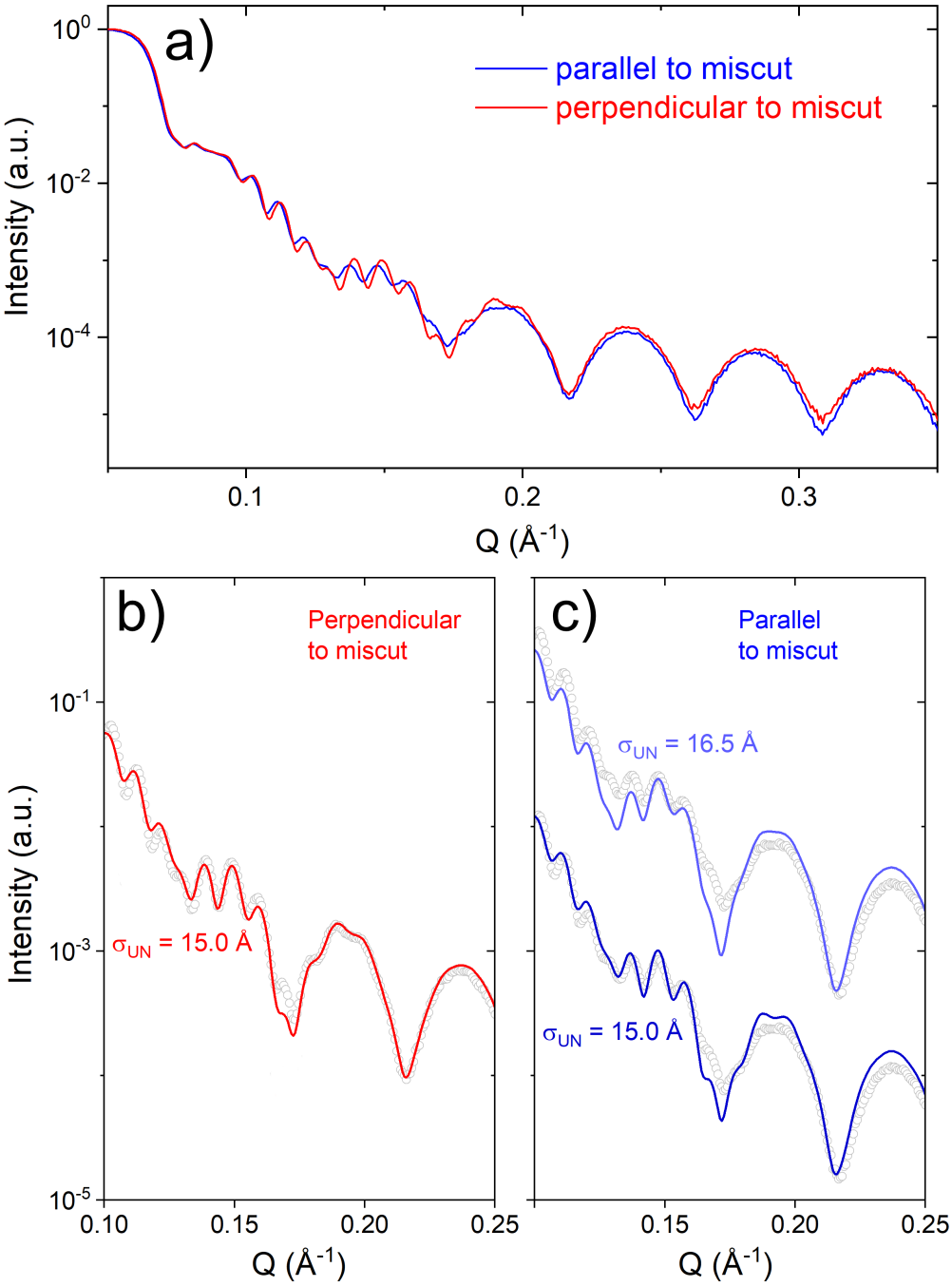

Figure 4.29: *X-ray reflectivity curves of* $(0\,0\,1)$ *UN film taken parallel (blue) and perpendicular (red) to the plane of the miscut shown in a), with close up of fitted data with UN layer roughness labeled shown in b) and c) for perpendicular and parallel, respectively.*

between the UN film and substrate shows that the model used does not adequately describe the the morphology of the UN layer. The match in reflectivity intensity but mismatch in fringe amplitude at σ_{UN} = 16.5 Å show that diffuse scattering is not as high as would be expected for this roughness. This suggests that the Gaussian function used to describe uncorrelated roughness is not suitable in this case. Contrasting this with the results seen in XRR taken perpendicular to the miscut, it can be concluded that there is some anisotropical correlated surface roughness in the UN layer of the $(0\,0\,1)$ UN thin film.

Polycrystalline Thin Films

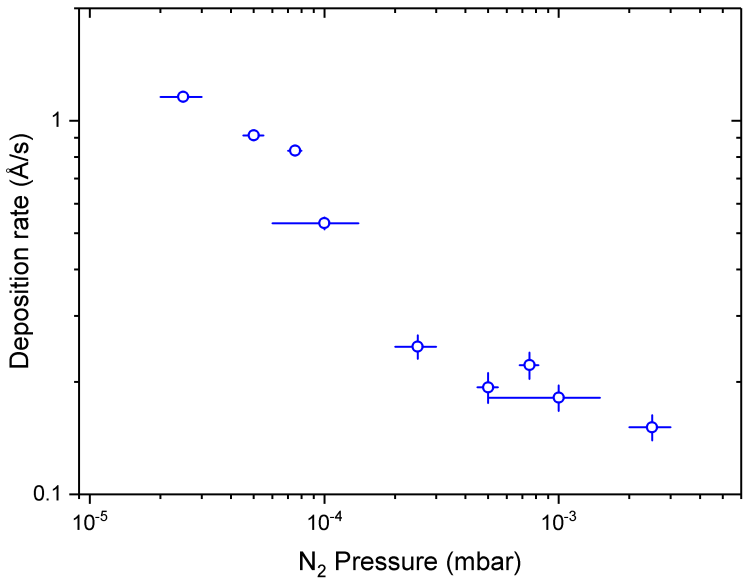

Figure 4.30: *Sputter deposition rates of uranium nitride thin films as a function of N_2 partial pressure during deposition.*

Figure 4.30 shows the effect on N_2 partial pressure on the deposition rate of uranium nitride films, calculated using XRR. This plot shows that an increase in N_2 partial pressure significantly reduces the deposition rate.

4.3.3 Discussion of Structural Characterisation Results

4.3.3.1 Polycrystalline Films

Investigations into the effect of N_2 partial pressure when depositing uranium nitride thin film using reactive sputtering have shown that higher N_2 pressure produces higher nitrides, as expected [6]. The measured lattice parameters of the deposited UN films were found to match literature values, within errors, but this was not true for the higher nitride films [45].

At low N_2 pressures, a slight increase in UN lattice parameter as a function of N_2 pressure is seen, which could be indicative of an increase in stoichiometry, however, UN is not known to exist with a wide range of stoichiometries. Alternatively, this change in lattice parameter could be due to varying strain in the film due to the differences in deposition rates or due to contamination.

The relative intensities of different reflections, such as the $(1\,1\,1)$ and $(0\,0\,2)$ reflections, show that the texture of the polycrystalline UN samples also varies with N_2 pressure. This change in texture could be a result of the change in deposition rate as a function of N_2 pressure, as shown in Figure 4.30. As deposition rate decreases, the deposited material will have more time to diffuse on the film surface before being restricted by the further deposition of material.

Similarly, a difference in texture of polycrystalline UN films was also seen when comparing films deposited at 20 (room temperature) and 500 °C, with the film deposited at higher temperature showing stronger texturing. At higher temperates, the deposited film will have more thermal energy, increasing diffusion rates on the film surface. With increased diffusion times or rates, deposited material will more easily be able to crystallise in a lower energy configuration. As the $(1\,1\,1)$ plane of UN is the closest packed plane, it is likely that this surface will be the lowest energy configuration, explaining the strong texturing with preferred orientation in the $(1\,1\,1)$ direction.

The results for the sample deposited with an N_2 pressure of 3.2×10^{-4} mbar show evidence of both UN and U_2N_3 in the sample. This suggests that for stoichiometries between 1 and 1.5, the deposited uranium nitride forms as a mixture of two separate phases, UN and U_2N_3, as shown in the phase diagram in Figure 2.1.

Considering the higher nitride thin films, only the film deposited with an N_2 pressure of 7×10^{-4} mbar was found to have a lattice parameter matching that of stoichiometric U_2N_3, within errors [45]. The increase in lattice parameter with

N_2 pressure seen for the higher nitride films is surprising, as lattice parameter is known to decrease with increasing stoichiometry, as shown in Figure 2.4 [2]. It is possible that this lattice expansion is caused by O contamination, however it is challenging to investigate this as no other peaks are present in the collected XRD scans and there is no literature data on the structure of uranium oxynitrides.

Considering the results presented above, the N_2 pressures found to produce UN and U_2N_3 films were 2.5×10^{-5} and 7×10^{-4} mbar, respectively. For each uranium nitride thin film deposition session, the pressures and rates were recalibrated, and the pressure required to deposit stoichiometric UN and U_2N_3 was found. As room temperature deposition of polycrystalline films was found to produce a less textured film, more accurately representing polycrystalline material, all nanocrystalline films used for experiments were deposited at room temperature.

4.3.3.2 Epitaxial UN Thin Films

XRD investigations of a UN film deposited on a Nb buffer on a $(1\,\bar{1}\,0\,2)$ Al_2O_3 substrate have shown it to be single crystal and single domain, oriented in the $(0\,0\,1)$ direction, with lattice parameters of 4.885±0.008 Å for a and 4.895±0.001 Å for c, giving a unit-cell volume of 116.8±0.5 $Å^3$. These values match very closely with the literature value of 4.89 Å, but with a small tetragonal distortion that conserves the unit-cell volume [45].

The quality of this single crystal film is not excellent, and is much lower than that of the $(0\,0\,1)$ U_2N_3 sample. This is evident in the broad peaks of the ω scans of the UN film and Nb buffer, with widths of 1.73±0.01 ° and 1.22±0.01 °, respectively, and in the presence of a large miscut between the film and substrate. This shows a lack of coherence between the UN film and Nb buffer and the Al_2O_3 substrate.

As the UN film grows epitaxially on the Nb buffer, the quality of the UN film can only be as good quality as the Nb buffer, and the broad width of the Nb ω scan shows that this factor is significant in determining the quality of the UN film. Since the epitaxial growth of Nb on $(1\,\bar{1}\,0\,2)$ Al_2O_3 has been shown to be optimised at 800 °C, the temperature used to produce these films, it is unlikely that the quality of the epitaxial UN film can be improved using this system [115].

The 2.6 ° miscut found between the UN $[0\,0\,1]$ and Nb $[0\,0\,1]$ direction and the specular Al_2O_3 $[0\,1\,2]$ direction was found to be in the same plane as that which contains both the Al_2O_3 specular and c direction. This result is consistent with the work of Gutekunst *et al.* on epitaxial Nb films on Al_2O_3 substrates [142]. Though this miscut is also reported

in other work on the subject, none of the past literature provide an explanation for such a large miscut [115, 142, 143]. Considering Figure 4.21, it can be seen that the Al_2O_3 lattice in the $(1\,\bar{1}\,0\,2)$ plane is not square, but rhombohedral, as can be seen by the 94.3 ° angle between 3 Al atoms shown. As a rhombus can be viewed as a tilted square, it is likely the misfit between the square Nb $(0\,0\,1)$ plane and Al_2O_3 $(1\,\bar{1}\,0\,2)$ plane is accommodated for by a relative tilt of the Nb $(0\,0\,1)$ plane.

X-ray reflectivity has been used to investigate the effect of this miscut on the morphology of the UN epitaxial films. XRR has been used for this purpose before, with investigations measuring the differences in transverse scans (ω scans) on the reflectivity profile parallel and perpendicular to the film miscut [144–147]. These investigations found features in the transverse scans parallel to the miscut that were not present in those performed perpendicular to the miscut, with diffuse peaks seen at angles corresponding to the film miscut. These features were described as being caused by anisotropic correlated interfacial roughness, oriented in a specific direction with respect to the direction of the miscut, with AFM measurements further showing evidence of wave-like terraces on the film surface [144, 147].

These investigations were performed on films, mostly Si/Ge superlattices, with miscuts of 0.3 to 0.5 °, meaning that these diffuse features are close to the specular ridge, where intensity is high. The epitaxial UN films investigated here here have a much larger miscut with α_{miscut} = 2.6 °. Consequently, if these diffuse features were present, they would be found at $\omega = \alpha_{miscut}$ and therefore can only be found at a minimum 2θ value of $2 \times \alpha_{miscut}$. At these high angles in the reflectivity, intensity is very low and no features were found. Instead, this work has taken a unique approach to using XRR to investigate the effect of this miscut on morphology, with differences in the specular reflectivity investigated rather than in the transverse scans.

Results of this investigation showed differences in the XRR taken parallel and perpendicular to the miscut, with parallel data showing Keissig fringes from the UN layer with smaller amplitude. This is indicative of anisotropic correlation in the UN surface roughness. Additionally, considering the low amplitude of these fringes, a higher intensity than expected was seen in the XRR parallel to the miscut.

Let us compare this result to the work of Phang *et al.* and Headrick *et al.*, where diffuse peaks were seen in the transverse (ω) scans when parallel to the miscut [144, 147]. Were similar features to be present in the UN film, they would be offset in χ (perpendicular to the scattering plane), rather than ω when measuring in the direction perpendicular

to the miscut. As this diffuse scattering would be consistently scattered away from the scattering plane at a fixed angle, the measured diffuse intensity and therefore roughness would be lower than from a film with uncorrelated roughness. In the parallel measurement, the opposite would be true, with a greater proportion of diffuse scattering being confined to the scattering plane. This provides an explanation for the higher than expected intensity seen in the XRR taken parallel to the miscut and difference in fringe amplitude between the two measurements. Therefore it is likely that the miscut in the epitaxial UN film has resulted in the formation of terraces on the UN layer surface perpendicular to the miscut, creating anisotropic correlation in the surface roughness.

4.3.3.3 Epitaxial U_2N_3 Thin Films

XRD analysis of SN1189, the 30 nm thick U_2N_3 film deposited on CaF_2, showed the film to be single crystal, oriented in the $(0\,0\,1)$ direction. The 90 ° symmetry of the off-specular $(2\,2\,6)$ reflection showed that only one domain was present in the film, with the narrow ω width of 0.03 ° indicating that the film is in excellent registry with the substrate.

Contrastingly, the 200 nm thick film, SN1431, was found to have a broad ω width of 0.98 °. This significant change in film quality with thickness is not unusual for epitaxial thin films, and can be seen in the work of Bao *et al.* on epitaxial UO_2 [148]. This occurs as the broad and narrow components of the ω peak, as seen in the ω scan on SN1189 in Figure 4.24, change in relative intensity with film thickness. As a film becomes thicker, registry with the substrate is lost and the broad component of the peak corresponding to this dominates, increasing the overall width of the ω peak.

The lattice parameters determined for the 30 nm thick sample, SN1182, were found to be 10.7±0.1 and 10.72±0.01 Å for a and c, respectively. This c value is higher than the bulk U_2N_3 value of 10.678 Å, as is the value for a, however, the error on this value is large [45]. The 200 nm thick U_2N_3 film, SN1431, had lower errors on XRD fitting results, allowing it to be determined that the film is clearly tetragonal, with an a lattice parameter of 10.61±0.03 Å and c lattice parameter of 10.802±0.005 Å. The value for a is lower than literature value, and c is higher, which is surprising as the lattice parameter of the CaF_2 substrate is 5.463 Å, and so it would be expected that a is greater than c [118]. Consequently, it can be said that the tetragonality of the U_2N_3 in this sample is not due to epitaxial strain. This is further supported by the 30 nm thick sample, which has better registry to the substrate, having a lower value, closer to bulk, for the c lattice parameter.

Despite the a and c lattice parameters differing from bulk values, the unit-cell volume of 1216 ± 7 Å^3 is very close to the literature value of 1217 Å^3, showing that unit-cell volume is conserved despite this distortion [45]. As lattice parameter and therefore unit-cell volume is know to decrease with increasing stoichiometry, this is good evidence that the deposited films are stoichiometric U_2N_3.

4.3.4 Conclusion

This section has provided structural analysis of uranium nitride samples grown by reactive DC magnetron sputter deposition. X-ray diffraction of polycrystalline samples grown with a range of different N_2 reactive gas partial pressures has shown that N_2 pressure can be successfully used to control which uranium nitride phase is deposited. Additionally, these measurements have shown that deposition temperature and deposition rate have an influence on the texture of the deposited films, with lower pressures and temperatures producing less textured films. Crystallite size analysis of XRD results using the Scherrer equation gave results of 9 ± 1 nm for both UN and U_2N_3 polycrystalline films.

UN films deposited on $(1\,\bar{1}\,0\,2)$ Al_2O_3 substrate with a $(0\,0\,1)$ Nb buffer were found to be single crystal, oriented in the $(0\,0\,1)$ direction, but with a broad rocking curve showing the poor mosaic of the film. The low registry between the UN film and Nb buffer is also shown by the large miscut between the UN film and Nb buffer and the Al_2O_3 substrate, which is likely to be a result of the poor match between the buffer and substrate. Through investigations using x-ray reflectivity, this miscut was found to give rise to anisotropic correlation in UN surface roughness. Lattice parameters of the epitaxial UN film measured using XRD were found to be 4.885 ± 0.008 Å for a and 4.895 ± 0.001 Å for c, close to the bulk value but with a small tetragonal distortion.

XRD analysis of U_2N_3 film deposited on $(0\,0\,1)$ CaF_2 substrates found the film to be $(0\,0\,1)$ oriented single crystal. Comparing films of 30 and 200 nm thickness, it was found that the thinner film had an excellent mosaic, with rocking curve width of only $0.03\,^\circ$, and lattice parameters close to bulk. Contrastingly, the thicker film had a much broader rocking curve and a tetragonal distortion, with 10.61 ± 0.03 Å for a and 10.802 ± 0.005 Å for c, however, bulk unit-cell volume was conserved, suggesting that the film is stoichiometric.

The above results show that single crystal epitaxial UN and U_2N_3 thin films have been successfully produced by reactive sputter deposition. These films are the first of their kind, with the U_2N_3 film being the first documented

synthesis of a U_2N_3 single crystal. These novel samples increase the range of possible experiments and measurements that can now be performed on the uranium nitrides.

Chapter 5

Resonant Scattering Investigations

Investigations into the magnetic ordering of UN and U_2N_3 samples using synchrotron radiation are presented in this chapter. An introduction to resonant scattering is given, with scattering results showing that the previously accepted magnetic structure of UN may not be correct. Anisotropic resonant scattering of U_2N_3 gives insight into the differences between the two U sites. The results from this chapter have been published in Physical Review B [149].

5.1 Resonant X-ray Scattering

Having previously considered x-ray scattering as the interaction between x-rays and a free electron, we will now consider the effects of the electron being bound to an atom. This leads to the possibility of resonant scattering, the elastic excitation and decay to and from a higher binding energy state. As this phenomenon significantly increases the interaction cross-section, it is used to investigate effects that would not otherwise be detectable, such as magnetic scattering. By combining both absorption and diffraction, sensitivity to both electronic structure and periodicity is achieved, allowing local electronic structure to be investigated. Furthermore, as resonant scattering is caused by a

specific transition, it provides a method of investigating individual electron states.

5.1.1 Resonant Interactions

Previously, when describing the interaction of x-rays with an atom, the classical Thomson scattering model has been used. This has given a scattering length of the atom of $-r_0 f^0(\mathbf{Q})$, the product of the Thomson length and atomic form factor, as shown in Equation 4.14. This form factor is the Fourier transform of the charge distribution, and therefore a real number. However, when examining the theory of x-ray reflectivity, it was found that when absorption is included, the scattering length has an imaginary term, as seen in Equation 4.31. This discrepancy shows the limitations of the classical model, as it cannot sufficiently describe both Thomson scattering and absorption [122].

One simple correction to this that can be made is accounting for electrons being bound to an atom. Classically, these electrons will then respond as damped harmonic oscillators, rather than as the free oscillators described in the Thomson scattering model [122]. Taking a single oscillator with resonant frequency ω_s and damping constant Γ, subject to an electric field $\mathbf{E}_{incident} = \hat{\mathbf{x}} E_0\, e^{-i\omega t}$, which is polarised in the x direction, the electron will have motion described by

$$\ddot{x} + \Gamma\dot{x} + \omega_s^2 = -\frac{eE_0}{m_e} e^{-i\omega t}, \tag{5.1}$$

where m_e is electron rest mass. This equation of motion has a solution

$$x(t) = x_0 e^{-i\omega t} \quad with \quad x_0 = -\frac{eE_0}{m}\frac{1}{\omega_s^2 - \omega^2 - i\Gamma\omega}, \tag{5.2}$$

where the amplitude of the forced oscillation of the electron is x_0.

The $\Gamma\dot{x}$ term in the equation of motion shows the velocity dependent dampening as energy is dissipated by radiation. Acceleration of the electron is shown by the $\ddot{x}$ term, and will cause an electric field E, at a point r in the plane perpendicular to the polarisation and time t, described by

$$E(r,t) = \frac{q_e}{rc^2}\,\ddot{x}(t - r/c) = \frac{\omega^2}{\omega_s^2 - \omega^2 - i\Gamma\omega}\,\frac{q_e^2}{m_e c^2} E_0 e^{-i\omega t}\,\frac{e^{ikr}}{r} \tag{5.3}$$

The time value used for the electron acceleration, $t - r/c$, accounts for the time taken for the radiated field to travel the distance r. Using the Thomson scattering length, r_0, shown in Equation 4.7, this can be simplified to

$$\frac{E(r,t)}{E_{incident}} = -r_0 \frac{\omega^2}{\omega^2 - \omega_s^2 + i\Gamma\omega}\,\frac{e^{ikr}}{r} \tag{5.4}$$

The amplitude of this radiated wave, e^{ikr}/r, is defined as the atomic form factor, f_s. For simplicity, this is defined in units of r_0, giving

$$f_s = \frac{\omega^2}{\omega^2 - \omega_s^2 + i\Gamma\omega} \tag{5.5}$$

If the incident radiation frequency is much greater than the resonant frequency, the atomic form factor of f_s = 1 is obtained, as found for Thomson scattering.

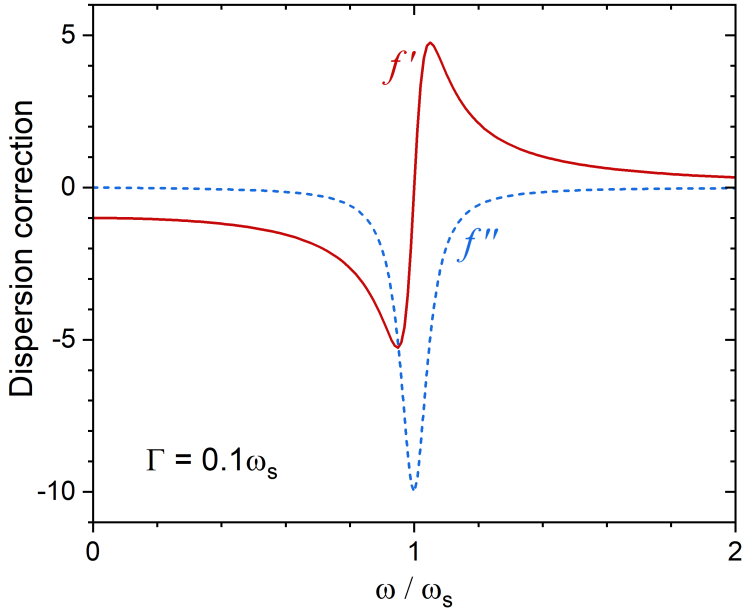

Figure 5.1: *Graph showing real and imaginary parts of dispersion corrections.*

The above equation can be rearranged using the fact that $\Gamma \ll \omega_s$ to give

$$f_s = 1 + \frac{\omega_s^2 - i\Gamma\omega}{\omega^2 - \omega_s^2 + i\Gamma\omega} \approx 1 + \frac{\omega_s^2}{\omega^2 - \omega_s^2 + i\Gamma\omega} \tag{5.6}$$

This form factor can now be clearly interpreted as the sum of the Thomson form factor and the dispersion correction described in Section 4.3, giving

$$f_s(\mathbf{Q}, \omega) = f^0(\mathbf{Q}) - f_s'(\omega) - if_s''(\omega) \tag{5.7}$$

with

$$f_s' = \frac{\omega_s^2(\omega^2 - \omega_s^2)}{(\omega^2 - \omega_s^2)^2 + (\Gamma\omega)^2} \quad and \quad f_s'' = -\frac{\omega_s^2\omega\Gamma}{(\omega^2 - \omega_s^2)^2 + (\Gamma\omega)^2} \tag{5.8}$$

These real and imaginary parts of the dispersion correction have been plotted as a function of ω/ω_s in Fig. 5.1, where their contrasting behaviour is clearly visible.

Considering Equation 5.7, it can be seen that the f^0 term is a function only of **Q**, as expected for Thomson scattering, whereas the f' and f'' dispersion correction terms are functions only of ω. This is based on the assumption that the electrons contributing to this scattering are spatially confined, as they are core electrons, and have a spherical distribution.

5.1.2 Non-Resonant Magnetic Scattering

When a system undergoes a antiferromagnetic (AF) ordering transition, the isotropic symmetry of electron spins is broken as an ordered magnetic structure is created. As electrons are bound to an atom, in a crystalline material the magnetic structure will have ordering related to the crystal lattice structure. Taking an f.c.c. AF structure that is composed of alternating + and - planes in the z direction, in can easily be seen that is the unit cell is doubled in the z direction.

Considering the Laue condition, this increase in the unit cell will mean that magnetic scattering will occur when **Q** = **G** + $\mathbf{q}_{AF}$, where **G** is the reciprocal lattice of the non-magnetically ordered structure and $\mathbf{q}_{AF}$ is the magnetic ordering vector. In the example described above, this ordering vector has a value of $\mathbf{q}_{AF} = \langle 0\,,\ 0\,,\ 1 \rangle$, whereas a system with + + - - planes would have $\mathbf{q}_{AF} = \langle 0\,,\ 0\,,\ 1\,/\,2 \rangle$.

This scattering will have a contribution to the form factor termed f^{mag}, with the total form factor for non-resonant scattering then becoming

$$f = f^0 + f^{mag} \tag{5.9}$$

The f^{mag} term has been described by the interaction of the incident wave with the electron density by Blume *et al.* and Hannon *et al.* in units r_0 as [150, 151]

$$f^{mag} = -i\frac{\hbar\omega}{m_e c^2}\left(\frac{1}{2}\mathbf{L(Q)}\cdot\mathbf{a} + \mathbf{S(Q)}\cdot\mathbf{b}\right) \tag{5.10}$$

where **L(Q)** and **S(Q)** are the Fourier transforms of the orbital and magnetic spin densities, respectively. The vectors **a** and **b** are dependent on the incident and outgoing wavevectors, **k** and **k'**, and polarisations, ϵ and ϵ'.

It should be noted that this magnetic form factor is imaginary, and has a term $\hbar\omega/m_e c^2$. Comparing the cross-section, σ, of this magnetic scattering to that of Thomson scattering, it has been shown by Blume *et al.* that [150]

$$\frac{\sigma_{mag}}{\sigma_{charge}} \approx \left(\frac{\hbar\omega}{m_e c^2}\right)^2 \left(\frac{Z^{mag}}{Z}\right)^2 \langle M \rangle^2 \left(\frac{f^{mag}}{f^0}\right)^2 \tag{5.11}$$

where $\langle M \rangle$ is the magnetic order, which has a maximum of 1, and Z and Z^{mag} are the number of electrons and magnetic electrons per atom, respectively. This relation shows that the magnetic cross-section is much smaller than the charge cross-section, with ratios typically of the order of 10^{-6}.

5.1.3 Resonant Magnetic Scattering

Due to the low intensity of non-resonant magnetic scattering in comparison to charge scattering, it is challenging to measure even when high intensity sources such as synchrotron radiation are used. However, Gibbs *et al.* found that when the incident x-ray energy was tuned to the L_3 edge of Ho there were large resonant enhancements in the magnetic scattering cross-section [152]. This effect was found to be even stronger when probing the M edges of actinide compounds [153].

This occurs as the imaginary nature of the magnetic form factor, shown as f^{mag} above, causes it to couple with the imaginary part of the charge form factor, f''. As the scattering due to f'' is strongly amplified at an absorption edge as the absorption cross-section increases, the magnetic scattering is also amplified. However, as magnetic moments have a direction, the cross-section for magnetic scattering is also dependent on polarisation.

Hill and McMorrow described the resonant scattering cross-section in the form of matrices that have basis components parallel and perpendicular to the scattering plane [154]. The form factor for n^{th} atom with magnetic moment unit vector $\hat{\mathbf{z}}_n$ is

$$f_n^{RXS} = (\hat{\epsilon}' \cdot \hat{\epsilon}) F^{(0)} - i(\hat{\epsilon}' \times \hat{\epsilon}) \cdot \hat{\mathbf{z}}_n F^{(1)} + (\hat{\epsilon}' \cdot \hat{\mathbf{z}}_n)(\hat{\epsilon} \cdot \hat{\mathbf{z}}_n) F^{(2)} \tag{5.12}$$

where $\mathrm{F}^{(0)}$, $\mathrm{F}^{(1)}$, and $\mathrm{F}^{(2)}$ are the 0, 1, and 2 rank tensors of the charge monopole, magnetic dipole, and electric quadrupole, respectively.

The first term is independent of magnetic moment and so contributes only to the charge Bragg peak. Consider the values of this $(\hat{\epsilon}' \cdot \hat{\epsilon})$ term for the two perpendicular polarisation directions, parallel and perpendicular to the scattering

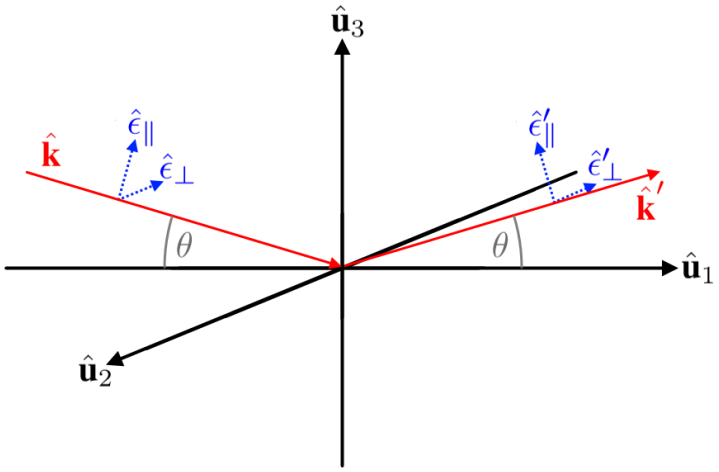

Figure 5.2: *Diagram showing incident and outgoing polarisation directions.*

plane, as depicted in Figure 5.2. This is denoted by $\hat{\epsilon}_{\perp}$ or σ for polarisation perpendicular to the scattering plane and $\hat{\epsilon}_{\parallel}$ or π for polarisation parallel to the scattering plane. The first term will be greatest when $\hat{\epsilon} = \hat{\epsilon}'$, i.e. the incident and outgoing polarisations are the same, which is only possible for $\sigma \rightarrow \sigma$ scattering. For $\pi \rightarrow \pi$ scattering, $\hat{\epsilon}' \cdot \hat{\epsilon} = \hat{\mathbf{k}}' \cdot \hat{\mathbf{k}}$, and so will be 1 when $\hat{\mathbf{k}}'$ and $\hat{\mathbf{k}}$ are parallel and 0 when they are perpendicular (see Equation 4.9). For $\sigma \rightarrow \pi$ or $\pi \rightarrow \sigma$ scattering, the incident and outgoing polarisation directions are perpendicular and the charge scattering term will be 0. This shows that polarisation direction will be unchanged by charge scattering.

The second term in this equation is dependent on the magnetic moment, therefore producing first order magnetic satellites at $\mathbf{Q} = \mathbf{G} \pm \mathbf{q}_{AF}$, as covered previously. The third term gives rise to second order magnetic satellites and can be neglected here. Considering the value of $(\hat{\epsilon}' \times \hat{\epsilon})$, this second term will always be 0 for $\sigma \rightarrow \sigma$ scattering. For $\sigma \rightarrow \pi$ and $\pi \rightarrow \sigma$, $(\hat{\epsilon}' \times \hat{\epsilon})$ will be equal to $-\hat{\mathbf{k}}$' and $\hat{\mathbf{k}}$, respectively. Scattering for $\pi \rightarrow \pi$ will produce $(\hat{\epsilon}' \times \hat{\epsilon}) = \hat{\mathbf{k}}' \times \hat{\mathbf{k}}$, and so be 1 at $2\theta = 0\,^{\circ}$ and 0 at $2\theta = 90\,^{\circ}$. Of course, these $(\hat{\epsilon}' \times \hat{\epsilon})$ values must then have a component in $\hat{\mathbf{z}}_n$ to have a non-zero magnetic contribution to the resonant scattering form factor.

These results show that when investigating resonant x-ray magnetic scattering, there are three features to be considered. Firstly, the presence of magnetic reflection at **Q** positions that are not predicted to occur for charge reflections based on the crystal structure. Secondly, a change in the polarisation of the scattered x-ray may be expected, depending on the relative polarisation of the incident x-ray. Thirdly, the shape of the energy dispersion at a magnetic

reflection will take the form of the imaginary part of the dispersion corrected form factor, f'' [154]. Furthermore, we can also look for the effects of magnetism, such as lattice distortions caused by the coupling of the magnetic ordering to the crystal structure.

5.1.4 Anisotropic Resonant Scattering

As resonant scattering occurs at energies and transitions unique to each element, the element selectivity of it is obvious, however, since the atomic form factor is used in calculating structure factors of Bragg reflections, more information can be obtained from resonant scattering and this selectivity can be taken a step further. By combining the periodicity investigations of diffraction with the enhancement of f' and f'' with resonant scattering, it is possible to obtain information that is site specific, rather than only element specific. This technique is more often used in bio-crystallography when investigating complex structures, where analysis focuses on the energy shifts showing valence states and nearest neighbour effects [155, 156]. However, our interest here is focused more on the symmetry of the state probed by resonant scattering.

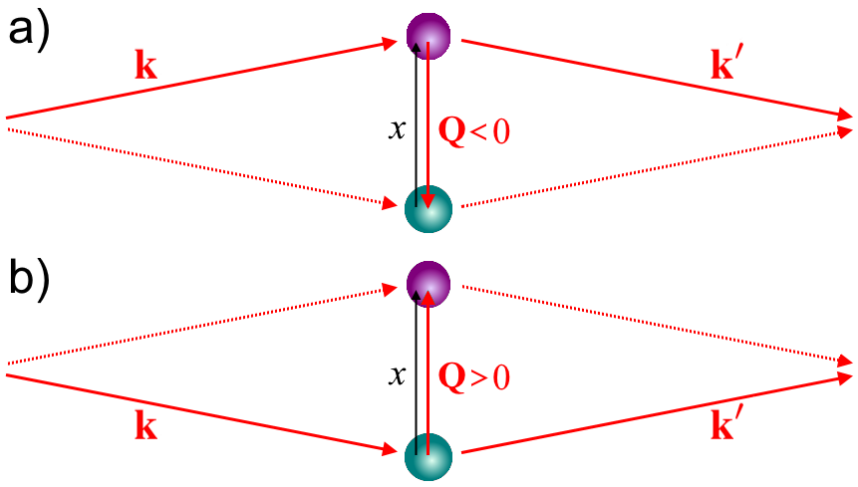

Figure 5.3: *Diagram showing scattering from non-identical atoms.*

Following the work of Bijvoet *et al.*, to consider the effects of resonance on diffraction, it is easiest to first consider two non-identical atoms, as shown in Figure 5.3, with real atomic form factors of f_1 and f_2 [157]. Scattering from these

pairs will result in a momentum transfer wave-vector of **-Q** for a) and **Q** for b), respectively resulting in form factors of

$$A_1(Q) = f_2 + f_1 e^{i(-Q)x} \quad and \quad A_2(Q) = f_1 + f_2 e^{iQx} \tag{5.13}$$

where x is the vertical direction. The scattered intensity will then be

$$I_1(Q) = (f_2 + f_1 e^{i(-Q)x})(f_2 + f_1 e^{-i(-Q)x}) \quad and \quad I_2(Q) = (f_1 + f_2 e^{iQx})(f_1 + f_2 e^{-iQx}) \tag{5.14}$$

$$= f_2^2 + f_1^2 + 2 f_2 f_1 cos(-Qx) \qquad = f_1^2 + f_2^2 + 2 f_1 f_2 cos(Qx) \tag{5.15}$$

As the cosine function is even, i.e. $cos(x) = cos(-x)$, the scattered intensity from scenario a) and b) will be the same, and more generally

$$I(\mathbf{Q}) = I(-\mathbf{Q}) \tag{5.16}$$

This is referred to as Friedel's law, though the law more generally applies to the Fourier transform of any real function [122].

Consider now the scattering with dispersion corrections taken into account for the atomic form factor, which can be rewritten to give

$$f_j = f_j^0 + f_j' + i f_j'' \approx r_j e^{i\phi_j} \tag{5.17}$$

where $j = 1, 2$, and r_j is the magnitude of the scattering length. The scattered amplitude can now be written as

$$A_1(Q) = r_2 e^{i\phi_2} + r_1 e^{i\phi_1} e^{-iQx} \tag{5.18}$$

giving an intensity of

$$I_1(Q) = \left|f_2^2\right| + \left|f_1^2\right| + 2\left|f_2\right|\left|f_1\right| cos(-Qx + \phi_1 - \phi_2) \quad and \quad I_2(Q) = \left|f_1^2\right| + \left|f_2^2\right| + 2\left|f_1\right|\left|f_2\right| cos(Qx + \phi_2 - \phi_1) \tag{5.19}$$

It is clear to see that in this case, if $\phi_1 \neq \phi_2$, then $I(Q) \neq I(-Q)$, showing that the dispersion corrections cause a breakdown of Friedel's law. This shows that resonant scattering can be used to distinguish between $(h\,k\,l)$ and $(\overline{h}\,\overline{k}\,\overline{l})$, therefore determining the relative positions of atoms.

Let us consider the special case of a structure where $(h\,k\,l)$ = $(\overline{h}\,\overline{k}\,\overline{l})$, known as a centrosymmetric structure. Taking the example of a system with atom 1 at $\pm x_1$ and atom 2 at $\pm x_2$, the unit cell scattering length will be

$$F = r_1 e^{i\phi_1} e^{-iQx_1} + r_1 e^{i\phi_1} e^{iQx_1} + r_2 e^{i\phi_2} e^{iQx_2} + r_2 e^{i\phi_2} e^{-iQx_2} \tag{5.20}$$

which can be simplified to

$$F = 2r_1 cos(Qx_1)e^{i\phi_1} + r_2 cos(Qx_2)e^{i\phi_2} \tag{5.21}$$

Calculating the intensity, it is found that

$$I(Q) = 4\left|f_1\right|^2 cos^2(Qx_1) + 4\left|f_2\right|^2 cos^2(Qx_2) + 8\left|f_1\right|\left|f_1\right| cos(Qx_1)cos(Qx_2)cos(\phi_1 - \phi_2) \tag{5.22}$$

This shows that the intensity is only dependent on even functions of Q and must therefore itself be even. Consequently, it is shown that Friedel's law is satisfied for centrosymmetric systems, even when dispersion corrections are included [122].

The results presented above can be used to investigate the scattering length and therefore charge density of a structure [158]. As $\phi_1 \neq \phi_2$ is the condition necessary for the breakdown of Friedel's law, it is clear that there must be nonequivalent imaginary parts of the form factor, f'', for the two scattering centres. This will be shown in the f'' profile of an energy dispersion curve for which the equivalent real parts of the scattering length cancel. By investigating this energy profile for different reflections, differences between different sites and anisotropy of charge distribution on a single site can be determined. However, as shown for cenrosymmetric systems, certain symmetry conditions must be met for this to be possible.

5.1.5 Measurement

All the work presented in this chapter was performed at the I16 beamline at Diamond Light Source, a beamline that focuses on x-ray scattering for magnetism and materials research. The generation of x-rays from synchrotron sources has been described in Section 4.1.2.2, and the optics set-up of the I16 beamline is shown in Figure 5.4. At this beamline, high intensity, low divergence x-rays are produced by an undulator under vacuum, which then pass through several collimators and double crystal monochromators. These monochromators allow continuous energy tuning from 3.3 keV (below the U M edges), to over 15 keV. Focusing mirrors then focus the x-ray beam down to a point size as small as 50 $\times$ 200 μm. The beam is then delivered to the sample through optional attenuators and final slits.

The experimental set-up is shown in Figure 5.5. The sample stage and detectors used were mounted on a 6-circle kappa diffractometer, allowing measurements to be taken in bisecting mode, where the incident and outgoing angle between beam and surface are equal. The sample stage consisted of a Cu mount with a Displex 4K cryocooler, a

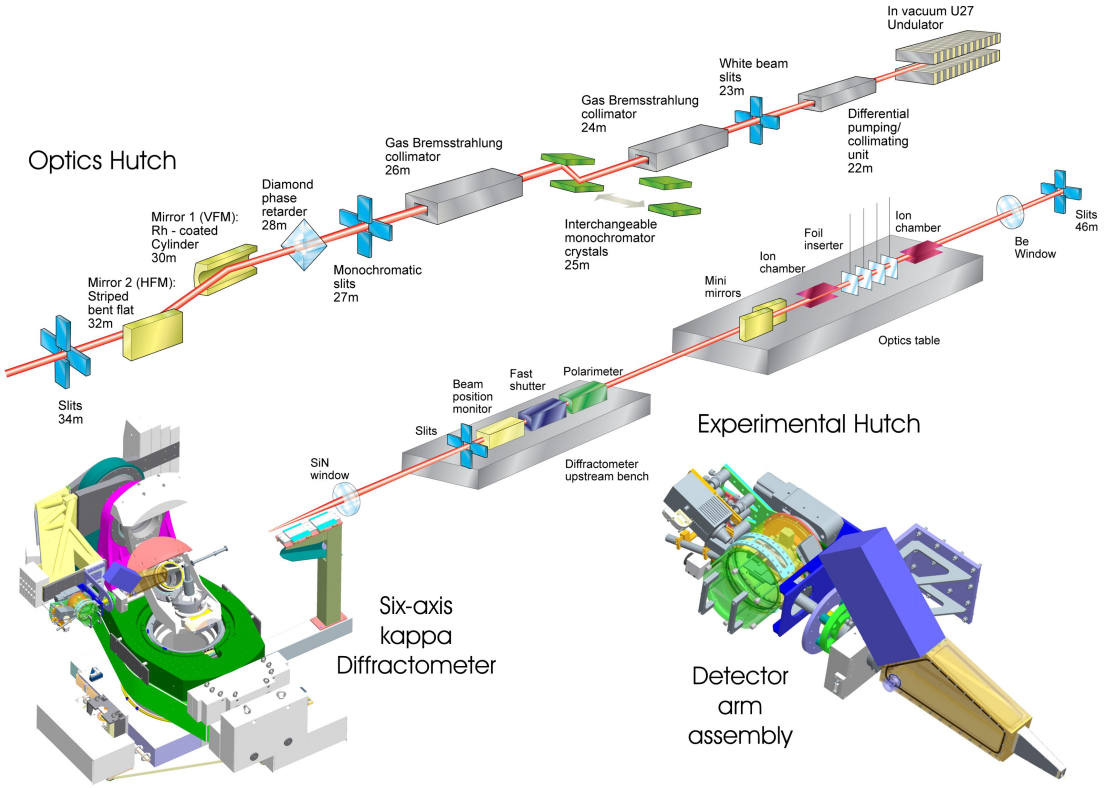

Figure 5.4: *Diagram of optics set-up for I16 beamline at Diamond Light Source, from [9].*

closed-cycle He refrigerator with a temperature range of 6 - 300 K. Temperature readings came from a thermocouple attached to the Cu mount with kapton tape. This sample stage was encased in a UHV Be dome, which allows x-rays to pass through to and from the sample while maintaining UHV pressures. Several detectors are permanently mounted on the detector arm, including an avalanche photodiode point detector, used for sample alignment, and Pilatus 100k (100,000 $\times$ 172 $\times$ 172 μm pixel photon counting detector), used for measurements.

All measurements were taken with vertical scattering geometry, meaning that all incident radiation had σ polarisation (perpendicular to the scattering plane). Linear polarisation analysis of the scattered radiation was performed using a permanently mounted crystal analyser. The crystal used in this analyser is selected to have a high intensity Bragg reflection at an angle of $2\theta \approx 90\,^{\circ}$, such that $\sigma \rightarrow \sigma$ scattering will have high intensity and $\pi \rightarrow \pi$ scattering will have none. In the case of U M_4 edge resonant scattering, the $(1\,1\,1)$ reflection of single crystal Au was used.

This U M_4 edge at 3.725 eV, corresponding to the $3d_{3/2}$ to $5f_{5/2}$ transition, was used for all resonant scattering

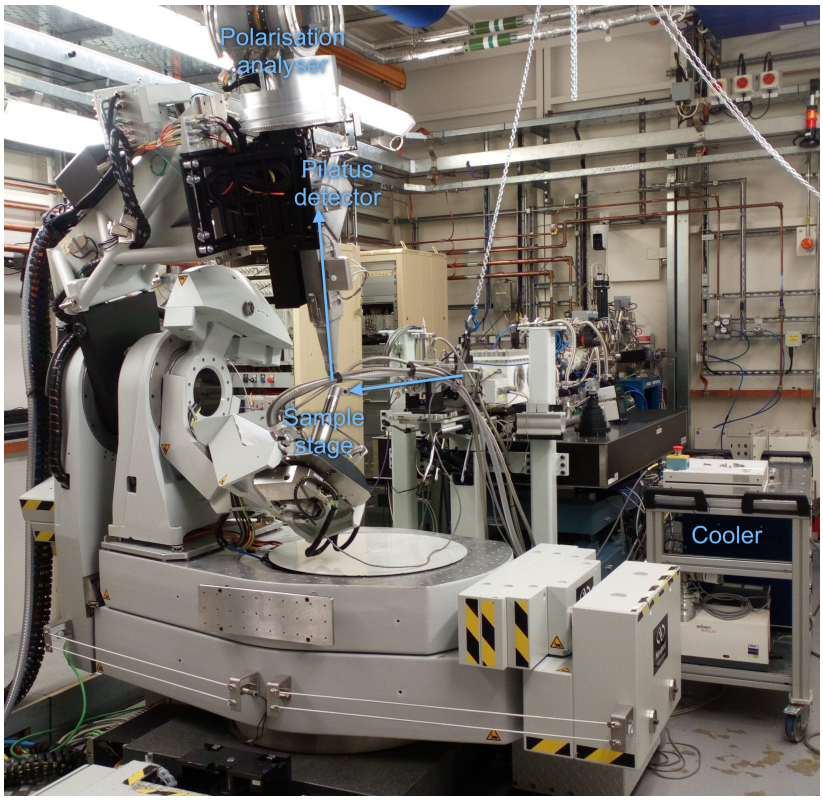

Figure 5.5: *Picture of I16 beamline during measurements.*

measurements. Though not resonant scattering, investigations into the effects of magnetic ordering on lattice parameters and distortions were performed at 15 keV. At this high energy the number of accessible reflections in reciprocal space is very high, allowing more precise measurements of charge reflection to be taken than would be possible at resonant energies.

A 70 nm thick $(0\,0\,1)$ UN thin film, SN1180, and a 200 nm thick $(0\,0\,1)$ U_2N_3 thin film, SN1431, were used for measurements.

5.2 UN

The high thermal conductivity of UN compared to UO_2, driven in large part by the electronic contribution, is one of the significant advantages of using it as a nuclear fuel. Consequently, knowledge of this electronic structure is essential to being able to understand and predict the thermal properties of UN. There is much debate in the literature

about the electronic structure of UN, particularly about the nature (localised, itinerant, or mixed) and number of the $5f$ electrons [50–58]. As these $5f$ electrons are responsible for the magnetic ordering in UN, investigations into the magnetism of UN gives great insight into the electronic structure, and is the specific focus of the present work.

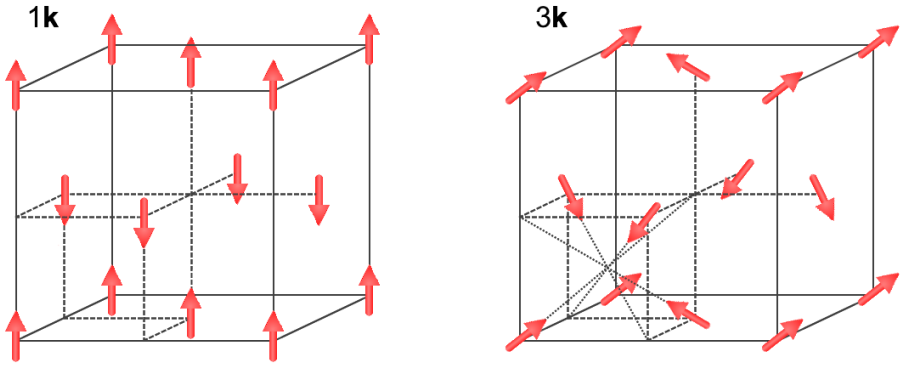

Figure 5.6: *Diagram showing type 1 antiferromagnetic 1**k** (left) and 3**k** (right) structures in a cubic system.*

UN is known to order antiferromagnetically at T_N = 53 K, as found by Curry using neutron scattering [55]. These measurements showed that the magnetic structure consists of ferromagnetic sheets of U moments arranged in a + - + - configuration.

In the simple type 1-1**k** structure, these moments are aligned to the direction of propagation, which can be any of the cubic axes. This 1**k** structure is shown in Figure 5.6 (left), with propagation vector $q = \langle 0\,0\,1 \rangle$. Considering cubic symmetry, it can be seen that **q** = $[1\,0\,0]$, **q** = $[0\,1\,0]$, and **q** = $[0\,0\,1]$ are all equivalent, and therefore 3 different domains with tetragonal symmetry are possible. It is expected that this tetragonal symmetry will cause a distortion of the cubic lattice at temperatures below T_N, with $a = b \neq c$ for a **q** = $[0\,0\,1]$ domain.

Alternatively, it is possible that the magnetic structure is the 3**k** structure shown in Figure 5.6 (right), with all moments pointing towards the nearest $(\frac{1}{4}\ \frac{1}{4}\ \frac{1}{4})$ point. This structure fits the + - + - configuration of ferromagnetic sheets description by Curry, with all domains existing in one unit cell [55]. As this structure has cubic symmetry, no lattice distortion is expected.

1**k** or 3**k**: Searching for a Tetragonal Distortion

Investigations into the magnetic structure of UN by Rossat-Mignod *et al.* found that UN had a 1**k** structure under uniaxial stress, with a tetragonal distortion of $c/a > 1$ [62]. Marples *et al.* used x-ray diffraction to determine whether the expected distortion of a 1**k** system was present in a single crystal UN sample, with a distortion of c/a = 0.99935(3) determined from the results. This $c/a < 1$ result is contradictory to that of Rossat-Mignod *et al.*. Subsequently, Knott *et al.* performed a similar study, concluding that the tetragonal distortion, if present, was smaller than reported by Marples *et al.* [61].

Though the magnetic structure of UN cannot be distinguished between a 1**k** system with 3 domains and a 3**k** system by the intensities of the reflections, these x-ray investigations into the presence of a distortion provide a possible method for determining the structure. As a distortion will change the d-spacings that are measured with XRD, reflections such as the $(0\,0\,6)$, $(6\,0\,0)$, and $(0\,6\,0)$ will shift in $|Q|$ position in a single domain, 1**k** system. If 3 domains are present in a 1**k** system, each of the $(6\,0\,0)$, $(0\,6\,0)$, and $(0\,0\,6)$ reflections will split into two peaks in $|Q|$, with an intensity ratio of 2:1, during a tetragonal distortion.

Considering the direction of **Q** for these reflections, rather than the magnitude, it is clear that there will be no change with a tetragonal distortion. However, if a reflection such as the $(5\,5\,5)$ is considered, there will be no relative shift in $|Q|$, but the **Q** directions of these reflections will change. These changes will cause a splitting the reflection in a transverse scan taken perpendicular to **Q**. In practice, the magnitude of the tetragonal distortion and resolution of the measurement may limit the ability to detect peak splitting in both the magnitude and direction of **Q**, with only a broadening of the peaks measured instead.

5.2.1 Magnetic Scattering Results

The results of resonant x-ray magnetic scattering (RXMS) of a $(0\,0\,1)$ UN thin film, taken at the U M_4 edge, are displayed here. Figure 5.7 shows the RXMS results from nine different magnetic reflections, all related by the known magnetic wave-vector of q = $\langle 0\,0\,1\rangle$. With all possible q = $\langle 0\,0\,1\rangle$ magnetic reflections that could be accessed, no absences were found, showing moments in the $[1\,0\,0]$, $[0\,1\,0]$, and $[0\,0\,1]$ directions. This supports the theory that the

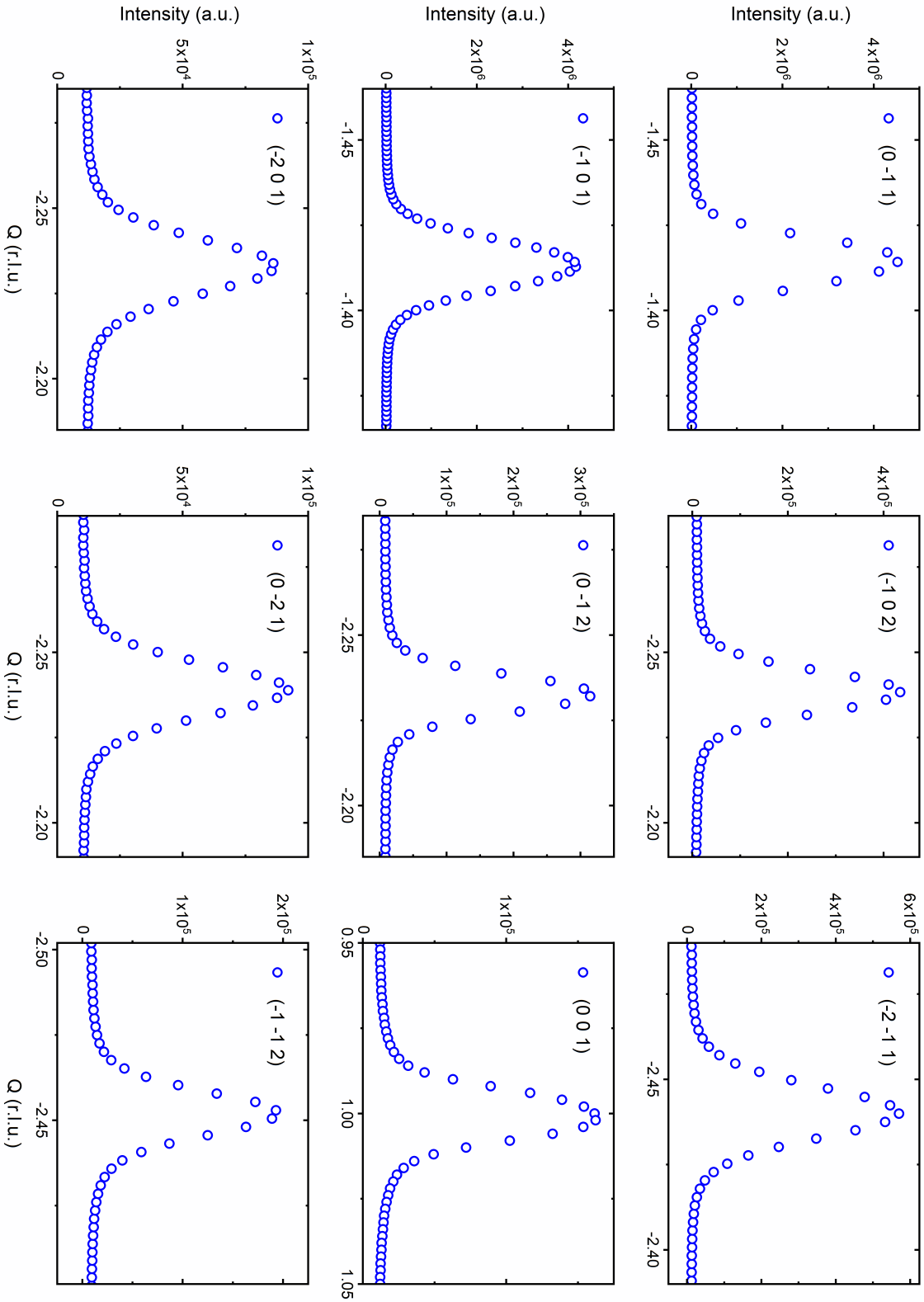

Figure 5.7: *Q scans of magnetic reflections of UN at 10 K, showing magnetic moments in the* [1 0 0], [0 1 0], *and* [0 0 1] *directions.*

$(0\,0\,1)$ UN thin film is either an AF 1**k** system with 3 domains, or an AF 3**k** system.

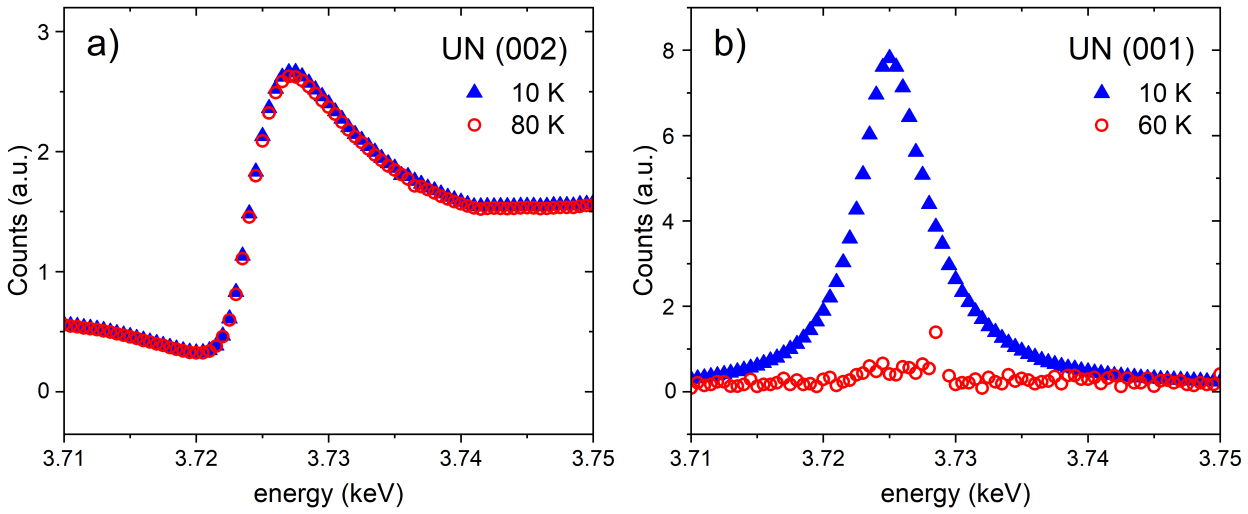

Figure 5.8: *Energy scans of the UN* $(0\,0\,2)$ *and* $(0\,0\,1)$ *reflections shown with red circles and blue triangles for above and below* T_N*, respectively.*

The energy dependence of the $(0\,0\,1)$ and $(0\,0\,2)$ reflections above and below T_N is shown in Figure 5.8. Comparing this figure to Figure 5.1, the calculated real and imaginary parts of the dispersion corrections to the atomic form factor, it can be seen that the energy dependence of the $(0\,0\,2)$ reflection has the same shape as the real part, f'. This is true both above and below T_N, showing that it is a charge reflection. Conversely, the $(0\,0\,1)$ reflection shows the shape of the imaginary part of the dispersion correction, f'', below T_N, with no peak present above T_N. This is the result expected of a magnetic reflection, as the magnetic scattering can be represented by a complex quantity, and therefore couples to the f'' term of the form factor [154].

The value of T_N and the critical exponent, β, for the phase transition of the UN thin film was determined by fitting the data displayed in Figure 5.9. As the magnetic scattering cross-section is proportional to the square of the magnetisation, M, as shown in Equation 5.11, the square root of the intensity (total peak area) is plotted against reduced temperature, t, giving

$$M \propto \sqrt{intensity} \propto t^{\beta} \quad with \quad t = \frac{T_N - T}{T_N} \tag{5.23}$$

Fitting this equation to the high T values shown in Figure 5.9, a T_N of 45.8±0.3 K and critical exponent of β =

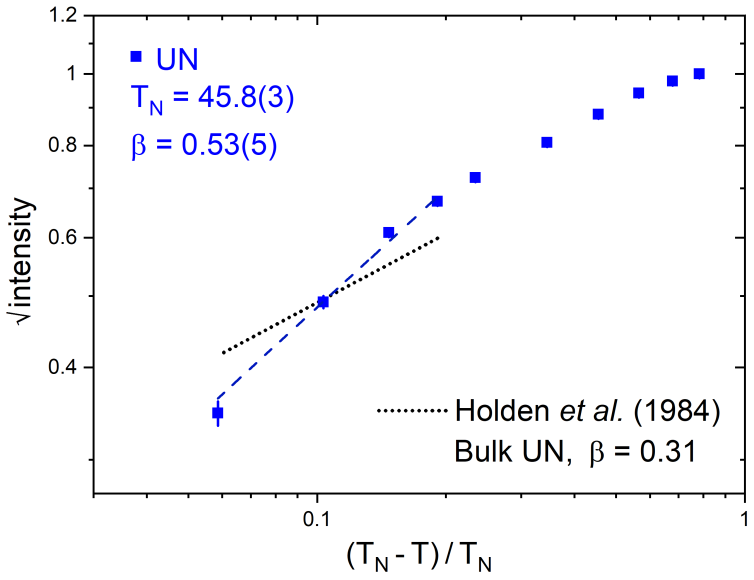

Figure 5.9: *Plot of square root of intensity of* $(0\,0\,1)$ *magnetic peak of UN against reduced temperature. The linear fit to the high temperature values is shown with the blue dashed line, data from Holden et al. on bulk UN is shown with a dotted black line for comparison [10].*

0.53±0.05 were found. For comparison, the β = 0.31 value obtained by Holden *et al.* from experiment on bulk UN is also displayed.

Figure 5.10 shows the lattice parameters calculated from Q scans of the specular reflections as a function of temperature, together with relative widths, $\Delta d/d$. All the reflections taken at 15 keV (shown with squares) were found to be in good agreement, as expected. However, lattice parameters measured at the resonant energy (shown with circles) are greater, due to refraction effects [159]. These effects are normally small, but we have the unusual case of using relatively long wavelength x-rays, λ = 3.327 Å, at the U M_4 resonant edge, and the electron density of the UN film, n_e = 3.41 electrons/Å^3, being high because of the U content.

For specular type reflections Greenberg has shown that Braggs law can be re-written to take into account refraction effects as

$$\lambda = 2d\,sin\theta(1 - \delta/sin^2\theta'), \tag{5.24}$$

where δ is the correction to the refractive index, as detailed in Equation 4.31, defined as $n = 1 - \delta$, assuming $n = 1$ in

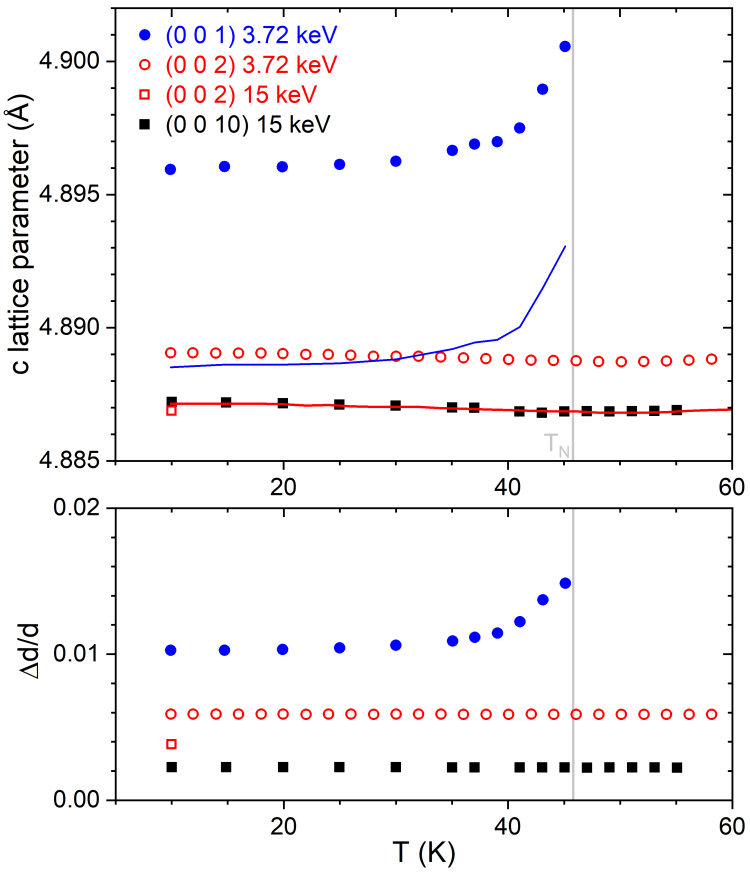

Figure 5.10: *Calculated lattice parameter (top) and d spacing spread (bottom) of* $(0\,0\,1)$ *magnetic peak, shown in blue, and* $(0\,0\,2)$ *and* $(0\,0\,1\,0)$ *charge peaks, shown in red and black. Data taken at 3.72 keV is represented by circles and data taken at 15 keV is represented by squares. Refraction corrected data taken at 3.72 keV are shown with solid lines.*

vacuum [160]. Due to the miscut in the UN film, what we consider 'specular' reflections are actually at a small angle away from the surface normal, and so the value θ' used in this refraction correction is the calculated angle between the incident beam and sample surface.

From $\delta = r_0\lambda^2 n_e/(2\pi)$, where r_0 is the Thomson scattering length, a value of δ = 1.7×10^{-4} was calculated for the UN film. This value has been used to perform refraction corrections on the reflections measured at resonant energy, with the results displayed in Figure 5.10 as solid lines. These results show that the refraction corrected lattice parameter from the $(0\,0\,2)$ reflection at resonant energy (shown in red) is in good agreement with the values obtained at 15 keV. However, the corrected results from the $(0\,0\,1)$ magnetic reflection are still higher than expected. These refraction effects are much

more significant for low incidence angle reflections, such as the $(0\,0\,1)$, as the effect is proportional to $1/sin^2\theta$, which implies that the effect for the $(0\,0\,1)$ reflection is ~ 4 times more pronounced than for the $(0\,0\,2)$. This discrepancy is likely due to the uncertainty in determining the angle between the incident beam and sample surface.

This position of this $(0\,0\,1)$ magnetic reflection shows changes with temperature very different to that of the $(0\,0\,2)$ and $(0\,0\,10)$ charge reflections, in position and width. While the charge reflections show a small decrease in effective c lattice parameter as temperature increases towards T_N, the magnetic reflection shows a large increase. This shift cannot be due to refraction effects as the wavelength does not change in these measurements. This is accompanied by a systematic increase in the width of the $(0\,0\,1)$ reflection, as shown in the lower panel of Figure 5.10.

5.2.2 Structural Investigation Results

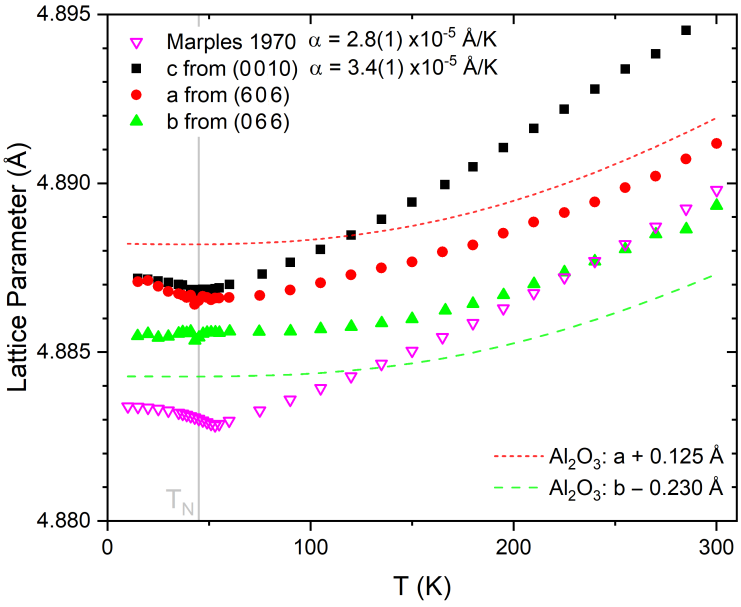

Figure 5.11: *Lattice parameters of UN film calculated from different Bragg reflections of the UN film. Data from Marples (1970) on bulk UN power is shown with pink triangles for comparison [11]. The linear thermal expansion coefficient, α, of the UN c parameter and Marples data is shown. Lattice parameters of Al_2O_3 substrate in the a and b directions of the film are shown by dashed lines, calculated from [12].*

Investigations into the presence of a lattice distortion in the UN film below T_N were performed with a 15 keV energy

x-ray beam, allowing high Q reflections to be accessed. Figure 5.11 shows the variation of the lattice parameters in the UN film as a function of temperature. The c lattice parameters (black squares) were calculated using the $(0\,0\,10)$ reflection, while a (red circles) and b (green triangles) were calculated using the $(0\,0\,10)$ reflection and the $(6\,0\,6)$ and $(0\,6\,6)$ reflection, respectively. For comparison, the values given by Marples (1970), measured from a polycrystalline sample, are shown as inverted pink triangles [11].

From this figure, it can be seen that at high T the UN film is slightly expanded by ~ 0.004 Å in the c direction. From the a and b lattice components we can see that the film is under tensile strain, with the c growth axis larger than the mean of the in-plane parameters. The lattice linear expansion coefficient (α) from 70 to 300 K is slightly higher for the c lattice parameter than that reported by Marples, though both clearly follow a linear trend [11]. Conversely, the a and b lattice parameters show similar expansion behaviour to the substrate lattice parameters in their respective directions (indicated by dashed lines in the figure), which is smaller than that of UN. These effective lattice parameters for the substrate were calculated using the epitaxial relationship described in Section 4.3, and have been shifted by 0.125 and -0.230 Å for a and b, respectively, in Figure 5.11.

The behaviour of the UN lattice parameters shows a significant change around the AF ordering temperature, T_N, with the lattice increasing with decreasing T. Both the a and c lattice parameters of the UN film show this behaviour, however, the b parameter does not. As at higher T, the behaviour of the b lattice parameter is very similar to that of the underlying substrate, showing little change below T_N. The T_N found for the UN film (45.8 K) was different to that of Marples (1970), and therefore this change in lattice expansion behaviour is seen at a different T value.

Figure 5.12 focuses on the expansion in the UN lattice as the material undergoes AF ordering. The values obtained for the c lattice parameter in the present work are compared to the data of previous studies data from previous studies [11, 13–15]. Apart from Marples (1970), all studies were performed on single crystals. The results of van Doorn *et al.* and Shrestha *et al.* were obtained using strain-gauge techniques, while the others used x-ray techniques. Above T_N, all results have a similar gradient, showing similar linear expansion coefficient. However, below T_N the lattice expansion varies greatly between different samples, with a factor of 3 difference between the smallest and largest expansion.

The relative widths of the d-spacings of the $(0\,0\,10)$ and $(5\,5\,5)$ reflections are displayed in Figure 5.13 with black

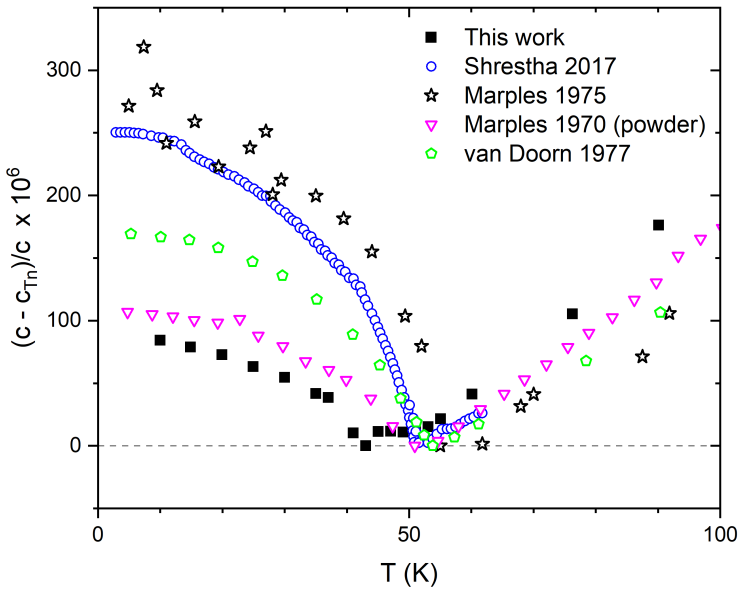

Figure 5.12: *Comparison of literature data on relative lattice expansion of UN below T_N. Data from [11, 13–15].*

squares and blue triangles, respectively. Graph a) shows a comparison of the relative broadening above T_N, showing that the broadening seen by Marples *et al.* in the $(0\,0\,6)$ reflection from a single crystal UN sample is an order of magnitude greater than found in the $(0\,0\,10)$ reflection in this work. Furthermore, the $(5\,5\,5)$ reflection was found to decrease in relative width.

A close-up of the results from the present work is shown in Figure 5.13 b), with the calculated in-plane component of the $(5\,5\,5)$ reflection shown with open blue triangles. This in-plane component of the $(5\,5\,5)$ relative width further shows the relative narrowing of the spread of the in-plane d-spacing, opposite to the behaviour seen from the out-of-plane $(0\,0\,10)$ reflection. While the width from the $(0\,0\,10)$ reflection is expected to increase with a tetragonal distortion (as expected from a 1**k** AF system with all three possible domains present), the $(5\,5\,5)$ reflection is expected to show no change.

Further considering this possible tetragonal distortion below T_N, its effects on the change in the relative width of the d-spacing measured in the UN film have been simulated. The relative broadening caused by tetragonal distortions of increasing proportions have been analytically calculated, with the results shown with black circles in Figure 5.14 a). These values have been fitted with a quadratic, displayed with a solid red line, with the close fit showing that no

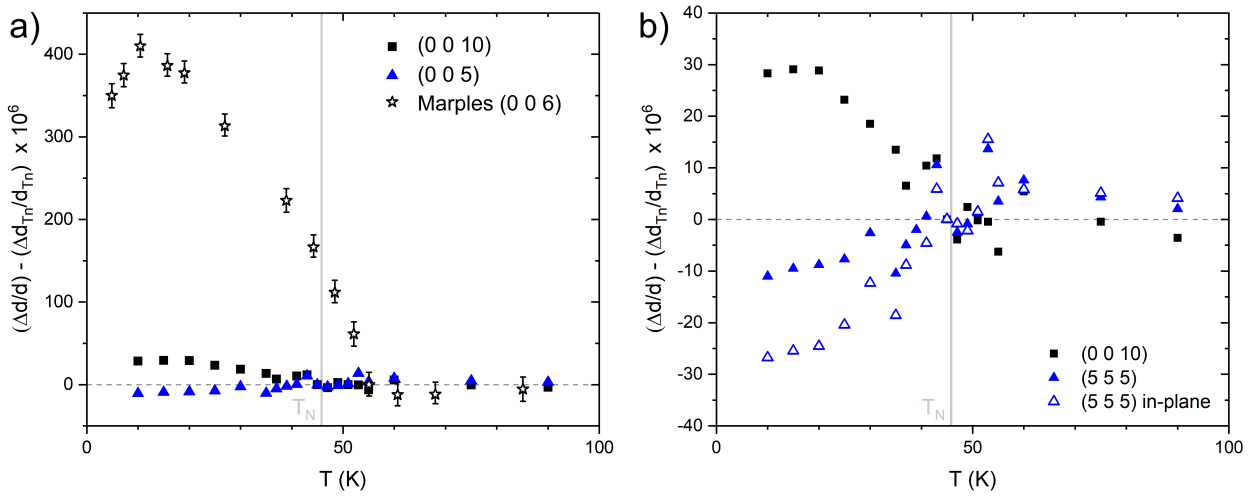

Figure 5.13: *a) Relative FWHM of* $(0\,0\,10)$ *(black squares) and* $(0\,0\,5)$ *(closed blue triangles) Bragg reflections of UN as a function of temperature, with data obtained by Marples et al. shown with stars [14]. b) Close-up of data shown in a), with calculated component of* $(0\,0\,5)$ *reflection in the plane of the film shown with open blue triangles.*

peak splitting or asymmetry would be expected from a tetragonal distortion in the UN thin film sample. Using these simulation results and the measured increase in relative width of the $(0\,0\,10)$ reflection, an upper limit of $|c/a - 1|$ = 2.3×10^{-4} can be placed on any possible tetragonal distortion in the UN thin film sample. This is almost a third of the value of 6.5×10^{-4} given by Marples *et al.* [14].

The value for the tetragonal distortion given by Marples *et al.* was calculated based on the broadening of the $(0\,0\,6)$ reflection, but unfortunately Marples *et al.* did not display the 2θ scan of this $(0\,0\,6)$ reflection. As it is known that these measurements were taken using a CuKα source and the peak width of the $(0\,0\,6)$ reflection was stated to be 0.28 °, it is possible to simulate the 2θ scan that would be expected with this tetragonal distortion. The results of this simulation are displayed in Figure 5.14 b). This clearly shows that the peak is split into CuKα_1 and CuKα_2 components and that each of these components show an obvious asymmetry due to the relative change of a and c components with a 2 to 1 ratio. It should be noted that Marples *et al.* give no mention of any asymmetry in their results.

To further investigate this possible tetragonal distortion, transverse scans taken perpendicular to the direction of **Q** were also performed on the $(5\,5\,5)$ reflection, with the results displayed as blue triangles in Figure 5.15. These results show no change in the transverse width of the $(5\,5\,5)$ reflection as a function of temperature, within errors. Using the

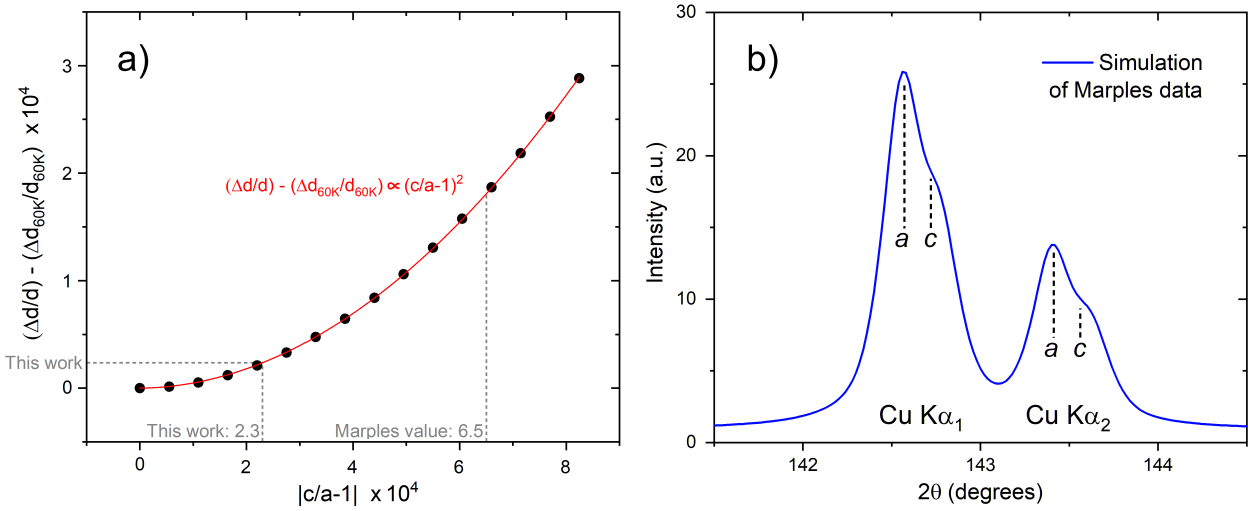

Figure 5.14: *a) Simulated relative change in FWHM of d spacing as a function of magnitude of tetragonal distortion, fitted with a quadratic curve shown in red. b) Simulation of the 2θ scan using a CuKα source expected from the tetragonal distortion calculated by Marples et al. (1975) [14].* $(6\,0\,0)$ *and* $(0\,6\,0)$ *reflections are labeled with a and* $(0\,0\,6)$ *reflections are labeled with c.*

upper limit of any possible tetragonal distortion in the UN film obtained from Figure 5.14 a), the expected broadening in the $(5\,5\,5)$ reflection was calculated, shown as a green circle. This value is well within the errors of the measurements, showing that resolution is too low to determine if this broadening is present.

A similar calculation was performed using magnitude of the distortion given by Marples *et al.*, shown as a red open circle. The broadening expected from this distortion is large enough to be resolved in the present measurements. Additionally, with the FWHM of 0.56 ° given by Marples *et al.* being lower than the 1.73 ° for the present UN thin film sample, this broadening would be more easily resolvable, however, no measurement of the kind was performed.

5.2.3 Discussion

Resonant x-ray magnetic scattering result from the $(0\,0\,1)$ UN thin film sample show antiferromagnetic order with a T_N of 45.8(3) K. The slight orthorhombic strain on the UN lattice shown in Figure 5.11 might be expected to induce a single 1**k** domain in the film, however, this was not found to be the case. Instead, ten different magnetic reflections, all related by the magnetic wave-vector $q = \langle 0\,0\,1 \rangle$, were found without absences. This result is possible with both a 1**k** structure

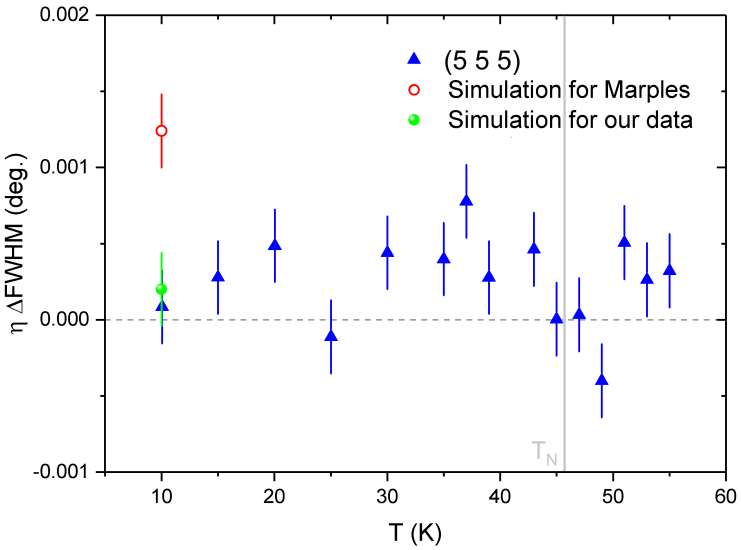

Figure 5.15: *Change in FWHM of transverse scan of UN* $(5\,5\,5)$ *reflection as a function of temperature, with the simulated change due to the maximum possible tetragonal distortion shown in green for the present data and red for the distortion calculated by Marples et al. [14].*

with three domains and a 3**k** structure.

In theory, it is possible to determine the relative domain population from the intensities of the magnetic reflections. Unequal domain population would only be possible in a 1**k** system, therefore proving the magnetic structure. In practice, these calculations are complicated as the observed intensities depend greatly on the large absorption and are not related directly to the value of the magnetic moment [154]. At the U M_4 edge (3.726 keV) in UO_2, absorption can reach values of $\sim 5\times10^4\,\mathrm{cm}^{-1}$, corresponding to a 1/e attenuation length of $\sim$150 nm in UN [161]. With a film thickness of 70 nm, some of the beam will pass through the film at this energy, but the absorption will depend greatly on the precise geometry, making corrections challenging. It should be noted that there is yet to be a report published in which quantitative analysis of the intensities of magnetic reflections at the U M_4 edge has been performed.

These high absorption levels on resonance are also relevant when considering the energy scan of magnetic reflection such as the $(0\,0\,1)$. When scanning energy over an absorption edge, as the attenuation length decreases, the volume of sample contributing to the scattering decreases. For a uniform bulk sample, this will have no effect on the measured scattering, however, for a film with a thickness similar to the attenuation length, the ratio of film to substrate sampled

will change as a function of energy. Work by Bernhoeft *et al.* showed that this effect gives an indication of the spatial location of the magnetic ordering below the film surface, with a single symmetric peak expected for a uniform AF film at the sample surface [162]. Bernhoeft *et al.* related this phenomenon to the FWHM of the energy scans of magnetic reflections [162]. Comparing to these results, it can be seen that the highly symmetric energy curve with a FWHM of $\sim$6 eV found here is typical of thin films and shows that the UN film is ordered throughout its depth.

The value of critical exponent determined for this AF transition from the $(0\,0\,1)$ reflection was β = 0.53$\pm$0.05, much larger than the value of 0.31$\pm$0.03 obtained by Holden *et al.* for bulk UN. Work on a similar bulk rocksalt uranium compound, USb, gave a similar value of 0.32$\pm$0.02 [163]. This differs greatly from the result obtained here, however, it is not unusual for thin film values to vary greatly from those found in bulk. For example, work by Bao *et al.* found β values of 0.43 and 0.22 for thick and thin epitaxial UO_2 films with a 2^{nd}-order phase transition, whereas bulk UO_2 has a 1^{st}-order transition at T_N [148].

Investigations into the position of the $(0\,0\,1)$ magnetic reflection as a function of temperature found significant differences to the charge peaks, with a shift towards higher lattice parameter values near T_N. This behaviour was mirrored in the broadening of this peak towards T_N, showing the decreasing correlation length in the magnetic ordering. The shift in $(0\,0\,1)$ position is more challenging to understand, and cannot be attributed to the magnetic structure becoming incommensurate with the crystal lattice as this would produce two peaks, symmetric about the expected position (one at $(0\,0\,0)$ + **q** and one at $(0\,0\,2)$ - **q**), which was not found to be the case.

This unusual effect has been observed at the U M_4 edge before by Bernhoeft *et al.* with the compounds UO_2, UPd_2Al_3, and URu_2Si_2 [164]. In particular, the behaviour of URu_2Si_2 is very similar to that of UN presented here. Bernhoeft *et al.* propose a somewhat complicated explanation of this effect, attributing the shift to Berry phase [164,165]. This effect has also been observed in USb and MnF_2 with neutrons by Prokes *et al.*, demonstrating that the effect is not related to the surface of the sample, nor is it a property unique to actinide compounds [166].

Considering the effects of the magnetic transition on the structure of UN, it can be seen from Figure 5.12 that the magnitude of the lattice expansion below T_N varies with the form of the sample. This shows that it is not a true bulk property, as it varies by almost a factor of three between different samples, contrasting with the very similar behaviour seen above T_N. A study by Shrestha *et al.* showed that this expansion may be partially suppressed by the application of

a magnetic field ($\sim$10 T), although no explanation for this behaviour is given [13].

Assessing the possible tetragonal distortion cause by a 1**k** structure, it was found that peak broadening of the $(0\,0\,10)$ reflection put an upper limit of $|c/a - 1| = 2.3\times10^{-4}$ on the magnitude of any distortion in the UN thin film sample. This is lower than the value given by Marples of 6.5×10^{-4}. Knott *et al.* also performed a similar experiment with a UN single crystal, obtaining a value of 3×10^{-4}. As with the varying lattice expansions below T_N, these inconsistent results are likely to be due to the form of the sample, rather than true bulk properties.

Simulations of the diffraction results expected from a tetragonal distortion of the magnitude given by Marples *et al.* showed a clear asymmetry that was not reported, and it is fair to assume not present, in the results given by Marples *et al.* [14]. For this to be the case, there must be another cause of broadening in their results, likely to be strain. Comparing to the results presented here, the 10 times smaller broadening in the $(0\,0\,10)$ and narrowing in the $(5\,5\,5)$ are indicative of strain effects, with the strain along the c axis (growth direction) of the film increasing, while the corresponding in-plane strain compensates by decreasing. This is clearly a complicated effect, driven by the film-substrate interaction, but it gives no support to the idea of a tetragonal distortion in UN.

This shows that a tetragonal distortion and 1**k** structure, though they cannot be ruled out, are certainly not proven. It is therefore possible that the true state of the magnetic configuration in UN is a type-1 3**k** structure, where a tetragonal distortion would not be expected. The only way to distinguish between these two possibilities is by analysis of the polarisation of spin waves, which involves a complicated inelastic neutron experiment that has previously only been performed on UO_2 and USb, which were both found to be 3**k** systems [167, 168].

5.3 U_2N_3

In comparison to UN, very little is known about the magnetic properties of U_2N_3 and higher stoichiometry compounds. Troć reported that the AF ordering temperature varies as a function of the U:N ratio between from 94 K for $UN_{1.55}$ to 20 K for $UN_{1.72}$, as shown in Figure 5.16 [16]. The type of this AF ordering, however, remains unknown.

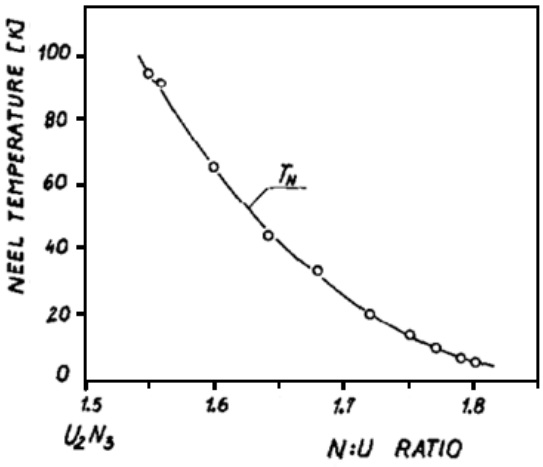

Figure 5.16: *Effect of stoichiometry of U_2N_3 on AF ordering temperature, as reported by Troć [16].*

5.3.1 Magnetic Scattering Results

The RXMS results from six different magnetic reflections from the $(0\,0\,1)$ U_2N_3 thin film sample are displayed in Figure 5.17. These reflections all appear in positions in which $h + k + l$ = odd, i.e. they do not overlap with the charge reflections from the b.c.c. structure where the $h + k + l$ = even. This is evidence that the magnetic ordering wave-vector of the U_2N_3 thin film is $q = \langle 0\,0\,1 \rangle$.

The changes in lattice parameter and peak width from the $(0\,0\,3)$ magnetic reflection as a function of temperature are displayed in Figure 5.18. The effective lattice parameter, shown in red with axis on the left, shows some fluctuations, however, there is no significant trend as a function of temperature, with the changes shown likely to be due only to uncertainty in measurement. Conversely, the width of this peak, shown in blue with axis on the right, shows a small decrease before increasing towards T_N.

The normalised square root of the intensity of the $(0\,0\,3)$ magnetic reflection (which is proportional to the ordered moment) is plotted as a function of reduced temperature, t, in Figure 5.19. The high temperature values in this plot showed a very good fit to $\sqrt{intensity} \propto t^{\beta}$, with T_N found to be 73.5$\pm$0.2 K and the critical exponent found to be β = 0.42$\pm$0.02.

Polarisation analysis was used to determine the type of the reflections found along the specular direction, with results shown in Figure 5.20. These measurements were taken using σ radiation and a vertical scattering plane, at a temperature

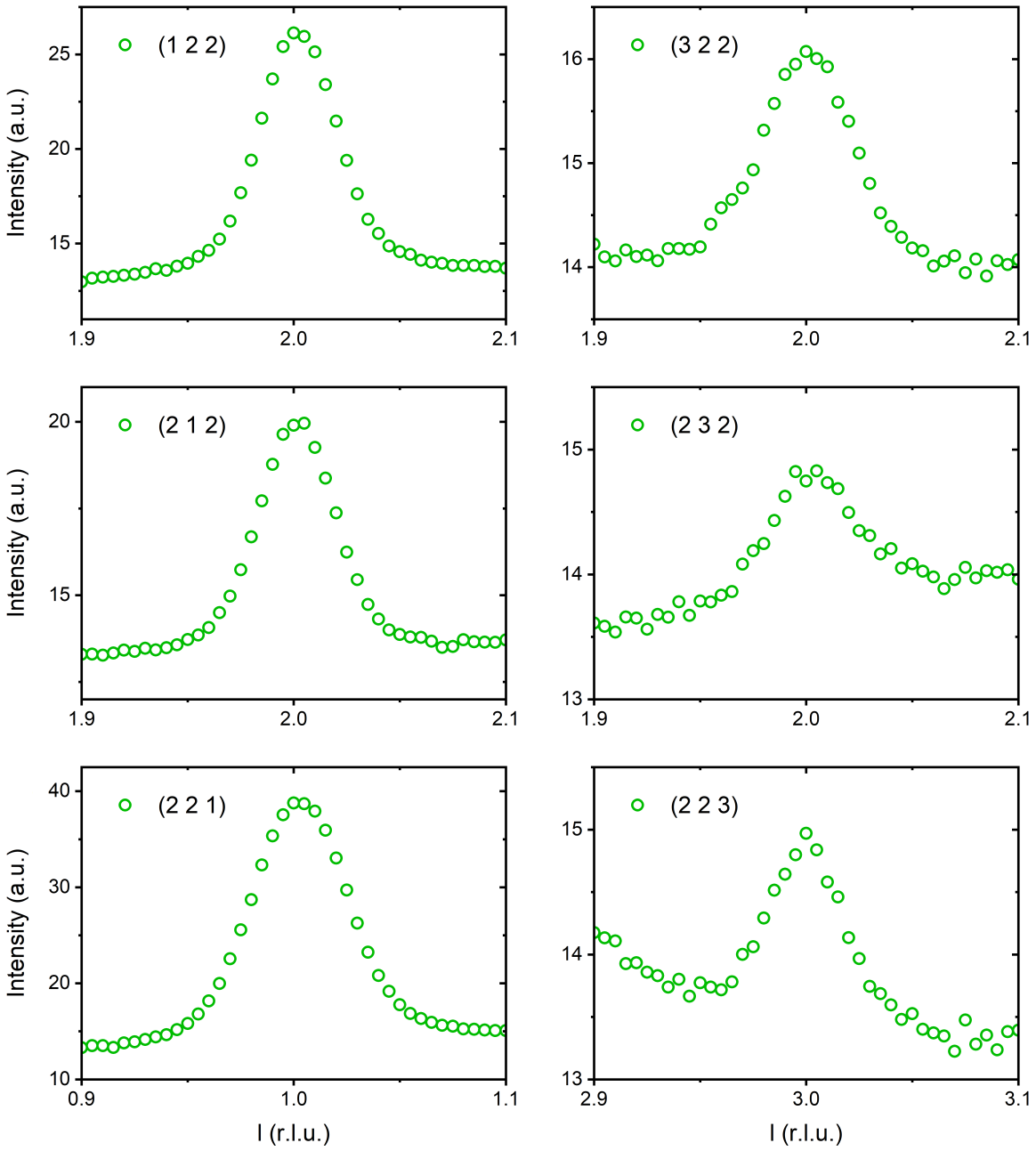

Figure 5.17: *Q scans of magnetic reflections of U_2N_3 taken at 8.5 K, showing magnetic moments in the* $[1\,0\,0]$, $[0\,1\,0]$, *and* $[0\,0\,1]$ *directions.*

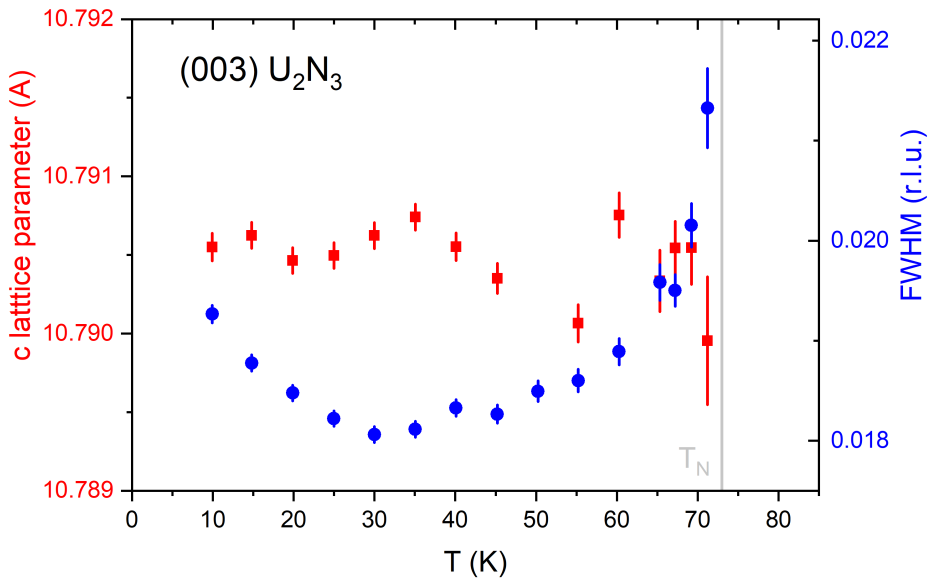

Figure 5.18: *Specular lattice parameter (red) and width (blue) of the* $(0\,0\,3)$ *magnetic reflection of* U_2N_3.

of 8.5 K, well below T_N. Rocking curves of the $(0\,0\,2)$ and $(0\,0\,4)$ reflections taken with the polarisation analyser in a $\sigma \rightarrow \sigma$ channel (blue squares) showed a clear peak, while the $\sigma \rightarrow \pi$ channel (open red circles) showed no peak. This is clear evidence that there is no rotation of the σ polarisation and the reflections are therefore charge reflections. Conversely, the rocking curve of the $(0\,0\,3)$ reflection showed a peak only in the $\sigma \rightarrow \pi$ channel, showing a 90 ° rotation of the polarisation, as expected for a magnetic peak in this experimental configuration.

Energy scans of the $(0\,0\,2)$, $(0\,0\,3)$, and $(0\,0\,4)$ reflections performed above (100 K, shown with open red circles) and below (8.5 K, shown with blue circles) the AF ordering temperature are displayed in Figure 5.21. The energy scan of the $(0\,0\,4)$ reflection shows the expected results, with the shape showing the real part of the form factor, f', both above and below T_N. The expected energy scan of a magnetic peak is found for the $(0\,0\,3)$ reflection, with a strong f'' shaped peak below T_N and no peak above T_N. Though the $(0\,0\,2)$ reflection has been shown to be a charge peak, the energy scan shows the form of f'' both above and below T_N.

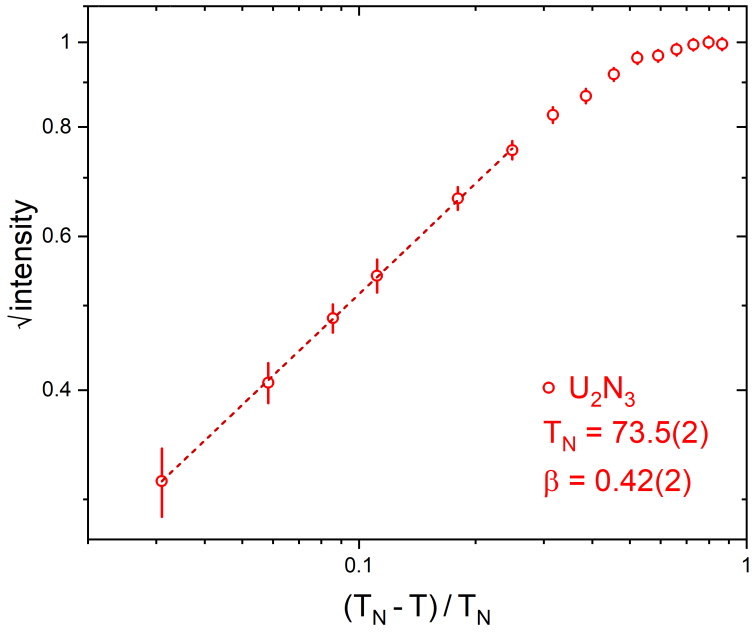

Figure 5.19: *Plot of square root of intensity of* $(0\,0\,3)$ *magnetic peak of* U_2N_3 *against reduced temperature. The linear fit to the high temperature values is shown with the red dashed line.*

5.3.2 Anisotropic Resonant Scattering Results

The resonant scattering results presented in this chapter so far have utilised the enhancement of the magnetic signal at resonance by coupling to the imaginary part of the scattering factor. However, the energy scans from the U_2N_3 sample have shown coupling to f'' even when there is no magnetic scattering. This shows that there are other factors contributing to the resonant scattering signal in U_2N_3, which are further investigated here.

To consider the contributions to resonant scattering, it is necessary to first examine the structure factors of different reflections. The U_2N_3 structure belongs to the centro-symmetric space group $Ia\bar{3}$, and has two different U sites. Eight U_1 atoms in the unit cell sit on centrosymmetric $(\frac{1}{4}\,\frac{1}{4}\,\frac{1}{4})$ etc. sites with three-fold rotational inversion symmetry (C_{3i}). Twenty-four U_2 atoms sit on sites with two-fold rotational symmetry (C_2). Considering the local configuration around each U atom, instead of a symmetric eightfold coordination of N about each U atom (as would be found for UN_2), there are only 6 for both sites. This is shown in Figure 5.22 with a slice through the U_2N_3 structure parallel to the $(0\,0\,1)$ plane, with U_1 sites in blue, U_2 sites in grey, and N in red. This diagram shows the differing U-N distances on each U

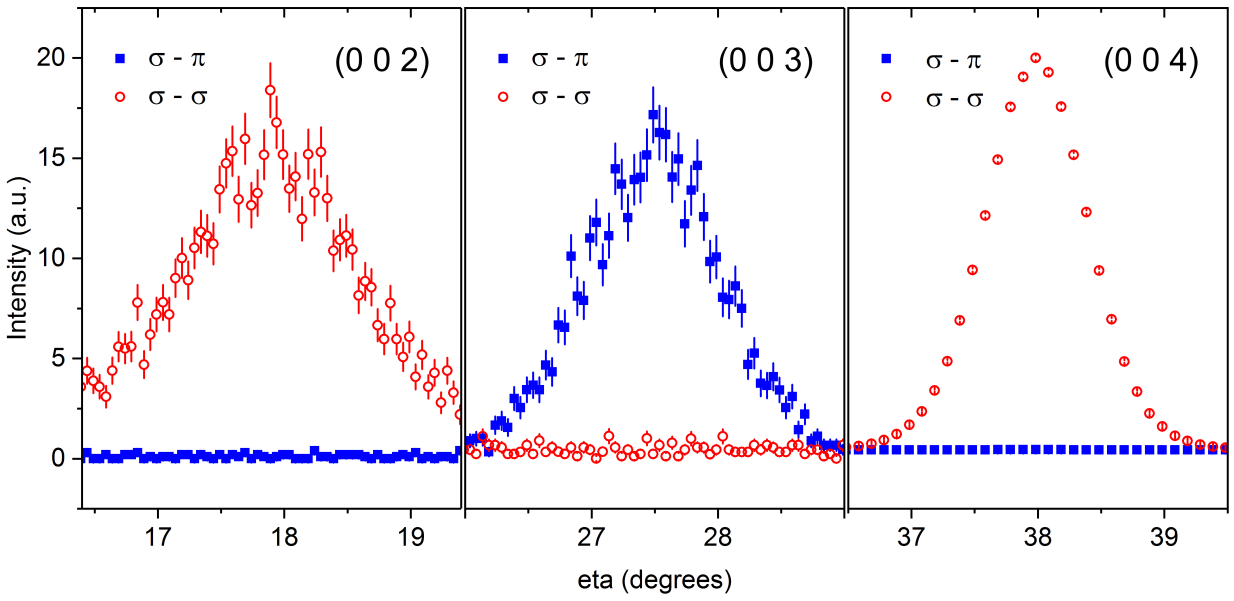

Figure 5.20: *Transverse scans of the* $(0\,0\,2)$, $(0\,0\,3)$, *and* $(0\,0\,4)$ *reflections of* U_2N_3 *taken at 8.5 K using a polarisation analyser. Closed blue squares show data taken in the* $\sigma \rightarrow \pi$ *channel, and open red circles show data taken in the* $\sigma \rightarrow \sigma$ *polarisation channel.*

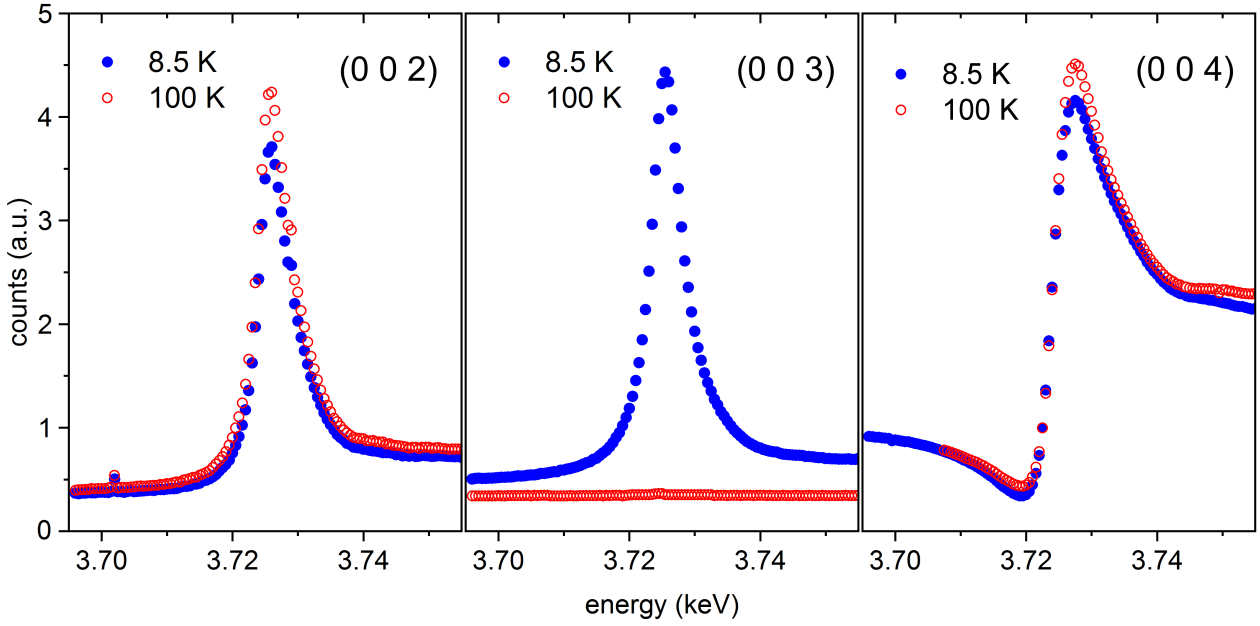

Figure 5.21: *Energy scans of the* $(0\,0\,2)$, $(0\,0\,3)$, *and* $(0\,0\,4)$ *reflections of* U_2N_3 *taken at 8.5 K, shown in blue, and 100 K, shown in red.*

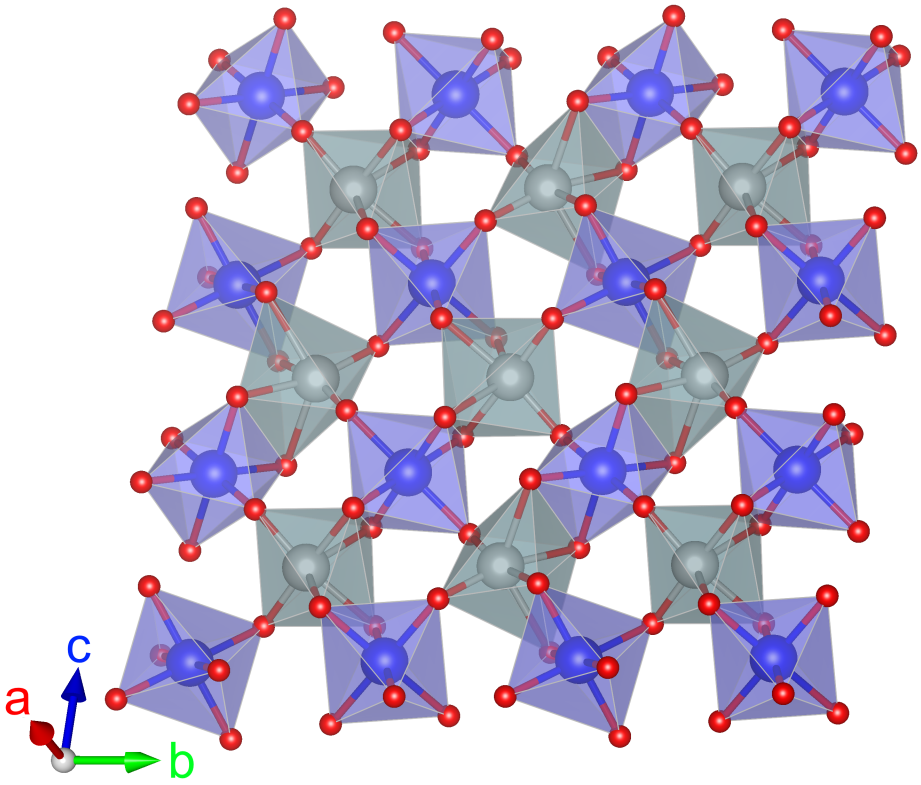

Figure 5.22: *Diagram of slice though the U_2N_3 structure parallel to the $(1\,0\,0)$ plane, showing the U_1 site in blue, U_2 site in grey, and N in red.*

site and asymmetry in U-N bond direction, i.e. the 6 N atoms around each U atom do not form a regular octahedron with the U site at the centre. This is particularly pronounced for the lower symmetry U_2 site. The lack of symmetry implies that an aspherical electron distribution may exist around both of the U sites.

There is one adjustable positional parameter x for the U_2 sites with positions $(x\,0\,\frac{1}{4})$ etc. X-ray and neutron diffraction have been used to determine the positional parameter for U_2 and the average value obtained is x = -0.02 [169, 170]. This value has been used to calculate the structure factors for U_2N_3 shown in Table 5.1. This table shows only the geometric term (not taking into account the U form factor) for the two U sites, and assumes spherical charge distributions. The 48 N atoms will contribute somewhat to the total intensity, but around the U M_4 edge this contribution will be independent of energy and can therefore be neglected. As the system is cubic, the $(h\,k\,l)$ values can be permuted.

Table 5.1: *Structure factors of the two U sites in U_2N_3, with energy dispersion shape shown under observation.*

$(h\,k\,l)$	$\lvert Q\rvert$ (Å^{-1})	SF U_1	SF U_2	Total SF	Group	Observation
(0 0 0)	0.000	8.00	24.00	32.00	A	
(1 1 0)	0.831	0.00	0.00	0.00	B	
(2 0 0)	1.176	-8.00	7.75	-0.25	C	f''
(2 1 1)	1.440	0.00	1.99	1.99	D	f'
(2 2 0)	1.662	8.00	-8.00	0.00	E	f''
(3 1 0)	1.859	0.00	0.00	0.00	B	f''
(2 2 2)	2.036	-8.00	23.25	-31.25	A	f'
(3 2 1)	2.199	0.00	-1.99	-1.99	D	
(4 0 0)	2.351	8.00	23.01	31.01	A	f'
(3 3 0)	2.494	0.00	0.00	0.00	B	
(4 1 1)	2.494	0.00	3.85	3.85	D	f'
(4 2 0)	2.494	-8.00	6.76	-1.24	C	

With the structure factors shown in Table 5.1, the reflections to be separated into 5 groups:

Group A - Structure factor from both U_1 and U_2 contribute in phase.

Group B - The reflection is forbidden.

Group C - U_1 and U_2 have different contributions, partially canceling, and would completely cancel if x = 0.

Group D - Contributions to the total structure factor from U_2 only.

Group E - The contributions from U_1 and U_2 cancel.

The results of energy scans of different reflections from the U_2N_3 sample are shown in Figure 5.23, with further results listed in Table 5.1 under 'Observation'. This shows the differences seen between reflections from different

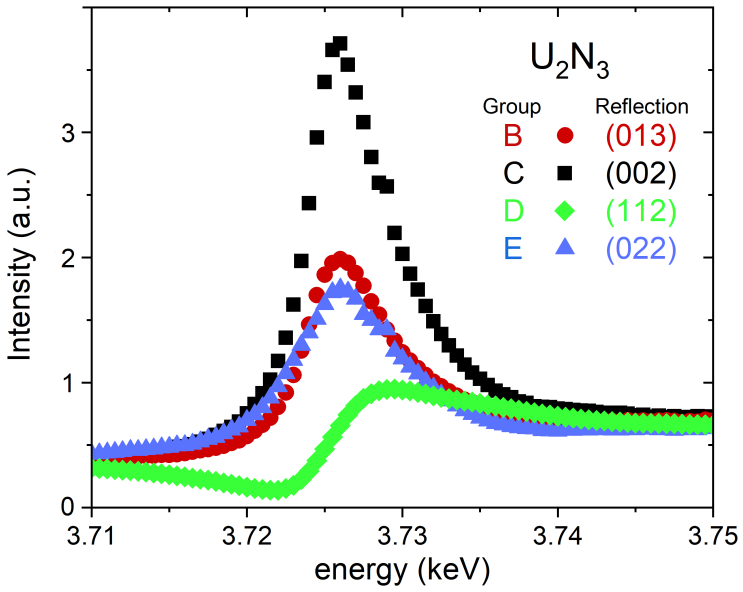

Figure 5.23: *Energy dependence of reflections of U_2N_3, showing how charge peaks vary in energy according to the groups listed in Table 5.1 and described in the text.*

groups, with the B, C, and E groups showing f'' shape, and the A and D groups showing f' shape. The f'' shape is most pronounced in group C, while B and E show very similar results.

As described in Section 5.1.4, when considering scattering from two similar but non-identical atoms, the much smaller asymmetric part cannot be resolved unless the symmetric part (the part common to both atoms) cancels. There are two case in which this occurs in the present results. Firstly in the Group B reflections, where the U_1 and U_2 scattering factors are self-canceling and secondly in the Group E reflections, where the scattering factors from U_1 and U_2 cancel each other. Consequently, it can be seen that these results show that the charge distribution around U_1 and U_2 sites are not identical, as coupling to the imaginary part of the form factor is seen for reflections in Group E and B. As reflections from Group B show results very similar to those seen for Group E in both shape and magnitude, and both have similar Q values, it suggests that one site has asymmetric charge distribution while the other has spherical or almost spherical charge distribution. As the U_1 site is the higher symmetry site in term of coordination, it is expected that the higher symmetry charge distribution is located on this site. This is evidenced by the reflections from Group D, where U_2 scattering is in phase and U_1 scattering cancels, showing the real part of the form factor. Group A reflections have both

contributions in phase and are not sensitive to the aspherical charge distribution.

5.3.3 Discussion

Investigations into the magnetic ordering of a $(0\,0\,1)$ U_2N_3 thin film sample using resonant x-ray magnetic scattering have shown that the sample orders anitferromagnetically below 73.5±0.2 K. As the U_2N_3 was found to be close to stoichiometric, this value is lower than that found by Troć for bulk U_2N_3, however, this is to be expected for a thin film [16, 148]. The magnetic wave-vector was found to be $q = \langle 0\,0\,1 \rangle$, but the magnetic structure could not be determined.

Comparing to a material that has the same bixbyite cubic structure as U_2N_3, α-Mn_2O_3 has been shown to have the same magnetic wave-vector [171]. This material was found to have a non-collinear magnetic structure, however, an orthorhombic distortion was also found which was not found in the present U_2N_3 results. Moon *et al.* found that the bixbyite structured Yb_2O_3 to have magnetic reflections for $h + k + l$ = odd, showing that the rare-earth sites related by the body-center translation have opposite moments [172]. This must also be true for the U sites related by the body-center translation in U_2N_3. Yb_2O_3 was found to have a complex non-collinear magnetic structure with the moments directed along their local symmetry axes. It is possible that U_2N_3 has a similar magnetic structure, however, as U_2N_3 and Yb_2O_3 are clearly different (Yb_2O_3 is an insulator and U_2N_3 is a semi-metal, Yb_2O_3 orders at only 2.25 K), there is no reason to expect so [172].

Analysis of the intensity of the $(0\,0\,3)$ magnetic reflection gave a critical exponent of β = 0.42±0.02. Bulk Yb_2O_3 was found to have β = 0.273 [172]. This differs greatly form the result obtained here, however, it is not unusual for thin film values to vary greatly from those found in bulk, as explained in the discussion of results from UN in Section 5.2.3.

This $(0\,0\,3)$ magnetic reflection was found to broaden in Q as T_N is approached, showing the decreasing correlation length of the AF magnetic ordering. However, unlike the RXMS from the UN film, no changes were seen in the effective lattice parameter of the magnetic reflection as a function of temperature. Similar to UN, the energy scan of the magnetic reflection is symmetric with a FWHM of ∼6 eV, showing that the U_2N_3 film is likely to be ordered throughout its depth [162].

Energy scans of charge peaks were also performed, with surprising results. Though the energy profiles of certain reflections, such as the $(0\,0\,2)$, show the f'' profile expected from a magnetic peak, the polarisation analysis in Figure

5.20 shows that they are not magnetic reflections. Furthermore, the same results are seen both above and below the ordering temperature. A magnetically-driven ordering of quadrupolar charge distribution, as found in UO_2 and NpO_2, would have a different energy dependence, and would be dependent on temperature, with no signal expected above T_N [173]. Consequently, it is can be concluded that these reflections are caused by anisotropic resonant x-ray scattering, and are evidence of the local asphericity in the charge distribution around U sites in U_2N_3 being an intrinsic property of the material.

Previously, anisotropic resonant scattering (ARS) has mainly been observed at transition metal K edges [158, 174]. This involves more complicated physics as the K edge corresponds to $1s$ to np dipole transitions, where n is the first partially filled p shell, and higher-order quadrupole transitions involving the d shells can also contribute. In the present case, it can be said that the aspherical part of the electron density involves only the $5f$ electrons since the effect is observed at the U M_4 edge. No comparable observations involving $5f$ electrons have been reported previously.

As the $5f$ electrons are involved in chemical bonding, the ARS results showing differences between the $5f$ electron density on the U_1 and U_2 sites are direct evidence of the different chemical bonding on these two sites. Furthermore, it is probable that the aspherical charge distribution, likely to be on the U_2 site, is related to the hybridization between the U $5f$ states and the N $2p$ states.

5.4 Conclusion

Resonant x-ray magnetic scattering investigations of a $(0\,0\,1)$ UN thin film found it to have antiferromagnetic ordering with a wave-vector of $q = \langle 0\,0\,1\rangle$ below 45.8±0.3 K. Neither a single 1**k** domain nor the tetragonal distortion expected from a type 1-1**k** structure were found, instead finding complicated strain effects likely caused by the epitaxial strains as UN expands below T_N. A Comparison of literature has shown that sample form clearly has a significant effect on lattice expansion and strain. Consequently, it has been concluded that the previously accepted 1**k** magnetic structure of UN is not certain, and there is no evidence against UN having a 3**k** structure.

Of the few theoretical calculations of the electronic structure of UN that have been performed, none reproduce the correct magnetic moment or determine the antiferromagnetic ground-state [175, 176]. With this being an excellent test

as to whether the calculated electronic structure is a true representation of the material, knowing if UN is a 1**k** or 3**k** system is important for improving understanding of its electronic structure.

Anisotropic resonant scattering from a U_2N_3 showed evidence of the different chemical bonding on the two U sites. This mixed bonding provides an explanation for the broadening seen in the U-4f spectra presented in Section 4.2.1.4. This is the first time such measurements have been performed on an actinide. The observation made here may be a widespread property of actinide compounds, however, observation requires the special conditions afforded by forbidden reflections, such as are found for the U_2N_3 structure.

As chemical differences have been found between the two U sites in U_2N_3, it raises the question of whether these two sites have also have different magnetic properties. The results presented here have for the first time determined the magnetic ordering wave-vector of U_2N_3 to be $q = \langle 0\,0\,1 \rangle$, however the magnetic structure is yet to be resolved. An investigation into the magnetic structure of U_2N_3 using neutron scattering could answer both of these questions.

Chapter 6

Oxidation of UN

An investigation into the oxidised surface of UN is presented in this chapter. A review of the literature shows that low temperature oxidation and the oxidation mechanism is not well understood. Consequently, the work presented here has used a combination of chemical and structural investigation of the ideal surface of an epitaxial $(0\,0\,1)$ *UN thin film to investigate the composition of the oxidised surface as a function of depth and the evolution of this oxide layer with time.*

6.1 The Oxidation of UN

The oxidation of UN is one of the main concerns when considering UN as a potential nuclear fuel, as it may have adverse consequences throughout the fuel cycle. Oxidation during manufacture or use of a UN fuel pellet can cause a loss of structural integrity of a fuel pellet, destroying the microstructure that is responsible for the retention of fission products. This loss of this structural integrity can be a significant hazard to fuel performance as well nuclear safety, as it plays a vital role in the thermal conductivity and mechanical properties of the fuel. Furthermore, the expansion of of the U-lattice that occurs during oxidation of UN may lead to the rupture of cladding, causing fission product release. This is

also a concern during the storage of spent fuel, where these fission products may then be releases into the environment. Consequently, it is of great importance to be able to understand, predict, and control this reaction.

Investigations into the oxidation of UN have historically focused on the oxidation rates of bulk powder samples as a function of temperature and atmospheric composition. Paljevic *et al.*, Rama Rao *et al.*, and Dell *et al.* found that oxidation occurs above 200 °C and ignition (rapid oxidation) occurs above 270 °C, with some dependence on specific surface area, mass, and geometry [44, 85, 86]. These experiments found that the reaction proceeded until all UN was reacted, resulting in the formation of UO_2 at 200 °C and UO_3N_x at higher temperatures.

6.1.1 U_2N_3 Interlayer

Using x-ray diffraction, Dell *et al.* showed that a U_2N_3 intermediate layer formed between the UN and the oxidation product, UO_2, finding that this was as a result of free N that was released during oxidation, and not molecular N_2 [44].

Sole *et al.* further investigated the U_2N_3 interlayer using transmission electron microscopy on a single crystal UN foil at temperatures above 600 °C. Sole *et al.* found that U_2N_3 grows epitaxially on $(0\,0\,1)$ surfaces, with the relation $\langle 0\,0\,1\rangle_{UN} \,||\, \langle 0\,0\,1\rangle_{U2N3} \,||\, \langle 0\,0\,1\rangle_{UO2}$ [63]. This is possible because half the lattice parameter of U_2N_3 is intermediate between the lattice parameters of UN and UO_2, allowing these layers to form with a gradual expansion of the underlying f.c.c. U lattice. Though this was found to be the case for a single crystal sample, the work by Paljevic *et al.* and Rama Rao *et al.*, which was performed on powder samples, found the U_2N_3 layer formed during oxidation to be weakly crystalline, suggesting that epitaxial oxidation is not as prevalent for polycrystalline UN [85, 86].

With these investigations focusing on high temperature oxidation, it is not known whether this U_2N_3 interlayer also forms at lower temperatures. Furthermore, evidence of this layer is based only on structural characterisation, with no chemical analysis performed.

6.1.2 Oxidation Mechanism

The work of Rama Rao *et al.* focused on the mechanism of the oxidation of UN and subsequent formation of the U_2N_3 interlayer, describing how initial oxidation of the UN surface produces UO_{2+x} and N, as described in the equation

below [86].

$$2\,UN + (2+x)\,O_2 \rightarrow 2\,UO_{2+x} + N_2 \tag{6.1}$$

O_2 is then chemisorbed onto the UO_2 surface, where a potential gradient causes the O to diffuse towards the UN / UO_2 interface. As the UN is further oxidised by this O, N is released, which will diffuse into both the UO_2 and UN, where it will either react with N to form N_2, or react with the bulk.

In the UN, the following reactions will take place:

$$2\,UN + N \rightarrow U_2N_3 \tag{6.2}$$

$$U_2N_3 + x\,N \rightarrow U_2N_{3+x} \tag{6.3}$$

$$U_2N_{3+x} + (2+y)\,O_2 \rightarrow 2\,UO_{2+y} + (3+x)\,N \tag{6.4}$$

As U_2N_{3+x} reacts with O_2, further N is released, continuing this chain of reactions. Rama Rao *et al.* found that UN oxidised at a higher temperature in air than in an atmosphere of 20 % O_2 and 80 %Ar, showing that the presence of N_2 in the atmosphere slows the oxidation of UN. From this, Rama Rao *et al.* concluded that the diffusion of N_2 out of the UN sample is the rate controlling process of UN oxidation. No explanation about what happens to the N that diffuses through the UO_2 layer was provided. However, Paljevic *et al.* found that N was retained in the sample after UN has been completely oxidised [85]. Additionally, Rama Rao *et al.*, Paljevic *et al.*, and Dell *et al.* all found that at temperatures above 250 °C, the UO_2 oxidation product further oxidised, and was found to be UO_3N_x.

This raises a question about whether N is also present in the UO_2. As some N is retained in the sample after oxidation to UO_2 at 200 °C, as shown by Paljevic *et al.*, it might be expected that this is the case, however, none of these investigations show any evidence of this [85]. These investigations all used x-ray diffraction to determine the phase of the oxidation products. It is possible that when analysing this data, UO_2N_x was mistaken for UO_{2+x}, as no chemical analysis of the oxidation product was performed. Identifying the presence of any uranium oxinitrides, let alone a specific composition, is challenging as literature on the U-N-O system is currently very limited. The solubility of O in uranium oxinitrides has been well investigated, both by experiment and modeling, however there are no investigations into the solubility of N in uranium oxides at present [177–180].

6.1.3 Low Temperature Oxidation

Historically, investigations into UN oxidation have focused on high temperature reactions, where oxidation occurs quickly and to completion, making it straightforward to investigate with bulk analytical techniques. More recently, a renewed interest in UN as a nuclear fuel, as well as improvements in surface sensitive techniques, have motivated investigations into surface reactions, allowing the relatively small changes caused by low temperature oxidation to be observed. When considering the manufacture of UN fuel pellets and their long-term storage, it important to consider this low temperature oxidation as it may have a significant effect on fuel properties.

Work has recently been conducted investigating the initial room temperature oxidation behaviours of UN_x films and layers using XPS and Auger electron spectroscopy (AES) [101, 132, 181]. Lu *et al.* showed chemical analysis of the surface by AES before and after oxidation, finding that $UN_{1.66}$ oxidised to form a UN_xO_y phase at the surface, while U, $UN_{0.23}$, and $UN_{0.66}$ formed UO_2. Conversely, Luo *et al.* found that $UO_{2-x}N_y$ formed on the surface of a $UN_{0.68}$ film [132]. Liu *et al.* investigated nitrided U surfaces, which resulted in mixed phases with UO_2, and found UNO_x compounds to form [181]. Most interestingly, they saw a reduction of UO_{2+x} on the oxidised surface after long-term storage in air, suggesting that this is due to the x being a result of interstitial N rather than O.

These investigations provide interesting results, however, as they are all performed on mixed phase samples, some including U metal and UO_2, it is difficult to determine if the results obtained are due to the presence of certain phases or possibly due to having mixed phases present. Additionally, there is low certainty in determining the phases present in these samples before and after oxidation as no crystallographic characterisation was performed and there is very limited spectroscopy literature with which to compare. Furthermore, the surface sensitive techniques used limited measurements to the first few nm on the sample surface. Though a depth profile analysis of the oxidised surface of UN_x samples was provided by Lu *et al.*, it showed only the atomic percentages of U, N, and O, and not the bonding states as a function of depth [101]. Consequently, from these studies it is not known whether the U_2N_3 intermediate layer that was observed during high temperature oxidation is also formed during room temperature oxidation.

There are many more aspects of the oxidation of UN at room temperature that remain unknown, such as the rate at which oxidation occurs. Though there are mentions of the UN surface oxide layer thickness in the literature, it is not

known how this changes as a function of time. It is expected that this surface oxide layer acts as a passivating layer, stalling further oxidation, however, it is not known how long it takes for this to occur. There is also uncertainty about the composition of this surface layer, as it has yet to be investigated on a single phase UN sample.

In order to investigate these problems, chemical, structural and crystallographic studies of the surface of a single phase sample are required. As both atmospheric composition and pressure have been shown to have an effect on how oxidation progresses, these studies should be performed in air to be representative of the oxidation that might occur on the surface of a fuel pellet [86, 181]. The work presented in this chapter has been conducted with the aim of fulfilling these requirements.

6.2 Investigation of the Oxidised Surface of UN

6.2.1 Experimental Procedures

Investigations into the oxidised surface of UN were performed by using x-ray reflectivity (XRR), x-ray photoelectron spectroscopy (XPS), and transmission electron microscopy (TEM) to examine the structural and chemical properties of a $(0\,0\,1)$ UN thin film. An epitaxial film was chosen as the sample to investigate, rather than a nanocrystalline film. Though it cannot be said that there are no crystallite boundaries in a $(0\,0\,1)$ UN film, those that are present will be very low-angle boundaries, as evidenced by the rocking curve in Figure 4.19. These will be more akin to the sub-grain boundaries than the grain boundaries found in polycrystalline materials, minimising any grain boundary effects on the film oxidation [182]. Additionally, as all crystallites are aligned, the surface of a $(0\,0\,1)$ UN film is predominantly composed of the $(0\,0\,1)$ plane of UN, whereas the surface of a nanocrystalline UN film is composed of a distribution of different $(h\,k\,l)$ planes. Furthermore, UO_2 has been shown to form epitaxially during the oxidation of UN, it is likely that the oxidised layer forming on a $(0\,0\,1)$ film will have lower roughness and be more uniform than on a nanocrystalline film [63]. This will reduce any possible surface area effects, and also allow more precise measurements to be taken.

Experiments with a controlled, ideal sample are important when trying to investigate intrinsic properties of a material, as any effects from the microstructure of the sample will be reduced. These experiments also provide a comparison for computational models, for which complex samples can be difficult to simulate.

The $(0\,0\,1)$ UN thin film samples used for these measurements were made following the procedures described in Section 3.3. As XPS measurements, which involved Ar sputtering of the sample, and TEM measurements, which require the dissection of the sample to remove a foil, are destructive, different samples were used for each data set. The crystallinity of each sample used was verified using x-ray diffraction to ensure each sample was single phase and single crystal, as expected.

Oxidation of each sample used was achieved by exposing them to air at room temperature. With the exception of XRR, measurements were taken at least 10 days after first exposure to air, to allow sufficient formation of the oxide surface layer.

6.2.1.1 XRR

In order to observe the change in thickness of the oxidised surface layer of a $(0\,0\,1)$ UN thin film, XRR measurements were taken at varying times. These measurements were performed on SN1430. Since oxidation begins on first exposure to air, which occurs on removal of the sample from the sputter system loading chamber, the first measurement was taken as soon after unloading as possible. As each measurement took 40 mins to collect, the time for each data point was taken to be the midpoint of this timespan.

When making repeat measurements, it is ideal to not have any changes in the experimental set-up, however, due to the timescale over which measurements were taken, it was necessary to move the sample before all measurements taken after 11000 mins. To minimise the changes caused by this, the sample and stage were marked to ensure that the sample was positioned in a similar orientation and position for each measurement.

XRR was also performed on SN1029, the sample used for STEM, after it had been oxidised and capped but before the removal of STEM foils, as detailed in Section 6.2.1.4.

Fitting of XRR data was performed using GenX software, as described in Section 4.3.2.2 [135]. The sample was modeled with only a UN and surface UO_2 layer, as it was found that including a U_2N_3 interlayer or UO_2 surface layer did not improve the fit. This is due to the very similar electron densities of UN and U_2N_3. When fitting XRR data, only UN and UO_2 layer thickness and roughness were allowed to vary.

6.2.1.2 XRD

To perform structural analysis of the oxidation products formed on the surface of $(0\,0\,1)$ UN thin film SN1430, x-ray diffraction (XRD) was performed on the sample after the last XRR measurement was taken. These XRD measurements were only performed at this time point as the XRD results are not likely to be sensitive to the very small changes in material volume that occurred during the oxidation of this sample. Additionally, high quality XRD measurements can take a considerably longer period of time than XRR measurements, so performing both on the same sample as a function of time would significantly limit the number of data points measured with XRR for low values of exposure time.

XRD measurements were performed using the methods described in Section 4.3.1. To measure any oxidation product that formed epitaxially on the UN film, a measurement was taken aligned to the UN $[0\,0\,1]$ direction. As the volume of the oxidation product is very low, in order to increase the scattering volume and therefore counting statistics, the existence of polycrystalline oxidation product was investigated using a grazing incidence XRD measurement with ω fixed at 3 °.

6.2.1.3 XPS depth profile

XPS measurements were performed at the Bristol nanoESCA facility, as described in Section 4.2.1.2, on SN1062. To create a depth profile of the oxidised surface of this sample, Ar sputtering was used to remove subsequent layers of the surface between collection of spectra. Sputtering was performed for 5 mins between each measurement, with the source perpendicular to the sample surface so that sputtering would be uniform. When not performing sputtering, a base pressure below 10^{-9} mbar was maintained in the XPS chamber, keeping subsequent sample oxidation low.

Between sputtering, spectra were collected from the U-4f, N-1s, valence band, and O-1s states with a pass energy of 6 eV, and a survey scan was taken with a pass energy of 50 eV. For data sets where a Fermi edge was present in the valence band spectra, this was used to calibrate the data. Fitting of spectra was performed using CasaXPS software, described in Section 4.2.1.3 [128].

To fit each state, multiple peaks with overlapping ranges on their binding energy were used, centred on the peaks present in the spectra presented in Section 4.2.1.4. The line-shapes used in the analysis of these results were also used in

fitting of the present results, and were not allowed to vary during fitting. For the lowest binding energy peak used in fitting of the U-4f spectra, the line-shape used to fit spectra from UN, with strong asymmetry level of t = 0.38, was used. When fitting N-1s spectra, two peaks were used, as seen in the spectra collected from U_2N_3. Fitting of this state was complicated by the presence of a shake-up satellite at similar binding energy, resulting from U(IV) present in UO_2. Total areas of fitted peaks were calculated as described in Section 4.2.1.3. These areas were then normalised to the total area of the U-4$f_{7/2}$ peak of the first spectra collected.

6.2.1.4 STEM

Scanning transmission electron microscopy (STEM) was used to collect high resolution images of the oxidised surface of a UN sample. This is a technique that involves the focusing of a beam of electron onto a thin sample foil using fields generated by solenoid coil lenses. This is performed under UHV (typically 10^{-10} mbar) to reduce beam scattering. As the sample is very thin, a portion of the electron beam will be transmitted and elastically scattered through the sample. This scattered beam is then focused onto a central detector directly in the beam path or an annular detector outside the beam path. As the beam is then rastered across the sample, an image is built up. The central detector will mostly detect the unscattered beam in a mode known as bright field imaging, whereas the annular detector will be sensitive to the scattered electrons, known as annular dark field (ADF) imaging. As scattering will increase with Z, contrast in ADF mode is directly related to Z. This is a brief overview of STEM, however, a much more complete description can be found in 'Introduction to scanning transmission electron microscopy' by R. Keyse [183].

STEM sample foils were taken from SN1029. This sample is a $(0\,0\,1)$ UN thin film deposited on a Al_2O_3 substrate with Nb buffer, which was allowed to oxidise by introducing O_2 into the sputtering chamber at room temperature. The oxidised sample was then capped with Nb to preserve the surface during preparation of STEM foils. Before STEM foils were extracted, XRR was performed on this sample, as described above.

STEM foils were prepared by assisting Dr James Darnbrough using a FEI Helios NanoLab 600i dual-beam at the School of Physics, University of Bristol. This instrument houses both an electron source and Ga ion source, allowing imaging of the sample using electron and ion microscopy and milling of the sample using the ion beam. Once the sample surface of the area to be extracted is protected by the chemical vapour deposition of Pt, trenches are etched down

into the sample with the Ga ion beam, isolating a slice down into the sample to be extracted. A lift-out needle is then positioned on this slice and further Pt deposition is used to join the two before the sample slice is cut away from the bulk using the Ga beam. The needle is then used to transfer this slice to a TEM grid, where it is attached with Pt and cut free from the needle. The sample slice is then thinned down to a foil using progressively lower Ga ion beam currents and voltages at grazing incidence. This is the most challenging but important part of the process as foils must be thin enough to allow electron transmission, making it particularly difficult with a high Z material such as UN.

STEM data collection was performed by Dr James Darnbrough and Dr Ian Griffiths using a JEOL ARM200F in the Materials Department at the University of Oxford. All the data presented here was collected in ADF imaging mode and processed using Digital Micrograph software distributed by Gatan [184].

6.2.2 X-ray Reflectivity Results

Results from the XRR of a $(0\,0\,1)$ UN thin film sample for varying times since first exposure to air are shown in Figure 6.1. On the left of this figure, the data (grey circles) and fit (solid lines) are plotted, and on the right, the scattering length density (SLD) plots obtained from fitting the XRR data are plotted. These results show a close up of the specific regions of the data where changes were seen as a function of exposure time. Due to the long duration of the experiment, the sample could not be left in the same position for all XRR scan, meaning the sample had to be repositioned for the final three data points.

The plotted XRR data in Figure 6.1, which have been offset for clarity, show that changes as a function of exposure time to air are very subtle, with the most notable changes seen below Q = 0.1 Å^{-1}. Since features at lower Q are more influenced by rougher surface layers, this shows that it is only the surface of the UN film that is changing as a function of exposure to air. These changes can be seen by a decrease in the intensity at the first dip in the reflectivity at 0.07 Å^{-1}, and the increase in intensity at 0.09 Å^{-1} as the fringe resulting from the surface oxide layer becomes narrower. This can also be seen by the shift in the Q position of the deepest trough in the tight fringes resulting from the UN layer thickness. The significance of these features is shown in the SLD plot, were it can be seen that the surface layer thickness increases with exposure to air. The small increase in the width of the tight fringes, which can be seen by the shift in trough position at high Q, shows the decrease in the UN layer thickness.

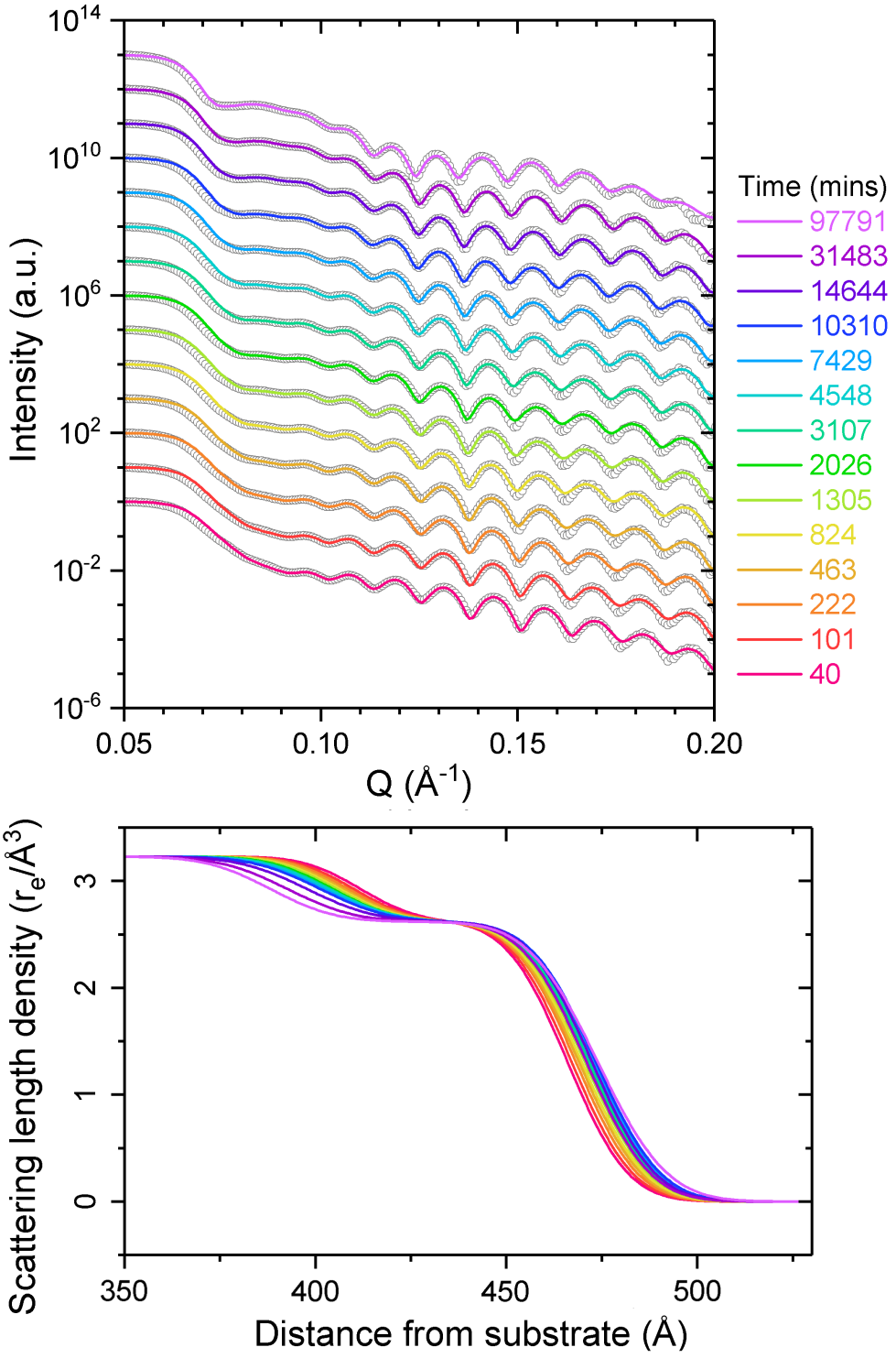

Figure 6.1: *Graph showing results from XRR measurements taken as a function of exposure to air time, with XRR data (grey circles) and fits (solid lines) top and scattering length density plots obtained from fits below.*

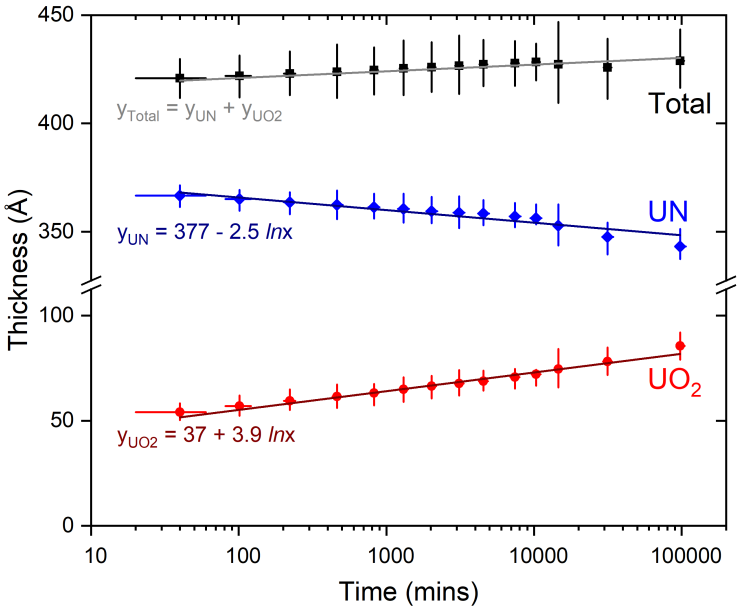

Figure 6.2: *Graph showing changes in UN (blue), UO_2 (red), and total (black) thicknesses of the* $(0\,0\,1)$ *sample obtained from XRR fitting.*

The SLD plot also shows an increase in total thickness of around 10 Å, shown by the shift in the position of the surface. This surface also shows a small increase in gradient, showing some small roughening of the sample surface.

The surface UO_2, UN, and total layer thickness results obtained from fitting of XRR data are plotted in Figure 6.2 in red, blue, and black, respectively, showing the decrease in UN thickness and increase in UO_2 thickness over time. As UO_2 has a larger volume per U atom than UN, this results in a small increase in total film thickness, as can also be seen in Figure 6.2.

These results have been fitted with the function y = a - b*ln*(x), as described by Mott for the formation of protective oxide films on metals [185]. This function, which appears linear on this log plot, shows a good fit to the data, though the fit is poorer for the last three data points. This result shows that the relative expansion of the UO_2 layer compared to the UN layer is 3.9/2.5 = 1.56. Comparing this to the relative expansion of the U lattice found below, a lower value of 1.36 is obtained, showing that the thickness increase due do oxidation is greater than expected. This is likely to be due to the accommodation of strains created epitaxial oxidation.

6.2.3 X-ray Diffraction Results

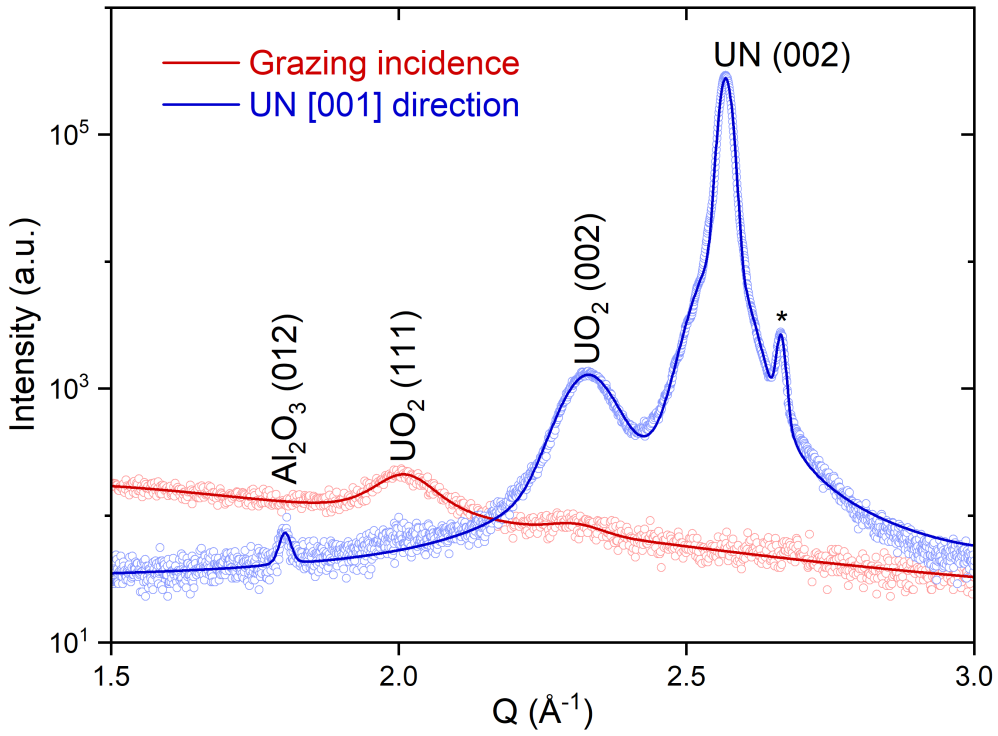

Figure 6.3: *XRD of oxidised* $(0\,0\,1)$ *UN thin film taken at grazing incidence (red) and aligned to the UN* $[0\,0\,1]$ *direction (blue). Data is shown by open circles and fit to data is shown by the solid line.*

The x-ray diffraction results from an oxidised $(0\,0\,1)$ UN thin film are displayed in Figure 6.3. In this plot, the scan performed aligned to the UN $[0\,0\,1]$ direction is shown in blue and the grazing incidence scan is shown in red, with data represented by open circles and fit to the data represented by a solid line. Each peak is labeled with the material and reflection, with the exception of the peak labeled with an asterisk, which is from the Al sample stage.

The scan aligned to the UN $[0\,0\,1]$ direction shows the high intensity UN $(0\,0\,2)$ reflection with some Laue fringes at low Q, as expected, and a less intense peak corresponding to the UO_2 $(0\,0\,2)$ reflection. The Al_2O_3 substrate peak seen at low Q has very low intensity due to the miscut in the UN film. Grazing incidence results show a weak UO_2 $(1\,1\,1)$ reflection and an even weaker UO_2 $(0\,0\,2)$ reflection.

All UO_2 reflections seen in these XRD results were found to be very broad, with a FWHM of 0.05 ± 0.01 Å^{-1} in Q. Their positions were found to be slightly higher in Q than expected for bulk stoichiometric UO_2, giving a lattice

parameter of 5.41±0.04 Å compared to 5.468 Å [45].

It is not possible to quantitatively compare the areas of the peaks seen in Figure 6.3 to determine relative quantities of polycrystalline and highly textured oxidation product as a different set-up was required for each measurement, however, some qualitative assessments can be made. Comparing the scan at grazing incidence to that taken aligned to the UN $[0\,0\,1]$ direction, the intensity of the $(0\,0\,2)$ UO_2 reflection is very high in the latter, while the $(1\,1\,1)$ reflection, the most intense reflection for UO_2, is absent. This shows that most of the oxidation product formed at the surface of the UN film is strongly textured, with the c axis of UN and UO_2 aligned. Conversely, this $(1\,1\,1)$ reflection is present in the grazing incidence scan, as is the $(0\,0\,2)$ reflection, but with lower intensity. This is the result that would be expected from a polycrystalline material, showing that not all of the oxidation product formed shows the texture described above, with some being more polycrystalline.

6.2.4 X-ray Photoelectron Spectroscopy Depth Profile Results

This section displays the results from XPS depth profiling of a $(0\,0\,1)$ UN thin film, obtained by Ar sputtering the film surface to remove layers before collecting spectra. Figure 6.4 shows the calibrated spectra collected for different total sputtering times, plotted on top of each other to facilitate a comparison of the data. This energy range covers the U-4$f_{7/2}$, U-4$f_{5/2}$, and N-1s states, as shown by the labels.

The first two spectra, collected after 0 and 5 mins sputtering time and shown in pink and red, show strong U-4f peaks at around 380 and 391 eV, consistent with U(IV), with no indication of the presence of a metallic peak. Clear satellite peaks can be seen at around 8 eV higher binding energy to these states. Additionally, an N-1s peak overlapping with a satellite peak can be seen at these sputtering times. For sputtering times greater than 5 mins, this N-1s shows a large shift to higher binding energy, and lower binding energy, asymmetric peaks appear in the U-4f spectra, indicating the detection of uranium nitride. As total sputtering time increases, the ratio of this metallic peak to the U(IV) peak gradually increases, showing the transition through the surface oxide layer. The final spectra, collected after a total of 60 mins sputtering, shows strong resemblance to the spectra of UN displayed in Figure 4.6.

A close-up of the fitted spectra of these N-1s, and U-4$f_{7/2}$ states, as well as the O-1s state is displayed in Figure 6.5. Plotted in this figure are the total fits to the spectra, shown with a solid line, and the different peaks used to fit each

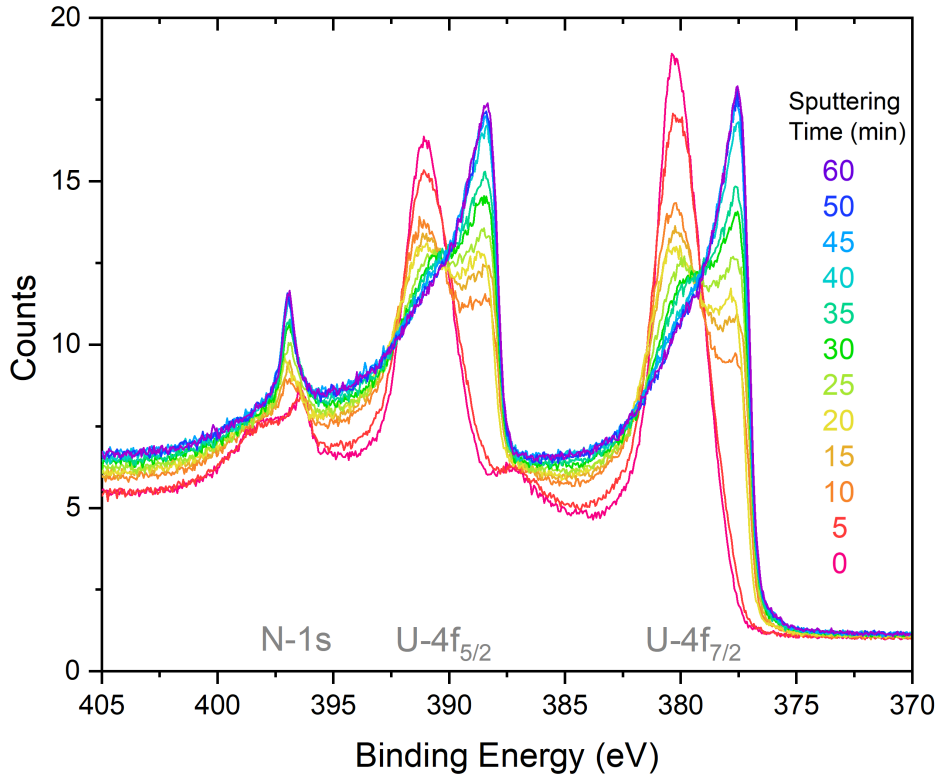

Figure 6.4: *U-4f and N-1s spectra of oxidised surface of UN as a function of Ar sputtering time.*

spectra, shown with long dashes, short dashes, or dots. To more clearly see the fitted peaks, the background has been removed in all of these plots.

The normalised areas of the peaks used to fit the XPS depth profile are plotted in Figure 6.6. These values are normalised to the total area of the U-4$f_{7/2}$ peak at 0 mins sputtering time, such that the N-1s and O-1s areas are equivalent to the stoichiometry.

The total fitted areas of the U-4f and N-1s peaks attributed to uranium nitrides and uranium oxide are shown in Figure 6.6 a). The data points before sputtering show that the surface of the UO_2 layer is hyperstoichiometric, and the UO_2 layer, seen after 5 mins sputtering time is stoichiometric. At both of these two sputtering times, the N-1s total peak area has a value of over 0.5, despite the area of U-4$f_{nitride}$ peak being 0. Between 5 and 40 mins sputtering time, the gradient of all peak areas shows that the XPS measurement were taken in a transitional range, where Ar sputtering had removed some but not all of the uranium oxide from the area of the sample being measured. Beyond 40 mins total

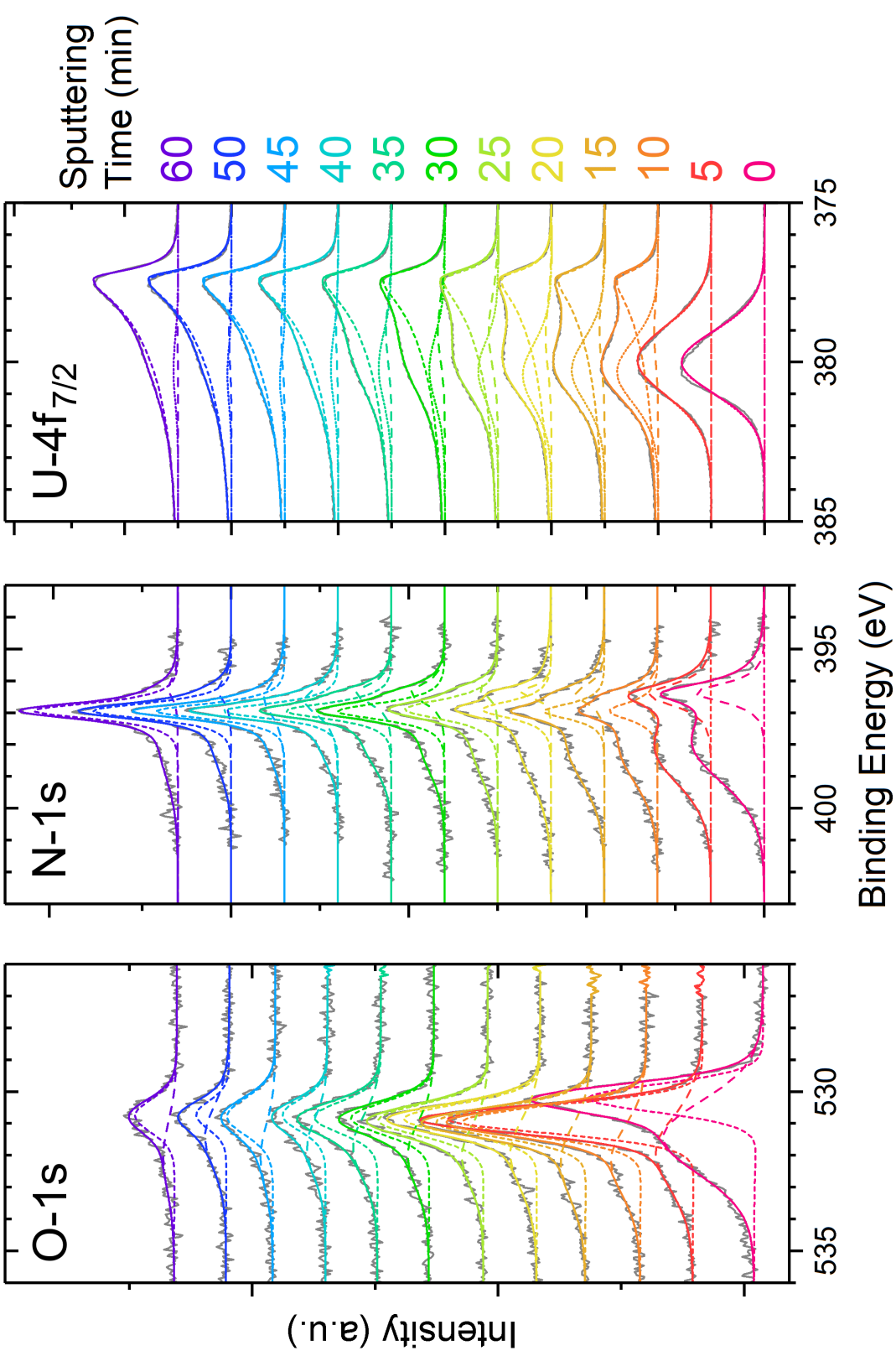

Figure 6.5: *Fitted O-1s, N-1s, and U-4f spectra from XPS depth profile of* (001) *UN thin film sample. Different peaks used to fit each state are shown with long dashes, short dashes, or dots, and total fit is shown with a solid line.*

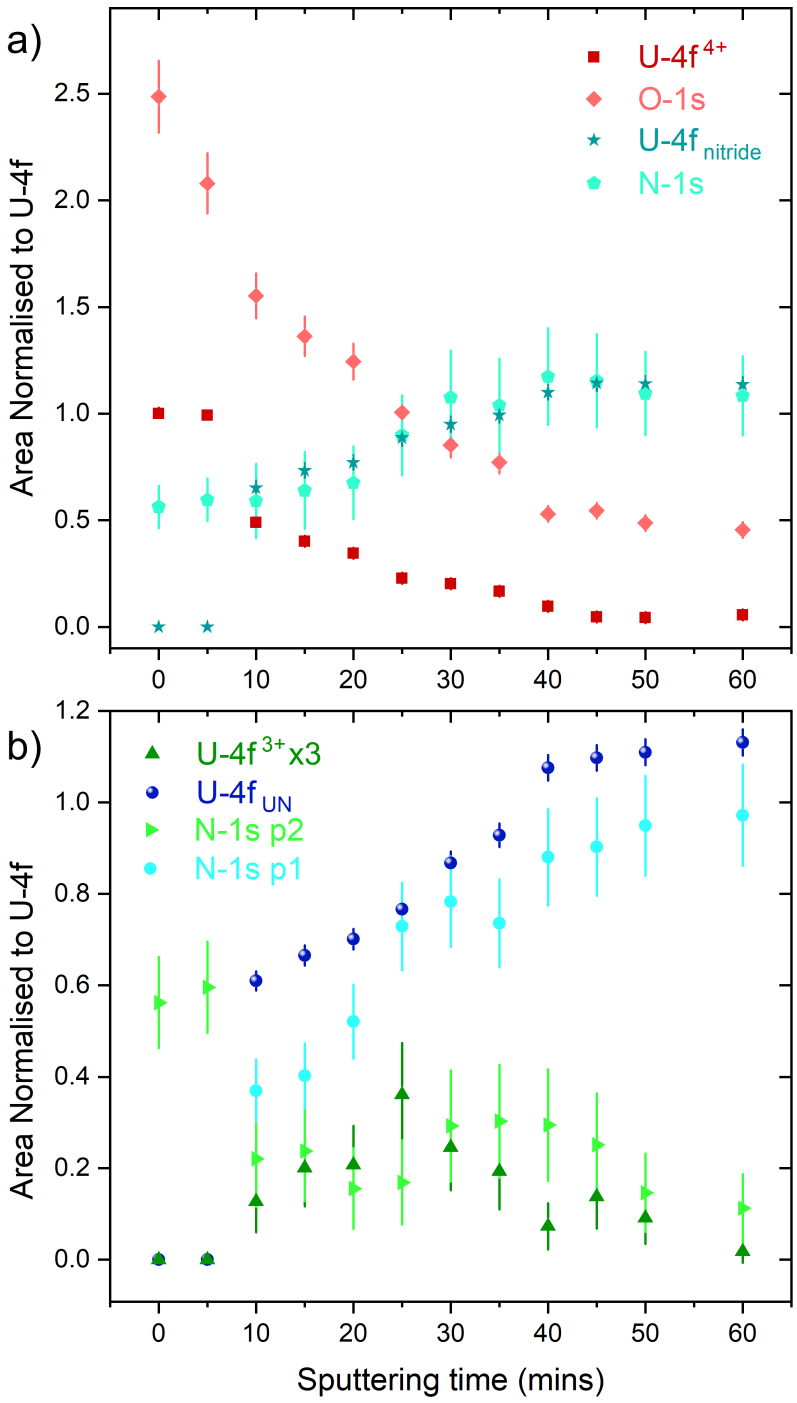

Figure 6.6: *Graph showing normalised intensities of fitted peaks from O-1s, N-1s, and U-4f$_{7/2}$ states collected from a UN sample after increasing sputtering times, with a) showing total fitted areas of peaks associated with uranium nitide and uranium oxide and b) showing the fitted components of the U-4f and N-1s peaks attributed to uranium nitrides.*

sputtering time, there are few changes in the fitted areas, and the matching values of the U-4$f_{nitride}$ and N-1s areas show that the measured volume of the sample is likely to be comprised of stoichiometric UN. Despite this, the fitted area of the O-1s peak has values over 0.4 in this region.

Figure 6.6 b) shows the results of closer analysis of the U-4f and N-1s peaks attributed to uranium nitrides, with U-4f^{3+} and N-1s p2 seen with much greater intensity in U_2N_3 than in UN and U-4f_{UN} and N-1s p1 seen in both UN and U_2N_3, as shown in Section 4.2. The work in this section showed differences between the U-4f_{UN} and N-1s p1 peaks in UN and U_2N_3, with the spectra from UN having lower FWHM values and a lower binding energy for U-4f. However, it was not possible to fit two components with these small differences when analysing the XPS data presented here. Consequently, a single peak was used to fit both U-4f_{UN} and N-1s p1, with the U-4f_{UN} at a position of 377.4±0.2 eV, and asymmetry factor of $t = 0.38$, as used for UN.

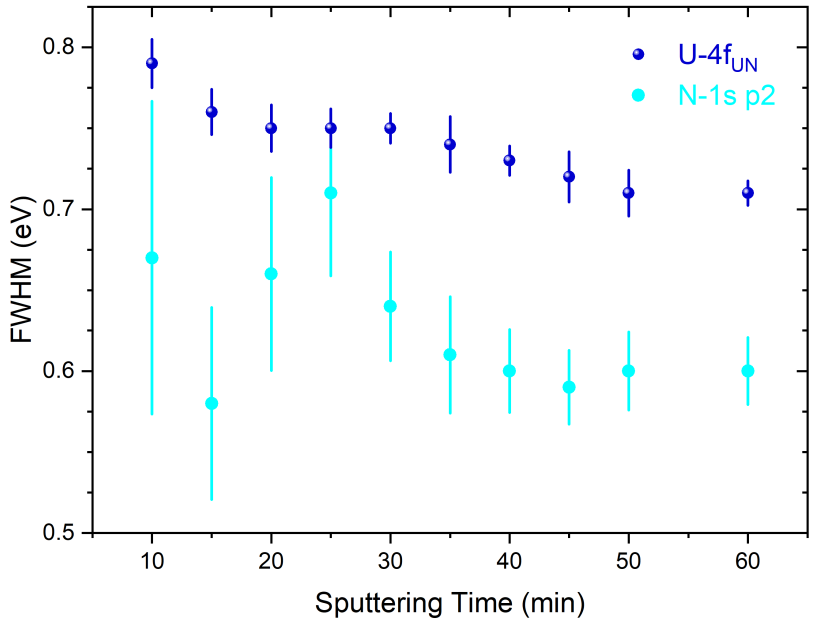

Figure 6.7: *Fitted FWHM of U-4f_{UN} and N-1s peaks as a function of sputtering time.*

The data displayed in Figure 6.6 b) shows that both the U-4f^{3+}, U-4f_{UN}, and N-1s p1 peaks are not present after 0 and 5 mins sputtering time, and beyond this time the area of the U-4f_{UN} peak increases strongly before leveling off after 40 mins sputtering time. The U-4f^{3+} peak, however, increases in area until 25 mins sputtering time, after which it decreases. This U-4f^{3+} peak shown in Figure 6.6 b) has been multiplied by 3 to more clearly display the fitted area. As

this peak is attributed to U_2N_3 and appears in the middle of the transitional range, it shows that there is a concentration of U_2N_3 at the interface between UO_2 and UN.

Between 10 and 30 mins total sputtering time, the N-1s p1 peak area increases at a higher rate than the U-4f_{UN} peak, before decreasing in rate, suggesting that there is a region of N concentration. The N-1s p2 peak area is highest at 0 and 5 mins sputtering time, showing that it is present in the UO_2 surface. Beyond this time, the area is much lower and seems to increase slightly before decreasing, however, the errors on these values are large due to the small area of this peak and the overlap with the U-4f^{4+} satellite, as seen in Figure 6.5.

The FWHM of the U-4f_{UN} and N-1s p1 peaks are shown in Figure 6.7. Since the U_2N_3 and UN contributions to these peaks could not be resolved, the differences in their FWHM values can instead be used to evaluate the relative contribution of each material to the fitted peak. From Section 4.2, it was found that the FWHM was 0.9 and 0.6 eV for U_2N_3 and UN, respectively, for the N-1s p1 state, and 1.1 and 0.7 eV for U_2N_3 and UN, respectively, for the U-4f_{UN} state. This plot shows a clear decrease of the U-4f_{UN} FWHM from around 0.8 to 0.7 eV, the value found for UN, suggesting that the relative amount of U_2N_3 contributing to this peak decreases as sputtering time increases. The general trend of the FWHM of the N-1s p1 peak is also a decrease with increasing sputtering time, however, the uncertainty in this data is high.

6.2.5 STEM Results

The results from XRR and STEM of a thin foil of the same $(0\,0\,1)$ UN sample are shown in Figure 6.8 and Figure 6.9. This sample was allowed to oxidise by exposing it to O_2 at room temperature in the sputter deposition chamber, before being capped with a layer of Nb to protect and preserve the surface oxide layer.

The XRR fit displayed in Figure 6.8 shows the result of the many layers present in this sample (Al_2O_3 substrate, Nb buffer, UN film, UO_2 oxide layer, and Nb cap), with the fit showing a good match to the data except for the narrow fringe amplitude. These fringes originate from scattering from the UN layer and the discrepancy between fringe amplitude in data and fit have been discussed in Section 4.3.2.3. From the fitted model, the layer thicknesses were found to be 555$\pm$10 Å for the UN layer and 70$\pm$6 Å for the UO_2 oxide layer.

Figure 6.9 a) shows the scattering length density (SLD) plot obtained from the above fit over an annular dark-field

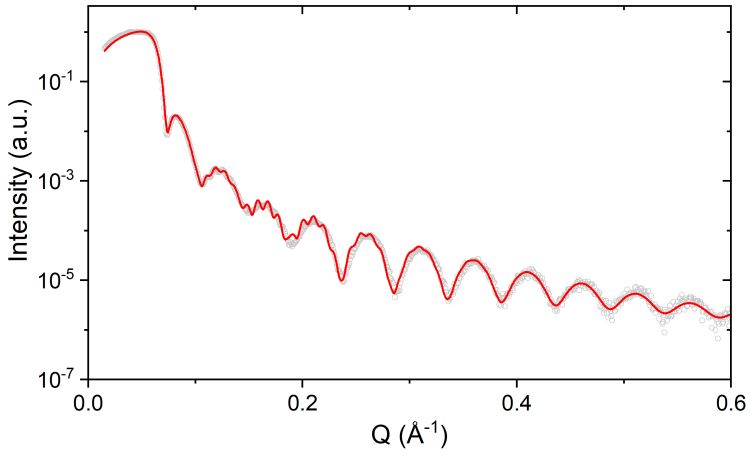

Figure 6.8: *Fitted XRR of SN1029, the* $(0\,0\,1)$ *UN sample from which TEM foils of were obtained, with data shown as grey circles and fit as a red line.*

(ADF) transmission electron micrograph of a cross-sectional TEM foil. The micrograph has been scaled to match the 'Distance from substrate' axis of the SLD plot, with this axis perpendicular to the interfaces seen in the micrograph. Additionally, both SLD and lightness of an ADF micrograph increase with Z so a correlation of these two parameters is expected.

This figure shows very good agreement between the micrograph and SLD plot, showing the high accuracy of XRR measurements. The sharp interfaces of the Al_2O_3 substrate and Nb buffer in the micrograph match closely with the high gradient of the SLD plot. At the interface between the UN film and oxide layer, a thin dark layer can be seen in the micrograph, however, no change in the SLD plot due to this layer is seen. Instead, the SLD plot shows the interface between the UN film and oxide layer at the top of this thin dark layer in the micrograph. As U_2N_3 and UN have very similar scattering length density, it is not possible to distinguish between them with XRR, and no change in the SLD plot at a UN / U_2N_3 interface would be expected. It is therefore possible that the thin layer between the UN film and oxide layer is composed of U_2N_3, though this does not explain the relative darkness of this layer in the micrograph.

Beyond the UN film, the oxide layer and Nb cap are difficult to distinguish as they have similar electron densities, as shown by the similar colours in the micrograph. This is also shown in the results of the XRR fit, but the rough surface of the Nb cap makes it difficult to distinguish in the SLD plot. At the sample surface there is a discrepancy between the

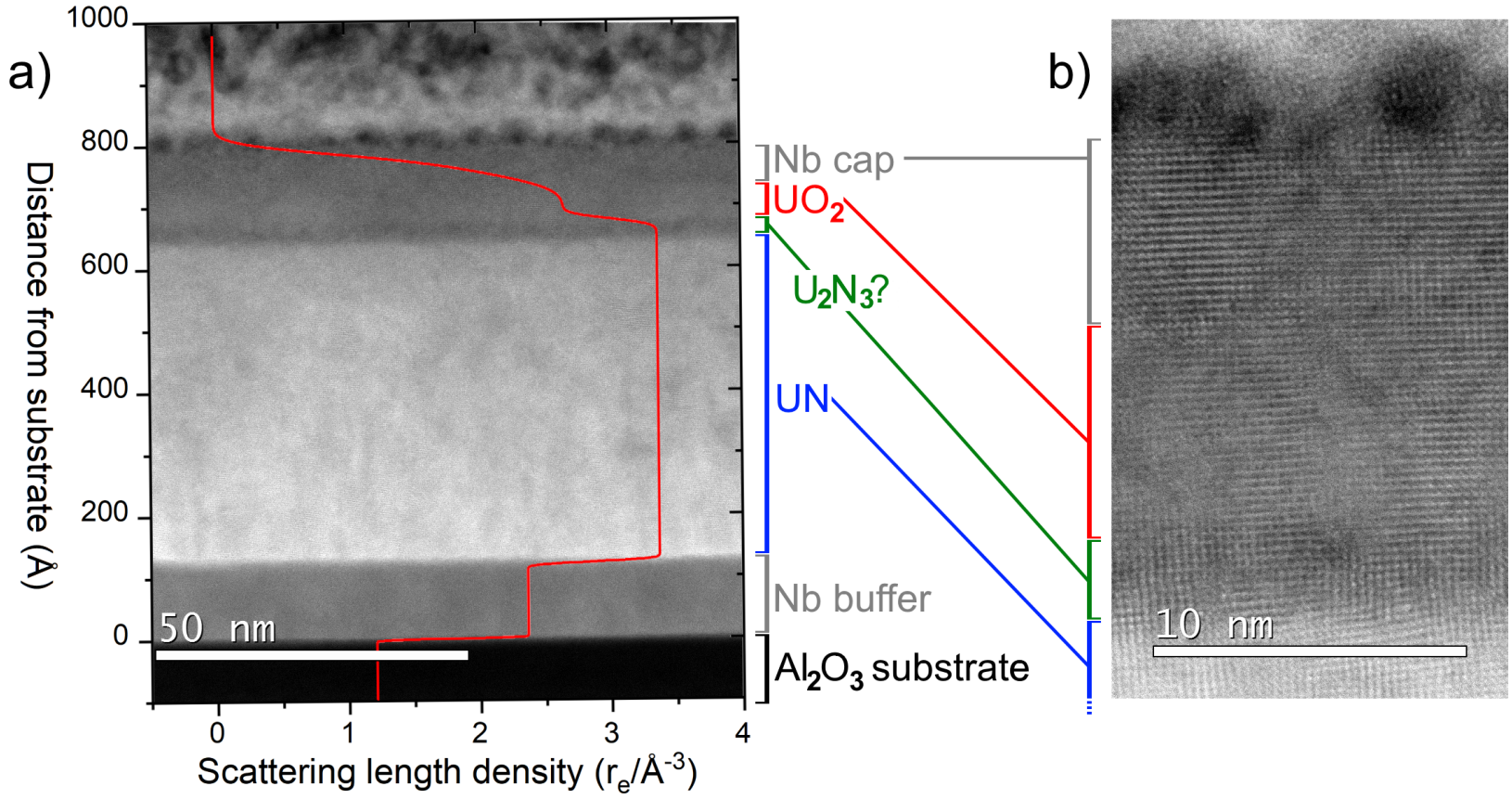

Figure 6.9: *a) Scatteing length density plot obtained from the XRR fit shown in Figure 6.8, overlaid on a transmission electron micrograph of a cross-section of the same sample, with matching scales. b) Close-up micrograph of the sample surface layer seen in a).*

SLD plot and micrograph as the Nb cap that formed the sample surface when the XRR was performed was covered by an additional protective Pt layer when preparing TEM foils and is visible in the micrograph.

A magnified image of the surface layer of the UN sample are shown in Figure 6.9 b), with the possible material composition of each layer labeled. From this image the UO_2 layer thickness can be estimated to be around 70±5 Å, while the layer between the UN and UO_2, possibly U_2N_3, is around 20±5 Å thick. Estimating the thickness of the UN layer from Figure 6.9 a) gives a value of 520±20 Å. The sum of the UN and possible U_2N_3 layer is then 540±25 Å, close to the value of 555±10 Å obtained from XRR fitting.

6.3 Discussion

6.3.1 Passivation

Results from the x-ray reflectivity of an uncapped $(0\,0\,1)$ UN thin film sample show the evolution of the surface oxide layer over time, with the passivating effect of the surface oxide layer shown by the decrease in oxidation rate. This result is to be expected as the Pilling-Bedworth ratio (the ratio of unit cell volume of the oxidant to unit cell volume of the metal) is 1.39 and passivation is predicted for values between 1 and 2 [186]. Additionally, this corroborates anecdotal evidence that UN is stable at room temperature and passivates with an oxide layer thickness low enough to preserve the metallic appearance of uncapped films.

The fit to the UN, oxidation, and total layer thickness in Fig 6.2 shows very good agreement with the data, even taking into account the slight difference seen after 10 000 mins when the sample was repositioned. This fitted equation shows oxidation occurs very rapidly on initial exposure to air before slowing. Though the fitted equation shows oxidation continuing indefinitely, within the errors of the measurements there is no significant increase in the oxidation layer thickness after around 10 days of exposure.

The gradient of the interfaces in the scattering length density plot do not change significantly with exposure time, showing that the oxidation occurs uniformly over the film. Additionally, the strong preferred orientation shown in the XRD of this sample shows that this oxidation predominantly grows epitaxially on the single crystal UN film. This is in agreement with the work of Sole *et al.*, who found the same results when investigating high temperature oxidation of

UN with transmission electron microscopy [63].

This uniform oxidation is to be expected from an highly controlled sample such as an epitaxial thin film, though the strains caused by this epitaxy may have effects on oxidation. Additionally, the crystallographic orientation of the film may have effects on oxidation rate and layer thickness, as has shown to be the case for UO_2 [100].

Comparing single crystal results such as this to more fuel-realistic polycrystalline samples, Dell *et al.* showed that oxidation of single crystals is slower than powders and ignition occurs at higher temperatures [44]. As the room temperature measurements presented here are well below these ignition temperatures and the Pilling-Bedworth ratio is of course the same for both single and polycrystalline samples, similar passivation behaviour may be expected for polycrystalline UN. Indeed, the measured thickness of the surface oxide layer on polycrystalline UN thin films, displayed in Figure 7.10, is 90±20 nm, the same as for the $(0\,0\,1)$ UN sample, within errors.

6.3.2 Surface Oxide Layer

XRD results showed that the surface oxide layer had a lattice parameter of 5.41±0.04 Å, lower than the bulk UO_2 value of 5.468 Å [45]. This could be partly due to some strain caused by the epitaxial oxidation, or it could be indicative of a higher oxide being produced during oxidation as uranium oxide lattice parameter is known to decrease with increasing stoichiometry [187, 188].

Considering the effects of epitaxial strain, an investigation into the effects of pressure on U_3O_8 found that a fluorite-type phase formed above 8.1 GPa [189]. (No phase transition is expected in UN below 34 GPa [190, 191].) This phase had a lattice parameter of 4.415 Å, very close to the value found for the surface oxide layer. The bulk modulus for this high pressure phase was found to be 78 GPa, much lower than the UN value of 200 GPa [189, 192]. It would therefore be expected that that strain from the expansion of the U lattice during oxidation have a greater effect on the softer oxide layer. This provides a possible explanation for the greater than expected increase in oxide layer thickness compared the decrease in UN layer thickness, as shown in Fig. 6.2.

Nonetheless, the U-4f states and relative U:O ratios found in the XPS results show no evidence of the presence of U_3O_8. Alternatively, it is possible that a similar phase with some amount of N in in place of O may be present. An examination of the XPS results give further insight into this possibility.

Figure 6.6 shows that the relative fitted area of the N-1s p2 peak is 0.6±0.1 in this oxide layer, showing the presence of nitrogen, while the O-1s peak goes from 2.5±0.2 to 2.0±0.2. These values are indicative of a stoichiometry higher than UO_2. Taking the average value for the O-1s area gives a stoichiometry equal to that of U_4O_9, however, a higher lattice parameter would be expected if this were the oxidation product.

The presence of N in the surface oxide layer is clearly shown in the XPS results. With an electron escape depth of less than 2 nm and measured oxide thickness of 7 nm, it is certain that this N is present in the oxide layer, and the N-1s intensity is not due to photoelectrons coming from the underlying UN film. Though there is limited literature data on the binding energy of the N-1s peak in uranium oxinitrides, the binding energy of 396.0 eV found here is that seen in oxynitrides of Ti and the oxidised surface of $UN_{1.66}$ [132, 133]. From this it can be concluded that the surface oxide layer is composed of uranium oxynitride, not simply UO_{2+x}.

Considering the state of the U in this oxinitride layer, only the peak attributed to U^{4+} is present in this oxynitride layer, as is found in UO_2, showing the bonding of the U in this layer to be the same as that seen in UO_2. Furthermore, the proportion of O in this layer is much greater then N. Consequently, this uranium oxynitride layer would best be described as uranium oxide containing some N, with formula $UO_{2+x}N_y$.

6.3.3 U_2N_3 Interlayer

Evaluating the possibility of a U_2N_3 interlayer between the UN film and the surface oxide, it is easiest to first consider the U-4f^{3+} state seen predominantly in U_2N_3, as shown in Section 4.2. First it should be noted that this state is not seen in the surface $UO_{2+x}N_y$ layer, showing that this state is not associated with uranium oxynitride and is instead a feature of U_2N_3. The N-1s p2 peak has been shown to be associated with uranium oxinitride, however, its presence after 40 mins sputtering time show that it could also be present in U_2N_3. This clarifies this point of discussion in Chapter 4.2.

Figure 6.6 b) shows a clear peak in the fitted area of this U-4f^{3+} state after 25 mins sputtering time, halfway between the regions that are predominantly oxide (below 10 mins) and UN (above 40 mins). Additionally, the ratio between the area of the N-1s p2 peak and that of U-4f_{UN} is highest at 25 mins. Furthermore, the FWHM of this U-4f_{UN} peak decreases with sputtering time. As this peak is broader in U_2N_3 than in UN, this indicates a decrease in the relative ratio of these materials with increasing sputtering time. These three points are strong evidence of a region of higher nitrogen

content at the interface between the UN film and surface oxide in the form of U_2N_3.

STEM and XRR results performed on the same oxidised sample also give evidence of an interlayer between the UN film and oxide layer. The very close match between the modeled SLD and micrograph layer thicknesses show that the interlayer seen in the micrograph is below the nitride / oxide interface in the SLD model, showing that the SLD of the interlayer is the same as that of the UN film, as would be expected for U_2N_3. However, the relative darkness of this interlayer in the transmission electron micrograph is unexpected.

These results match reports of oxidation at temperatures above 200 °C on both single crystal and polycrystalline UN samples, where a U_2N_3 interlayer was found [44, 63, 85, 86]. These reports relied on diffraction analysis to show the presence of this U_2N_3, however, the work presented here shows chemical evidence of this interlayer being present even during room temperature oxidation. This chemical approach allowed the O present in this U_2N_3 interlayer to be detected, shown by the strength of the O-1s peak in the XPS depth profile. Furthermore, this chemical analysis indicates that the bonding of the U in this layer has the character of that of U_2N_3. This was not possible to determine with the diffraction techniques used in previous studies, and is of significance as it is the oxidation state and stability of U that matters most when considering corrosion and degradation of UN as a nuclear fuel.

6.3.4 Passivation Mechanism

Having shown that the surface of UN forms a passivating oxide layer and having determined the composition of this layer, the mechanism for this passivation can now be considered. The work of Rama Rao *et al.* on UN oxidation above 200 °C showed that the diffusion of N produced by the oxidation of uranium nitride out of the sample was the rate-limiting step in the reaction mechanism [86]. Let us the processes that could lead to passivation of the UN surface, as depicted in Fig. 6.10.

It is expected that initial oxidation of a pristine UN surface occurs readily to begin with, as evidenced by calculations predicting spontaneous disassociation of O_2 on a UN $(0\,0\,1)$ surface [193]. This oxidation will release N, which will either diffuse through the surface oxide or the UN bulk. In the UN, this free N can react to form U_2N_3, as described in Section 6.1.2. In the surface oxide, this N may either diffuse out of the material or remain in the layer, forming uranium oxynitrides. For further oxidation to occur, O must diffuse through the surface oxide to reach the non-oxidised uranium

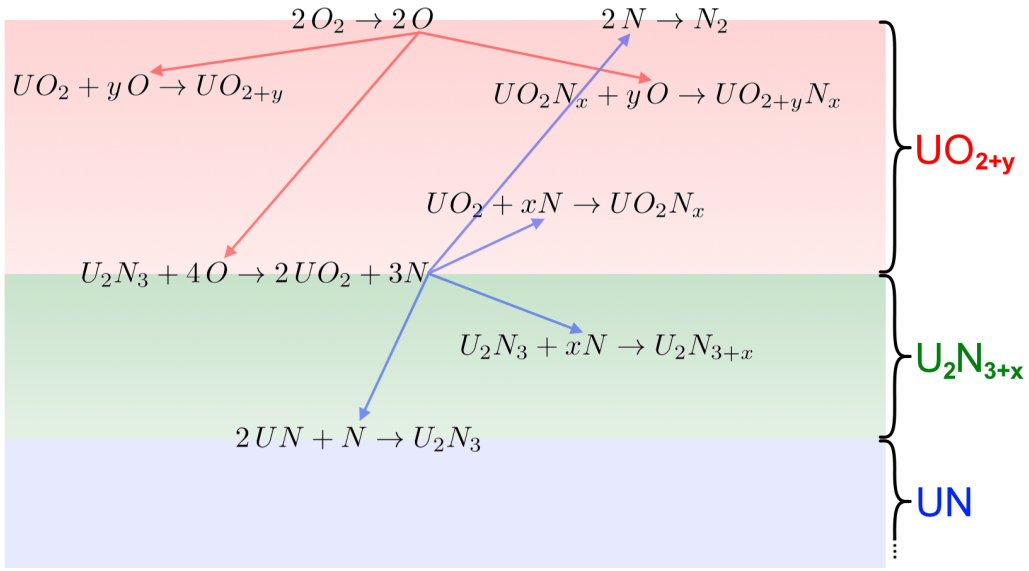

Figure 6.10: *Diagram showing possible reactions during oxidation of the UN surface.*

nitride. The thickness of the surface oxide layer will effect the rate at which O can reach the uranium nitride interface, however, this diffusion will also be somewhat impeded by the presence of N in the surface oxide. As further oxidation occurs, more N will be released, causing oxygen diffusion through the surface oxide to be further slowed, creating a negative feedback loop. As the two competing processes of O diffusion in and N diffusion out of the surface slow, the rate of oxidation will decrease, making the surface oxide act as a passivating layer.

With this passivation mechanism, it would be expected that O content in the surface oxide is highest at the surface, decreasing with proximity to the oxide / nitride interface, with low content levels beyond this interface. It would also be expected that N content is highest at the oxide / nitride interface, with high content on either side of the interface. To consider whether this is the case, the relative ratios of U, O, and N determined by the XPS depth profile can be compared. As the UN samples contain some O contamination before oxidation, these results should be compared with the chemical characterisation of the UN films presented in Chapter 4.2.

Previous work by Lu *et al.* has presented a depth profile of the atomic percentages of U, O, and N though the oxidised surface of a $UN_{0.68}$ thin film, determined using Auger electron spectroscopy [101]. This work found decreasing N content towards the surface, but did not distinguish between the different chemical states of the U, O, and N present

and was not performed on a single phase sample, making it difficult to draw any conclusions. Additionally, the high surface roughness will have a significant blurring effect on the depth profile.

The results from the XPS depth profile presented in Figure 6.6 show high O (above that expected for stoichiometric UO_2) and N content in the surface oxide layer, with values of 2.5 and 0.6, respectively. This O content is notably lower after 5 mins sputtering time, while the N content is the same. At the oxide / nitride interface, total relative areas do not show a region of higher N content, within errors, however, there is known to be a U_2N_3 from the peak in area of the U(III) state. Beyond this layer, UN is stoichiometric but O content is high, with a relative area of over 0.4. Furthermore, the O-1s to U-4f^{4+} area ratio increases with sputtering time.

Comparing this result to the O content in a pristine $(0\,0\,1)$ UN film, as shown in Section 4.2, it can be seen that the U-4f^{4+} area is the same, while the O-1 area is much lower in the pristine film. However, there are several instrument factors to consider with these results.

Mixing of the measured signal from different layers may occur due to roughness in the surface and interfaces, however, XRR and TEM results show that these are extremely smooth. Mixing may also occur due to inhomogeneity in the Ar sputtering, with visual examination of the sample after measurements showing that this was the case. This explains the blurring between the layers seen in Figure 6.6, but does not explain the high O content in the UN layer.

A possible cause for this is the redeposition of sputtered species. As O is more likely to react with the exposed surface than U or N, it would be expected that this effect is greatest for O, and would explain the higher than expected levels. As these effects must increase with sputtering time, it is difficult to determine the true levels of O content in the UN film beneath the surface oxide, however, they are likely to be lower than measured. Considering only the data points for low sputtering times, where redeposition effects will be small, the high O and N content, with O content highest at 0 mins sputtering, match the results predicted by the passivation mechanism.

6.4 Conclusion

A multi-technique approach has been used to investigate the room temperature surface oxidation of $(0\,0\,1)$ UN thin films in this chapter. X-ray reflectivity results have shown that this oxidation forms a passivating layer, slowing the

reaction rate. An x-ray photoelectron depth profile taken through this layer showed higher than expected levels of O and N, suggesting that the mechanism for this passivation could be the competing processes of O and N diffusion into and out of the sample.

The results from x-ray diffraction of this surface oxide layer showed that oxidation predominantly occurs epitaxially, as expected, and gave further insight into the stoichiometry. With a lattice parameter of 5.41$\pm$0.04 Å, below the UO_2 value of 5.468 Å, it is hypothesised that the presence of N in the oxide layer causes a reduction of the lattice parameter. Despite the hyperstoichiometry of this $UO_{2+x}N_y$ layer, only the U(VI) state was present. The UO_2 character with high N content seen in this oxidation product provides an explanation for the N retention after complete oxidation seen by Paljevic *et al.* [85].

Analysis of the U-4f^{3+} state in the XPS depth profile has for the first time provided chemical evidence that a U_2N_3 interlayer forms between the surface oxide and UN, and shown this it is present even during low temperature oxidation. Though not discernible with XRR, transimission electron micrographs showed the presence of this interlayer, with a thickness of 20$\pm$5 Å.

As both the surface oxide and this U_2N_3 interlayer contain O and N, they might both be described as oxynitrides, but, when considering the oxidation and corrosion of uranium compounds, it is the oxidation state of U that is of greatest importance. The XPS results showed these layers to have U-4f character the same as seen in UO_2 and U_2N_3, and consequently it has been argued that they would best be described as such, irrespective of their O and N content.

Chapter 7

Corrosion of UN in H_2O_2

This chapter is a comparative investigation into the corrosion of UN, U_2N_3, and UO_2 in H_2O_2 solution, in order to simulate the highly corrosive species that are produced by water radiolysis. Corrosion of UN in water is well documented, however, the effects of radiolysis on UN corrosion are yet to be studied. This work provides a first investigation into this important aspect of spent nuclear fuel corrosion. Results of this chapter have been published in the Journal of Nuclear Materials [194].

7.1 Corrosion of UN

The rapid corrosion of UN in water and steam is considered one of the main roadblocks to UN being used as an advanced technology nuclear fuel [195]. This reaction is of great importance as the majority of current commercial nuclear power plants use water coolant. Though future generations of reactors are not likely to use water as a coolant, it is probable that spent fuel will still be stored in water, awaiting reprocessing or disposal. If the disposal route is taken, and the unprocessed spent fuel stored in a deep geological repository, there is further possibility of interaction between UN and

water. In each of these scenarios, the main concern is that corrosion of UN will cause a degradation of the fuel matrix, leading to the dangerous release of radionuclides, as has shown to be the case with UO_2 [72].

The likely temperatures, pressures, and water chemistry will differ in each of the above scenarios, but as each of these scenarios occur after or during the burning of the fuel, a strong radiation field will be present at the fuel surface. Investigations into the effects of this radiation field have shown it to cause the excitation and dissociation of water molecules creating highly reactive reducing and oxidising radical species in a process known as water radiolysis [17,196]. These radical species have been shown to react readily with UO_2, contrasting with the well-known stability of UO_2 in water [73, 74, 197]. As this reaction has a significant effect on the rate of dissolution of UO_2 in scenarios such as spent fuel storage and disposal, it is crucial that it be considered when predicting and understanding UO_2 fuel corrosion and consequently it is a widely researched topic.

The existing literature on corrosion of UN covers reactions in pure water, in superheated steam, or in solutions of HCl, H_2SO_4, or NaOH, where its performance has been poor, however, the effects of other products of water radiolysis have not yet been considered. Work from the 60s by Sugihara *et al.* showed UN to react with water vapour above 250 °C, releasing H_2, and producing UO_2 and U_2N_3 [198]. Similar work was also carried out by Dell *et al.*, and it was suggested that the oxidised surface on UN afforded it higher corrosion resistance compared to ThN and PuN [81]. Investigations into the effect of pH by Sunder *et al.* showed corrosion rates at only 90 °C to be high at both pH 6 and pH 10, with UO_2 showing very low corrosion rates under the same conditions [78]. It is important to make this comparison as, if it is to be used as an ATF, UN will most likely be replacing UO_2, and UO_2 therefore provides a benchmark for any potential ATF. Additionally, as U_2N_3 has been shown to form during UN oxidation, including U_2N_3 in comparative studies provides insight into the reaction mechanism.

These literature results have shown UN to corrode more rapidly than UO_2, but before UN is dismissed as a potential nuclear fuel, further efforts should be made to explore the reactions that may occur at the UN fuel / water interface. A deeper understanding of these reactions can then allow improved prediction or even mitigation of UN corrosion. As the effect of radiation has been shown to be highly significant in determining the rate of corrosion of UO_2, it is proposed that these effects must be of primary concern when investigating the potential of UN as a nuclear fuel.

To date, no study has investigated the effect of radiation on the corrosion of UN in water. Consequently, the work

described in this chapter has been undertaken to provide an initial investigation into this important factor in nuclear fuel corrosion.

7.1.1 The Effect of Radiation on Corrosion

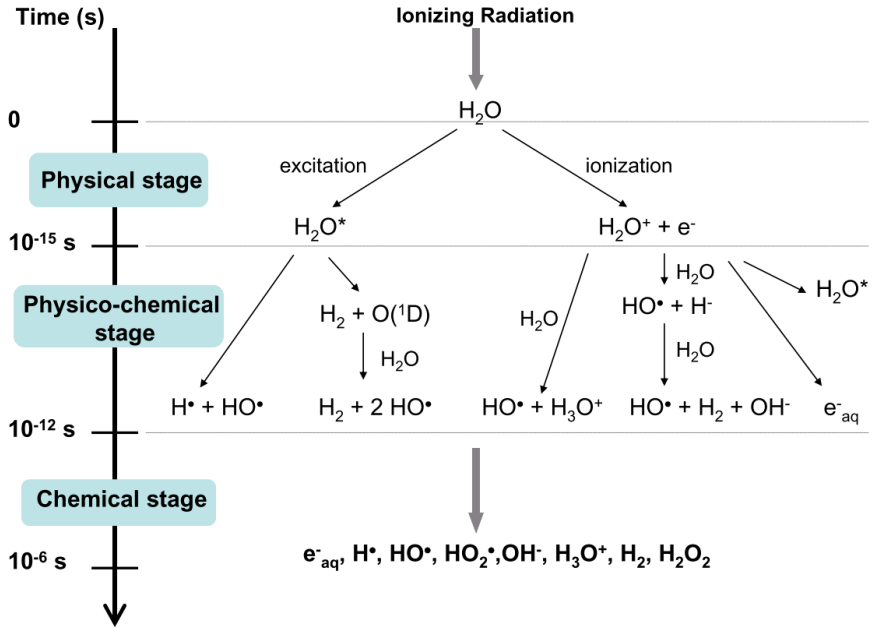

Figure 7.1: *Reactions caused by ionising radiation incident on water molecues, from [17].*

The effect of ionising radiation on water is to produce a wide range of oxidising and reducing species with a wide range of lifetimes, as shown in Figure 7.1 [17]. This happens as the radiation imparts energy to a water molecule, initially causing excitation or ionisation. These species can then dissociate, relax, and react with other molecules, creating a wide range of species. Subsequently, these species then diffuse into the solution, further reacting with each other and surrounding water molecules, producing species such as e^-_{aq}, $H^{\cdot}$, $HO^{\cdot}$, $HO^{\cdot}_2$, OH^-, H_3O^+, H_2, and H_2O_2. Studies have shown that the relative yields of these different products is dependent on the type of radiation [17, 199]. This is of significance to the corrosion of spent fuel, as the levels of neutron, α, β, and γ radiation will change over time.

In the case of UO_2, the highly oxidising species produced by water radiolysis have been shown to be reactive enough to overcome the reducing conditions expected for spent fuel storage and disposal [72]. These species can therefore cause dissolution of the UO_2 fuel matrix by oxidising U(IV) to U(VI), allowing the formation of soluble UO_2^{2+} ions.

Investigations into radiolytic dissolution can either be performed by using a radiation source to induce water radiolysis, by driving the reaction electrochemically, or by simulating the chemical products [74–76, 200]. As many of the radiolytic products have very short lifetimes, the latter approach is often achieved by using solutions of H_2O_2, as it is a product with a relatively long life-time. Additionally, H_2O_2 has been shown to be the most important oxidant in the dissolution of UO_2 under α-radiolysis [201]. Consequently, solutions of H_2O_2 have been used to investigate the effects of water radiolysis on nuclear fuel corrosion in this chapter.

7.2 Corrosion Experiments in H_2O

While the focus of this experiment was to compare corrosion of UN, UO_2, and U_2N_3 in H_2O_2, a preliminary investigation was made into the corrosion of UN, UO_2, and U_2N_3 in water. This was performed in order to investigate their stability in water, to compare results from the present samples with literature results, and to provide a comparison to the effects of H_2O_2.

7.2.1 Experimental Procedures

This investigation was conducted on nanocrystalline films of UN, UO_2, and U_2N_3. All films were grown at room temperature, under the conditions described in Section 3.3. In order to have consistent samples for each material, samples were grown by depositing on two adjacent 10 x 10 mm substrates at a time. These were then cut using a diamond wire saw to produce 8 near identical samples of each material.

One sample each of UN, UO_2, and U_2N_3 was used to investigate corrosion in water by placing the samples individually in 5 ml of MilliQ water at room temperature for a duration of 24 hr. The effect of this exposure to water on the morphology of each sample was measured by performing XRR before and after exposure.

Fitting of the XRR results was performed using GenX software, as described in Section 4.3.2. Films were modeled as a layer of the sample material (UN, UO_2, and U_2N_3), with an oxidised surface layer consisting of UO_2, in the case of the UN and U_2N_3 samples, and UO_x in the case of the UO_2 samples. For consistency, the only variables allowed to change between the fits for before and after exposure were sample material layer (UN, UO_2, or U_2N_3) thickness, oxide

layer thickness, sample material layer roughness, and oxide layer roughness. The density of the UO_x layer at the surface of UO_2 layers was also allowed to vary.

Though there is evidence of a U_2N_3 interlayer forming between UN and its oxidised UO_2 surface, as shown in Section 6.2, it was not included in the model of the UN samples. This is due to the fact that UN and U_2N_3 have very similar scattering length densities, making them indistinguishable with XRR. Consequently, the inclusion of an U_2N_3 interlayer in the model of oxidised UN films makes no discernible difference to the fitted results.

7.2.2 Results

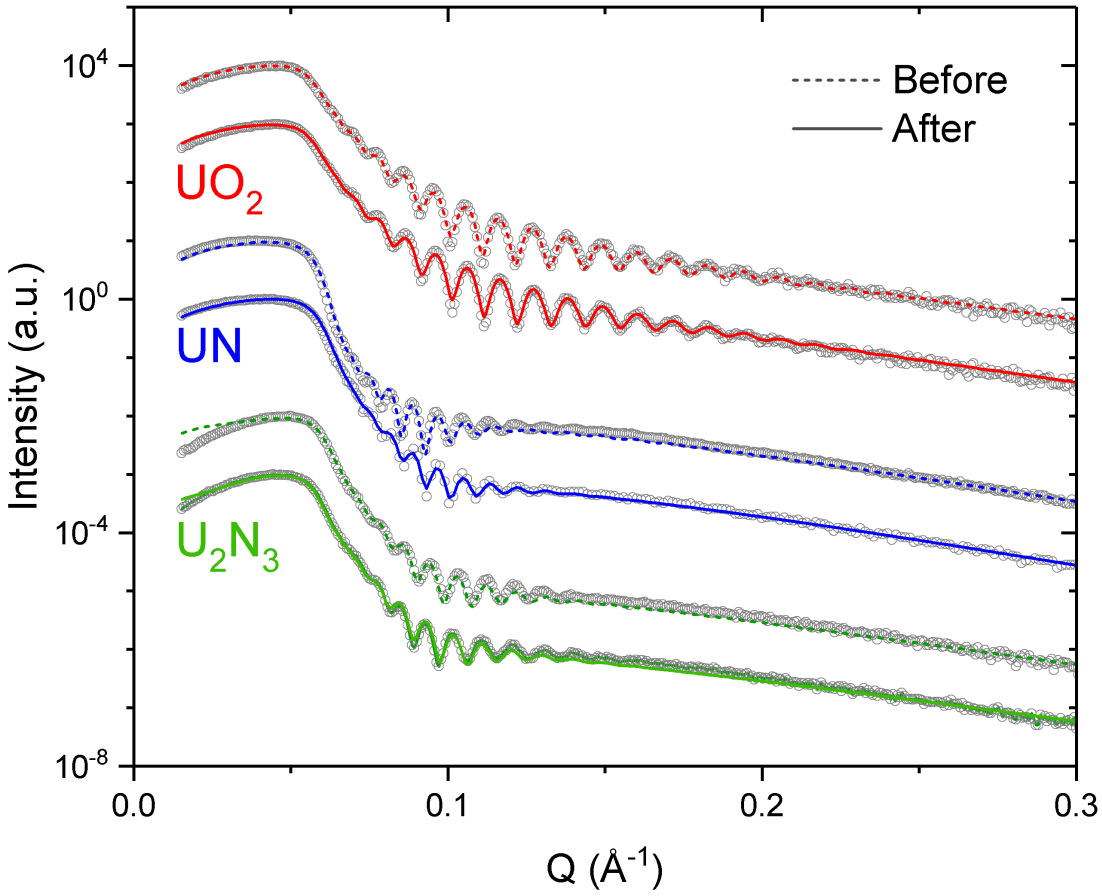

Figure 7.2: *XRR results from before (dashed line) and after (solid line) exposure to H_2O for 24 hr, with UO_2 shown in red, UN shown in blue, and U_2N_3 shown in green.*

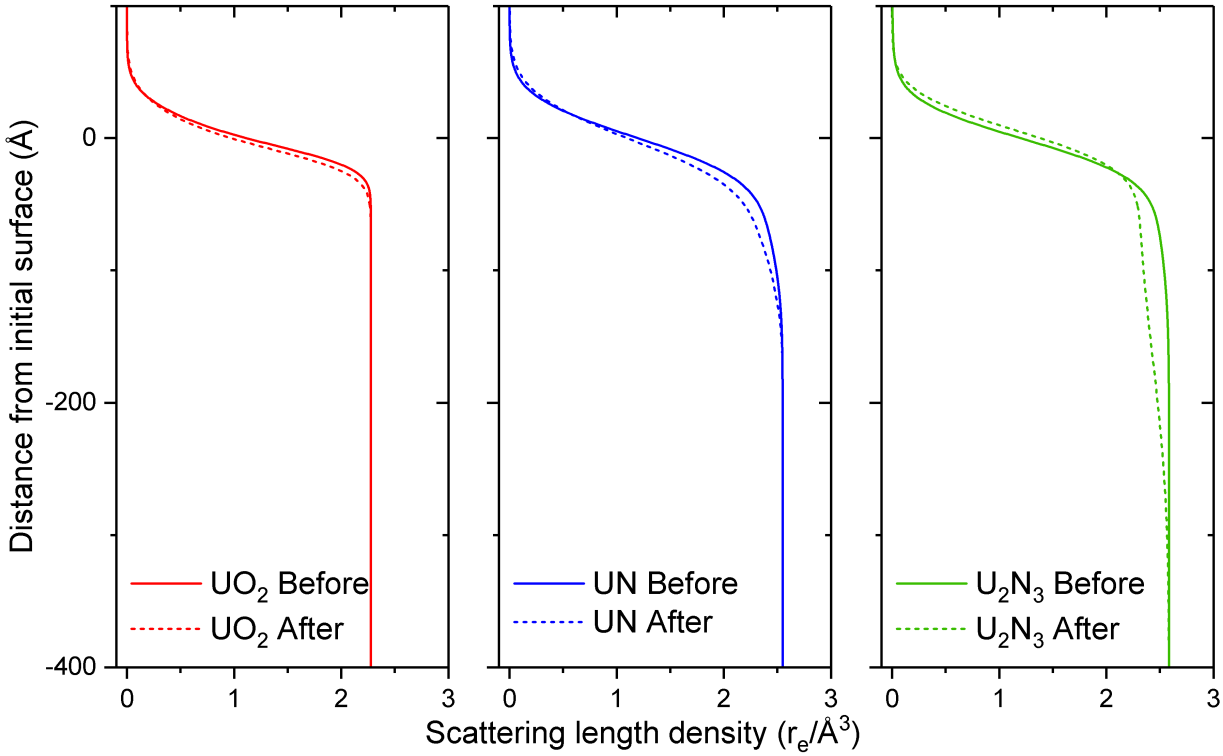

Figure 7.3: *Scattering length density plots obtained from the fitting of XRR data shown in Figure 7.2. Dashed lines show results from before and solid lines after exposure to H_2O for 24 hr, with UO_2 shown in red, UN shown in blue, and U_2N_3 shown in green.*

The results of XRR measurements of UN, UO_2, and U_2N_3 nanocrystalline thin film samples before (dashed line) and after (solid line) exposure to water for 24 hr are shown in Figure 7.2. This figure shows almost no difference in the XRR of the UO_2 sample before and after exposure to water. This is reiterated in the plot of the SLD obtained from XRR fitting shown in Figure 7.3. Only a very small change in gradient at the surface is visible in this plot, indicating a slight roughening.

Conversely, there are some visible changes in the results from the UN and U_2N_3 samples. XRR of the UN sample after exposure to water, shown in Fig 7.2, shows a change in shape compared to before exposure. This is most clearly seen by the lowest trough in the fringes appearing at higher Q after exposure. The respective SLD plot in Fig 7.3 shows this as a drop in density below the surface, corresponding to an increase in the thickness of UO_2 oxide layer. A small

gradient change at the surface in the SLD plot additionally shows some roughening of the surface.

XRR results from the U_2N_3 sample show a decrease in fringe width, showing an increase in sample thickness. This is displayed in the SLD in Fig 7.3. In addition to the fringe width change, the lowest trough in the fringes moves to lower Q. As with UN, the SLD of U_2N_3 after exposure shows a drop in density below the surface, corresponding to an increase in the thickness of the UO_2 oxide layer.

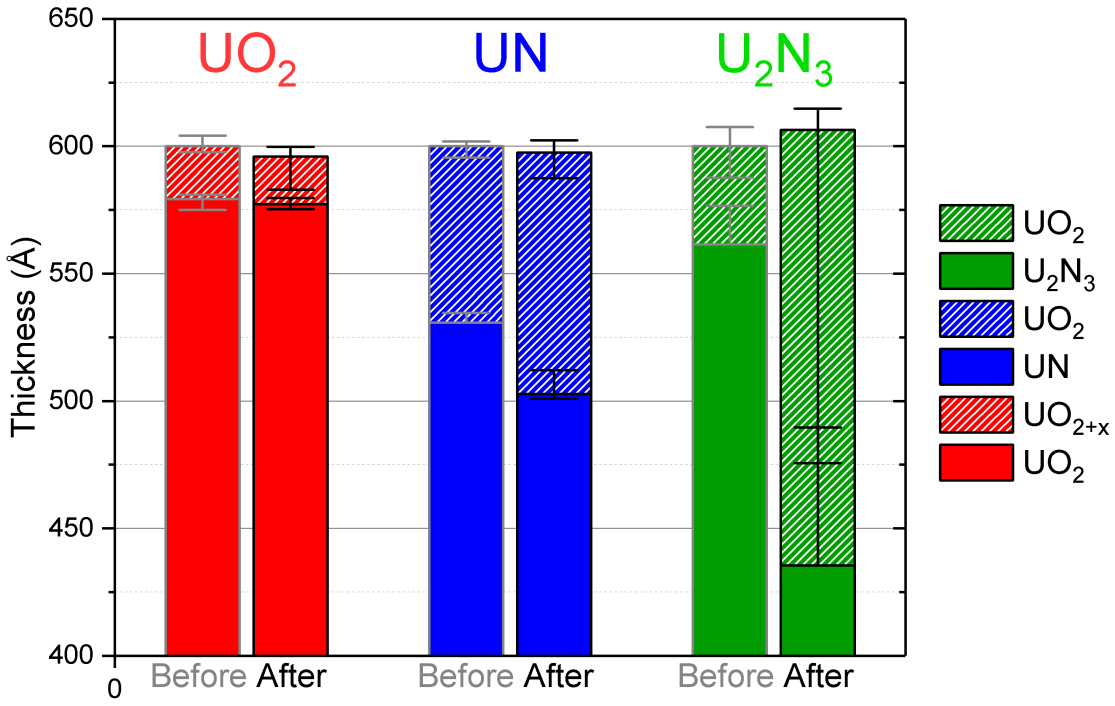

Figure 7.4: *Thickness of film and oxidised surface layer before and after 24 hr exposure to H_2O, with UO_2 shown in red, UN shown in blue, and U_2N_3 shown in green.*

Figure 7.4 shows the overall changes in thickness and oxidised layer thickness of the UN, UO_2, and U_2N_3 samples, before and after exposure to water for 24 hr. This figure shows that UO_2 is unchanged, within errors, as would be expected. UN shows a definite decrease in UN layer thickness of around 20 Å due to the increase of the thickness of the UO_2 oxidised layer after exposure to water for 24 hr.

The results shown in Figure 7.4 suggest large changes in the U_2N_3 samples, however, the uncertainty in these results in greater than for UO_2 and UN, as shown by the error bars. These error bars are largest over the lower bound for the

thickness of the UO_2 oxidised layer and the upper bound of the U_2N_3 layer. From the SLD plots in Fig 7.3, it can be seen that the roughness between the UO_2 oxidised layer and the U_2N_3 layer is high, as shown by the shallow gradient. There is therefore great difficulty in fitting precise values for the thickness of either layers, resulting in the large error values seen in Figure 7.4.

7.3 Corrosion Experiments in H_2O_2

7.3.1 Experimental Procedures

In order to investigate the effects of radiation on the corrosion of UN, UO_2, and U_2N_3, samples of each were exposed to H_2O_2 solution for varying times, with the subsequent change in thickness measure using XRR. A concentration of 0.1 M H_2O_2 solution was selected for use in this experiment. Despite this being much higher than the concentration of H_2O_2 that would be expected at the surface of a submerged spent fuel pellet, it was selected to reproduce the high corrosion rates seen when radiolytic dissolution is simulated with synchrotron radiation [76, 100]. This discrepancy is likely due to much of the radiolytic dissolution being driven by the shorter-lifetime oxidising species when radiolysis is caused by x-rays. Though it may not be representative of spent fuel storage and disposal, a high H_2O_2 concentration and high dissolution rate is more representative of the conditions that could be expected in an accident scenario. Additionally, this high H_2O_2 concentration allows experiments to be completed on a shorter timescale, reducing any errors that could arise from the decomposition of H_2O_2 and other factors such as fluctuations in temperature.

The nanocrystalline UN, UO_2, and U_2N_3 samples used for this experiment are described in Section 7.2.1. The samples of UN, UO_2, and U_2N_3 were individually submerged in 0.1 M H_2O_2 solution for time periods of either 50 s, 250 s, 1250 s, 6000 s, or 4 exposures of 1250 s. A solution volume of greater than 10 ml, large enough to avoid solution saturation, was used, with samples dried upon removal from the solution.

XRR was used to measure the change in surface morphology, with data taken from each sample directly before and after exposure. This data was modeled using GenX software, as described in Section 4.3.2. All instrument parameters were kept constant, with only sample material and oxidised layer thickness, and sample material and oxidised layer roughness allowed to vary across each data set.

7.3.2 Results

7.3.2.1 UO_2

The XRR data and fit of UO_2 samples exposed to 0.1 M H_2O_2 solution for varying times are shown in Figure 7.5 a), with the corresponding SLD plots shown in b). Additionally, a schematic illustration of the fitted values of roughness and thickness, with relative changes to scale, are show in part c). The XRR results in Figure 7.5 a) show an increase in fringe width as a function of exposure time, showing the decrease in thickness of the UO_2 samples, which can be clearly seen in the SLD plots in b). This trend continues until 6000 s, which shows very different XRR results, with very weak, broad fringes and a critical angle which has shifted to Q = 0.03 $Å^{-1}$. A critical angle at this value of Q corresponds to that of the density of the substrate. This shows that much of the substrate is exposed, with some thin remaining UO_2 film causing the broad fringes. From this evidence, it can be said that the UO_2 sample is almost entirely corroded after 6000 s exposure to 0.1 M H_2O_2.

In addition to the XRR data for 6000 s exposure time, a second critical angle at Q = 0.03 $Å^{-1}$ is also present in the results for 250 s and 1250 s. This shows that there are areas of the UO_2 films that have been entirely corroded after 250 s and 1250 s exposure. The relative intensity of this second critical angle in comparison to the critical angle of the UO_2 film, shows that a larger area of the UO_2 film was entirely corroded on the sample exposed for 1250 s compared to that of 250 s. The appearance of this second critical angle, as well as the decrease in the depth of the fringes in the XRR data show a significant increase in UO_2 surface roughness as a function of exposure time. This is apparent in the change in gradient of the SLD plots at the surface of each sample.

It should be noted that there is a large discrepancy between the XRR data and modeled fit for the sample exposed for 1250 s, with the difference in fringe depth showing that the modeled sample should have higher values of roughness.

7.3.2.2 UN

Figure 7.6 shows the fitted XRR data of UN thin film samples exposed to H_2O_2 solution for varying times in a), with the resultant SLD plots in b). The fitted increase in XRR fringe width is shown in the SLD plots as a decrease in total film thickness as a function of exposure time. An exception to this trend comes from the results from the UN sample

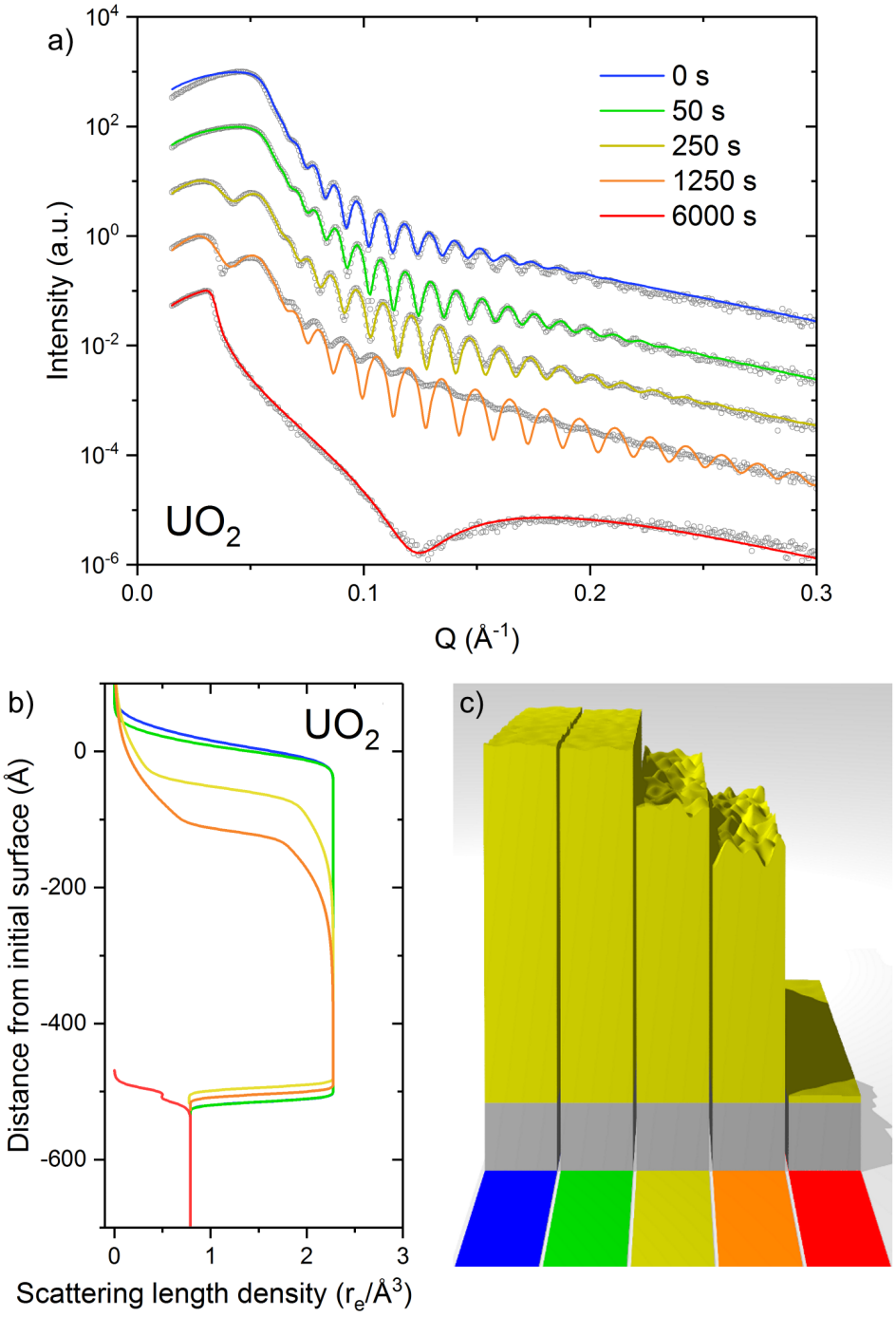

Figure 7.5: *a) Data (grey cirles) and fits (solid lines) of XRR of UO_2 samples after 0 s, 50 s, 250 s, 1250 s, and 6000 s of exposure to H_2O_2, b) SLD obtained from the XRR model as a function of depth, and c) schematic illustrations of UO_2 thin film samples after each exposure time.*

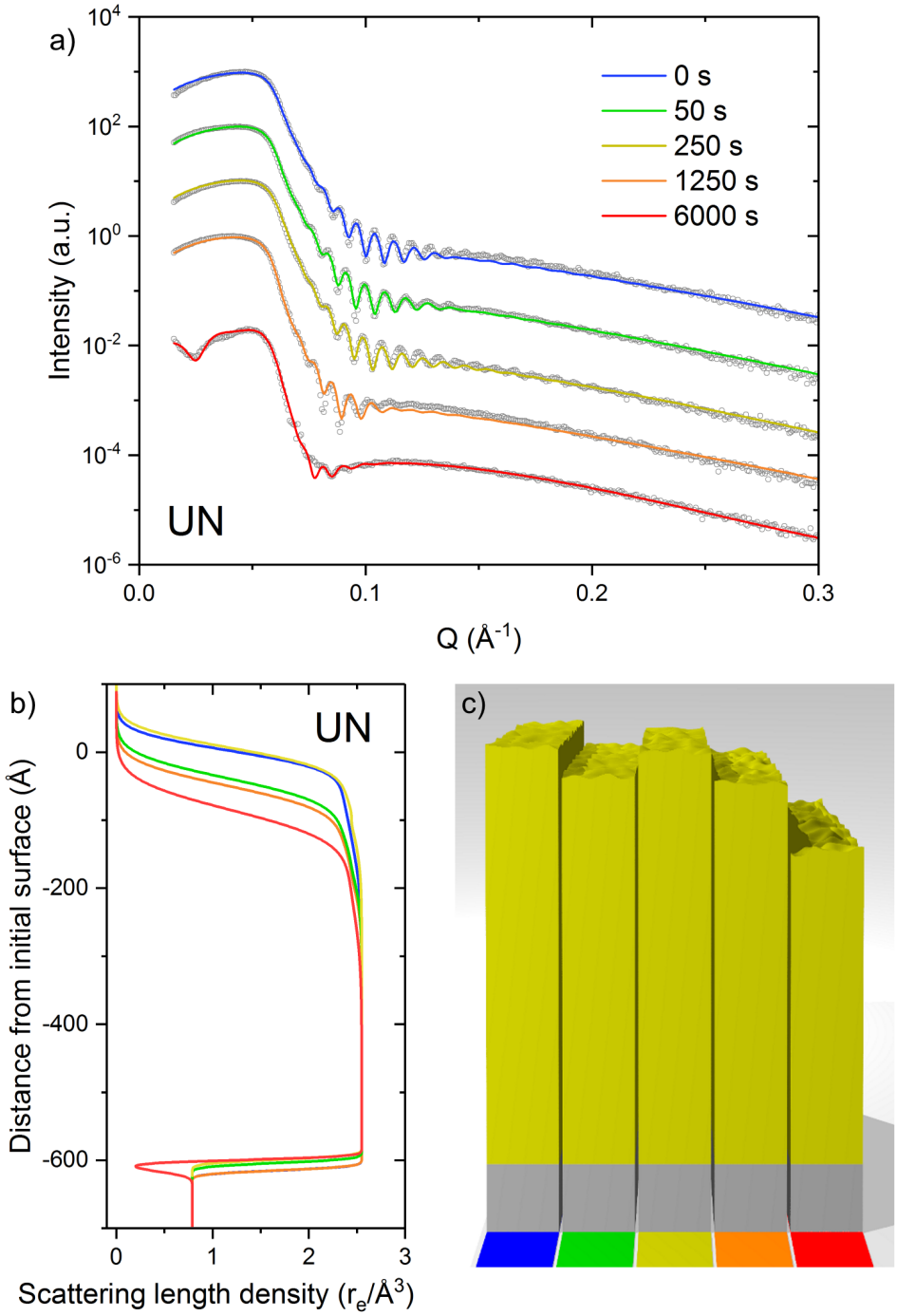

Figure 7.6: *a) Data (grey cirles) and fits (solid lines) of XRR of UN samples after 0 s, 50 s, 250 s, 1250 s, and 6000 s of exposure to H_2O_2, b) SLD obtained from the XRR model as a function of depth, and c) schematic illustrations of UN thin film samples after each exposure time.*

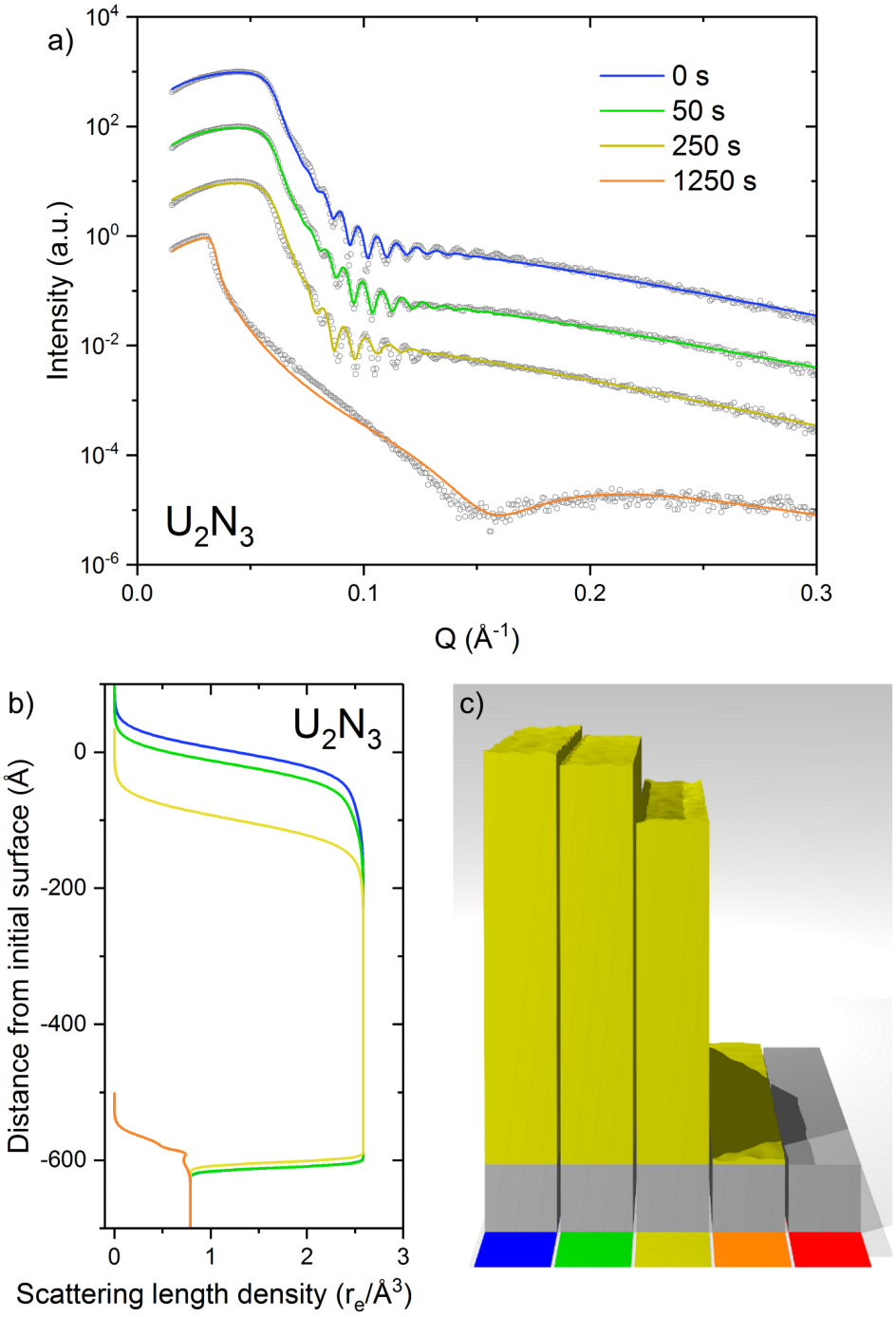

Figure 7.7: *a) Data (grey cirles) and fits (solid lines) of XRR of U_2N_3 samples after 0 s, 50 s, 250 s, and 1250 s of exposure to H_2O_2, b) SLD obtained from the XRR model as a function of depth, and c) schematic illustrations of U_2N_3 thin film samples after each exposure time.*

exposed for 250 s, which shows very little change compared to 0 s.

The UO_2 oxidised surface of the UN samples is not discernible in the XRR data and fit, but can be seen clearly by the dip in density at the surface of the film in the resultant SLD plots. This lower density layer and the gradient of the SLD plots at the surface of this layer do not change significantly as a function of H_2O_2 exposure time up to 1250 s, showing that though UN layer thickness decreases, the surface roughness and oxidised layer do not change with exposure time.

The SLD plot from the UN sample exposed for 6000 s does not quite follow this trend, as it shows a small change in gradient as a result of the decrease in XRR fringe depth, indicative of an increase in surface roughness. This roughness is also shown by the trough in density at the substrate surface, at around -600 Å. This feature is a result of fitting the dip before the critical angle in the XRR data. As with the UO_2 film, this second critical angle corresponds to the density of the substrate, showing that there are some areas of the film which have completely corroded.

7.3.2.3 U_2N_3

XRR results from the U_2N_3 samples exposed to H_2O_2 for varying times are shown in Figure 7.7 a), with SLD plots in b). The XRR data and fit and resultant SLD plots show an increase in fringe width with exposure time, showing the decrease in sample thickness. This trend continues until 1250 s exposure time, where the XRR results show a broad fringe width and shift of the critical angle to Q = 0.03 $Å^{-1}$. These features show that the film is almost entirely corroded, with the critical angle corresponding to the substrate showing that most of the substrate is exposed.

Roughness of the U_2N_3 samples as a function of exposure time show almost no change, as there is no significant change in the depth of the fringes in the XRR data. This is again shown by the shape of the surface in the SLD plots not changing with exposure time, with the exception of the results from the sample exposed for 1250 s, as it is completely corroded.

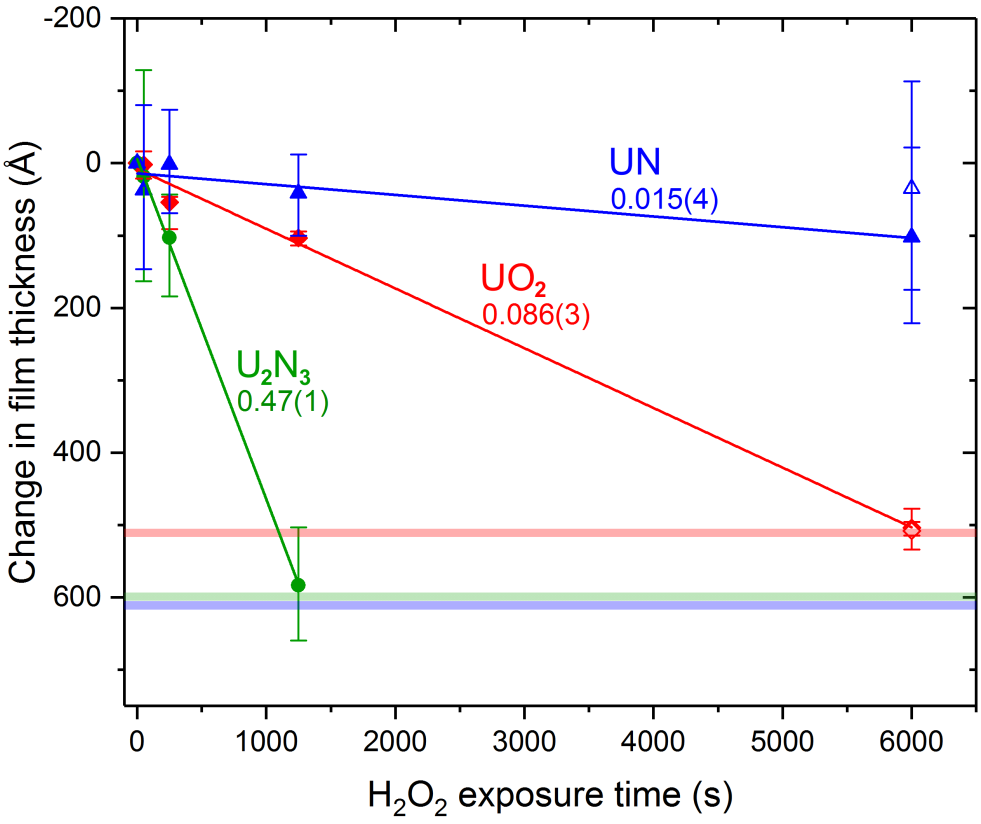

Figure 7.8: *Changes in sample thickness of UO_2 (red diamonds), UN (blue triangles), and U_2N_3 (green circles) as a function of exposure time to H_2O_2. Closed points show single exposures and open points show cumulative time after 4 exposures of 1250 s. The solid line shows a linear fit to the data, labeled with the gradient, and the pale lines denote the initial total sample thickness.*

7.3.2.4 Total Changes

A comparison of the changes in total thickness of the UO_2, UN, and U_2N_3 samples as a function of H_2O_2 exposure time are shown in Figure 7.8. Results for UO_2, UN, and U_2N_3 are shown as red diamonds, blue triangles, and green circles, respectively, with single exposures shown by closed points and 4 x 1250 s exposures shown by open points. As the starting thickness of each sample was not identical, the difference between thickness of each sample before and after exposure has been plotted. Additionally, as there were significant differences in starting thickness between the UO_2, UN, and U_2N_3 samples, the negative average thickness of the samples of each material is denoted by the pale thick lines in red, blue, and green, respectively. This lines therefore indicates the maximum thickness that can be corroded for each

material.

The solid lines in Figure 7.8, showing the linear fits to the data with gradient labeled, display the corrosion rates of the UO_2, UN, and U_2N_3 samples. This plot show that UN is slowest and U_2N_3 is fastest to corrode in 0.1 M H_2O_2, with rates of 0.086±0.003, 0.015±0.004, and 0.47±0.01 $Å s^{-1}$ for UO_2, UN, and U_2N_3, respectively.

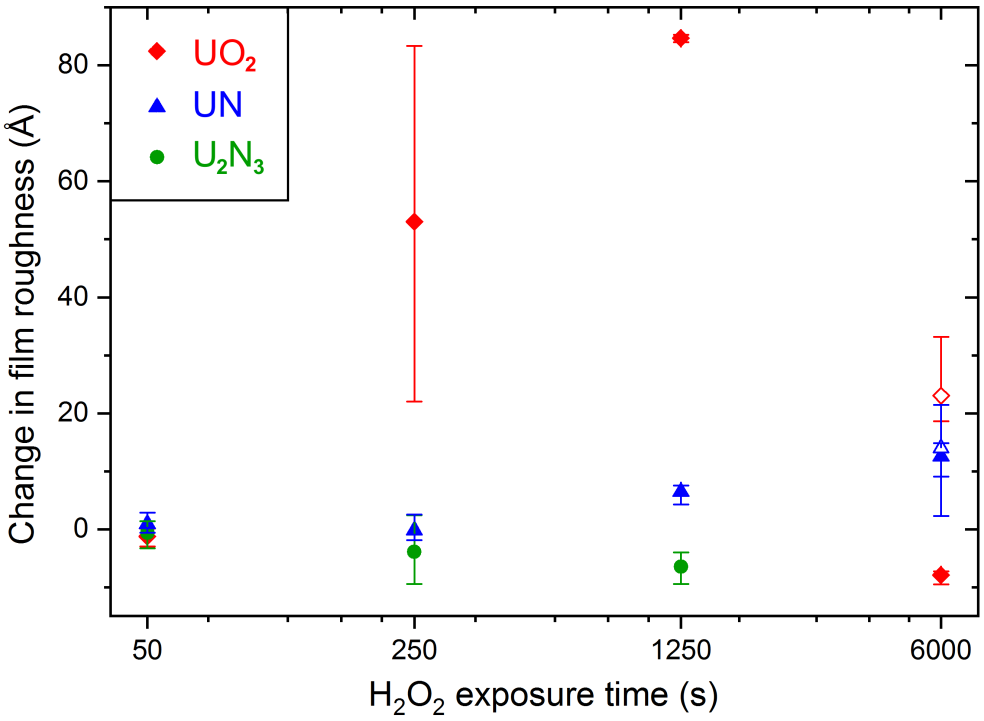

Figure 7.9: *Change in sample roughness of UO_2 (red diamonds), UN (blue triangles), and U_2N_3 (green circles) as a function of exposure time to H_2O_2. Closed points show single exposures and open points show the cumulative time after 4 exposures of 1250 s.*

The changes in the surface roughness of UO_2, UN, and U_2N_3 samples as a function of H_2O_2 exposure time, obtained from XRR fitting, are shown in Figure 7.9. The UO_2 samples show a large increase in roughness with exposure times, while the U_2N_3 samples show a small decrease in roughness. The exceptions to this trend come from the 1250 s U_2N_3 and 6000 s and 4 x 1250 s UO_2 data points, as XRR shows the films so have almost entirely corroded at these times. Consequently, these roughness values are highly influenced by the low roughness of the substrate. This also accounts for the 30 Å discrepancy between the 6000 s and 4 x 1250 s UO_2 data points. Results for the UN samples show a small

increase in roughness with increasing exposure times, with the values for the 6000 s and 4 x 1250 s exposure times being the same, within errors.

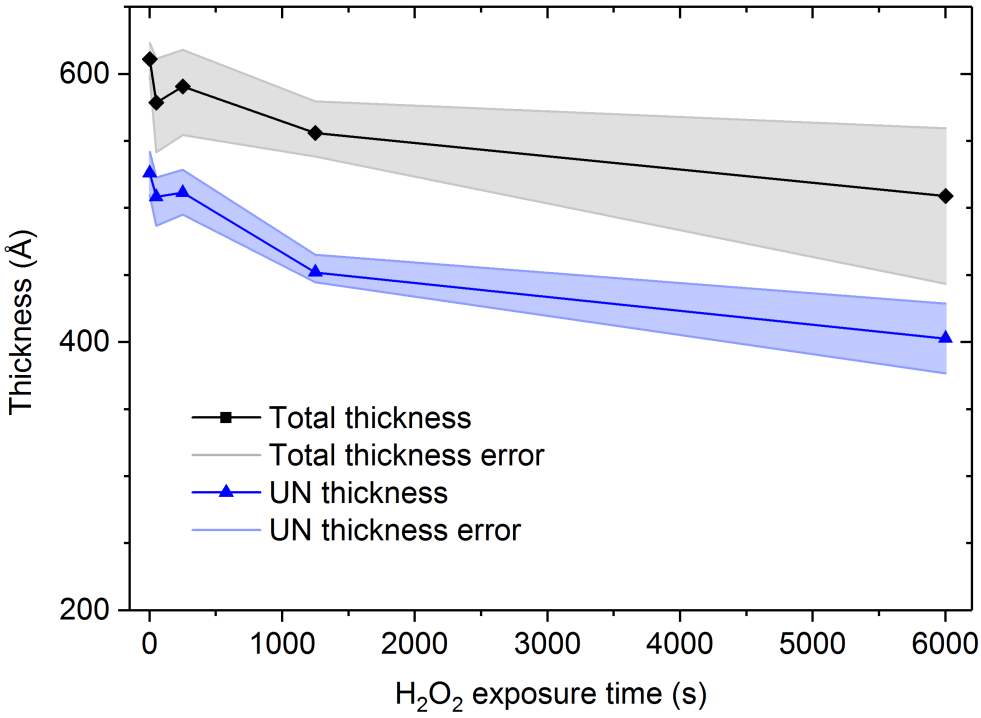

Figure 7.10: *UN layer thickness (blue) and total thickness (black) of the UN thin film samples as a function of H_2O_2 exposure time.*

In order to provide a more detailed look at the H_2O_2 corrosion results from the UN samples, the total sample thickness and UN layer thickness have been plotted in Figure 7.10. Here, the plotted total thickness is the sum of the UN layer thickness and UO_2 oxidised layer thickness. This figure shows that the thickness of the surface oxidised layer of the UN samples does not vary significantly and is therefore independent of exposure time, within errors.

7.4 Discussion

7.4.1 Corrosion Rates

The results obtained from the exposure of UO_2, UN, and U_2N_3 samples to water for 24 hr show that there were no appreciable changes in the UO_2 sample. Though there was a large error on the oxide layer thickness on the U_2N_3 sample

after exposure, the increase in total film thickness shown in Figure 7.2 is most likely caused by a volume expansion that occurred due to the oxidation of the U_2N_3 film, as the U density of UO_2 is 7% lower than U_2N_3. A small increase in the oxide layer thickness was seen for the UN sample. These results are as expected considering the literature on hydrolysis of UO_2, UN, and U_2N_3 [79–81, 198].

Conversely, the results form the corrosion of UO_2, UN, and U_2N_3 samples in 0.1 M H_2O_2 are surprising, with UN slowest to corrode. Linear fits of the data produced corrosion rates of 0.086±0.003, 0.015±0.004, and 0.47±0.01 $Å s^{-1}$, equivalent to 0.033±0.001, 0.013±0.002, and 0.19±0.03 $mg\,cm^{-2}\,hr^{-1}$, for UO_2, UN, and U_2N_3, respectively.

More commonly, exponential or parabolic functions may be used to fit corrosion and oxidation data, as the surface area increases with breakaway oxidation or surface passivation slows corrosion. However, as thin films deposited on highly polished substrates have been used in this experiment, the surface of the samples remains smooth enough that surface area is not a significant factor in corrosion rates, as evidenced by the linear trends in Figure 7.8.

7.4.2 Roughness Changes

Though roughness changes may not be significant in terms of surface area increase, the changes give an insight into the different ways in which corrosion progresses for each material.

UO_2 samples showed a large increase in roughness with exposure time, with an increase of over 80 Å after 1250 s. Considering the large difference in fringe depth between the XRR model and data for this time point, shown in Figure 7.5, it is likely that the true roughness value for this time is even higher. This demonstrates that corrosion was not uniform across the film. In addition to the roughness values, there is evidence for this from the critical angle corresponding to the glass substrate that is present in the XRR data after 250 and 1250 s exposure time, showing that there were areas where film thickness is around 400 Å, and others where the substrate is exposed. This lack of spatial uniformity in the corrosion of the UO_2 samples could possibly be caused by relative differences in the rate of corrosion between different grain orientations or between grains and grain boundaries. Different surface orientations have previously been shown to corrode at different rates during radiolytic dissolution of UO_2 [100].

Contrastingly, the U_2N_3 samples showed no change in surface roughness after exposure to H_2O_2 despite large decreases in thickness, showing that corrosion progressed uniformly and rapidly across the samples. This also contrasts

with the result from exposure of U_2N_3 to H_2O, where the large error on the oxide layer thickness after exposure suggests that U_2N_3 / UO_2 interface roughness is high and is not uniform across the sample.

Results from the UN samples showed some that roughness increased with corrosion, but to a much lesser extent than the UO_2 samples, suggesting that corrosion occurs fairly uniformly across the film.

7.4.3 UN Corrosion Mechanism

Comparing these results to the literature on hydrolysis of UN pellets in steam gives some insight into the surprising differences in corrosion rates between UN and UO_2. Experiments on UN pellets composed of microcrystalline grains in steam environments found that pellet degradation occurred due to intergranular cracking resulting from expansion due to oxidation [79, 80]. The rate of degradation was shown to increase with porosity and grain size. In comparison with these pellets, the thin film samples used in this experiment have high density and much smaller crystallite size. Subsequently, the corrosion of UN is less likely to progress intergranularly and cause microstructural degradation, resulting in fairly uniform corrosion across the film, as is shown by the relatively small changes in UN film roughness during corrosion. Therefore the corrosion rates of UN films in H_2O_2 are likely to be lower than for a UN fuel pellet. This will also be the case for UO_2 thin films and pellets to some extent, and so a comparison of the relative corrosion rates of UN and UO_2 thin films is still meaningful when considering the relative corrosion of UN and UO_2 fuel pellets.

The result that UN corrodes slower than UO_2 in 0.1 M H_2O_2 is surprising considering the literature, but also because the surface of UN is comprised of an UO_2 oxidised layer. This surface layer is displayed by Figure 7.10, which shows it to be independent of corrosion time. However, it is not known if this oxidised layer decreases in thickness during exposure to H_2O_2, reforming on exposure to air, or if it maintains constant thickness during corrosion.

Figure 7.10 showed that this oxidised surface layer is 90 Å thick, so it could be expected that the corrosion rate of the UN would match the corrosion rate of the UO_2 samples for at least the first 90 Å of corrosion, but this does not appear to be the case. It is therefore likely that there is a UO_2 layer of some thickness between 0 and 90 Å present on the surface of UN during exposure to H_2O_2. This contrasts with the results from the U_2N_3 samples, which also have a UO_2 surface layer and corroded rapidly. Consequently, it is suggested that there is a rate limiting step in the oxidation of UN to UO_2^{+2} that is not present in the oxidation of UO_2 to UO_2^{+2} or U_2N_3 to UO_2^{+2}.

The work of Rama Rao *et al.* showed that the rate controlling process of oxidation of UN is the diffusion of nitrogen through the surface UO_2 layer [86]. However, this does not explain the discrepancy between UN and U_2N_3, assuming no significant micro-structural differences between the two. This therefore shows that the corrosion of UN to UO_2^{+2} in H_2O_2 does not follow the oxidation mechanism described by Rama Rao *et al.*, and that the difference between these two mechanisms in not merely the UO_2 to UO_2^{+2} step.

In order to further investigate this mechanism, it would be desirable to measure the thickness of the UO_2 surface layer during corrosion, allowing for the rate at which UN is being oxidised to UO_2 to be determined. This could be performed by *in-situ* measurements of relative intensities of XRD peaks during corrosion. The low volume of the UO_2 layer would produce XRD peaks with very low intensity, creating the need to compromise on error in time in order to reduce the error in peak intensity. This problem could be reduced by the use of an x-ray synchrotron source. Synchrotron radiation can also be simultaneously used to cause water radiolysis, mimicking γ-rays and driving the radiolytic dissolution without the need for H_2O_2 solution [76, 100].

7.5 Conclusion

This work has investigated the effect of water radiolysis on corrosion of UN in comparison with UO_2 an U_2N_3 for the first time, using 0.1 M H_2O_2 to mimic radiolytic products. XRR, performed before and after exposures of varying times, measured the changes in thickness and morphology over time, with corrosion rates found to be 0.086±0.003, 0.015±0.004, and 0.47±0.01 $Å s^{-1}$ for UO_2, UN, and U_2N_3, respectively. Additionally, large changes in roughness were seen for UO_2, but not U_2N_3 and UN, showing that corrosion in H_2O_2 progresses in different ways for each of these materials.

The result that UN corrodes more slowly than UO_2 contrasts with results from corrosion in water. Compared with literature on corrosion of UN in steam, the rates determined in this work are likely slower than would be found for a UN pellet due to differences in microstructure and morphology. Nonetheless, the comparative result with UO_2 is intriguing and suggests that it would be well worth continuing investigations into radiolytic corrosion, altering variables such as microstructure and pressure to replicate more realistic scenarios.

Furthermore, the work presented here has provided some insight into the reaction mechanism for UN corrosion in H_2O_2, showing that it is different to oxidation of UN in air. It is suggested that this mechanism is the cause for the low corrosion rate of UN compared to UO_2, and further work to investigate this hypothesis and better our understanding of UN corrosion is proposed.

Chapter 8

Conclusions and Further Work

When considering the future of commercial nuclear power generation, improvements to safety and economic efficiency are imperative and could be provided in part by using UN as a nuclear fuel. While the robust thermal properties and high uranium density of UN makes it an attractive fuel, there is still much to be understood about its properties and behaviour if it is to become widely used. When trying to expand knowledge on UN, it is sensible to take a fundamental approach to understanding the intrinsic properties of the material. This can be achieved by using ideal samples rather than fuel-realistic samples for investigations, reducing the complexity of measurements and providing easier comparison to theoretical studies.

To achieve this, epitaxial thin film samples of both UN and U_2N_3 have successfully been produced for the first time using reactive DC magnetron sputtering. This is likely to be the first ever single crystal sample of U_2N_3 produced, a material that is of interest as it forms during the oxidation of UN. These novel samples enable a range of measurements and experiments that would not be possible with polycrystalline material. Furthermore, they can be used to create highly uniform samples, and samples sets, giving better control over experiments.

These samples could potentially also be used to further explore the U-N phase diagram. As reactive DC sputtering is

challenging at high reactive gas partial pressures, a U_2N_3 film could be nitrided *ex-situ* to produce a higher nitride film. Since the higher nitrides have similar lattice parameters to U_2N_3, it is possible that this nitriding could be performed epitaxially, producing a single crystal UN_{2-x} sample.

Thin film samples have been characterised with x-ray techniques, giving insight into not only the properties of these films but also the intrinsic properties of UN and U_2N_3. In particular, high resolution x-ray photoelectron spectroscopy (XPS) has shown differences between the bonding in UN and U_2N_3, which have not previously been recognised in the literature. Most significantly, it has allowed the identification of the U(III) valence state and mixed bonding in U_2N_3.

X-ray reflectivity (XRR) has been used in an original way when characterising epitaxial UN films, showing anisotropic roughness correlations at the film interfaces believed to be caused by the miscut between the film and substrate. The method of investigating anisotrpoic roughness correlation of buried interfaces used previously is limited to samples with small miscut angle, however, the approach used here is not. This non-destructive approach could be furthered by using synchrotron radiation, where a smaller beam width would increase the resolution of transverse scans and 2D detectors would give insight into the roughness correlation.

The production of epitaxial U_2N_3 has allowed anisotropic resonant scattering (ARS) measurements, a technique which combines the site selectivity of diffraction with the information provided by resonant scattering, to be performed. This investigation showed that there are differences in the $5f$ states and therefore the bonding on the two distinct U sites in U_2N_3, confirming the mixed bonding seen in XPS results. Furthermore, it was found that the $5f$ charge distribution on the more asymmetric site, U_2, is very likely to have local asphericity. A theoretical investigation would provide more certainty in these results and possibly allow further information to be extracted.

This is the first time that such observations have been made for $5f$ electrons, and shows that ARS measurements can be easily performed at the M_4 edge. These measurements could be insightful for any actinide material with appropriate symmetry conditions. One potential candidate for an ATS study is α-U metal, which has two unique U sites in its orthorhombic structure [202, 203].

Resonant scattering has also been used to investigate the anitferromagnetic (AF) ordering of epitaxial UN and U_2N_3 thin films. This work found that U_2N_3 has a magnetic ordering wave-vector of $q = \langle 0\,0\,1 \rangle$, however, the magnetic structure could not be determined. An experiment at ISIS Neutron and Muon Source using the Wish long-wavelength

diffractometer is planned to resolve this magnetic structure.

Investigations into magnetic ordering of UN confirmed the magnetic ordering wave-vector of $q = \langle 0\,0\,1 \rangle$, however, no single AF domain was found despite the slight tetragonality of the lattice. Comparing results presented here and literature results, it was concluded that the previously accepted type 1-1**k** AF structure of UN was not certain, with a strong possibility that the true structure is type 1-3**k**. Understanding these magnetic properties of UN is important for evaluating models of the electronic structure of UN. As the thermal conductivity of UN is dominated by its electronic contribution, such models are likely to form the basis of predictions of UN nuclear fuel behaviour.

Representing an ideal surface, thin films are useful samples for investigating surface reactions. As the ready oxidation and consequent degradation of UN is one of the main concerns when considering the use of UN as a nuclear fuel, this has been a topic of investigation. The ideal surface of a $(0\,0\,1)$ UN thin film has been used to investigate oxidation at room temperature by using a multi-technique approach to characterise the evolution and composition of the surface oxide layer. This work has shown the passivating effect of the surface layer, and the presence of a U_2N_3 interlayer that was previously only recognised during high temperature oxidation. This result shows that U_2N_3 will always be present at any oxidised UN surface and therefore must been considered when building a complete picture of UN as a nuclear fuel.

This research could be furthered by investigating the effect of temperature on the rate of oxidation and passivation layer thickness with the aim of providing further insight into the reaction mechanism and its rate determining factors. With the precise control of sample properties that is possible when possible using thin film deposition, the effect of factors such as surface orientation and grain boundary density could be explored. Furthermore, nitriding of the sample surface prior to oxidation could be used to investigate the role of the U_2N_3 interlayer in surface oxidation.

XPS results for an oxidised film displayed significant amounts of N present in the surface oxide layer, showing retention of N in $UO_{2+x}N_y$ phase. This provides an explanation for previous work that found that not all N was released after oxidation of UN at high temperature was completed [85]. The fate of N in the oxidation of UN is particularly important when considering the reprocessing of nuclear fuel. If UN fuel is enriched in ^{15}N, it is likely to be costly, possibly making the processing of spent fuel to retrieve and recycle ^{15}N economically viable. This could be achieved by the oxidation of spent fuel, instead of or prior to reprocessing methods such as the PUREX process, which uses nitric

acid and would therefore mix ^{14}N and ^{15}N [204].

This work has highlighted the critical need for a much improved knowledge of the uranium oxynitride system in order to identify the products of UN oxidation. Though there is both theoretical and experimental work on the solubility of O in UN, there is a dearth of data on the crystalline phases that may form and their chemical properties. Consequently, exploration of the U-N-O phase diagram is paramount to improving understanding of the oxidation of UN.

The degradation of UN by the products of water radiolysis has been investigated using H_2O_2 solution to mimic highly corrosive radioytic products. XRR was used to measure the subsequent changes in thickness and morphology of thin films samples caused by this exposure. Despite much recent interest in the corrosion of potential ATFs and evidence that radiolysis can cause the dissolution of UO_2, this important variable has not previously been investigated [76]. Surprisingly, this preliminary study found that polycrystalline UN films corroded more slowly than both UO_2 and U_2N_3. This calls into question the assumption that the poor corrosion performance of UN compared to UO_2 in air and steam environments is representative of behaviour in spent fuel scenarios and shows that it is a topic that should be investigated further to understand the corrosion behaviour of UN nuclear fuel.

Investigating variables such as pH and temperature is vital for considering radiolytic corrosion in realistic scenarios, however, it is likely that in-situ investigations will be necessary to improve the fundamental understanding of these reactions. Recently, chromium doping has shown promise at improving the corrosion resistance of UN during exposure to boiling water [205]. As doping can be easily performed when using sputter deposition, the methodology employed in this work could be used to further investigate the effects of various dopants on these radiolytic corrosion reactions.

Overall, this work has produced novel samples that have allowed measurements to be taken that are the first of their kind. The results have given new insight into the chemical bonding, magnetic properties, and corrosion of uranium nitrides, helping to build understanding of the fundamental physical behaviour and degradation of UN and gaining knowledge which is essential to assessing its viability as a nuclear fuel.

Bibliography

[1] IAEA. *Nuclear Power Reactors in the World*. Number 2 in Reference Data Series. International Atomic Energy Agency, Vienna, 2019.

[2] Tagawa Hiroaki. Phase relations and thermodynamic properties of the uranium-nitrogen system. *Journal of Nuclear Materials*, 51:78–89, 1974.

[3] Jonathan A. Webb and Indrajit Charit. Analytical determination of thermal conductivity of W-UO2 and W-UN CERMET nuclear fuels. *Journal of Nuclear Materials*, 427:87–94, 2012.

[4] Ken Kurosaki, Kimihiko Yano, Kazuhiro Yamada, Masayoshi Uno, and Shinsuke Yamanaka. A molecular dynamics study of the thermal conductivity of uranium mononitride. *Journal of Alloys and Compounds*, 311(2):305–310, 2000.

[5] Jitka Zakova and Janne Wallenius. Fuel residence time in BWRs with nitride fuels. *Annals of Nuclear Energy*, 47:182–191, 2012.

[6] L. Black, F. Miserque, T. Gouder, L. Havela, J. Rebizant, and F. Wastin. Preparation and photoelectron spectroscopy study of UNx thin films. *Journal of Alloys and Compounds*, 315:36–41, 2001.

[7] Sandra Garcia. Free-Electron Lasers. *https://www.helmholtz-berlin.de/forschung/oe/fg/mi-synchrotron-radiation/synchrotron/photons/x-ray-pulses/free-electron-lasers/index_en.html*, page accessed 09/07/2019.

[8] Koichi Momma and Fujio Izumi. VESTA 3 for three-dimensional visualization of crystal, volumetric and morphology data. *Journal of Applied Crystallography*, 44:1272–1276, 2011.

[9] S. P. Collins, A. Bombardi, A. R. Marshall, J. H. Williams, G. Barlow, A. G. Day, M. R. Pearson, R. J. Woolliscroft, R. D. Walton, G. Beutier, and G. Nisbet. Diamond beamline I16 (materials & magnetism). *AIP Conference Proceedings*, 1234:303–306, 2010.

[10] T. M. Holden, J. L. Buyers, E. C. Svensson, and G. H. Lander. Spin correlations in uranium nitride near the ordering temperature. *Physical Review B*, 26(11):6227–6238, 1982.

[11] J. A.C. Marples. An X-ray study of the structures of UN, UP, US and USe at cryogenic temperatures. *Journal of Physics and Chemistry of Solids*, 31(11):2431–2439, 1970.

[12] W. M. Yim and R. J. Paff. Thermal expansion of AlN, sapphire, and silicon. *Journal of Applied Physics*, 45(3):1456–1457, 1974.

[13] K. Shrestha, D. Antonio, M. Jaime, N. Harrison, D. S. Mast, D. Safarik, T. Durakiewicz, J. Griveau, and K. Gofryk. Tricritical point from high-field magnetoelastic and metamagnetic effects in UN. *Scientific Reports*, 7:6642, 2017.

[14] J. A.C. Marples, C. F. Sampson, F. A. Wedgwood, and M. Kuznietz. Actinide pnictides and chalcogenides. IV. X-ray search for tetragonal distortion in UN and UAs in the antiferromagnetic state. *Journal of Physics C: Solid State Physics*, 8(5):708–716, 1975.

[15] C. F. Doorn and P. De V. Plessis. Magnetic properties of single-crystal uranium mononitride. *Journal of Low Temperature Physics*, 28(3-4):391–400, 1977.

[16] R. Troc. Magnetic susceptibility of the uranium nitrides. *Journal of Solid State Chemistry*, 13:14–23, 1975.

[17] Sophie Le Caër. Water Radiolysis: Influence of Oxide Surfaces on H2 Production under Ionizing Radiation. *Water*, 3(4):235–253, 2011.

[18] H. Shimizu. The Properties and Irradiation Behavior of U3Si2. Technical report, Atomics International, 1965.

[19] J. T. White, A. T. Nelson, J. T. Dunwoody, D. D. Byler, D. J. Safarik, and K. J. McClellan. Thermophysical properties of U3Si2 to 1773 K. *Journal of Nuclear Materials*, 464:275–280, 2015.

[20] J. Rest, Y. Kim, G. Holmes, M. Meyer, and S. Hayes. U-Mo Fuels Handbook. Technical report, Argonne National Lab., Argonne, IL, USA, 2006.

[21] Lise Meitner and Otto R. Frisch. Disintegration of Uranium by Neutrons: a New Type of Nuclear Reaction. *Nature*, 143(3615):239, 1939.

[22] H. L. Anderson, E. Fermi, and Leo Szilard. Neutron production and absorption in uranium. *Physical Review*, 56(3):284–286, 1939.

[23] Enrico Fermi. Experimental Production of a Divergent Chain Reaction. *American Journal of Physics*, 20(9):536–558, 1952.

[24] H. H. Windsor. Atomic Reactor Makes Electricity. *Popular Mechanics*, page 105, mar 1952.

[25] N. J. MacKay and E. Hardwick. Electrical installation at Calder Hall nuclear power station. *Proceedings of the IEE Part A: Power Engineering*, 106(27):245, 1958.

[26] Raymond Murray and Keith E. Holbert. *Nuclear energy: an introduction to the concepts, systems, and applications of nuclear processes*. Elsevier, Oxford, UK, 7th edition, 2015.

[27] H. Safa. Heat recovery from nuclear power plants. *International Journal of Electrical Power and Energy Systems*, 42:553–559, 2012.

[28] C. Bagger, M. Mogensen, and C. T. Walker. Temperature measurements in high burnup UO2 nuclear fuel: Implications for thermal conductivity, grain growth and gas release. *Journal of Nuclear Materials*, 211:11–29, 1994.

[29] D. Manara, C. Ronchi, M. Sheindlin, M. Lewis, and M. Brykin. Melting of stoichiometric and hyperstoichiometric uranium dioxide. *Journal of Nuclear Materials*, 342:148–163, 2005.

[30] Mitchell Rogovin. Three Mile Island: A report to the commissioners and to the public. Technical report, Nuclear Regulatory Commission, Washington DC, USA, 1979.

[31] R. S. Denning. The Three Mile Island Unit 2 core: a post-mortem examination. *Annual Review of Energy*, 10:35–52, 1985.

[32] Masayoshi Yamamoto. Overview of the Fukushima Dai-ichi Nuclear Power Plant (FDNPP) accident, with amounts and isotopic compositions of the released radionuclides. *Journal of Radioanalytical and Nuclear Chemistry*, 303(2):1227–1231, 2015.

[33] Ken Buesseler, Minhan Dai, Michio Aoyama, Claudia Benitez-Nelson, Sabine Charmasson, Kathryn Higley, Vladimir Maderich, Pere Masqué, Paul J. Morris, Deborah Oughton, and John N. Smith. Fukushima Daiichi-Derived Radionuclides in the Ocean: Transport, Fate, and Impacts. *Annual Review of Marine Science*, 9:173–203, 2017.

[34] Naohiro Yoshida and Jota Kanda. Tracking the Fukushima Radionuclides. *Science*, 336(6085):1115–1116, 2012.

[35] Shannon Bragg-Sitton. Development of advanced accident-tolerant fuels for commercial LWRs. *Nuclear News*, 57(3):83–91, 2014.

[36] S. J. Zinkle, K. A. Terrani, J. C. Gehin, L. J. Ott, and L. L. Snead. Accident tolerant fuels for LWRs: A perspective. *Journal of Nuclear Materials*, 448(1-3):374–379, 2014.

[37] Gilles J. Youinou and R. Sonat Sen. Impact of Accident-Tolerant Fuels and Claddings on the Overall Fuel Cycle: A Preliminary Systems Analysis. *Nuclear Technology*, 188(2):123–138, 2014.

[38] Xiaoli Wu, Wei Li, Yang Wang, Yapei Zhang, Wenxi Tian, Guanghui Su, Suizheng Qiu, Tong Liu, Yongjun Deng, and Heng Huang. Preliminary safety analysis of the PWR with accident-tolerant fuels during severe accident conditions. *Annals of Nuclear Energy*, 80:1–13, 2015.

[39] L. J. Ott, K. R. Robb, and D. Wang. Preliminary assessment of accident-tolerant fuels on LWR performance during normal operation and under DB and BDB accident conditions. *Journal of Nuclear Materials*, 461:178–179, 2015.

[40] Bo Cheng, Young Jin Kim, and Peter Chou. Improving Accident Tolerance of Nuclear Fuel with Coated Mo-alloy Cladding. *Nuclear Engineering and Technology*, 48(1):16–25, 2016.

[41] Fauzia Khatkhatay, Liang Jiao, Jie Jian, Wenrui Zhang, Zhijie Jiao, Jian Gan, Hongbin Zhang, Xinghang Zhang, and Haiyan Wang. Superior corrosion resistance properties of TiN-based coatings on Zircaloy tubes in supercritical water. *Journal of Nuclear Materials*, 451:346–351, 2014.

[42] Hyun Gil Kim, Jae Ho Yang, Weon Ju Kim, and Yang Hyun Koo. Development Status of Accident-tolerant Fuel for Light Water Reactors in Korea. *Nuclear Engineering and Technology*, 48:1–15, 2016.

[43] K. A. Terrani, D. Wang, L. J. Ott, and R. O. Montgomery. The effect of fuel thermal conductivity on the behavior of LWR cores during loss-of-coolant accidents. *Journal of Nuclear Materials*, 448:512–519, 2014.

[44] R. M. Dell, V. J. Wheeler, and E. J. McIver. The Oxidation and Ignition of Uranium Mononitride and Uranium Monocarbide. *Transactions of the Faraday Society*, 62:3591–3606, 1966.

[45] R. E. Rundle, N. C. Baenziger, A. S. Wilson, and R. A. McDonald. The structures of the carbides, nitrides and oxides of uranium. *Journal of the American Chemical Society*, 70(55):99–105, 1948.

[46] A. A. Aczel, G. E. Granroth, G. J. Macdougall, W. J. L. Buyers, D. L. Abernathy, G. D. Samolyuk, G. M. Stocks, and S. E. Nagler. Quantum oscillations of nitrogen atoms in uranium nitride. *Nature Communications*, 3:1124, 2012.

[47] C. L. Hoenig. Phase Equilibria, Vapor Pressure, and Kinetic Studies in the Uranium-Nitrogen System. *Journal of the American Ceramic Society*, 54:391–398, 1971.

[48] A. Yu Kuksin, S. V. Starikov, D. E. Smirnova, and V. I. Tseplyaev. The diffusion of point defects in uranium mononitride: Combination of DFT and atomistic simulation with novel potential. *Journal of Alloys and Compounds*, 658:385–394, 2016.

[49] E. A. Kotomin, R. W. Grimes, Y. Mastrikov, and N. J. Ashley. Atomic scale DFT simulations of point defects in uranium nitride. *Journal of Physics: Condensed Matter*, 19(10):106208, 2007.

[50] Mehmet Erbudak and Jaime Keller. Electronic Structure of Cubic Uranium Compounds. *Zeitschrift for Physik B*, 32:281–286, 1979.

[51] J. M. Fournier, J. Beille, A. Boeuf, C. Vettier, and F. A. Wedgwood. Magnetic structure of UN under pressure. *Physica B: Physics of Condensed Matter*, 102(1-3):282–284, 1980.

[52] B. Reihl, G. Hollinger, and F. J. Himpsel. Angle-resolved photoemission and temperature dependence of 5f electronic states in uranium nitride. *Journal of Magnetism and Magnetic Materials*, 29:303–304, 1982.

[53] B. Reihl, G. Hollinger, and F. J. Himpsel. Itinerant-5f-electron antiferromagnetism in uranium nitride: A temperature-dependent angle-resolved photoemission study. *Physical Review B*, 28(3):1490–1494, 1983.

[54] Shin Ichi Fujimori, Takuo Ohkochi, Tetsuo Okane, Yuji Saitoh, Atsushi Fujimori, Hiroshi Yamagami, Yoshinori Haga, Etsuji Yamamoto, and Yoshichika Onuki. Itinerant nature of U-5f states in uranium mononitride revealed by angle-resolved photoelectron spectroscopy. *Physical Review B*, 86(23):235108, 2012.

[55] N. A. Curry. An investigation of the magnetic structure of uranium nitride by neutron diffraction. *Proceeding of the Physical Society*, 86:1193–1198, 1965.

[56] R. H. Lemmer and J. E. Lowther. Magnetic properties of uranium monopnictides. *Journal of Physics C: Solid State Physics*, 11:1145, 1978.

[57] M. Samsel-Czekała, E. Talik, P. de V. Du Plessis, R. Troc, H. Misiorek, and C. Sulkowski. Electronic structure and magnetic and transport properties of single-crystalline UN. *Physical Review B*, 76(14):144426, 2007.

[58] R. Troć, M. Samsel-Czekała, A. Pikul, A. V. Andreev, D. I. Gorbunov, Y. Skourski, and J. Sznajd. Electronic structure of un based on specific heat and field-induced transitions up to 65 T. *Physical Review B*, 94(22):224415, 2016.

[59] M. S. S. Brooks. Electronic structure of NaCl-type compounds of the light actinides. II. Uranium monochalcogenides and monopnictides. *Journal of Physics F: Metal Physics*, 14:653–661, 1984.

[60] P. R. Norton, R. L. Tapping, D. K. Creber, and W. J. L. Buyers. Nature of the 5f electrons in uranium nitride: A photoelectron spectroscopic study of UN, U, UO2, ThN, and Th. *Physical Review B*, 21(6):2572–2577, 1980.

[61] H. W. Knott, G. H. Lander, M. H. Mueller, and O. Vogt. Search for lattice distortions in UN, UAs, and USb at low temperatures. *Physical Review B*, 21(9):4159–4165, 1980.

[62] J. Rossat-Mignod, P. Burlet, S. Quezel, and O. Vogt. Magnetic ordering in cerium and uranium monopnictides. *Physica B: Physics of Condensed Matter*, 102:237–248, 1980.

[63] M. J. Sole and C. M. Van der Walt. Oxidation and deformation studies of uranium nitride by electron microscopy. *Acta Metallurgica*, 16:501–510, 1968.

[64] H. Serizawa, K. Fukuda, Y. Ishii, Y. Morii, and M. Katsura. Crystallographic study on the phase transition of alpha-U2N3. *Journal of Nuclear Materials*, 208:128–134, 1994.

[65] Xiaofang Wang, Zhong Long, Ren Bin, Ruilong Yang, Qifa Pan, Fangfang Li, Lizhu Luo, Yin Hu, and Kezhao Liu. Study of the decomposition and phase transition of uranium nitride under UHV conditions via TDS, XRD, SEM, and XPS. *Inorganic Chemistry*, 55:10835–10838, 2016.

[66] Lizhu Luo, Lei Lu, Donghai Zhao, Huanlin Zhang, Taihui Jing, and Kezhao Liu. Surface oxidation on U2N(3+x)Oy films in oxygen atmosphere by XPS. *Journal of Electron Spectroscopy and Related Phenomena*, 217:6–10, 2017.

[67] R. A. Evarestov, A. I. Panin, A. V. Bandura, and M. V. Losev. Electronic structure of crystalline uranium nitrides UN, U2N3 and UN2: LCAO calculations with the basis set optimization. *Journal of Physics: Conference Series*, 117(1):012015, 2008.

[68] S. L. Hayes, J. K. Thomas, and K. L. Peddicord. Material property correlations for uranium mononitride. IV. Thermodynamic properties. *Journal of Nuclear Materials*, 171:262–270, 1990.

[69] D. G. Martin. The thermal expansion of solid UO2 and (U, Pu) mixed oxides - a review and recommendations. *Journal of Nuclear Materials*, 152:94–101, 1988.

[70] Nicholas R. Brown, Arnold Aronson, Michael Todosow, Ryan Brito, and K. J. McClellan. Neutronic performance of uranium nitride composite fuels in a PWR. *Nuclear Engineering and Design*, 275:393–407, 2014.

[71] M. F. Lyons, R. F. Boyle, J. H. Davies, V. E. Hazel, and T. C. Rowland. UO2 properties affecting performance. *Nuclear Engineering and Design*, 21(2):167–199, 1972.

[72] D. W. Shoesmith. Fuel corrosion processes under waste disposal conditions. *Journal of Nuclear Materials*, 282:1–31, 2000.

[73] D. W. Shoesmith. Used Fuel and Uranium Dioxide Dissolution Studies: A Review. Technical Report July, Nuclear Waste Management Organisation, 2007.

[74] M. G. Bailey, L. H. Johnson, and D. W. Shoesmith. The effects of the alpha-radiolysis of water on the corrosion of UO2. *Corrosion Science*, 25(4):233–238, 1985.

[75] S. Sunder, D. W. Shoesmith, and N. H. Miller. Oxidation and dissolution of nuclear fuel (UO2) by the products of the alpha radiolysis of water. *Journal of Nuclear Materials*, 244:66–74, 1997.

[76] Ross Springell, Sophie Rennie, Leila Costelle, James Darnbrough, Camilla Stitt, Elizabeth Cocklin, Chris Lucas, Robert Burrows, Howard Sims, Didier Wermeille, Jonathan Rawle, Chris Nicklin, William Nuttall, Thomas Scott, and Gerard Lander. Water corrosion of spent nuclear fuel: radiolysis driven dissolution at the UO2 /water interface. *Faraday Discussions*, 180:301–311, 2015.

[77] M. E. Torrero, E. Baraj, Joan De Pablo, Javier Giménez, and Ignasi Casas. Kinetics of Corrosion and Dissolution of Uranium Dioxide as a Function of pH. *International Journal of Chemical Kinetics*, 29(4):261–267, 1997.

[78] S. Sunder and N. H. Miller. XPS and XRD studies of corrosion of uranium nitride by water. *Journal of Alloys and Compounds*, 271-273:568–572, 1998.

[79] Mikael Jolkkonen, Pertti Malkki, Kyle Johnson, and Janne Wallenius. Uranium nitride fuels in superheated steam. *Journal of Nuclear Science and Technology*, 54(5):513–519, 2017.

[80] Denise Adorno Lopes, Selim Uygur, and Kyle Johnson. Degradation of UN and UNU3Si2 pellets in steam environment. *Journal of Nuclear Science and Technology*, 54(4):405–413, 2017.

[81] R. M. Dell, V. J. Wheeler, and N. J. Bridger. Hydrolysis of uranium mononitride. *Transactions of the Faraday Society*, 63:1286–1294, 1967.

[82] Jennifer K. Watkins, Darryl P. Butt, and Brian J. Jaques. Microstructural degradation of UN and UN-UO2 composites in hydrothermal oxidation conditions. *Journal of Nuclear Materials*, 518:30–40, 2019.

[83] J. E. Antill and B. L. Myatt. Kinetics of the oxidation of UN and U(CO) in carbon dioxide, steam and water at elevated temperatures. *Corrosion Science*, 6:17–23, 1966.

[84] Katsuichi Ikawa and Kiyoaki Taketani. Room temperature oxidation of UN powder. *Journal of Nuclear Science and Technology*, 7(9):433–438, 1970.

[85] M. Paljević and Z. Despotović. Oxidation of uranium mononitride. *Journal of Nuclear Materials*, 57:253–257, 1975.

[86] G. A. Rama Rao, S. K. Mukerjee, V. N. Vaidya, V. Venugopal, and D. D. Sood. Oxidation and hydrolysis kinetic studies on UN. *Journal of Nuclear Materials*, 185(2):231–241, 1991.

[87] H. Matzke. On the rim effect in high burnup UO2 LWR fuels. *Journal of Nuclear Materials*, 189(1):141–148, 1992.

[88] J. Rest, M. W.D. Cooper, J. Spino, J. A. Turnbull, P. Van Uffelen, and C. T. Walker. Fission gas release from UO 2 nuclear fuel: A review. *Journal of Nuclear Materials*, 513:310–345, 2019.

[89] F. Cappia, D. Pizzocri, M. Marchetti, A. Schubert, P. Van Uffelen, L. Luzzi, D. Papaioannou, R. Macián-Juan, and V. V. Rondinella. Microhardness and Young's modulus of high burn-up UO2 fuel. *Journal of Nuclear Materials*, 479:447–454, 2016.

[90] Masaki Amaya, Mutsumi Hirai, Hiroshi Sakurai, Kenichi Ito, Masana Sasaki, Terumitsu Nomata, Katsuichiro Kamimura, and Ryo Iwasaki. Thermal conductivities of irradiated UO2 and (U,Gd)O2 pellets. *Journal of Nuclear Materials*, 300:57–64, 2002.

[91] Trygve E. Eriksen, Ulla Britt Eklund, Lars Werme, and Jordi Bruno. Dissolution of irradiated fuel: a radiolytic mass balance study. *Journal of Nuclear Materials*, 227:76–82, 1995.

[92] Frédérico Garrido, Laetitia Vincent, Lech Nowicki, Gaël Sattonnay, and Lionel Thomé. Radiation stability of fluorite-type nuclear oxides. *Nuclear Instruments and Methods in Physics Research B*, 266:2842–2847, 2008.

[93] William F. Cureton, Raul I. Palomares, Jeffrey Walters, Cameron L. Tracy, Chien Hung Chen, Rodney C. Ewing, Gianguido Baldinozzi, Jie Lian, Christina Trautmann, and Maik Lang. Grain size effects on irradiated CeO2, ThO2, and UO2. *Acta Materialia*, 160:47–56, 2018.

[94] E. D. Albrecht, A. J. Rothman, J. D. Lee, J. M. Johnson, and W. N. Hayes. A high-temperature irradiation and post-irradiation analysis of uranium nitride fuel. Technical report, Lawrence Livermore Laboratory, Univeristy of California, USA, 1969.

[95] Steven B. Ross, Mohamed S. El-Genk, and R. B. Matthews. Uranium nitride fuel swelling correlation. *Journal of Nuclear Materials*, 170:169–177, 1990.

[96] R. B. Matthews, K. M. Chidester, C. W. Hoth, R. E. Mason, and R. L. Petty. Fabrication and testing of uranium nitride fuel for space power reactors. *Journal of Nuclear Materials*, 151(3):345, 1988.

[97] Krishna Seshan. *Handbook of Thin Film Deposition: techniques, processes, and technologies*. Elsevier, Oxford, UK, 3rd edition, 2012.

[98] S. D. Senanayake, G. I. N. Waterhouse, A. S. Y. Chan, T. E. Madey, D. R. Mullins, and H. Idriss. Probing surface oxidation of reduced uranium dioxide thin film using synchrotron radiation. *Journal of Physical Chemistry C*, 111(22):7963–7970, 2007.

[99] S. Stumpf, A. Seibert, T. Gouder, F. Huber, T. Wiss, J. Römer, and M. A. Denecke. Development of fuel-model interfaces: Characterization of Pd containing UO2 thin films. *Journal of Nuclear Materials*, 397:19–26, 2010.

[100] S. Rennie, E. Lawrence Bright, J. E. Sutcliffe, J. E. Darnbrough, R. Burrows, J. Rawle, C. Nicklin, G. H. Lander, and R. Springell. The role of crystal orientation in the dissolution of UO2 thin films. *Corrosion Science*, 145:162–169, 2018.

[101] Lei Lu, Fangfang Li, Yin Hu, Hong Xiao, Bin Bai, Yanzhi Zhang, Lizhu Luo, Jing Liu, and Kezhao Liu. The initial oxidation behaviors of uranium nitride UNx (x=0, 0.23, 0.68, 1.66) films. *Journal of Nuclear Materials*, 480:189–194, 2016.

[102] Mark J. Noordhoek, David Andersson, and Theodore M. Besmann. Structure determination and stability for Pa-Si, Np-Si and U-X-Si (X = Mo, Th, Np) phases from first-principles. *Journal of Nuclear Materials*, 479:593–607, 2016.

[103] Michael R. Tonks, Xiang Yang Liu, David Andersson, Danielle Perez, Aleksandr Chernatynskiy, Giovanni Pastore, Christopher R. Stanek, and Richard Williamson. Development of a multiscale thermal conductivity model for fission gas in UO2. *Journal of Nuclear Materials*, 469:89–98, 2016.

[104] R. Springell, B. Detlefs, G. H. Lander, R. C. C. Ward, R. A. Cowley, N. Ling, W. Goetze, R. Ahuja, W. Luo, and B. Johansson. Elemental engineering: Epitaxial uranium thin films. *Physical Review B*, 78(19):193403, 2008.

[105] A. Kaul, O. Gorbenko, M. Novojilov, A. Kamenev, A. Bosak, A. Mikhaylov, O. Boytsova, and M. Kartavtseva. Epitaxial stabilization - A tool for synthesis of new thin film oxide materials. *Journal of Crystal Growth*, 275:2445–2451, 2005.

[106] C. M. Silva, R. D. Hunt, L. L. Snead, and K. A. Terrani. Synthesis of phase-pure U2N3 microspheres and its decomposition into un. *Inorganic Chemistry*, 54:293–298, 2015.

[107] K. van Dijk, H. G. Schaeken, C. H. M. Marée, J. Verhoeven, J. C. G. Wolke, F. H. P. M. Habraken, and J. A. Jansen. Influence of Ar pressure on r.f. magnetron-sputtered Ca5(PO4)3OH layers. *Surface and Coatings Technology*, 76-77:206–210, 1995.

[108] Yeon Sik Jung, Dong Wook Lee, and Duk Young Jeon. Influence of dc magnetron sputtering parameters on surface morphology of indium tin oxide thin films. *Applied Surface Science*, 221(1-4):136–142, 2004.

[109] Eugenia Mirica, Glen Kowach, Paul Evans, and Henry Du. Morphological Evolution of ZnO Thin Films Deposited by Reactive Sputtering. *Crystal Growth and Design*, 4(1):147–156, 2004.

[110] C. Sürgers, C. Strunk, and H. v. Löhneysen. Effect of substrate temperature on the microstructure of thin niobium films. *Thin Solid Films*, 239:51–56, 1994.

[111] P. Eklund, M. Beckers, J. Frodelius, H. Högberg, and L. Hultman. Magnetron sputtering of Ti3SiC2 thin films from a compound target. *Journal of Vacuum Science & Technology A*, 25(5):1381, 2007.

[112] Jörg Neidhardt, Stanislav Mráz, Jochen M. Schneider, Erik Strub, Wolfgang Bohne, Bartosz Liedke, Wolfhard Möller, and Christian Mitterer. Experiment and simulation of the compositional evolution of Ti-B thin films deposited by sputtering of a compound target. *Journal of Applied Physics*, 104(6):063304, 2008.

[113] M. Eckle and T. Gouder. Photoemission study of UNxOyand UCxOy in thin films. *Journal of Alloys and Compounds*, 374:261–264, 2004.

[114] Melissa M. Strehle, Brent J. Heuser, Mohamed S. Elbakhshwan, Xiaochun Han, David J. Gennardo, Harrison K. Pappas, and Hyunsu Ju. Characterization of single crystal uranium-oxide thin films grown via reactive-gas magnetron sputtering on yttria-stabilized zirconia and sapphire. *Thin Solid Films*, 520(17):5616–5626, 2012.

[115] J. H. Claassen, S. A. Wolf, S. B. Qadri, and L. D. Jones. Epitaxial growth of niobium thin films. *Journal of Crystal Growth*, 81:557–561, 1987.

[116] J. Williams and R. A. J. Sambell. The uranium monocarbide-uranium mononitride system. *Journal of the Less-Common Metals*, 1(3):217–226, 1959.

[117] R. L. Barns. Niobium: Lattice parameter and density. *Journal of Applied Physics*, 39:4044–4045, 1968.

[118] Howard E. Swanson, Marlene C. Morris, and Eloise H. Evans. Standard X-ray diffraction powder patterns. *National Bureau of Standards, USA*, 1953.

[119] E. Lawrence Bright, S. Rennie, M. Cattelan, N. A. Fox, D. T. Goddard, and R. Springell. Epitaxial UN and α-U2N3 thin films. *Thin Solid Films*, 661:71–77, 2018.

[120] Andre Authier. *Early Days of X-ray Crystallography*. Oxford University Press, Oxford, UK, 1st edition, 2013.

[121] Bipin K. Agarwal. *X-Ray Spectroscopy: An Introduction*. Springer, Heidelberg, Germany, 2nd edition, 1991.

[122] J. Als-Nielsen and D. McMorrow. *Elements of modern X-ray physics*. A John Wiley & Sons, Chichester, UK, 2nd edition, 2011.

[123] T. Koopmans. Über die Zuordnung von Wellenfunktionen und Eigenwerten zu den Einzelnen Elektronen Eines Atoms. *Physica*, 1(1-6):104–113, 1934.

[124] Ingvar Lindgren. Chemical shifts in X-ray and photo-electron spectroscopy: A historical review. *Journal of Electron Spectroscopy and Related Phenomena*, 137-140(Special Issue):59–71, 2004.

[125] P. S. Kowalczky, L. Ley, R. L. Martin, F. R. McFeeley, and D. A. Shirley. Relaxation and final-state structure in XPS of atoms, molecules, and metals. *Faraday Discussions*, 60:7–17, 1975.

[126] J. J. Yeh and I. Lindau. Atomic Subshell Photoionisation Cross Sections and Asymmetry Parameters: $1 < Z < 103$. *Atomic Data and Nuclear Data Tables*, 32:1–155, 1985.

[127] F. Hadjarab and J. L. Erskine. Image properties of the hemispherical analyzer applied to multichannel energy detection. *Journal of Electron Spectroscopy and Related Phenomena*, 36:227–243, 1985.

[128] John Walton, Paul Wincott, Neal Fairley, and Alan Carrick. *Peak Fitting with CasaXPS*. Accolyte Science, Knutsford, UK, 2010.

[129] Zhong Long, Lizhu Luo, Yong Lu, Yin Hu, Kezhao Liu, and Xinchun Lai. Study on the electronic structure of U2N3 by XPS and first principles. *Journal of Alloys and Compounds*, 664:745–749, 2016.

[130] Elisabeth Thibaut, Jean-Pol Boutique, Jacques J. Verbist, Jean-Claude Levet, and Henri Noelt. Electronic structure of uranium halides and oxyhalides in the solid state. An x-ray photoelectron spectral study of bonding ionicity. *Journal of the American Chemical Society*, 104:5266–5273, 1982.

[131] G. C. Allen, I. R. Trickle, and P. M. Tucker. Surface characterization of uranium metal and uranium dioxide using X-ray photoelectron spectroscopy. *Philosophical Magazine B*, 43(4):689–703, 1981.

[132] Lizhu Luo, Yin Hu, Qifa Pan, Zhong Long, Lei Lu, Kezhao Liu, and Xiaolin Wang. Extended study on oxidation behaviors of UN0.68 and UN1.66 by XPS. *Journal of Nuclear Materials*, 501:371–380, 2018.

[133] A. Glaser, S. Surnev, F. P. Netzer, N. Fateh, G. A. Fontalvo, and C. Mitterer. Oxidation of vanadium nitride and titanium nitride coatings. *Surface Science*, 601:1153–1159, 2007.

[134] John M. Cowley. *Diffraction Physics*. Elsevier, Amsterdam, Netherlands, 3rd edition, 1995.

[135] Matts Björck and Gabriella Andersson. GenX: An extensible X-ray reflectivity refinement program utilizing differential evolution. *Journal of Applied Crystallography*, 40(6):1174–1178, 2007.

[136] A. L. Patterson. The scherrer formula for X-ray particle size determination. *Physical Review*, 56(10):978–982, 1939.

[137] L. G. Parratt. Surface Studies of Solids by Total Reflection of X-Rays. *Physical Review*, 95(2):359–369, 1954.

[138] L. Névot and P. Croce. Caractérisation des surfaces par réflexion rasante de rayons X. Application à l'étude du polissage de quelques verres silicates. *Revue de Physique Appliquée*, 15(3):761–779, 1980.

[139] S. K. Sinha, E. B. Sirota, S. Garoff, and H. B. Stanley. X-ray and neutron scattering from rough surfaces. *Physical Review B*, 38(4):2291–2311, 1988.

[140] A. Gibaud and S. Hazra. X-ray reflectivity and diffuse scattering. *Current Science*, 78(12):1467–1477, 2000.

[141] A. Gibaud, G. Vignaud, and S. K. Sinha. The correction of geometrical factors in the analysis of Xray reflectivity. *Acta Crystallographica Section A*, 49(4):642–648, 1993.

[142] G. Gutekunst, J. Mayer, V. Vitek, and M. Rühle. Atomic structure of epitaxial Nb-Al2O3 interfaces II . Misfit dislocations. *Philosophical Magazine A*, 75(5):1357–1382, 1997.

[143] S. B. Qadri, J. H. Claassen, P. R. Broussard, and S. A. Wolf. Orientation relationships and sapphire substrates. *Journal of the Less Common Metals*, 155:327 – 330, 1989.

[144] Y. H. Phang, C. Teichert, M. G. Lagally, L. J. Peticolos, J. C. Bean, and E. Kasper. Correlated-interfacial-roughness anisotropy in S1-x, Gex /Si superlattices. *Physical Review B*, 50(19):14435–14445, 1994.

[145] S. K. Sinha, M. K. Sanyal, S. K. Satija, C. F. Majkrzak, D. A. Neumann, H. Homma, S. Szpala, A. Gibaud, and H. Morkoc. X-ray scattering studies of surface roughness of GaAs/AlAs multilayers. *Physica B: Physics of Condensed Matter*, 198(1-3):72–77, 1994.

[146] Z. H. Ming, A. Krol, Y. L. Soo, Y. H. Kao, J. S. Park, and K. L. Wang. Microscopic structure of interfaces in Si1-xGex/Si heterostructures and superlattices studied by x-ray scattering and fluorescence yield. *Physical Review B*, 47(24):16373–16381, 1993.

[147] R. L. Headrick, J. M. Baribeau, and Y. E. Strausser. Anisotropic roughness in Ge/Si superlattices. *Applied Physics Letters*, 66:96–98, 1995.

[148] Z. Bao, R. Springell, H. C. Walker, H. Leiste, K. Kuebel, R. Prang, G. Nisbet, S. Langridge, R. C. C. Ward, T. Gouder, R. Caciuffo, and G. H. Lander. Antiferromagnetism in UO2 thin epitaxial films. *Physical Review B*, 88(13):134426, 2013.

[149] E. Lawrence Bright, R. Springell, D. G. Porter, S. P. Collins, and G. H. Lander. Synchrotron x-ray scattering of UN and U2N3 epitaxial films. *Physical Review B*, 100(13):134426, 2019.

[150] M. Blume. Magnetic scattering of x rays. *Journal of Applied Physics*, 57:3615–3618, 1985.

[151] J. P. Hannon, G. T. Trammell, M. Blume, and Doon Gibbs. X-ray resonance exchange scattering. *Physical Review B*, 61(10):1245–1248, 1988.

[152] Doon Gibbs, D. R. Harshman, E. D. Isaacs, D. B. McWhan, D. Mills, and C. Vettier. Polarization and resonance properties of magnetic X-ray scattering in holmium. *Physical Review Letters*, 61(10):1241–1244, 1988.

[153] E. D. Isaacs, D. B. McWhan, C. Peters, G. E. Ice, D. P. Siddons, J. B. Hastings, C. Vettier, and O. Vogt. X-Ray Resonance Exchange Scattering in UAs. *Physical Review Letters*, 62(14):1671–1674, 1989.

[154] J. P. Hill and D. F. Mcmorrow. X-ray resonant exchange scattering: Polarization dependence and correlation functions. *Acta Crystallographica Section A*, 52:236–244, 1996.

[155] D. C. Creagh. The atomic form factor and the X-ray dispersion corrections as tensor quantities: Comparisons between theory and experiment. *Radiation Physics and Chemistry*, 56:61–83, 1999.

[156] Wayne A. Hendrickson. Determination of Macromolecular Determination Structures from Anomalous Diffraction of Synchrotron Radiation. *Science*, 254(5028):51–58, 1991.

[157] J. M. Bijvoet, A. F. Peerdeman, and A. J. van Bommel. Absolute configuration of optically active substances. *Nature*, 142(3584):271–272, 1938.

[158] J. Kokubun and V. E. Dmitrienko. Anisotropic resonant X-ray scattering: Beauty of forbidden reflections. *European Physical Journal: Special Topics*, 208:39–52, 2012.

[159] R. W. James. *The Optical Principle of the Diffraction of X-rays*. Cornell Univ. Press., Ithaca, NY, USA, 1965.

[160] B. Greenberg. Bragg's law with refraction. *Acta Crystallographica Section A*, 45(3):238–241, 1989.

[161] J. O. Cross, M. Newville, J. J. Rehr, L. B. Sorensen, C. E. Bouldin, G. Watson, T. Gouder, G. H. Lander, and M. I. Bell. Inclusion of local structure effects in theoretical x-ray resonant scattering amplitudes using ab initio x-ray-absorption spectra calculations. *Physical Review B*, 58(17):11215–11225, 1998.

[162] N. Bernhoeft, A. Hiess, S. Langridge, A. Stunault, D. Wermeille, C. Vettier, G. H. Lander, M. Huth, M. Jourdan, and H. Adrian. Probe coherence volume and the interpretation of scattering experiments. *Physical Review Letters*, 81(16):3419–3422, 1998.

[163] G. H. Lander, S. K. Sinha, D. M. Sparlin, and O. Vogt. Spin Correlations in Actinide Materials: A Neutron Study of USb. *Physical Review Letters*, 40(8):523–526, 1978.

[164] N. Bernhoeft, G. H. Lander, M. J. Longfield, S. Langridge, D. Mannix, S. D. Brown, W. J. Nuttall, A. Hiess, C. Vettier, and P. Lejay. Anomalous displacement of magnetic Bragg peaks in the presence of short range order. *Journal of Physics: Condensed Matter*, 16(23):3869–3878, 2004.

[165] Michael V. Berry. Quantal phase factors accompanying adiabatic changes. *Proceedings of the Royal Society of London A*, 392:45–57, 1984.

[166] K. Prokeš, G. H. Lander, and N. Bernhoeft. Anomalous shift of magnetic diffuse scattering studied by neutron diffraction. *Journal of Physics: Condensed Matter*, 21(28):285402, 2009.

[167] E. Blackburn, R. Caciuffo, N. Magnani, P. Santini, P. J. Brown, M. Enderle, and G. H. Lander. Spherical neutron spin polarimetry of anisotropic magnetic fluctuations in UO2. *Physical Review B*, 72(18):184411, 2005.

[168] N. Magnani, R. Caciuffo, G. H. Lander, A. Hiess, and L. P. Regnault. Polarized-neutron-scattering study of the spin-wave excitations in the 3-k ordered phase of uranium antimonide. *Journal of Physics: Condensed Matter*, 22(11):116002, 2010.

[169] N. Masaki, H. Tagawa, and T. Tsuji. Uranium position in cubic U2N3+x. *Journal of Nuclear Materials*, 45:230–234, 1972.

[170] J. Tobisch and W. Hase. Structure Investigations of Two Uranium Nitrides U2N3+x. *Physica Status Solidi (b)*, 21(11), 1967.

[171] Eric Cockayne, Igor Levin, Hui Wu, and Anna Llobet. Magnetic structure of bixbyite α-Mn2O3: A combined DFT+U and neutron diffraction study. *Physical Review B*, 87(18):184413, 2013.

[172] R. M. Moon, W. C. Koehler, H. R. Child, and L. J. Raubenheimer. Magnetic Structures of Er2O3 and Yb2O3. *Physical Review*, 176(2):722–731, 1968.

[173] Paolo Santini, Stefano Carretta, Giuseppe Amoretti, Roberto Caciuffo, Nicola Magnani, and Gerard H. Lander. Multipolar interactions in f-electron systems: The paradigm of actinide dioxides. *Reviews of Modern Physics*, 81(2):807–863, 2009.

[174] S. P. Collins, D. Laundy, and A. Stunault. Anisotropic resonant diffraction from HoFe2. *Journal of Physics: Condensed Matter*, 13:1891–1905, 2001.

[175] Quan Yin, Andrey Kutepov, Kristjan Haule, Gabriel Kotliar, Sergey Y. Savrasov, and Warren E. Pickett. Electronic correlation and transport properties of nuclear fuel materials. *Physical Review B*, 84(19):195111, 2011.

[176] B. Szpunar and J. A. Szpunar. Thermal Conductivity of Uranium Nitride and Carbide. *International Journal of Nuclear Energy*, 2014:178360, 2014.

[177] G. C. Jain and C. Ganguly. Experimental evaluation of oxygen solubility in UN , PuN and (U,Pu)N. *Journal of Nuclear Materials*, 202:245–251, 1993.

[178] N. A. Javed. Oxygen solubility in uranium mononitride phase. *Journal of the Less-Common Metals*, 29:155–159, 1972.

[179] D. Yu. Lyubimov, A. V. Androsov, G. S. Bulatov, and K. N. Gedgovd. Thermodynamic Modeling of Oxygen Dissolution in Uranium Mononitride at 900 1400 K. *Radiochemistry*, 56(5):496–500, 2014.

[180] D. Bocharov, D. Gryaznov, Yu. F. Zhukovskii, and E. A. Kotomin. Ab initio modeling of oxygen impurity atom incorporation into uranium mononitride surface and sub-surface vacancies. *Journal of Nuclear Materials*, 416(1-2):200–204, 2011.

[181] Kezhao Liu, Lizu Luo, Lili Luo, Zhong Long, Zhanglian Hong, Hui Yang, and Sheng Wu. Initial oxidation behaviors of nitride surfaces of uranium by XPS analysis. *Applied Surface Science*, 280:268–272, 2013.

[182] D. Kuhlmann-Wilsdorf and Niels Hansen. Geometrically necessary, incidental and subgrain boundaries. *Scripta Metallurgica et Materiala*, 25(7):1557–1562, 1991.

[183] Robert Keyse. *Introduction to scanning transmission electron microscopy*. Routledge, London, UK, 1998.

[184] D. R. G. Mitchell and Bernhard Schaffer. Scripting-customised microscopy tools for Digital Micrograph. *Ultramicroscopy*, 103(4):319–332, 2005.

[185] N. F. Mott. The theory of the formation of protective oxide films on metals.-III. *Transactions of the Faraday Society*, 43:429–434, 1947.

[186] N. B. Pilling and R. E. Bedworth. The oxidation of metals at high temperature. *Journal of the Institute of Metals*, 29:529–582, 1923.

[187] D. J. M. Bevan, I. E. Grey, and B. T. M. Willis. The crystal structure of β-U4O(9-y). *Journal of Solid State Chemistry*, 7:1–7, 1986.

[188] K. Teske, H. Ullmann, and D. Rettig. Investigation of the oxygen activity of oxide fuels and fuel-fission product systems by solid electrolyte techniques. Part I: Qualification and limitations of the method. *Journal of Nuclear Materials*, 116:260–266, 1983.

[189] F. X. Zhang, M. Lang, J. W. Wang, W. X. Li, K. Sun, V. Prakapenka, and R. C. Ewing. High-pressure U3O8 with the fluorite-type structure. *Journal of Solid State Chemistry*, 213:110–115, 2014.

[190] J. Staun Olsen, L. Gerward, and U. Benedict. A New High-Pressure Phase of Uranium Nitride Studied by X-ray Diffraction and Synchrotron Radiation. *Journal of Applied Crystallography*, 18:37–41, 1985.

[191] V. I. Tseplyaev and S. V. Starikov. The atomistic simulation of pressure-induced phase transition in uranium mononitride. *Journal of Nuclear Materials*, 480:7–14, 2016.

[192] S. L. Hayes, J. K. Thomas, and K. L. Peddicord. Material property correlations for uranium mononitride. II. Mechanical properties. *Journal of Nuclear Materials*, 171:271–288, 1990.

[193] Yu F Zhukovskii, D Bocharov, and E A Kotomin. Chemisorption of a molecular oxygen on the UN (0 0 1) surface : Ab initio calculations. *Journal of Nuclear Materials*, 393:504–507, 2009.

[194] E. Lawrence Bright, S. Rennie, A. Siberry, K. Samani, K. Clarke, D. T. Goddard, and R. Springell. Comparing the corrosion of uranium nitride and uranium dioxide surfaces with H2O2. *Journal of Nuclear Materials*, 518:202–207, 2019.

[195] Brian J. Jaques, Jennifer Watkins, Joseph R. Croteau, Gordon A. Alanko, Beata Tyburska-Püschel, Mitch Meyer, Peng Xu, E. J. Lahoda, and Darryl P. Butt. Synthesis and sintering of UN-UO2 fuel composites. *Journal of Nuclear Materials*, 466:745–754, 2015.

[196] J. W. T Spinks and R. J. Woods. Water and Inorganic Aqueous Systems. *An Introduction to Radiation Chemistry*, pages 243–313, 1990.

[197] D. W. Shoesmith and S. Sunder. The prediction of nuclear fuel (UO2) dissolution rates under waste disposal conditions. *Journal of Nuclear Materials*, 190:20–35, 1992.

[198] Sunao Sugihara and Shosuke Imoto. Hydrolysis of uranium nitrides. *Journal of Nuclear Science and Technology*, 6(5):237–242, 1969.

[199] William G Burns. Effect of Radiation Type in Water Radiolysis. *Journal of the Chemical Society, Faraday Transactions I*, 77:2803–2813, 1981.

[200] S. Sunder, N. H. Miller, and D. W. Shoesmith. Corrosion of uranium dioxide in hydrogen peroxide solutions. *Corrosion Science*, 46(5):1095–1111, 2004.

[201] Ella Ekeroth, Olivia Roth, and Mats Jonsson. The relative impact of radiolysis products in radiation induced oxidative dissolution of UO2. *Journal of Nuclear Materials*, 355:38–46, 2006.

[202] Giuseppe Fadda and Giovanni Zanzotto. Symmetry breaking in monoatomic 2-lattices. *International Journal of Non-Linear Mechanics*, 36(3):527–547, 2001.

[203] G. H. Lander and M. H. Mueller. Neutron diffraction study of α-uranium at low temperatures. *Acta Crystallographica Section B*, 26:129–136, 1970.

[204] W. B. Lanham and T. C. Runion. PUREX process for plutonium and uranium recovery. Technical report, Oak Ridge National Laboratory, Tennessee, USA, 1949.

[205] Klara Insulander Björk, Aneta Herman, Marcus Hedberg, Christian Ekberg, Klara Insulander, Aneta Herman, Marcus Hedberg, Christian Ekberg, and Klara Insulander Björk. Scoping Studies of Dopants for Stabilization of Uranium Nitride Fuel. *Nuclear Science and Engineering*, 193(11):1255–1264, 2019.

.